Improving Type Ia Supernova Standard Candle Cosmology Measurements Using Observations of Early-Type Host Galaxies

by

Joshua Evan Meyers

A dissertation submitted in partial satisfaction of the

requirements for the degree of

Doctor of Philosophy

in

Physics

in the

Graduate Division

of the

University of California, Berkeley

Committee in charge:

Professor Saul Perlmutter, Chair

Professor Mark Davis

Professor Stephen Beckwith

Fall 2012

Improving Type Ia Supernova Standard Candle Cosmology Measurements Using Observations of Early-Type Host Galaxies

Abstract

Improving Type Ia Supernova Standard Candle Cosmology Measurements Using Observations of Early-Type Host Galaxies

by

Joshua Evan Meyers

Doctor of Philosophy in Physics

University of California, Berkeley

Professor Saul Perlmutter, Chair

Type Ia supernovae (SNe Ia) are the current standard-bearers for dark energy but face several hurdles for their continued success in future large surveys. For example, spectroscopic classification of the myriad SNe soon to be discovered will not be possible, and systematics from uncertainties in dust corrections and the evolution of SN demographics and/or empirical calibrations used to standardize SNe Ia must be studied. Through the identification of low-dust host galaxies and through increased understanding of both the SN – progenitor connections and empirical calibrations, host galaxy information may offer opportunities to improve the cosmological utility of SNe Ia.

The first half of this thesis analyzes the sample of SNe Ia discovered by the *Hubble Space Telescope (HST)* Cluster Supernova Survey augmented with *HST*-observed SNe Ia in the Great Observatories Origins Deep Survey (GOODS) fields. Correlations between properties of SNe and their host galaxies are examined at high redshift. Using galaxy color and quantitative morphology to determine the red sequence in 25 clusters, a model is developed to distinguish passively evolving early-type galaxies from star-forming galaxies in both clusters and the field. With this approach, 6 early-type cluster member hosts and 11 SN Ia early-type field hosts are identified. For the first time at $z > 0.9$, the correlation between host galaxy type and the rise and fall time of SN Ia light curves is confirmed. The relatively simple spectral energy distributions of early-type galaxies also enables stellar mass measurements for these hosts. In combination with literature host mass measurements, these measurements are used to show, at $z > 0.9$, a hint of the correlation between host mass and Hubble residuals reported at lower redshift. By simultaneously fitting cluster galaxy formation histories and dust content to the scatter of the cluster red sequences, it is shown that dust reddening of early-type cluster SN hosts is likely less than $E(B-V) \lesssim 0.06$. Hence, the early-type-hosted SNe Ia identified here occupy a more favorable environment to use as well-characterized high-redshift standard candles than other SNe Ia.

The second half of this thesis analyzes a sample of 40 deep, very high signal-to-noise ratio spectra of nearby SN Ia host galaxies. These host galaxies are chosen from the Nearby Supernova Factory, the SDSS-II SN Survey, and *Swift*-observed SNe, with the requirement that they have passive stellar populations suitable for detailed absorption line measurements. From these spectra, ages and the abundances of multiple elements, including Fe,

Mg, C, N, and Ca are derived. The correlation between SN decline rate and host galaxy age is rediscovered at high significance. SN decline rate is also shown to be correlated with host [Fe/H], [C/Fe], and [N/Fe]. In contrast to studies of mixed-host samples, however, no evidence is found supporting a correlation with SN Hubble residuals and host galaxy properties. The wide range in age spanned by the sample, in particular, suggests that age is not responsible for the host-mass – Hubble residual relation reported in the literature.

To Mom and Dad

Acknowledgments

Many people helped enable me to complete this thesis. First, I would like to thank **Saul Perlmutter** for providing me with the opportunity to study Type Ia supernovae. His guidance has improved my own research and reporting skills, not to mention a multitude of proposals, papers, posters and presentations. His ceaseless optimism had fueled not just my own, but I think the entire group's drive to slowly but surely unravel the inner workings of the Universe.

I have had a fantastic group to work with while at Berkeley. I could not hope to enumerate all of the ways that my colleagues have helped me, but here are at least a few. Thanks goes to **Kyle Dawson** for recruiting me to the group, and for his genuine interest in my graduate school career. Thanks goes to **Nao Suzuki** and **David Rubin** for usually being the first people I bounce new ideas off of, and for their consistently constructive responses. Thanks to **Kyle Barbary** for figuring out how this whole graduating thing works and thus enabling me to copy his example. Thanks to **Hannah Fakhouri** for being both someone to celebrate with and commiserate with depending on the success and failure of the Kansas basketball team (Rock chalk Jayhawk!) **Rahman Amanullah, Eric Hsiao, Xiaosheng Huang, Jakob Nordin, Eli Rykoff and Clare Saunders** have also all provided valuable insights into my research and have been a pleasure to work with.

Special thanks goes to **Chris Lidman** who always provided detailed comments on my work, and introduced me to astronomical data reduction. He and **Tomoki Morokuma** provided me with many of the spectra presented in the first part of this thesis. **Greg Aldering** likewise always gives thoughtful feedback on paper drafts and proposals. He played an essential role in developing the observing program which constitutes the second part of this thesis, as did **Genevieve Graves**, whose galaxy expertise and software were indispensable. Thanks to **Joe Hennawi** for his expertise and excellent spectroscopic reduction package. Special thanks to **Tony Spadafora** for all of his administrative work which has made my life that much easier.

I also wish to thank my wonderful family, who have supported me and my academic endeavors all the way through the "24th grade" now. My parents, **Jane and Evan** encouraged me to pursue my love of mathematics and science from an early age. I am fortunate to have a younger brother, **Daniel**, who can always make me laugh. His wife **Laura** and their son **Anderson** (and **Wicket** is on the way!) also help fill my life with joy.

Finally, I need to thank my wife **Jennie**, my constant cheerleader, who listened the worst of my personal doubts but never doubted in me herself. She is an amazing woman who continues to impress me every day. Her companionship is the best thing (among many good things!) that I will take away from grad school.

Contents

List of Figures

List of Tables

CHAPTER 1

Cosmology, Type Ia Supernovae and Host Galaxies

Observations of supernovae have played a role in determining the nature of the Universe for over a century now, the first case likely being SN1885 in the Andromeda galaxy. In his 1920 great debate with Heber Curtis concerning the size of the Milky Way galaxy and the Universe, Harlow Shapley invoked SN1885 (ultimately incorrectly) as evidence that the "spiral nebulae" such as Andromeda were likely within the confines of the Milky Way galaxy, for otherwise the inferred peak magnitude of SN1885 would be unbelievably bright. We now know that SN1885 was in fact a supernova with peak brightness thousands of times greater than garden variety novae (and that Andromeda does, indeed, reside far outside the confines of the Milky Way).

Our view of cosmology today is much larger than the view of either Shapley or Curtis in 1920. We know that the Milky Way is only one out of many tens of billions of galaxies in the observable Universe. We know that on large scales these galaxies are mutually moving away from each other; i.e. that the Universe is expanding. In fact, at the end of the preceding millennium, observations of Type Ia SNe much more distant than SN1885 surprisingly revealed that the Universe's rate of expansion is accelerating, precisely the opposite of expectations at the time. Fifteen years and orders of magnitude more data later, the origin of this acceleration is still quite mysterious, apparently contributing $\sim 75\%$ of the energy budget of the Universe and exhibiting negative pressure. Due mostly to our lack of understanding, it has been dubbed "dark energy."

This thesis details my own efforts to make a small contribution towards understanding the nature of dark energy.

1.1 The expansion history of the Universe

The composition of the Universe and nature of its components are encoded in the history of its expansion. Under Einstein's general theory of relativity, a homogeneous, isotropic universe has just one degree of freedom, the scale factor $a(t)$, which parame-

terizes the relative distance between any two positions as the universe expands or contracts. The scale factor is conventionally set equal to 1 today. The redshifting of spectroscopic features is directly related to the scale factor at the time the light was emitted as $1 + z = \lambda_{\rm obs}/\lambda_{\rm em} = 1/a(t_{\rm em})$. Assuming the Universe is currently dominated by matter and dark energy, the evolution of the scale factor depends on cosmological parameters $\Theta = \{H_0, \Omega_M, \Omega_X, w_X(z)\}$ through the Friedman equation[1]:

$$H(z;\Theta) = \frac{\dot{a}}{a} = H_0\sqrt{\Omega_M(1+z)^3 + \Omega_X f_X(z; w_X(z)) + (1-\Omega_M-\Omega_X)(1+z)^2}, \tag{1.1}$$

where

$$f_X(z; w_X(z)) = \exp\left(3\int_0^z \frac{1+w_X(z')}{1+z'}dz'\right) \tag{1.2}$$

characterizes the scale-factor dependence of dark energy as a generic perfect fluid with equation of state $w_X(z) = p_X(z)/\rho_X(z)$, $\Omega_M = \rho_M/\rho_{\rm crit}$ is the energy density of matter relative to the critical density $\rho_{\rm crit} = 3H_0^2c^2/8\pi G$, $\Omega_X = \rho_X/\rho_{\rm crit}$ is the energy density of dark energy relative to $\rho_{\rm crit}$ and H_0 is the current expansion rate.

The Universe's expansion history can be measured in different ways, one of which is through the mapping of the luminosity distance – redshift relation using a standard candle. By definition, a standard candle with intrinsic luminosity L will have flux F if observed from a luminosity distance of $d_L = \sqrt{L/4\pi F}$. Under general relativity, the luminosity distance depends on Θ as:

$$d_L(z;\Theta) = \begin{cases} \frac{1+z}{\sqrt{|1-\Omega_M-\Omega_X|}}\ \sin\left[\sqrt{|1-\Omega_M-\Omega_X|}\int_0^z H(z';\Theta)^{-1}dz'\right] & \text{if } \Omega_M+\Omega_X > 1 \\ (1+z)\int_0^z H(z';\Theta)^{-1}dz' & \text{if } \Omega_M+\Omega_X = 1 \\ \frac{1+z}{\sqrt{|1-\Omega_M-\Omega_X|}}\ \sinh\left[\sqrt{|1-\Omega_M-\Omega_X|}\int_0^z H(z';\Theta)^{-1}dz'\right] & \text{if } \Omega_M+\Omega_X < 1 \end{cases} \tag{1.3}$$

In practice, because of the great dynamic range of luminosity distances studied with cosmological standard candles, the distance modulus is often used in place of the luminosity distance:

$$\mu_{GR}(z,\Theta) = 5\log_{10}(d_L(z,\Theta)/10\text{ pc}) \tag{1.4}$$

where the GR distinguishes the theoretical general relativistic distance modulus from measured standard candle distance moduli developed in the next section.

1.2 SN Measurements of the expansion history

The usefulness of any standard candle depends on how accurately brightness differences due to distance can be distinguished from intrinsic luminosity differences. The first

[1]For details of the derivation of $H(z;\Theta)$ or other equations in this section, please see any of a large number of cosmology textbooks or the excellent review article of Frieman et al. (2008).

suggestion that SNe could be used as standard candles came from Baade (1938), who estimated that their intrinsic brightness dispersion was ~ 1.1 magnitudes. Soon thereafter, it became known that supernovae existed in at least two flavors, those with hydrogen in their spectra (type II) and those without (type I)(Minkowski 1941). Using better light curve data, Kowal (1968) showed that the intrinsic peak brightness dispersion of the Type I subclass was just 0.61 magnitudes, and published the first SN Hubble diagram. Later, the Type I class would be further divided, with the subclass Type Ia defined by the presence of strong Si II $\lambda 6355$ absorption blueshifted to $\sim 6100\mathring{A}$. This subclass was found to be an even better standard candle, with an intrinsic dispersion of just 0.35 magnitudes(Sandage & Tammann 1993), close to the value accepted today.

The utility of the SN Ia subclass as a standard candle is secured by exploiting empirical calibrations between their peak brightnesses and secondary light curve properties. The most common of these are the brighter–broader and the bluer–brighter relations, in which SNe Ia with light curves that rise and fall more slowly or have bluer $B - V$ color at the time of maximum have brighter peak magnitudes (Phillips 1993; Tripp 1998) (Figure 1.1). Various light curve fitting software packages exist to quantify the light curve breadth and color from photometry. The SALT2 light curve fitter uses the variable x_1 to quantify light curve shape, c to quantify the color, and m_B to quantify the observed peak brightness in the B-band (Guy et al. 2007). With these variables, the broader–brighter and bluer–brighter relations are used to estimate the distance modulus to the $i^{\rm th}$ SN Ia as

$$\mu^i_{\rm SN} = m^i_B - M_B + \alpha x^i_1 - \beta c^i, \tag{1.5}$$

where α, and β are the slopes of the calibration relations and M_B is the absolute magnitude of a "typical" SN Ia with $x_1 = c = 0$. The difference between the distance modulus obtained from the SN Ia (Equation 1.5) and that inferred from the redshift and cosmological parameters (Equation 1.4) is then known as the Hubble residual:

$$HR^i = \mu_{\rm SN}(z^i, x^i_1, c^i, m^i_B; \alpha, \beta, M_B) - \mu_{\rm GR}(z^i; \Theta) \tag{1.6}$$

Although details concerning the covariance of errors and the treatment of intrinsic dispersion vary, generically, constraints on cosmological parameters Θ and SN Ia parameters $\{\alpha, \beta, M_B\}$ are determined simultaneously by minimizing the χ^2 statistic of Hubble residuals. Intuitively, one can imagine that the derived distance to a SN, together with the known speed of light, constrains the length of time in which light has traveled since the SN explosion. The redshift of the light directly measures the relative size of the Universe at the time of explosion. Taken together, these give the expansion history of the Universe as a function of look-back time.

At the tail end of the preceding millennium, a few score SNe Ia up to moderate redshift ($z \sim 0.5$) were used to discover the remarkable result that the expansion of the Universe was not decelerating as expected due to attractive pull of gravity on the Universe's matter content, but instead was accelerating due to some unknown component of the Universe, potentially Einstein's cosmological constant (Riess et al. 1998; Perlmutter et al. 1999).

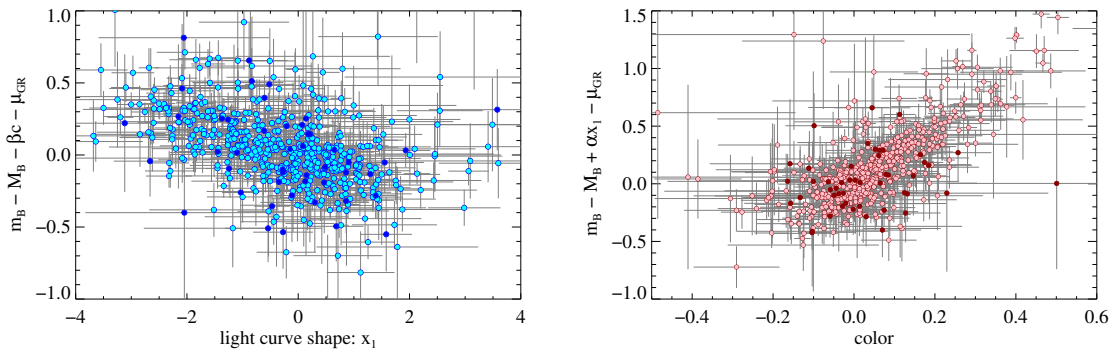

Figure 1.1. Left: Illustration of the broader–brighter relation. The SALT2 light curve shape parameter x_1 is plotted against the Hubble residual when accounting for color but not light curve shape. The slope of the relation is $-\alpha$. **Right:** Illustration of the bluer–brighter relation. The SALT2 peak light curve color parameter c is plotted against the Hubble residual when accounting for light curve shape but not color. The slope is $-\beta$. In both plots, brighter SNe Ia are toward the bottom, and darker symbols indicate SNe Ia with $z > 0.9$, showing that these calibration relations are relatively unconstrained at high redshift.

Today, compilations of SNe number in the hundreds and reach $z \sim 1.4$ (Kowalski et al. 2008; Hicken et al. 2009; Amanullah et al. 2010; Suzuki et al. 2012), with a handful of even higher redshift objects (Riess et al. 2001; Rodney et al. 2012; Rubin et al. 2012) (Figure 1.2). The Union 2 compilation of 557 SNe Ia observed before the start of my research constrained the constant dark energy equation of state in a flat universe to be $w_X = -0.997^{+0.077}_{-0.082}$ (Amanullah et al. 2010), which is compatible with a cosmological constant in which w_X is precisely -1. However, dynamical models of dark energy in which w_X may vary with redshift are also compatible with this data. Constraints on time-varying dark energy can be greatly improved by adding SNe Ia at high redshift ($z \gtrsim 1$). At lower and intermediate redshifts, the systematic uncertainties associated with SNe Ia are now comparable to the statistical uncertainties, implying that progress in distinguishing dark energy from a cosmological constant will also require refining the SN Ia technique to address systematics.

1.3 Improving SN Ia distance measurements using early-type host galaxies

This thesis describes my own efforts to improve SN Ia dark energy constraints through two different programs, both of which address SN Ia systematic uncertainties by exploiting properties of host galaxies. Early-type hosts, in particular, offer several paths towards the reduction of SN Ia systematic uncertainties and the improvement of SN Ia distance measurements:

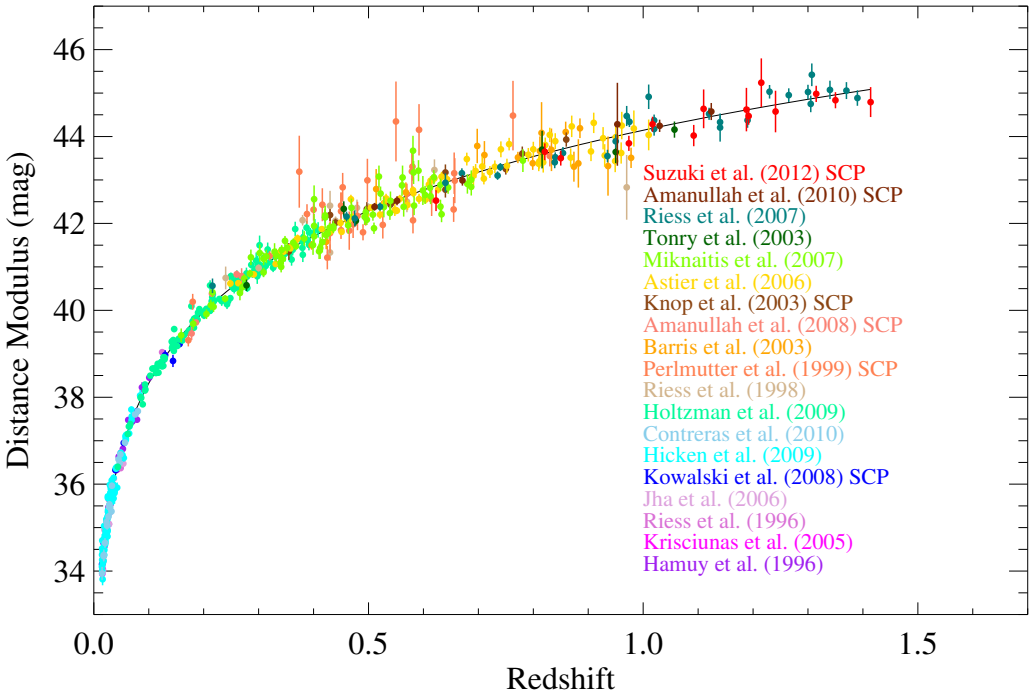

Figure 1.2. The Hubble diagram published in Suzuki et al. (2012). The SNe Ia are color coded by the publication in which they first appear. Note the paucity of data above redshift one, particularly before the addition of the Suzuki et al. (2012) data. This redshift range is sensitive to measurements of time-varying dark energy.

Typing: Contamination of the Hubble diagram by non-Type-Ia SNe can bias cosmological parameter constraints. Classifying SN types is most robustly done spectroscopically. Unfortunately, spectroscopic observations can be expensive and sometimes inconclusive, especially at the highest redshifts where SNe are most capable of measuring time-varying dark energy. SNe hosted by early-type galaxies, however, are almost always Type Ia, providing an inexpensive alternative classification mechanism.

Dust: The interpretation of the effects of host galaxy dust is the largest astrophysical uncertainty in SN Ia distance measurements. While the sign of the observed SN Ia color–magnitude relation is consistent with dust, i.e. redder SNe Ia are also fainter, the slope of this relation ($\beta \sim 2.5$) is markedly different from the total-to-selective extinction coefficient of Milky Way dust ($R_B \sim 4.1$). Analysis of SN Ia spectrophotometric time series suggests that part of the relation is intrinsic, related to the diversity of particular spectral features (Chotard et al. 2011). SNe Ia hosted by early-types galaxies, which are expected to be largely dust-free, offer another way to decouple the intrinsic component of β from dust. Lessons learned about the intrinsic color–magnitude relation can then be applied to mixed host samples.

Demographic shifts: Another possible contribution to SN Ia distance modulus systematic uncertainties is the evolution of SN Ia properties. By classifying hosts as early- and late-type, we can check for evolution of SN Ia host demographics.

Understand SN Ia calibrations: The calibrations that bring the intrinsic dispersion of distance moduli down from $\sim 35\%$ to $\sim 15\%$ are empirical. Early-type galaxy spectra are well understood and offer a window into the nature of SN progenitor properties, such as age, metallicity, and element abundances. By probing the relations between SN properties, and their progenitor population properties, we can unravel the underlying physics of empirical calibrations. Additionally, we can predict what effect, if any, changes in progenitor properties with redshift may have on SNe Ia.

The remainder of this thesis is broken into two parts. The first part analyzes SN Ia host galaxies at $z > 0.9$, primarily from the *Hubble Space Telescope* Cluster Supernova Survey, a program designed to efficiently discover and follow high redshift SNe Ia by targeting massive galaxy clusters. Early-type galaxies dominate these clusters, providing ample opportunity to study high redshift SN Ia typing, dust and demographic shifts. The second part of this thesis analyzes very high signal-to-noise ratio spectroscopy of a sample of nearby SN Ia host galaxies. The detailed measurements of absorption line strengths in these spectra reveal the ages, metallicities, and individual element abundances of the progenitor populations of SNe Ia. This data is analyzed to uncover the fundamental progenitor properties responsible for SN Ia diversity and empirical calibrations.

Part I

High Redshift Host Galaxies of Type Ia Supernovae

CHAPTER 2

Introduction

The use of Type Ia supernovae (SNe Ia) as standard candles in estimating astronomical distances has proven indispensable for modern cosmology, leading to the remarkable discovery that the expansion of the Universe is accelerating (Riess et al. 1998; Perlmutter et al. 1999). Together with measurements of the cosmic microwave background (Dunkley et al. 2009; Komatsu et al. 2011) and baryon acoustic oscillations (Eisenstein et al. 2005; Percival et al. 2010), our recent compilation of the myriad SN surveys that led to and followed the initial discovery has now constrained the dark energy equation of state to be $w = -0.974^{+0.054}_{-0.058}(\text{stat})^{+0.075}_{-0.080}(\text{stat+sys})$ (Amanullah et al. 2010). The constraints from the 557 SNe Ia in this compilation are now limited by systematic uncertainties. Additional SN Ia observations will not greatly improve dark energy constraints until the systematic errors are reduced.

Improvements in SN Ia distance estimates have historically followed two paths. The first path is to identify subsets of SNe with smaller intrinsic brightness dispersion (e.g. the Type Ia subset or "Branch-normal" SNe Ia). The second path is to make corrections exploiting empirical correlations between SN brightness and other observables (e.g. light curve shape and color). The properties of SN Ia host galaxies offer additional variables with which to search for smaller dispersion subsets or correlated observables. In fact, such a correlation has recently been reported: SNe Ia in more massive hosts are brighter after light curve shape and color corrections (Kelly et al. 2010; Sullivan et al. 2010; Lampeitl et al. 2010).

The brightnesses of SNe Ia are correlated with their colors at maximum light: bluer SNe Ia are brighter. This trend is broadly consistent with extinction due to dust as commonly described by $R_B = A(B)/E(B-V)$ (Cardelli et al. 1989). When relating SN Ia colors to peak magnitudes, the parameter $\beta = \Delta M_B/\Delta c$ is used, where $c = (B-V)_{max} - \langle B-V\rangle_{max}$; e.g. c is the excess color at maximum brightness with respect to the average. Direct fits of SN Ia observations have found that β is considerably smaller than the value of R_B observed in the Milky Way diffuse interstellar medium, suggesting that an intrinsic component to the bluer–brighter relation is also important (Tripp 1998; Astier et al.

[2]This part is meant to stand alone, and some material from Chapter 1 may be repeated here.

2006; Conley et al. 2007; Nobili & Goobar 2008). The systematic errors associated with the interpretation of β, i.e., what fraction is attributable to dust and how might that evolve with redshift, are now comparable to the statistical errors of SN Ia surveys (Kowalski et al. 2008; Wood-Vasey et al. 2007). However, if one were to identify SN Ia hosts with small extinction, then a single component of the SN Ia color-magnitude relation, the intrinsic component, could be isolated.

Here we analyze the host galaxies of $z > 0.9$ SNe Ia drawn from the *HST* Cluster SN Survey (Dawson et al. 2009, PI-Perlmutter: GO-10496) and surveys of the GOODS fields (Blakeslee et al. 2003b; Riess et al. 2004, 2007). We investigate how host properties correlate with SN Ia properties and identify hosts minimally affected by dust. Particularly interesting host properties such as age and metallicity are usually difficult to obtain, but are correlated with the position of a galaxy on its cluster's red sequence (Gallazzi et al. 2006). The environment of the *HST* Cluster SN Survey thus lends itself to a particular analysis strategy: how does the location of a host galaxy on its cluster's red sequence correlate with its SN, what does it imply about the SN type, and how does it begin to parse the origin of the SN reddening law?

Our analysis is organized as follows: In Chapter 3 we describe progress to date of SN host galaxy studies at lower redshifts. In Chapter 4 we describe the *HST* Cluster SN Survey and the *HST* SN surveys of the GOODS fields, the data taken, and the various photometric, morphological, and spectroscopic quantities that we derive from them. In Chapter 5 we describe how, by using the color-magnitude locations of spectroscopically confirmed red-sequence cluster members, we predict the location of the red sequence for each cluster, including those without extensive spectroscopic coverage. Additionally, we demonstrate how quantitative morphology parameters can be used to enhance the contrast of the red sequence to more easily fit a color-magnitude relation (CMR) for each cluster. In Chapter 6 we describe criteria to classify the observed SN hosts, and in Chapter 7 we use expected rates of SNe Ia and core collapse SNe (SNe CC) in their individual galaxies to help type the SNe. In Chapter 8 we investigate limits on extinction for SNe hosted by early-type galaxies. In Chapter 9 we investigate correlations between SN properties and properties of their host galaxies. Finally, in Chapter 10 we summarize our conclusions and discuss their implications.

This analysis is part of a series of ten papers that report supernova results from the *HST* Cluster Supernova Survey (PI: Perlmutter, GO-10496), a survey to discover and follow SNe Ia of very distant clusters. Paper I (Dawson et al. 2009) describes the survey strategy and discoveries. Paper II (Barbary et al. 2012a) reports on the SN Ia rate in clusters. The current work, which is also presented in Paper III (Meyers et al. 2012), addresses the properties of the galaxies that host SNe Ia. Paper IV Ripoche et al. (2011) introduces a new technique to calibrate the "zeropoint" of the NICMOS camera at low count rates, which is critical for placing NICMOS-observed SNe Ia on the Hubble diagram. Paper V (Suzuki et al. 2012) reports the SN Ia light curves and cosmology from the *HST* Cluster SN Survey. Paper VI (Barbary et al. 2012b) reports on the volumetric field SN Ia rate. Melbourne et al. (2007), one of several unnumbered papers in this series, present a Keck Adaptive Optics

observation of a $z = 1.31$ SN Ia in *H*-band. Barbary et al. (2009) report the discovery of the extraordinary luminous supernova, SN SCP06F6. Morokuma et al. (2010) present the spectroscopic follow-up observations for SN candidates. Hsiao et al. (2011) develop techniques to remove problematic artifacts remaining after the standard STScI pipeline. A separate series of papers, ten to date, reports on cluster studies from the *HST* Cluster SN Survey: Brodwin et al. (2011); Eisenhardt et al. (2008); Jee et al. (2009); Hilton et al. (2007, 2009); Huang et al. (2009); Santos et al. (2009); Strazzullo et al. (2010); Rosati et al. (2009); and Jee et al. (2011).

CHAPTER 3

SN Ia Hosts

In this chapter we briefly discuss the relationships between SNe and their host galaxies with particular emphasis on early-type host galaxies of SNe Ia. We also introduce the *HST* Cluster SN Survey, which targets massive galaxy clusters to increase the yield of SN Ia discoveries, particularly those in low-dust early-type hosts.

3.1 SN typing by host

Early-type galaxies have almost never been observed to host Type Ib/c or Type II SNe (hereafter SNe CC), which are generally thought to originate from the collapse of the cores of massive (and hence young) stars. In an extensive literature search of hundreds of SNe CC, Hakobyan et al. (2008) uncovered 22 examples reported as being hosted by early-type galaxies, but ultimately reclassified 19 of these galaxies as late-type. The SN associated with one of the remaining three galaxies has since been reclassified as a cataclysmic variable star within the Milky Way (Leonard 2010). The SNe hosted by the remaining two early-type hosts, SN2000ds and SN2005cz, are both members of the SN2005E-like subset of faint "Ca-rich" SNe Ib. The origins of SNe in this subset are still under debate, though it is clear that they are readily distinguishable from SNe Ia by their faint peak magnitudes ($M_B \sim -15$ compared to $M_B \sim -18$ for even a very faint SN Ia) (Perets et al. 2010; Kawabata et al. 2010). In a separate analysis of the near ultraviolet and optical colors of early-type SN hosts (including two which were reclassified by Hakobyan et al.), Suh et al. (2011) find that the early-type hosts of SNe CC have had more recent star formation and occupy a different part of the UV-optical color-magnitude diagram than identically selected early-type hosts of SNe Ia.

Despite these rare possible exceptions, SNe hosted by early-type galaxies are overwhelmingly Type Ia. Typing high-redshift ($z > 0.9$) SNe spectroscopically can be done from space with *HST* (Riess et al. 2004) but requires a significant investment of orbits (4-8 per SN at $z \sim 1.2$). Not only are SNe increasingly faint at higher redshift, but the rest-frame features used to identify a Type Ia become shifted out of the optical wavelengths. Ground-based spectroscopy faces the additional difficulty that the night sky becomes increasingly

bright at redder wavelengths. With ideal conditions and by targeting the SN near the peak of its light curve, Morokuma et al. (2010) have shown it is possible to spectroscopically type SNe Ia as high as $z = 1.34$ from the ground, but this is by no means typical. In fact, many of the lower redshift targets in this paper (of which many also had higher signal-to-noise ratio spectra) yielded inconclusive types. Classifying SNe in ellipticals galaxies as Type Ia can therefore provide an efficient and robust alternative to potentially expensive spectroscopic typing at high redshift.

3.2 Dust in early-type SN Ia hosts

Early-type SN Ia hosts offer an additional advantage to typing: they generally contain only small amounts of dust. Although *HST* images of the cores of nearby early-type galaxies indicate that $\sim 50\%$ exhibit optical absorption due to dust in small disks or filaments, these are usually confined to the central few hundred parsecs (van Dokkum & Franx 1995; Tomita et al. 2000; Rest et al. 2001; Tran et al. 2001; Lauer et al. 2005; Ferrarese et al. 2006). In contrast, SNe Ia hosted by early-type galaxies are spatially distributed following the optical light of their host galaxies (Förster & Schawinski 2008). Observations of emission from dust at far-infrared (FIR) wavelengths suggest that additional dust is diffusely distributed throughout at least some nearby early-type galaxies (Goudfrooij & de Jong 1995; Temi et al. 2004, 2007). The inferred dust mass relative to the stellar mass of these galaxies varies greatly; at fixed optical luminosity, Temi et al. (2007) measure FIR luminosities that span two orders of magnitude. At the low dust-mass end, at least several early-type galaxies (3 elliptical and 3 S0) with $M_B \sim -18$ to -20, are undetected in the *Herschel Space Observatory* survey of the Virgo cluster. Upper limits constrain the associate dust mass of these galaxies to be $< 10^4$ M $_\odot$ (Clemens et al. 2010). For comparison, the Virgo cluster spiral galaxies in the same B-band luminosity range also observed by Herschel have dust masses of $\sim 10^7 - 10^8$ M $_\odot$) (Davies et al. 2011). Early-type galaxy dust masses derived from Spitzer tend to fall in the range $10^4 - 10^6$ (Kaneda et al. 2007). To estimate the extinction associated with a certain mass of dust, we use $\langle A_V \rangle = M_d \Gamma / \Sigma$, with Σ the area of the dust feature, $\langle A_V \rangle$ the average V-band absorption in that area, and $\Gamma \sim 6 \times 10^{-6}$ mag kpc^2 M$_\odot^{-1}$ the visual mass absorption coefficient (van Dokkum & Franx 1995). For dust uniformly distributed throughout a disc with radius 3 kpc, which is representative of the half-light radii of the galaxies considered here, the absorption ranges from $A_V < 0.002$ to ~ 0.2. Since dust is not actually distributed in a uniform foreground screen, but rather is embedded within the galaxy, these values only provide a rough guide to the expected extinction along the lines of sight toward early-type hosted SNe Ia.

At high redshift, FIR observations of SN Ia hosts are impractical. However, optical observations of the integrated colors of galaxies can also place constraints on the extinction expected from diffuse dust. For example, consider the case where galaxy colors are the combined result of stellar population age, metallicity, and dust. The contributions of age and metallicity to the integrated color can be removed by using an auxiliary correlated vari-

able. At low redshift, the spectral absorption feature Mg_2 is such a variable. The equivalent width of Mg_2 is expected to correlate with the rest-frame intrinsic (i.e. unextinguished) $B-V$ color of elliptical galaxies (Faber et al. 1989). The line strength increases with increasing galaxy age and metallicity, and consequently color, but because the wavelength interval of the line is relatively narrow it should not correlate significantly with dust. Schlegel et al. (1998) measured the scatter about the Mg_2-color relation for nearby elliptical galaxies to be just $\sigma_{BV} = 0.0257$ mag. If at least some elliptical galaxies are effectively dust-free ($A_V < 0.01$), which seems likely given the range of dust masses discussed above, then this scatter measurement implies an absolute limit on dust reddening at the $E(B-V) \sim 0.03$ level. While spectroscopy of the Mg_2 feature may not be feasible at high redshift, the red sequence may provide a readily available alternative calibrator.

Two mechanisms have been proposed to explain the origin of the dust found in elliptical galaxies. Elliptical galaxies may accrete dust and gas during (minor) mergers with dusty late-type galaxies. This scenario is supported by observations that the motions of dust and gas in some nearby early-type galaxies seem unrelated to the motions of their stars (Goudfrooij et al. 1994; van Dokkum & Franx 1995; Caon et al. 2000). As part of the Galaxy-Zoo project, Kaviraj et al. (2011) find that early-type galaxies with prominent dust lanes are likely associated with mergers due to the frequency with which they present disturbed morphologies compared to a control sample without dust lanes. Prominent dust lane early-type galaxies are relatively rare, however, constituting just 4% of the early-type Galaxy-Zoo sample, and are even rarer in cluster environments..

Noting that the dynamical freefall time for a merging galaxy (several $\sim 10^8$ yr) is comparable to the sputtering lifetime of dust grains in the hot interstellar medium of early-type galaxies ($\sim 10^7 - 10^8$ yr), Temi et al. (2007) argue that dust originating from mergers must be resupplied at least every $\sim 10^8$ yr. Such a high rate of early-type – late-type mergers is not observed, however. As an alternative, they propose an internal origin for diffuse dust in early-type galaxies: dust is generated in the atmospheres of evolved red giant stars (Knapp et al. 1989; Athey et al. 2002) and may accumulate in the concentrated disks of dust commonly observed in the centers of early-type galaxies(Mathews & Brighenti 2003). Intermittent AGN activity can then buoyantly transport this dust out to large radii where it will be destroyed by sputtering in the hot interstellar medium.

One possible caveat to the expectation of low extinction SNe Ia in early-type galaxies is small amounts of recent star-formation seen in some early-type galaxies, especially lenticular galaxies, and associated dust (Yi et al. 2005; Donas et al. 2007; Schawinski et al. 2007; Kaviraj et al. 2007, 2008; Temi et al. 2009a,b). Together with the expected increase in the SN Ia rate with star-formation rate (see §3.3 below), it is possible that an SN Ia in a mostly dust-free galaxy could, nevertheless, suffer from extinction. Fortunately, recent star-formation in early-type galaxies is usually confined to their inner regions (Kuntschner et al. 2006; Sarzi et al. 2006), whereas, as mentioned above, the spatial distribution of SNe Ia follows the optical light distribution. Furthermore, we have directly constrained star-formation using spectroscopy of our host galaxies and its possible effect in increasing the galactic SN Ia rate (see Chapter 7). We expect that most of our early-type hosted SNe Ia

are not associated with recent star-formation.

3.3 SN Ia properties by host

Several lines of evidence suggest that the demographics of SNe Ia hosted by early-type galaxies are different than those of SNe Ia hosted by late-type galaxies. Using infrared magnitudes of low-redshift SN Ia host galaxies in the 2MASS survey, Mannucci et al. (2005) measured the SN Ia rate per unit stellar mass for different host types. They found a rate ~ 20 times larger in late-type galaxies than in E/S0 galaxies. Splitting the galaxies by color (as a proxy for star formation) they found a rate ~ 30 times larger in blue galaxies than in red galaxies. Sullivan et al. (2006) fit SED models to five-band galaxy photometry to directly constrain the star formation rate and mass of intermediate redshift SN Ia host galaxies in the Supernova Legacy Survey (SNLS). This analysis showed that the SN Ia rate is ~ 10 times larger per unit stellar mass in actively star-forming galaxies than in passive galaxies. For a given episode of star formation, the SN Ia rate quickly peaks and declines as the progenitor population ages.

Perhaps not surprisingly, the properties of SNe themselves are also correlated with the properties of their hosts. At low redshift, SNe Ia hosted by late-type, spiral galaxies tend to have broader (slower) light curves on average (Hamuy et al. 1996; Gallagher et al. 2005), although interestingly, Hicken et al. (2009) find that the broadest SN light curves are found in SNe hosted by Sb-Sc galaxies and not younger Sd-Irr galaxies. Sullivan et al. (2006) showed that this distinction extends to intermediate redshift hosts with actively star-forming galaxies (generally late-type) hosting SNe Ia with broader light curves. Several analyses suggest that SNe Ia hosted by early-type galaxies may have a smaller intrinsic peak brightness dispersion after light curve and color corrections are applied (Sullivan et al. 2003; Jha et al. 2007; Sullivan et al. 2010; Lampeitl et al. 2010), though at least one analysis finds the opposite result (Hicken et al. 2009).

Since SN Ia properties are correlated with the properties of their host galaxies, and the demographics of galaxies change with redshift, the demographics of SNe Ia will also change with redshift. This shift can bias inferred cosmological parameters if not handled carefully. Tests for bias in cosmology constructed by segregating SNe Ia by host-type were discussed in Perlmutter et al. (1997) and carried out with a small sample of SNe Ia (17) in Perlmutter et al. (1999), and a larger sample (39) in Sullivan et al. (2003) without any differences in fitted cosmological parameters apparent within the statistical uncertainties. However, with a much larger sample from the SNLS (Sullivan et al. 2010), it becomes possible to see subtle differences in β dependent on the host. SNe Ia hosted by lower specific star-formation rate galaxies obey a shallower relation than SNe Ia hosted by higher specific star-formation rate galaxies ($\beta \sim 2.8$ compared to $\beta \sim 3.5$; the exact value depends on the choice of specific star-formation rate delineating the low and high star-forming samples). Similarly, using SNe drawn from the Sloan Digital Sky Survey (SDSS), Lampeitl et al. (2010) find $\beta \sim 2.5$ for passive hosts and $\beta \sim 3$ for star-forming hosts. Since β reflects

the combined effect of host galaxy dust extinction and an intrinsic SN color-luminosity relation, it is not surprising that β should be closer to the Milky Way dust total-to-selective extinction coefficient of $R_B = 4.1$ in dusty star-forming galaxies than in passive galaxies. This result also suggests that as the fraction of low star-forming early-type galaxies decreases with redshift and the fraction of high star-forming galaxies increases, the average value of the relation $\langle \beta\,(z) \rangle$ will increase and introduce a bias on measurements of w if the subpopulations are not treated separately.

Perhaps a more important consideration, however, is the recently reported evidence for a correlation between host galaxy mass and Hubble residual after applying corrections for light curve shape and color. By fitting SEDs derived from the PEGASE2 (Fioc & Rocca-Volmerange 1997, 1999) stellar population synthesis models to SDSS photometry of host galaxies, Kelly et al. (2010) measured the host masses of the low-z SNe in the Hicken et al. (2009) analysis and compared these to their Hubble residuals obtained with a variety of light curve fitters. They found that SNe Ia in more massive galaxies are brighter (after stretch and color corrections) by about ~ 0.1 mag. Sullivan et al. (2010) found a similar relation in SNLS SNe and host galaxy photometry using PEGASE2 SEDs and the SiFTO light curve fitter (Conley et al. 2008). Finally, Lampeitl et al. (2010) found a similar relationship in the SDSS-II SN survey by segregating SNe by host type, with passive galaxies hosting brighter post-correction SNe. However, because the passive galaxies in this dataset are on average more massive than the star-forming galaxies, this relation can also be framed in terms of host galaxy mass. These results are particularly important for targeted surveys, such as those that target massive galaxies at low redshift or the HST Cluster SN Survey which targets clusters of massive galaxies at high redshift. The demographics of hosts from these surveys are substantially different than for untargeted surveys. The SNe they discover should be on average brighter (after color and light curve shape corrections) than those in other surveys, a property which needs to be corrected for in cosmological analyses.

3.4 The HST Cluster SN Survey

By targeting massive galaxy clusters, the *HST* Cluster SN Survey was designed to efficiently discover well-characterized SNe Ia at high redshift. Clusters are rich in elliptical galaxies, which constitute a linear red sequence in a color-magnitude diagram. The observed evolution of the red-sequence slope indicates that ellipticals in the cores of clusters have passively evolved since forming at high-redshift ($z > 2$) and that the redder colors of more massive galaxies is due to increased metallicity (Kodama 1997; Kodama & Arimoto 1997; Kauffmann & Charlot 1998; Gladders et al. 1998). With filters straddling the 4000Å break, the red sequence can be readily isolated from foreground and background galaxies, a technique also used to find clusters (e.g. Gladders & Yee 2000).

Clusters also provide a convenient mechanism for probing the dust contents of cluster early-type galaxies. Just as the Mg_2 absorption feature traces age and metallicity at low redshift, the magnitude axis of the red sequence traces metallicity at high redshift. A

dispersion in the residuals from the color-magnitude relation of roughly 3% is found in clusters ranging from Coma to high redshift (z $\sim$ 1.5) (Bower et al. 1992; Ellis et al. 1997; Stanford et al. 1998; Blakeslee et al. 2003a; Mei et al. 2006b,a; Lidman et al. 2008; Mei et al. 2009). Some of this dispersion can be attributed to differences in galaxy ages, and what remains sets a limit on dust. Finally, we also note that the uniform old stellar populations of elliptical galaxies imply simpler SEDs and hence better mass estimates with which to address the trends of §3.3.

The completed *HST* Cluster SN Survey produced 19 $z > 0.9$ SNe, eight of which were found in the clusters themselves. Deep two-color images of the cluster galaxies (including SN hosts) were also produced by stacking together SN search and follow-up epochs. Similar data exist from the SN surveys of the GOODS fields, which have discovered 26 $z > 0.9$ SNe Ia, all in the field. We analyze the host galaxies of these two sets of SNe here.

CHAPTER 4

Data

To identify a set of SNe Ia hosted by a uniform stellar population and minimally affected by dust, we compare the photometry of SN host galaxies to the photometry of red-sequence galaxies and look for star-formation indicators in SN host spectroscopy. Identifying the red sequence requires careful measurement of galaxy magnitudes and colors, which we describe in this chapter. We also measure quantitative morphology parameters which we use to enhance the contrast of the red sequence in color-magnitude diagrams by exploiting the early-type galaxy population dominance along the red sequence.

4.1 Image reduction and photometry

Twenty-five massive high-redshift $(0.9 < z < 1.46)$ galaxy clusters selected from X-ray, optical, and IR surveys were chosen for the *HST* Cluster SN Survey (Dawson et al. 2009). Clusters were each visited by *HST* four to nine times between July 2005 and December 2006. Each visit typically consisted of four ~ 500 second exposures in the F850LP filter (hereafter z_{850}) of the Advanced Camera for Surveys (ACS) wide field camera (WFC) and one ~ 500 second exposure in the F775W filter (hereafter i_{775}) of the ACS WFC. The i_{775} filter roughly matches rest-frame U-band for clusters with $0.9 < z < 1.25$, with the best match occurring at $z = 1.1$. The z_{850} filter roughly matches the rest-frame B-band in this redshift range with its closest match occurring at $z = 1.05$. For more distant clusters with $1.25 < z < 1.46$, the z_{850} filter more closely matches rest-frame U-band, with the best overlap at $z = 1.45$. In the present analysis we look principally at the deep coadditions of exposures from all observation epochs. Due to gyroscopic constraints, *HST* visits to individual clusters necessarily occurred at different position angles, resulting in coadditions in which pixels near the edges have smaller effective exposure time than pixels near the center (Figure 4.1). Each exposure specifically targeted the cluster core, so total integration time is nearly constant in the central region of each coaddition. Four clusters, RDCS J0910+54 (Mei et al. 2006a), RDCS J0848+44 (Postman et al. 2005), RDCS J1252-29(Blakeslee et al. 2003a) and XMMU 2235.3-2557 (Jee et al. 2009), had been previously targeted by ACS in i_{775} and z_{850} (PID9290 and PID9919), and we have included these additional exposures

in our coadded images. Cluster CL 1604+4304 (Postman et al. 2005) had also been observe with ACS, but not in i_{775} and z_{850}. The individually sky subtracted exposures were stacked using MULTIDRIZZLE (Fruchter & Hook 2002; Koekemoer et al. 2002) with a square kernel, $\mathrm{pixfrac} = 0.8$ and the native output pixel scale of $0.05''$.

We similarly processed images obtained by *HST* ACS as part of the *HST* Great Observatories Origins Deep Survey (GOODS) Treasury program (Giavalisco et al. 2004). The *HST* GOODS program targeted two high galactic latitude fields to obtain deep multiband images for studies of galaxy evolution and included a "piggy-back" SN program to follow suspected $z > 1$ SNe with ACS and the Near Infrared Camera and Multi-object Spectrograph (NICMOS). The original search consisted of five epochs over 15 ACS pointings for each of the two GOODS fields. A subsequent extension contributed an additional 14 epochs. The survey used nearly identical exposures in i_{775} and z_{850} for SN discovery and follow-up as our program. The initial GOODS SN survey yielded 11 $z > 0.9$ SNe Ia and its extension yielded an additional 13 $z > 0.9$ SNe Ia (Riess et al. 2004, 2007). We also add the host of one $z > 0.9$ SN Ia discovered in a previous search of these fields – SN2002dd Blakeslee et al. (2003b). One other $z > 0.9$ SN has been discovered in these fields – SN1997ff, but its most likely redshift, $z = 1.76$ is tentative and far beyond that of the clusters studied here. Lacking a comparison cluster red-sequence we do not analyze this SN host.

Galaxies that hosted SNe required special attention to prevent the SN light from biasing photometric and morphological statistics of the galaxies themselves. For each SN we created postage stamp images of each epoch in both bands. From these images, we subtracted a PSF model (described below) scaled to the flux of the light curve fit (details in Suzuki et al. (2012)) of the SN in each epoch. The postage stamp images are then stacked and processed in the same manner as the full mosaics. When the final catalogs are created, the values derived from the SN-subtracted postage stamp images of SN hosts are substituted for the values derived from the full mosaics. To test the accuracy of the PSF subtractions, we also generated postage-stamp images of SN hosts by stacking only the subset of epochs in which the SN was far from its peak. Except for a few cases in which only one or two such epochs were available, we obtained consistent photometric and morphological results to those obtained from the PSF-subtracted images.

4.1.1 Object detection

To form initial object catalogs we used SEXTRACTOR version 2.8.6 (Bertin & Arnouts 1996) in dual image mode, relying on the z_{850} images for object detection. Determining appropriate parameters for the extraction proved challenging due to galaxy crowding near cluster cores. One needs to simultaneously be able to deblend neighboring galaxies while avoiding the dissection of single complexly structured galaxies into multiple catalog entries. We found that the two-pass Cold/Hot method (Rix et al. 2004) produced the best catalogs, particularly near cluster cores. This method works by aggressively deblending relatively bright objects (such as cluster core galaxies) in an initial pass of SEXTRACTOR,

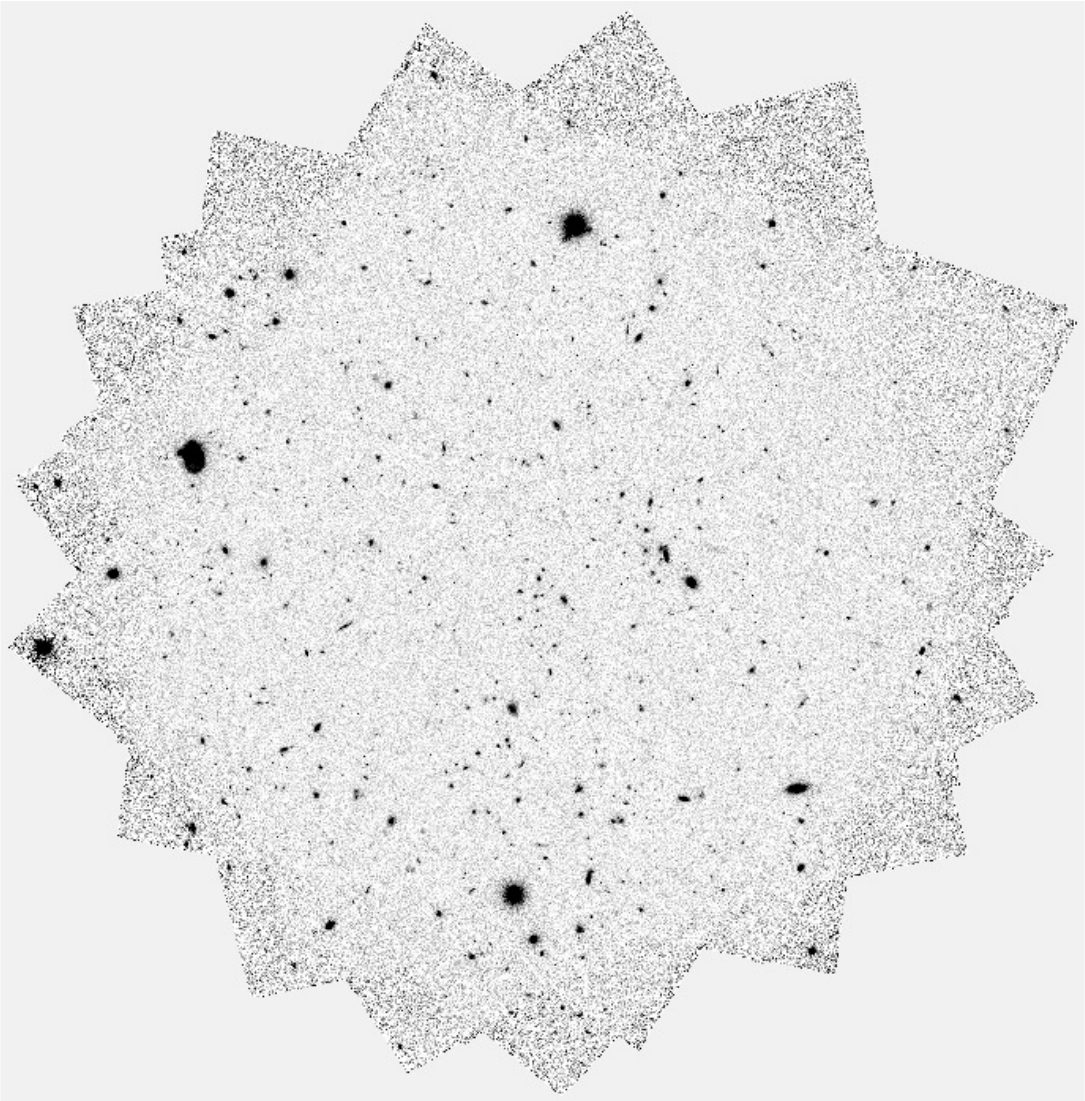

Figure 4.1. Final z_{850} mosaic for cluster ISCS J1432.4+3332. The differences in background noise as a function of position are apparent towards the edges of the mosaic.

and subsequently filling in the object catalog with fainter objects in a second pass with the deblending parameters set less aggressively. The specific parameters for the two steps were optimized by trial and error judged by the successful identification and segmentation of galaxies near cluster cores.

4.1.2 PSF construction

In order to accurately measure the colors of galaxies we require PSF estimates for both the i_{775} and z_{850} bands. To identify stars in each field with which to construct a PSF we used the SExtractor FLUX_RADIUS statistic. Objects with FLUX_RADIUS in the range $[1.4, 1.72]$ pixels are likely to be stars. For fields with many stars, we selected all stars within $1.3'$ of the cluster center and z_{850} MAG_AUTO between 18 and 24. For more sparsely populated fields, we selected the 10 stars closest to the cluster center falling in the same magnitude range. For each band of each field, an initial PSF was constructed by subtracting a local background (described below) from each star, oversampling each pixel 9×9 times with the IDL procedure CONGRID, renormalizing each oversampled image by the flux near the stellar core, aligning the oversampled images to the nearest subpixel and taking the subpixel by subpixel median image. This PSF model was then refined by iteratively fitting it to the original stars and adding the oversampled median residual back into the model. The final PSF was trimmed to 31×31 pixels, which contains more than 92% of the encircled energy in both i_{775} and z_{850} bands (Sirianni et al. 2005).

For more shallowly exposed fields, the wings of the PSF derived this way are relatively noisy and tend to be biased high when compared with PSFs from more deeply exposed fields. To reduce this bias, we match the radial profile of each PSF to the radial profile of the PSF derived from a reference field, that of cluster RDCS J1252.9-2927, which was both exposed more deeply than other fields and contained many stars. To measure the radial profiles of each PSF, we fit a 1D B-spline to the subpixel values as a function of radius. We then scale the PSF subpixel values by the ratio of the target field B-spline and the reference field B-spline. This procedure produces PSF grids that are consistent with the encircled energy functions of Sirianni et al. (2005) to $\sim 1\%$. They also individually retain the correct azimuthal structure for coadditions of exposures which occurred at many different position angles. Finally, we note that while a more precise PSF model would vary across the field of each exposure, ours is sufficient for correcting the effects of differential blurring between the i_{775} and z_{850} filters when computing a galaxy color.

4.1.3 Galaxy magnitudes and colors

Nonstellar objects with $19 < z_{850} < 26$ (measured with MAG_AUTO) and $-1 < i_{775} - z_{850} < 2$ (measured with MAG_APER with a 10 pixel radius), were then selected as galaxies of interest for further processing. For each of these galaxies, postage stamp images were cut out of the main z_{850} mosaic for processing with GALFIT version 3.0 (Peng et al. 2010). We used GALFIT to obtain two key statistics: the z_{850} magnitude, and the half-light

radius R_e. We also used GALFIT to produce an interloper-subtracted image used later when measuring quantitative morphology parameters.

Initial parameters for GALFIT were chosen using a variant of the GALAPAGOS algorithm (Häussler et al. 2007). Galaxies were modeled as Sérsic (1968) profiles with their Sérsic indices constrained between one and four. Interloper galaxies near each target galaxy were either masked out or simultaneously fit depending on the degree of overlap. For each galaxy, an adaptively sized elliptical annulus (typically with $6''$ semimajor axis and $\sim 3''$ width) with all galaxies and stars aggressively masked out was used to find the local sky background level, which was held fixed during the fit. We provided GALFIT with our estimated z_{850} PSF to internally convolve with its model before fitting to the actual image. The Sérsic profile magnitudes (and magnitude uncertainties) from the GALFIT fits, corrected for Milky Way extinction with the dust maps of (Schlegel et al. 1998), are the z_{850} magnitudes and uncertainties reported throughout this analysis.

Measurements of galaxy color are complicated by the fact that the z_{850} PSF is $\sim 10\%$ broader than the i_{775} PSF. To account for this difference we implemented a PSF matching scheme where, when measuring color, the z_{850} image is convolved with the i_{775} PSF and vice-versa. To fairly treat any color gradients in galaxies of different angular sizes, we measure color within a circular aperture with radius equal to the *apparent* (as opposed to intrinsic) half-light radius R_e of the cross-convolved z_{850} image. Measuring this radius requires us to run GALFIT a second time on each galaxy, this time using the cross-convolved z_{850} image and *not* providing a PSF for GALFIT to internally convolve with its model. A minimum color aperture radius of 3 pixels, corresponding to 1.2 kpc at $z \sim 1$, was enforced.

We modeled the errors for each band's flux as the sum in quadrature of the Poisson error from the object flux and the error in the background (e.g. sky, CCD readout noise). Because some of the clusters are not evenly exposed over the analysis region, we estimated the background contribution to the error for each galaxy using $\sigma_{\rm bkg}$, the local pixel-by-pixel standard deviation within the same elliptical annulus previously defined in order to measure the local background level. If the pixels in the coadded images were uncorrelated, then the aperture uncertainty $\sigma_{\rm aperture}$ would be related to the pixel-by-pixel uncertainty $\sigma_{\rm bkg}$ by a factor of the square-root of the number of pixels in the aperture. However, since both MULTIDRIZZLE and cross-convolution introduce correlations between nearby pixels, we need to empirically calibrate the relation between $\sigma_{\rm aperture}$ and $\sigma_{\rm bkg}$. We measured $\sigma_{\rm bkg}$ (in the unconvolved coadded images) and the local background subtracted flux (in the cross-convolved coadded images) of 1000 sky apertures (selected to avoid galaxies and stars) in each cluster field and GOODS tile. For each aperture center we measured the flux at 15 different radii logarithmically spaced from 1 pixel to 15 pixels. For a given radius, the average value of $\sigma_{\rm bkg}$ for each field is tightly correlated with the standard deviation of the 1000 aperture fluxes for that field (Figures 4.2, 4.3). The correlation is slightly different between the cluster fields and the GOODS tiles, presumably due to different average exposure times, different mosaic patterns and subsequent MULTIDRIZZLE artifacts. The right-hand panels of Figures 4.2 and 4.3 show the deviations from the scalings expected for uncorrelated

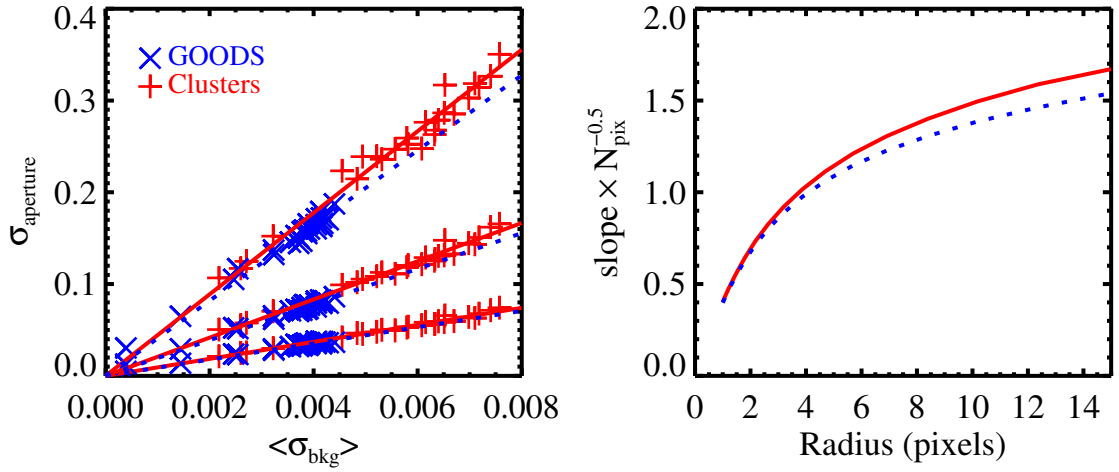

Figure 4.2. Left: Empirically measured photometric error contribution from background fluctuations in the i_{775} filter, including sky level, readout noise, and MULTIDRIZZLE artifacts. The x-axis is the average of $\sigma_{\rm bkg}$ for galaxies in the central region of each GOODS tile or cluster field, where $\sigma_{\rm bkg}$, as described in the text, is the standard deviation of background pixels (in the pre – cross-convolved images) surrounding an individual galaxy. The y-axis is the standard deviation of circular sky apertures (in the cross-convolved images) of fixed radius in the central region of each GOODS tile or cluster field. The different curves from bottom to top are computed for aperture radii of 4.7, 8.4, and 15.0 pixels; solid red for cluster fields and dashed blue for GOODS tiles. The empirical relation is slightly different for the GOODS tiles compared to the cluster fields, presumably due to a different mosaic pattern and subsequent MULTIDRIZZLE artifacts. **Right:** The slope of the relation in the left-hand panel scaled by $1/\sqrt{N_{pix}}$ as a function of aperture radius. The solid red curve indicates cluster fields and dashed blue curve indicates GOODS tiles. For uncorrelated pixels, this relation should be horizontal. The deviation from horizontal confirms that the pixels are correlated, justifying our empirical calibration.

noise, which would show up as horizontal lines.

To apply these data to galaxies we interpolate the slope of the $\sigma_{\rm aperture} - \sigma_{\rm bkg}$ relation from the data plotted in the right-hand panels of Figures 4.2 and 4.3 at the measured galaxy half-light radius R_e. In cases where R_e is larger than 15 pixels, we extrapolate using a linear fit to the data with radius between 8 and 15 pixels. This leads to an over-estimate of the background uncertainties for very bright galaxies. Fortunately, less than 6% of the red-sequence galaxies in our sample have $R_e > 15$ pixels, and only 1% have $R_e > 25$ pixels. In this way the background error is dependent on each individual object's exposure depth (quantified by $\sigma_{\rm bkg}$), even when the exposure depth varies across the image. Errors in flux are then converted to errors in magnitude, and the cataloged color error is the sum in quadrature of the i_{775} magnitude error and the z_{850} magnitude error. Exposure depth varies from field to field, but typical uncertainties in $i_{775} - z_{850}$ (for red galaxies) are 0.01 mag at $z_{850} = 21$ mag and 0.05 mag at $z_{850} = 24$ mag.

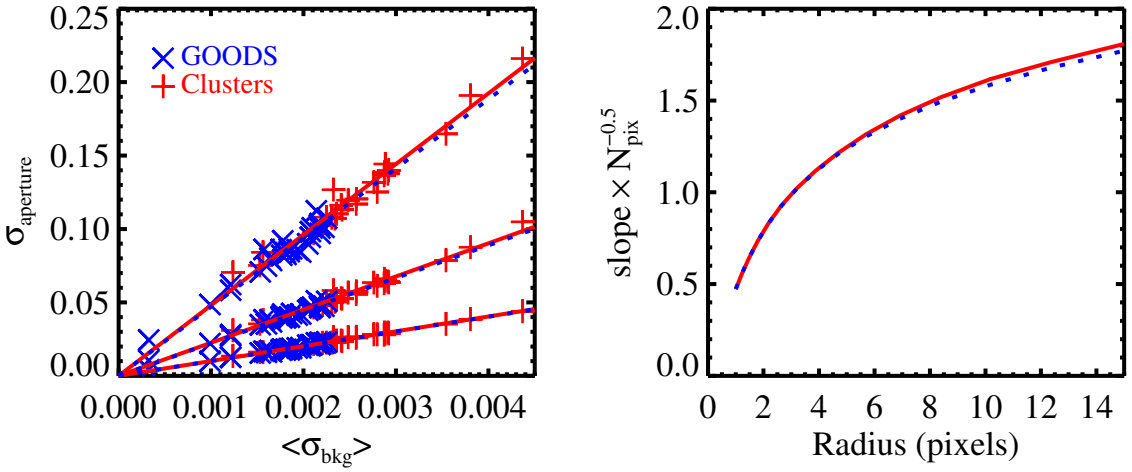

Figure 4.3. Same as Figure 4.2 but for the z_{850} filter.

4.2 Quantitative morphology

We use quantitative morphology measurements to identify likely red-sequence members. The two parameters we use are the Gini coefficient (Abraham et al. 2003) and asymmetry (Abraham et al. 1996). The Gini coefficient is a measure of the inequality in the distribution of pixel fluxes belonging to a galaxy, independent of their positions. The minimum Gini coefficient of zero indicates perfect equality; i.e. the flux in each pixel is identical. The maximum Gini coefficient of one indicates maximum inequality, in which the total flux of all pixels within the chosen aperture is actually contained in just one pixel (and all other pixels contain zero flux). The concentrated cores of elliptical galaxies typically generate higher Gini coefficients for these galaxies than in later-type galaxies.

The asymmetry measures how poorly a galaxy image matches itself when rotated 180 degrees about its center. It is defined as half the sum of the absolute values of the 180 degree subtraction residual pixels divided by the sum of the unsubtracted pixels in a given aperture. Elliptical galaxies typically have smaller asymmetry than later-type galaxies.

Just as the crowding in cluster cores is an issue when forming SExtractor catalogs, it is also an issue when selecting apertures for morphology measurements. To overcome this difficulty, we construct interloper-subtracted images by using GALFIT to subtract models of nearby interfering galaxies for each target galaxy. For each interloper-subtracted image, a preliminary aperture is created by collecting all pixels exceeding $1.5\sigma_{\rm bkg}$ contiguous to the pixel at the target galaxy's center. Using this aperture, we then compute the galaxy's quasi-Petrosian flux (Abraham et al. 2007). If the calculation converges, then a new isophotal aperture is created by selecting pixels from the preliminary aperture which exceed the quasi-Petrosian flux. The quasi-Petrosian flux fails to converge for a small number of galaxies which are then excluded from the subsequent analysis. These galaxies are usually quite

faint and would have had large uncertainties had the fits converged.

The Gini coefficient is measured within the isophotal aperture. Since the Gini coefficient calculation does not depend on the relative geometry of the aperture pixels but only on the pixel values, the error can be estimated from bootstrap resampling (Abraham et al. 2003) (i.e. by repeatedly resampling from the original pixel values, with replacement, and recomputing the Gini coefficient on these resamplings. We recompute the Gini coefficient this way 1000 times to determine the Gini coefficient probability distribution function for each galaxy and record the standard deviation of this distribution as the Gini coefficient error).

We measure the asymmetry within a symmetrized aperture consisting of the intersection of the isophotal aperture with its 180 degree rotation. The center of the rotation is fit iteratively to minimize the asymmetry (so the symmetrized aperture changes with each iteration, depending on the current candidate center). Since the random fluctuations present in the background contribute some asymmetry (positive by definition), a correction must be applied. To estimate this correction, we generate 1000 Gaussian background images with standard deviation $\sigma_{\rm bkg}$ and measure their asymmetry (but without normalization) in the same symmetrized aperture as the galaxy. We can then subtract this background contribution to the galaxy's asymmetry. The standard deviation of these background measurements is our estimated error for each galaxy's asymmetry (note that galaxy photon noise is much smaller than the background noise).

4.3 Spectroscopy

As the *HST* Cluster SN Survey produced SN candidates, they were spectroscopically targeted using prescheduled observing time on DEIMOS on Keck II (Faber et al. 2003) and FOCAS on Subaru (Kashikawa et al. 2002) and with ToO requests on FORS1 and FORS2 on Kueyen and Antu at the VLT (Appenzeller et al. 1998). The FORS1, FORS2 and DEIMOS observations are described in Dawson et al. (2009); the FOCAS observations are described in Morokuma et al. (2010). By observing SN candidates through slitmasks we were able to simultaneously target likely cluster members and form spectroscopic catalogs of many galaxies in the cluster fields. Galaxy redshifts were found through cross-correlation with template eigenspectra derived from SDSS spectra (Agol et al. 2011).

The flux and equivalent width of the [O II] 3727Å emission line doublet was measured by fitting the simple stellar population (SSP) templates from Bruzual & Charlot (2003, hereafter BC03) assuming a Chabrier (2003) initial mass function to data on both sides of the feature to define the continuum. The flux and equivalent width were computed by integrating from 500 km/s blueward of the line centered at 3726.032Å to 500 km/s redward of the line centered at 3728.815Å. To mitigate slit losses in the spectroscopy, we normalized the spectra to the observed i_{775} photometric magnitude.

Additional literature redshifts and [O II] equivalent width measurements were used as available (Andreon et al. 2008; Bremer et al. 2006; Brodwin et al. 2006; Demarco et al.

2007; Eisenhardt et al. 2008; Hilton et al. 2007, 2009; Postman et al. 1998; Rosati et al. 1999; Stanford et al. 2002, 2005). Spectra of $z > 0.9$ SN hosts from the *HST* Cluster SN Survey are presented in Figure 4.4. A few of these spectra merit individual discussion. The redshift of SN SCP06T1 is determined from a single well-detected emission line, which we assume to be [O II]. Likewise, the redshift of SN SCP06X26 is determined from a single [O II] emission line, however the detection of this line is much more tentative than for SN SCP06T1 and is only barely visible in the 2D spectrum. Finally, we have not identified any features in the spectrum of SN SCP06E12 that would allow us to determine a redshift. The color of this galaxy is consistent with the color of the red sequence of the targeted cluster in the same field of view, so it may be a cluster member. However, we note that the colors of the four early-type field SN hosts from the *HST* Cluster SN Survey identified later are also roughly consistent with the colors of the red sequences of the targeted clusters in their fields of view. Though there is considerable uncertainty in the redshift of SN SCP06E12 and its host, we follow through with our analysis of this galaxy assuming it is a cluster member. We note that it is not used for cosmological analyses or analyses of SN correlations with their hosts. All of the remaining SN hosts have secure redshifts.

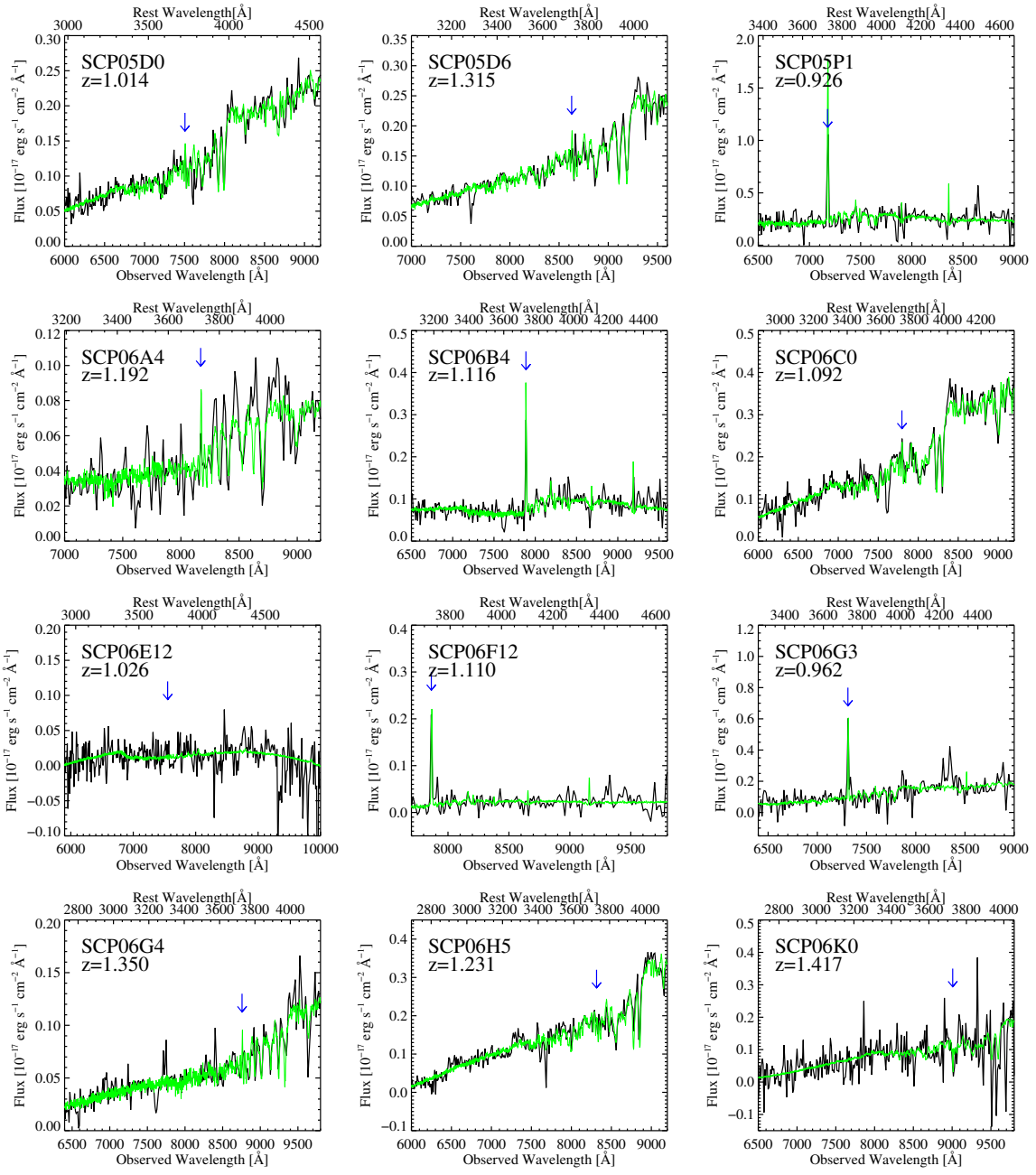

Figure 4.4. SCP supernovae host spectroscopy. For each host, data are in black, and the best fitting linear combination of eigenspectra at the fitted redshift is in green. The blue arrow indicates the wavelength of the [O II] 3727 emission line doublet. Note that the green line, used here for determining the redshift, is not the same as the BC03 template (which does not contain [O II] emission) used in fitting the [O II] equivalent width.

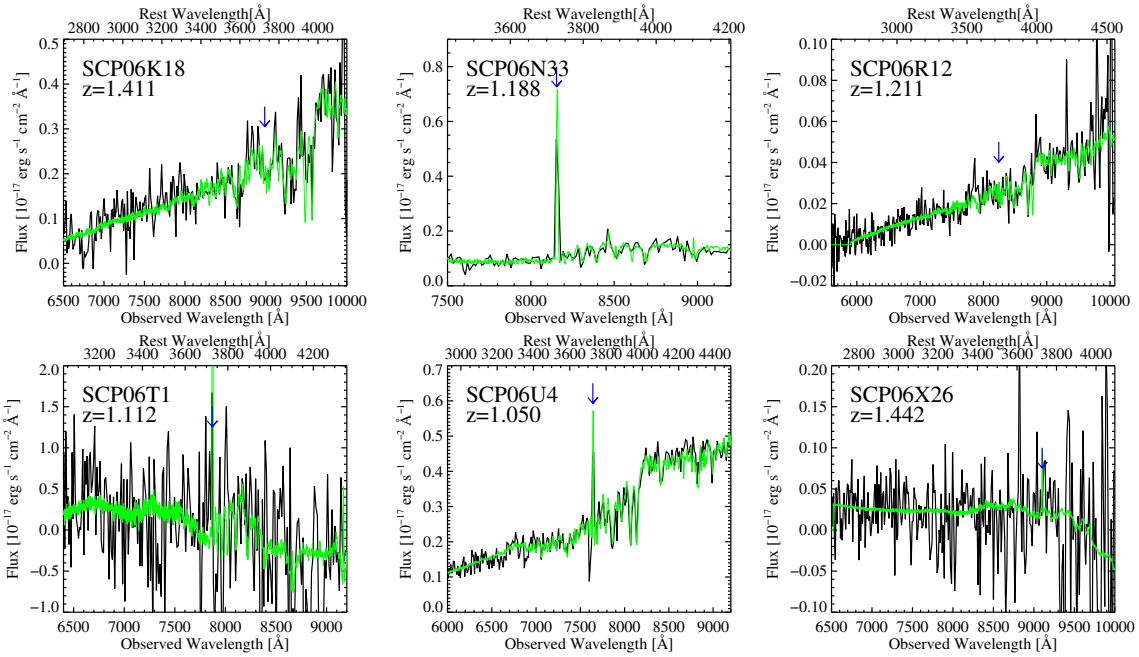

Figure 4.4. Host galaxy spectra (continued)

CHAPTER 5

Analysis

In this chapter we describe our determination of the red sequence in clusters and in the field, which we later use to characterize SN host galaxies. To consistently identify cluster red-sequence galaxies, especially in poorer clusters where the contrast between bluer foreground or late-type galaxies and the cluster red sequence is less distinct, we generate a composite red sequence using spectroscopically confirmed members of multiple clusters with colors loosely consistent with the red sequence. When there is no cluster red sequence with which to compare SN host galaxies, as is the case for the field hosted SNe in the *HST* Cluster SN Survey and for all the GOODS fields SNe, this composite red sequence will serve as the reference red sequence. We use an evolving SED model to *K*-correct and evolution correct red-sequence members from their original redshifts to a target redshift. In this way we predict the location of the red sequence across the redshift range of the clusters in the survey.

5.1 Quantitative morphology calibration

Cluster red sequences are dominated by early-type galaxies. To enhance the contrast of the red sequence against the background color magnitude diagram, we use the Gini coefficient and asymmetry from §4.2 to select these galaxies. We calibrate our selection against visually derived morphology catalogs (by co-author MP) for three clusters: ISCS J1432.4+3332, RDCS1252.9-2927, and ISCS J1438.1+3414 at redshifts 1.10, 1.24, and 1.41 respectively. The left panel of Figure 5.1 shows the locus of *red* ($i_{775} - z_{850} > 0.75$) visually classified elliptical galaxies compared to other visually classified morphological types in the Gini coefficient – asymmetry plane. The color cut eliminates many of the bluer galaxies (which we are not interested in here) but is not so red (for these clusters) that red-sequence members are cut. To select visually classified ellipticals we can evidently choose galaxies with Gini coefficient greater than 0.45 and asymmetry less than 0.08, cuts which we refer to as our *narrower* morphological cuts. With these cuts, $\sim 90\%$ of all red visually classified elliptical galaxies are selected. S0 galaxies make up about 40% of the objects selected. The contamination from late-type galaxies is $\lesssim 5\%$. Later, when we fit

the CMRs of clusters we choose to use somewhat more lenient cuts of Gini > 0.4 and asymmetry < 0.1, which we refer to as our *broader* morphological cuts. This increases the number of red-sequence early-type galaxies included by $\sim 50\%$ but only increases the late-type contamination to $\sim 10\%$. The *broader* cuts further increase the contrast of the red sequence but, critically, we find they only marginally increase the scatter of the red sequence (from 0.045 ± 0.003 to 0.048 ± 0.003 when clusters are stacked; §3.1).

As an independent test of the reliability of our cuts, we also investigate the strength of [O II] line emission in the Gini coefficient – asymmetry plane. The right panel of Figure 5.1 shows the locus of red galaxies with weak or no [O II] emission (equivalent width greater than -5Å). Our broader cuts select $\sim 90\%$ of [O II] quiet galaxies, though the contamination of [O II] emitting galaxies is higher ($\sim 35\%$) than the contamination of late-type galaxies in the visual morphology case. This is partly a selection effect: redshifts are easier to obtain from emission lines than from absorption lines so [O II] emitting galaxies are more likely to be spectroscopically confirmed as cluster members and hence appear in the plot. The observed fraction of [O II] emitting galaxies is compatible with results reported in Postman et al. (2001), in which 45% of galaxies within the central $1.0h_{65}^{-1}$ Mpc were observed to have [O II] equivalent width less than -15Å. Also, Yan et al. (2006) have analyzed ~ 55000 SDSS low-redshift spectra and determined that while nearly 38% of red galaxies show [O II] emission, only 9% of these show the emission line ratios characteristic of star formation. The remaining [O II]-emitting galaxies show line ratios indicative of LINERS or AGN. Lemaux et al. (2010) have recently extended this analysis to high-redshift by obtaining near-infrared spectroscopy of $z > 0.8$ cluster galaxies. Of the five [O II]-emitting red-sequence early-type galaxies in their sample, four were found to be consistent with AGN/LINERs, with some evidence that the fifth might contain AGN/LINER activity as well. We are unable to directly check for AGN/LINER-like line ratios in our spectra because at high redshift the necessary comparison lines are shifted out of the wavelength range of our spectroscopic coverage. However, we suspect that most of the [O II]-emitting morphologically early-type red galaxies in our sample are not actively forming stars.

5.2 The composite red sequence

The identification of red-sequence galaxies in clusters with incomplete spectroscopy can be challenging, especially for poorer clusters where it is difficult to distinguish red-sequence members from interloping galaxies in the foreground or background of the cluster. We therefore use the spectroscopically confirmed red-sequence members from all of our clusters to construct a composite red sequence which serves as both a guide for fitting the CMR of individual cluster red sequences and also as a reference red sequence for field elliptical SN hosts. We start by assuming that our sample of spectroscopically confirmed cluster members with quantitative morphology measurements consistent with elliptical galaxies (passing our broader morphology cuts) and colors loosely consistent with an old stellar population are each members of their own cluster's red sequence. By using

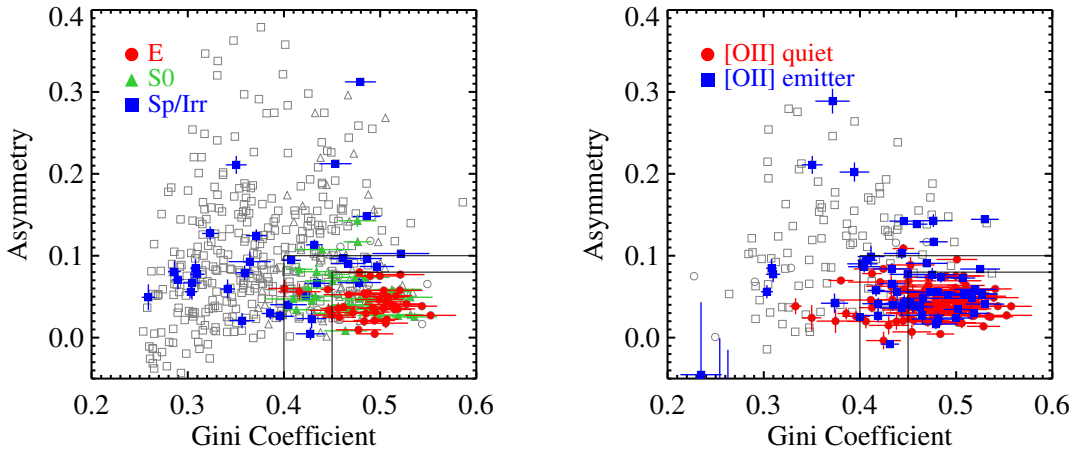

Figure 5.1. Left: Comparison of visually derived morphologies to quantitative morphology measurements for three clusters. Blue boxes represent visually classified late-type galaxies with T-type from 0 to 6. Green triangles represent S0 galaxies with visual T-type from -2 to -1. Red circles represent elliptical galaxies with visual T-type from -6 to -3. Colored filled symbols represent galaxies with $i_{775} - z_{850} > 0.75$, consistent with the red sequence, light grey open symbols represent galaxies bluer than the red sequence. The two boxes in the lower-right show the position of our *broader* and *narrower* morphology cuts. The horizontal and vertical lines extending from plotting symbols indicate 1σ uncertainties. **Right:** Spectroscopically confirmed galaxies' asymmetry and Gini coefficient distributions. Red circles indicate galaxies with an [O II] equivalent width greater than -5Å (small or no emission). Blue squares indicate galaxies with strong [O II] emission with an equivalent width less than -5Å. Colored filled symbols represent galaxies with $i_{775} - z_{850} > 0.75$, consistent with the red sequence, light grey open symbols represent galaxies bluer than the red sequence. The two boxes in the lower-right show the position of our *broader* and *narrower* morphology cuts. The horizontal and vertical lines extending from plotting symbols indicate 1σ uncertainties.

a suitable *K*-correction and evolution correction, we can then project each galaxy's magnitude and color from their measured values at the galaxy's original redshift to a target redshift. To accomplish this we assume that the each sample galaxy's SED takes the form:

$$F_\lambda = \frac{M_{\rm gal}}{M_\odot} \frac{{\rm BC03}_\lambda \left(T\left(z\right), Z, z\right)}{\left(D_L\left(z\right)\right)^2} \tag{5.1}$$

where $D_L(z)$ is the luminosity distance to redshift z, ${\rm BC03}_\lambda \left(T\left(z\right), Z, z\right)$ indicates the luminosity density of the BC03 SSP template SED of age $T\left(z\right)$ and metallicity Z with wavelength redshifted by $(1+z)$, and $M_{\rm gal}$ is the initial stellar mass of the BC03 template. We only have two band photometry for galaxies, so we can only constrain two parameters affecting the SED. One parameter needs to be the size of the galaxy ($M_{\rm gal}$), leaving the choice of either constraining the galaxy age or metallicity as the second parameter. Since these two parameters are largely degenerate, we simply fix the age $T(z)$ such that galaxies all form at the same redshift $z_{\rm form}$ and fit for the metallicity Z. In a few cases, the range of colors produced by Equation 5.1 for the available BC03 metallicities was not red enough to cover the observed galaxy color. This could happen either because of a chance positive fluctuation of the galaxy color or because the particular galaxy happens to have formed earlier than our chosen $z_{\rm form}$. Since we are not interested in the metallicity values themselves, but only in using them to project colors and magnitudes from one redshift to another, we allow this parameter to be extrapolated outside of the BC03 range. In practice, we extrapolated metallicities for 27 out of 198 galaxies to a maximum of Z = 0.07 (the range of BC03 metallicities is 0.0001 to 0.05) when choosing $z_{\rm form} = 3.0$. To then project each galaxy to a target redshift, we evaluate the best-fit BC03 template at age $T\left(z\right)$ given the target redshift z, which automatically captures luminosity evolution. We calculate i_{775} and z_{850} from this template. This procedure is imperfect, and in particular can introduce errors when *K*-correcting and evolution correcting over large differences in redshift. To mitigate this effect we de-weight galaxies with redshifts far from the target redshift. Specifically, we assign a Gaussian weight $w \propto \exp(-(z - z_{targ})^2/(2 \cdot 0.15^2)$ to each galaxy. The characteristic size of the redshift window in this weighting, 0.15, is arbitrary but we have confirmed that our results do not significantly change with window sizes ranging from 0.10 to 0.25. The composite red sequences at redshifts 1.0, 1.2, and 1.4 are shown in Figure 5.2 for $z_{\rm form} = 3.0$.

5.3 Individual cluster red sequences

To determine the red sequences of individual clusters we assume a model in which galaxies are normally distributed with intrinsic scatter $\sigma_{\rm int}$ in color about the mean color-magnitude relation (characterized by slope m and intercept at $z_{850} = 22$, b_{22}) and have their magnitudes distributed like a Schechter (1976) function (described by parameters ϕ^*, L^* and α). Additionally, foreground and background galaxies will contaminate the color-magnitude diagram. We model the density of these galaxies in color-magnitude space as a

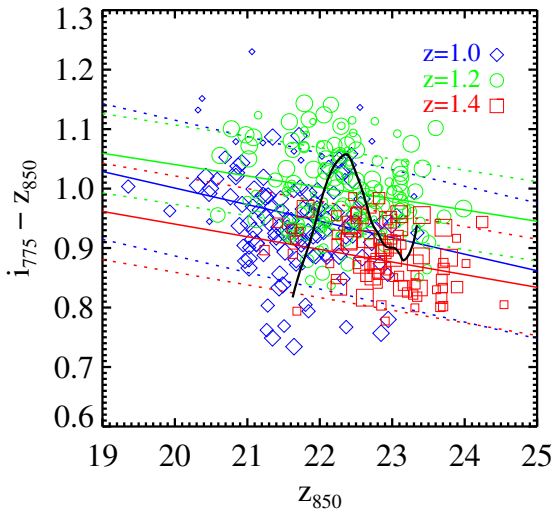

Figure 5.2. The composite red sequence at redshifts 1.0 (blue diamonds), 1.2 (green circles), and 1.4 (red squares), with linear fits. The size of the plotting symbol is proportional to the weight of the galaxy in the linear fit. The dashed lines indicate the measured residual scatter about the fits. The black line shows the predicted evolution from $z = 0.9$ to $z = 1.5$ of an L^* cluster member. The redward then blueward evolution of the red sequence with redshift is the result of the rest-frame 4000Å Balmer break crossing the gap between the i_{775} and z_{850} filters.

plane characterized by its average value (B) and derivatives with respect to magnitude and color ($d\mathrm{B}/dz_{850}$ and $d\mathrm{B}/d(i_{775} - z_{850})$). To break degeneracies between the red-sequence parameters and the foreground/background parameters, we simultaneously fit each cluster field with the GOODS fields which serve as a control.

We consider only galaxies that pass our broader morphology cuts and fall within a redshift dependent color-magnitude rectangle for this analysis. The allowed color range is $b_{22}^{\mathrm{comp}} \pm 0.3$ mag where b_{22}^{comp} is the intercept of the composite red sequence. The allowed magnitude range is $[M^*_{\mathrm{model}} - 2.2, M^*_{\mathrm{model}} + 1.0]$ where M^*_{model} is determined by passive evolution (Eqn. 5.1) of a red-sequence characteristic magnitude of $z_{850} = 22.7$ at redshift $z = 1.24$ (Blakeslee et al. 2003a). We construct a likelihood function for these galaxies and the GOODS fields control galaxies falling in the same color-magnitude rectangle as in Andreon et al. (2005) and use a Markov chain Monte Carlo algorithm to explore the nine-dimensional space (σ_{int}, m, b_{22}, ϕ^*, L^*, α, B, $d\mathrm{B}/dz_{850}$ and $d\mathrm{B}/d(i_{775} - z_{850})$). The techniques presented in Dunkley et al. (2005) are used to determine the convergence of the Markov chains. The marginal distributions of fitting parameters can then be extracted directly from the Markov chains.

In Figure 5.3, we compare the slopes of individual cluster red-sequence CMRs to the slopes of the composite red-sequence CMRs generated assuming a variety of values of z_{form} between 2.5 and 7.0. The effects on the composite CMR slope of changing z_{form} are much smaller than the statistical uncertainties in individual CMR slope fits. In fact, the slopes of the individual cluster fits are statistically consistent with the narrow range of slopes of the composite red sequence regardless of z_{form} ($\chi^2 = 19$ for 23 clusters assuming $z_{\mathrm{form}} = 3$ and changes negligibly for other values of z_{form}). In order to consistently treat both field and cluster hosted SNe and also to avoid using physically perplexing positive slopes, we choose to fix the slope of each cluster to the value of the composite red sequence. We

choose $z_{\rm form} = 3.0$ as a typical galaxy formation epoch and refit each cluster red-sequence CMR. The results of these fixed-slope fits are presented in Table 5.1.

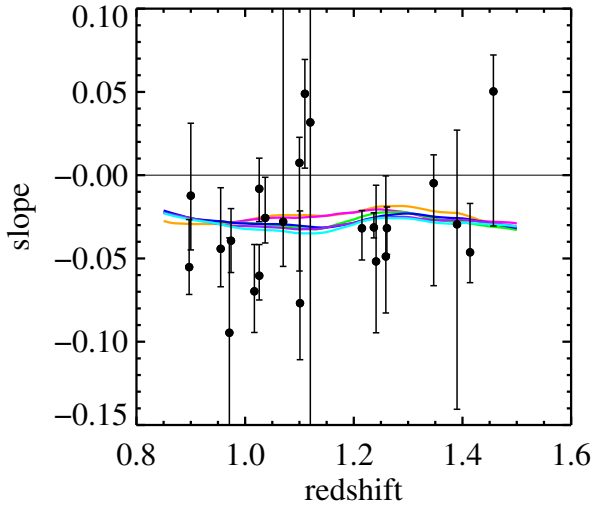

Figure 5.3. Comparison of the slopes of the composite red-sequence CMR fits to individual cluster CMR fits when allowing the slope to float. The multicolor curves are fits to the composite red sequence assuming different values of $z_{\rm form}$ in the range [2.5,7.0]. The black points show the locations of maximum likelihood from the MCMC fits to 23 individual clusters. The error bars are the smallest confidence intervals containing 68% of the marginal posterior probability.

Table 5.1. Color-Magnitude Relation fits

ID	Cluster Name	Redshift	Intercept	Slope	$\sigma(i_{775}-z_{850})$	$\sigma(U-V)_{z=0}$	$N_{\rm gal}$
A	XMMXCS J2215.9-1738	1.457	0.923	-0.020	$0.051^{+0.034}_{-0.020}$	$0.101^{+0.068}_{-0.040}$	23.3
B	XMMU J2205.8-0159	1.12	1.028	-0.023	$0.040^{+0.186}_{-0.002}$	$0.079^{+0.372}_{-0.003}$	9.7
C	XMMU J1229.4+0151	0.974	0.906	-0.028	$0.066^{+0.003}_{-0.014}$	$0.131^{+0.007}_{-0.028}$	54.8
D	RCS J022144-0321.7	1.017	0.953	-0.026	$0.069^{+0.017}_{-0.017}$	$0.137^{+0.034}_{-0.035}$	32.1
E	WARPS J1415.1+3612	1.026	0.969	-0.025	$0.060^{+0.015}_{-0.013}$	$0.119^{+0.029}_{-0.026}$	27.0
F	ISCS J1432.4+3332	1.110	1.031	-0.023	$0.046^{+0.016}_{-0.016}$	$0.093^{+0.032}_{-0.031}$	18.8
G	ISCS J1429.3+3437	1.259	0.989	-0.019	$0.062^{+0.019}_{-0.034}$	$0.125^{+0.038}_{-0.068}$	23.3
H	ISCS J1434.4+3426	1.241	0.964	-0.018	$0.061^{+0.037}_{-0.013}$	$0.122^{+0.073}_{-0.026}$	22.5
I	ISCS J1432.6+3436	1.347	0.969	-0.023	$0.042^{+0.014}_{-0.025}$	$0.083^{+0.029}_{-0.050}$	14.8
J	ISCS J1434.7+3519	1.37	...	...	...	...	...
K	ISCS J1438.1+3414	1.414	0.944	-0.021	$0.008^{+0.011}_{-0.008}$	$0.016^{+0.023}_{-0.016}$	30.4
L	ISCS J1433.8+3325	1.37	...	...	...	...	...
M	CL J1604+4304	0.897	0.749	-0.026	$0.050^{+0.019}_{-0.006}$	$0.100^{+0.038}_{-0.012}$	27.1
N	RCS J022056-0333.4	1.026	0.982	-0.025	$0.043^{+0.014}_{-0.004}$	$0.086^{+0.027}_{-0.008}$	30.4
P	RCS J033750-2844.8	1.1[a]	0.988	-0.023	$0.023^{+0.026}_{-0.010}$	$0.047^{+0.051}_{-0.020}$	15.6
Q	RCS J043934-2904.7	0.955	0.858	-0.027	$0.045^{+0.021}_{-0.010}$	$0.091^{+0.041}_{-0.019}$	24.8
R	XLSS J0223.0-0436	1.215	1.013	-0.019	$0.015^{+0.017}_{-0.015}$	$0.029^{+0.034}_{-0.029}$	20.6
S	RCS J215641-0448.1	1.07	1.022	-0.024	$0.005^{+0.084}_{-0.005}$	$0.010^{+0.168}_{-0.010}$	7.1
T	RCS2 J151104+0903.3	0.971	0.899	-0.028	$0.087^{+0.040}_{-0.023}$	$0.174^{+0.080}_{-0.045}$	15.7
U	RCS J234526-3632.6	1.037	0.957	-0.025	$0.047^{+0.015}_{-0.007}$	$0.093^{+0.030}_{-0.014}$	29.1
V	RCS J231953+0038.0	0.900	0.766	-0.026	$0.051^{+0.027}_{-0.007}$	$0.101^{+0.054}_{-0.015}$	30.3
W	RX J0848.9+4452	1.261	0.985	-0.019	$0.028^{+0.013}_{-0.005}$	$0.057^{+0.026}_{-0.009}$	20.1
X	RDCS J0910+5422	1.101	1.001	-0.023	$0.060^{+0.024}_{-0.012}$	$0.119^{+0.047}_{-0.024}$	18.4
Y	RDCS J1252.9-2927	1.237	0.965	-0.018	$0.029^{+0.003}_{-0.007}$	$0.058^{+0.007}_{-0.014}$	34.5
Z	XMMU J2235.3-2557	1.390	0.926	-0.022	$0.031^{+0.017}_{-0.016}$	$0.061^{+0.033}_{-0.032}$	17.4

[a] Photometric cluster redshift.

Intercept indicates the CMR color at $z_{850} = 22$. The slope for each fit is fixed to the slope of the composite red sequence at the cluster redshift. $\sigma(i_{775}-z_{850})$ ($\sigma(U-V)_{z=0}$) is the observer-frame (rest-frame) intrinsic scatter of morphologically selected red-sequence members. The uncertainties reported indicate the smallest intervals containing 68% of the posterior probability for $\sigma(i_{775}-z_{850})$ and $\sigma(U-V)_{z=0}$. $N_{\rm gal}$ is the effective number of red-sequence galaxies in the fitted magnitude range computed by integrating a Schechter function with the best fit values of ϕ^*, L^*, and α over the magnitude range of the fit.

CHAPTER 6

SN Host Classification

In this chapter, we describe how, for each SN host, we use the color–magnitude, quantitative morphology, and spectroscopic information to classify the host as either a passively evolving early-type galaxy, or a potentially star-forming late-type galaxy. We restrict our attention to redshifts greater than 0.9, which is the lowest cluster redshift in the *HST* Cluster SN Survey. Dawson et al. (2009) lists 17 SNe with $z > 0.9$. From this list we subtract SN SCP06C1, a spectroscopically confirmed SN Ia at $z = 0.98$ with an uncertain host, but for completeness add SN SCP06E12 and SN SCP06X26 for consideration, which are likely $z > 0.9$ SNe but lack conclusive spectroscopic redshifts. The host of SN SCP06E12 is faint but has photometry consistent with the red sequence of the cluster in the same field of view, and we assume here that its redshift is that of this cluster: 1.026. Spectroscopy of the host of SN SCP06X26 shows a possible emission line at 9100Å, which if [O II] indicates $z = 1.44$. There are 26 $z > 0.9$ SNe Ia discovered in surveys of the GOODS fields, 19 of which are spectroscopically confirmed as Type Ia (Gilliland et al. 1999; Blakeslee et al. 2003b; Riess et al. 2004, 2007). We were unable to identify the host galaxy of one of these: HST04Gre. This SN is approximately $1.7''$ from each of two potential hosts. Also, the host of SN1997ff has a tentative redshift much greater than that of any of the clusters considered here, preventing us from comparing its color and magnitude to the red sequence. We do not consider either of these SNe in the following analysis.

The principle criteria that our hosts must pass to be considered passively evolving early-types are: (A) they pass our broader morphology cuts and (B) they lie within 2σ of the red sequence where $\sigma = \sqrt{\sigma_{\rm int}^2 + \sigma_{\rm col}^2}$, and $\sigma_{\rm col}$ is the color uncertainty. For (B) we use the cluster red sequence for cluster member hosts, and the composite red sequence with an assumed intrinsic scatter of 0.10 mag (greater than the measured intrinsic scatter of any of our clusters) for field hosts. Where spectroscopy is available, we also take note of possible star formation indicators.

In summary, from the *HST* Cluster SN Survey we classify six out of nine cluster SN hosts and four out of nine field SN hosts as early-type. One host galaxy, that of SN SCP06E12, we were unable to classify due to its faintness. The remaining *HST* Cluster SN Survey hosts are classified as late-type. From the GOODS SN Survey, we classify

seven out of 24 field SN hosts as early-type, and the remaining 17 hosts as late-type. Classifications are presented in Tables 6.1 and 6.2 and details are below.

Early-type Hosts of SCP SNe

Cluster members

SN SCP06H5, SN SCP06K18, SN SCP06R12. The hosts of these three SNe Ia are spectroscopically consistent with early-type galaxies, have photometry placing them on their clusters' red sequences, and pass our narrower morphology cuts.

SN SCP05D0. The host of this SN has photometry placing it on its cluster's red sequence and passes our broader morphology cuts. The somewhat large asymmetry of this galaxy appears to result from a slightly skewed core light distribution, though not from any spiral structure or clumps of star formation. A small amount of [O II] emission is observed in its spectrum which might indicate star formation but is also not uncommon in passively evolving galaxies with LINERs in their cores.

SN SCP06K0. The host of this SN is spectroscopically consistent with an early-type galaxy, has photometry placing it on its cluster's red sequence, and passes our broader morphology cuts, though it has a somewhat small Gini coefficient. We note that the Gini coefficient is biased small for low signal-to-noise ratio images (Lotz et al. 2004) (such as the image of SN SCP06K0's host) and it is likely that with increased exposure time the Gini coefficient would increase.

SN SCP06U4. The host of this SN has photometry placing it on its cluster's red sequence and passes our narrower morphology cuts. Its spectrum exhibits moderate [O II] emission but otherwise is consistent with an early-type spectrum.

Field galaxies

SN SCP06C0, SN SCP06D6. The hosts of these SNe have photometry placing them on the composite red sequence and pass our narrower morphology cuts. Small amounts of [O II] emission are observed in their spectra.

SN SCP06G4. The host of this SN has photometry placing it on the composite red sequence and passes our narrower morphology cuts. Its spectrum shows relatively strong hydrogen Balmer absorption features consistent with an "E+A" spectrum (Dressler & Gunn 1983, 1992), which may indicate it is younger than the other early-type galaxies in our sample (though still likely older than the cutoff timescale for SNe CC).

SN SCP06A4. The host of this SN has photometry placing it on the composite red sequence and passes our narrower morphology cuts. A small amount of [O II] emission may be present in its spectrum and hydrogen Balmer absorption lines indicate an "E+A" classification.

Late-type Hosts of SCP SNe

Cluster members

SN SCP06B4. The host of this SN fails our broader morphology cuts, is significantly bluer than its cluster's red sequence, and shows strong [O II] emission in its spectrum. It is likely that this galaxy is star-forming.

SN SCP06F12. Although the host of this SN only barely fails our broader Gini coefficient cut, its color is significantly bluer than its cluster's red sequence, and it shows strong [O II] emission in its spectrum.

Field galaxies

SN SCP05P1, SN SCP06T1. The hosts of these SNe fail both of our broader morphology cuts, are significantly bluer than the composite red sequence, and show strong [O II] emission in their spectra.

SN SCP06N33. Although the host of this SN passes our broader Gini coefficient cut, its color is significantly bluer than the composite red sequence and it shows strong [O II] emission in its spectrum.

SN SCP06X26. Although we do not detect strong [O II] emission from the host of this SN, it fails our broader Gini coefficient cut and its color is significantly blue.

SN SCP06G3. Although the host of this SN passes our narrow Gini coefficient cut, passes (barely) our broader asymmetry cut and is only moderately bluer than the composite red sequence, its spectrum shows very strong [O II] emission. We also note that the axis-ratio of the z_{850} GALFIT model for this galaxy ($b/a = 0.25$) is 3.5σ smaller than the model axis-ratios of the galaxies classified as early-types above; it is likely an edge-on disk galaxy.

Unclassified Hosts of SCP SNe

SN SCP06E12. We do not have a redshift for the host of this SN. Its color is consistent with the red sequence of the cluster in the same field of view. Its Gini coefficient is small but this galaxy, like SN SCP06K0, has a low signal-to-noise ratio image and its Gini coefficient is likely biased low. We do not have enough information to classify this galaxy, and do not include it in any subsequent analysis.

Host Galaxies of GOODS SNe

From the GOODS SN Survey, we analyze the morphology and photometry (but not spectroscopy) of 24 of the 26 $z > 0.9$ SN hosts mentioned in Riess et al. (2007). The hosts of seven SNe pass our morphological and photometric cuts: SN2003az, SN2003XX, SN2003es, HST04Sas, HST04Tha, HST05Lan and SN2002hp. Riess et al. (2007) classifies the hosts of all of these but SN2003az as elliptical. The remaining 17 GOODS SN Ia hosts analyzed here are classified as late-type.

Table 6.1. Early-type $z > 0.9$ SN Hosts

Name	$z_{\rm host}$	$z_{\rm cluster}$	[O II] EW (Å)	Confidence Interval	Gini Coefficient	Asymmetry	$i_{775} - z_{850}$	CMR residual	Notes
SCP Cluster SN Hosts									
SN SCP05D0	1.014	1.017	-1.7	$[-2.6, -0.6]$	0.525 ± 0.021	0.084 ± 0.003	0.939 ± 0.021	-0.016 ± 0.072	s,h,x,c
SN SCP06H5	1.231	1.241	-0.4	$[-1.5, -0.0]$	0.541 ± 0.017	0.059 ± 0.003	1.075 ± 0.022	$+0.106 \pm 0.065$	L,h
SN SCP06K0	1.416	1.414	-0.4	$[-2.4, -0.0]$	0.419 ± 0.018	0.027 ± 0.008	0.951 ± 0.066	$+0.020 \pm 0.066$	L,h,x,c
SN SCP06K18	1.412	1.414	-0.1	$[-0.7, -0.0]$	0.456 ± 0.015	0.021 ± 0.006	0.986 ± 0.037	$+0.038 \pm 0.038$	
SN SCP06R12	1.212	1.215	-0.2	$[-1.1, -0.0]$	0.455 ± 0.025	0.054 ± 0.011	0.956 ± 0.050	-0.019 ± 0.052	L,h
SN SCP06U4	1.050	1.037	-9.6	$[-10.9, -8.1]$	0.481 ± 0.018	0.055 ± 0.004	0.926 ± 0.017	-0.053 ± 0.050	s,c
SCP Field SN Hosts									
SN SCP06A4	1.193	1.457	-1.6	$[-3.6, -0.0]$	0.468 ± 0.021	0.020 ± 0.006	0.976 ± 0.044	-0.013 ± 0.109	L,h,x,c
SN SCP06C0	1.092	0.974	-3.6	$[-5.6, -1.7]$	0.476 ± 0.021	0.027 ± 0.003	1.072 ± 0.017	$+0.014 \pm 0.101$	L,h,x,c
SN SCP05D6	1.314	1.017	-3.2	$[-4.2, -2.2]$	0.516 ± 0.017	0.043 ± 0.005	0.960 ± 0.027	$+0.044 \pm 0.103$	L,h,x,c
SN SCP06G4	1.350	1.259	-0.3	$[-1.5, -0.0]$	0.492 ± 0.022	0.000 ± 0.006	1.004 ± 0.040	$+0.103 \pm 0.108$	s,h,x,c
GOODS SN Hosts									
SN2002hp	1.305	...	...	...	0.501 ± 0.025	0.032 ± 0.005	0.919 ± 0.019	$+0.015 \pm 0.102$	h,x,c
SN2003az	1.270	...	...	...	0.435 ± 0.023	0.054 ± 0.008	0.927 ± 0.048	$+0.018 \pm 0.111$	s,h,x,c
SN2003es	0.954	...	...	...	0.497 ± 0.018	0.047 ± 0.001	0.942 ± 0.006	$+0.039 \pm 0.100$	s,x,c
SN2003XX	0.935	...	...	...	0.504 ± 0.028	0.025 ± 0.001	0.789 ± 0.005	-0.081 ± 0.100	s,h,x,c
HST04Sas	1.390	...	...	...	0.431 ± 0.023	0.071 ± 0.007	0.792 ± 0.032	-0.081 ± 0.105	s,h,x,c
HST04Tha	0.954	...	...	...	0.432 ± 0.031	0.058 ± 0.001	0.886 ± 0.008	$+0.027 \pm 0.100$	s,x,c
HST05Lan	1.235	...	...	...	0.492 ± 0.022	0.078 ± 0.004	0.997 ± 0.016	$+0.050 \pm 0.101$	s,h,x,c

The [O II] EW reported is the median of the posterior probability of the true EW given the observed EW, the spectroscopic uncertainties, and a prior that the EW be positive. The reported confidence interval is the smallest interval containing 90% of the posterior probability. The CMR residual is computed using the fixed-slope fits to individual clusters for cluster member hosts and the composite red sequence fits for field hosts. The CMR residual uncertainties reported are $\sqrt{\sigma_{\rm int}^2 + \sigma_{\rm col}^2}$ where $\sigma_{\rm int}$ is the measured intrinsic scatter of the parent cluster for cluster member hosts and a conservative 0.10 mag for field hosts.

[s] SN is classified as Type Ia from spectrum (Blakeslee et al. 2003a; Riess et al. 2004, 2007; Barbary et al. 2012a)

[L] SN is classified as Type Ia from light curve (Riess et al. 2004, 2007; Barbary et al. 2012a)

[h] SN passes Union2.1 cuts and has reliable Hubble residual measurement (Suzuki et al. 2012)

[x] SN has SALT2 X1 uncertainty less than 1.0 (Suzuki et al. 2012)

[c] SN has SALT2 color uncertainty less than 0.1 (Suzuki et al. 2012)

Table 6.2. Late-type and Unclassified $z > 0.9$ SN Hosts

Name	$z_{\rm host}$	$z_{\rm cluster}$	[O II] EW (Å)	Confidence Interval	Gini Coefficient	Asymmetry	$i_{775} - z_{850}$	CMR residual	Notes
SCP Cluster SN Hosts									
SN SCP06B4	1.116	1.12	-48.2	$[-60.0, -36.0]$	0.362 ± 0.010	0.144 ± 0.011	0.281 ± 0.045	-0.722 ± 0.060	
SN SCP06E12[a]	1.026[b]	1.026	-26.4	$[-47.4, -0.0]$	0.358 ± 0.017	0.056 ± 0.017	0.985 ± 0.143	$+0.077 \pm 0.154$	L
SN SCP06F12	1.110	1.110	-80.0	$[-103.8, -59.2]$	0.392 ± 0.022	0.031 ± 0.014	0.424 ± 0.052	-0.549 ± 0.070	L,h
SCP Field SN Hosts									
SN SCP06G3	0.962	1.259	-69.1	$[-75.6, -62.4]$	0.473 ± 0.018	0.087 ± 0.004	0.689 ± 0.024	-0.200 ± 0.103	L
SN SCP06N33	1.188	1.026	-45.5	$[-47.5, -43.6]$	0.426 ± 0.013	0.131 ± 0.007	0.606 ± 0.033	-0.402 ± 0.105	L,h,x
SN SCP05P1	0.926	1.1[d]	-49.8	$[-53.0, -46.3]$	0.327 ± 0.006	0.200 ± 0.010	0.239 ± 0.035	-0.612 ± 0.106	L,x
SN SCP06T1	1.112	0.971	-38.1	$[-84.8, -0.0]$	0.333 ± 0.021	0.119 ± 0.042	0.167 ± 0.262	-0.824 ± 0.280	
SN SCP06X26	1.44	1.101	-4.0	$[-13.5, -0.0]$	0.367 ± 0.020	0.024 ± 0.020	0.448 ± 0.079	-0.417 ± 0.128	L
GOODS SN Hosts									
SN2002dd	0.950	...	...	...	0.345 ± 0.016	0.114 ± 0.018	0.187 ± 0.037	-0.589 ± 0.106	s,h,x,c
SN2002fw	1.300	...	...	...	0.365 ± 0.012	0.113 ± 0.007	0.647 ± 0.043	-0.215 ± 0.109	s,h,x,c
SN2002fx	1.400	...	...	...	0.304 ± 0.018	0.024 ± 0.025	0.278 ± 0.107	-0.550 ± 0.147	L,h
SN2002ki	1.141	...	...	...	0.376 ± 0.009	0.091 ± 0.006	0.522 ± 0.039	-0.513 ± 0.107	s,h,x
SN2003eb	0.900	...	...	...	0.396 ± 0.011	0.150 ± 0.004	0.267 ± 0.019	-0.523 ± 0.102	s,x,c
SN2003aj	1.307	...	...	...	0.419 ± 0.021	0.143 ± 0.007	0.589 ± 0.031	-0.294 ± 0.105	L,h,x,c
SN2003ak	1.551	...	...	...	0.469 ± 0.026	0.104 ± 0.004	0.333 ± 0.026	-0.684 ± 0.103	L,c
SN2003dy	1.340	...	...	...	0.405 ± 0.012	0.279 ± 0.004	0.492 ± 0.014	-0.417 ± 0.101	s,h,x,c
HST04Eag	1.019	...	...	...	0.389 ± 0.008	0.200 ± 0.003	0.370 ± 0.013	-0.585 ± 0.101	s,h,x,c
HST04Mcg	1.357	...	...	...	0.324 ± 0.007	0.243 ± 0.009	0.773 ± 0.042	-0.124 ± 0.108	s,h,x,c
HST04Pat	0.970	...	...	...	0.358 ± 0.007	0.140 ± 0.007	0.584 ± 0.025	-0.330 ± 0.103	s,h,c
HST04Omb	0.975	...	...	...	0.423 ± 0.016	0.287 ± 0.002	0.191 ± 0.008	-0.704 ± 0.100	s,h,x,c
HST05Fer	1.020	...	...	...	0.477 ± 0.030	0.049 ± 0.008	0.496 ± 0.028	-0.410 ± 0.104	s,h,x,c
HST05Gab	1.120	...	...	...	0.252 ± 0.019	-0.088 ± 0.048	0.618 ± 0.187	-0.356 ± 0.212	s,h,x,c
HST05Koe	1.230	...	...	...	0.284 ± 0.007	0.119 ± 0.011	0.625 ± 0.117	-0.318 ± 0.154	s,x,c
HST05Red	1.189	...	...	...	0.404 ± 0.029	0.079 ± 0.004	0.247 ± 0.014	-0.730 ± 0.101	L,h,x,c
HST05Str	1.027	...	...	...	0.336 ± 0.006	0.121 ± 0.007	0.496 ± 0.038	-0.457 ± 0.107	s,h,c

The [O II] EW reported is the median of the posterior probability of the true EW given the observed EW, the spectroscopic uncertainties, and a prior that the EW be positive. The reported confidence interval is the smallest interval containing 90% of the posterior probability. The CMR residual is computed using the fixed-slope fits to individual clusters for cluster member hosts and the composite red sequence fits for field hosts. The CMR residual uncertainties reported are $\sqrt{\sigma_{\rm int}^2 + \sigma_{\rm col}^2}$ where $\sigma_{\rm int}$ is the measured intrinsic scatter of the parent cluster for cluster member hosts and a conservative 0.10 mag for field hosts.

[a] Unclassified galaxy.

[b] Redshift undetermined; assumed to be a cluster member at $z = 1.026$

[d] Photometric cluster redshift.

[s] SN is classified as Type Ia from spectrum (Blakeslee et al. 2003a; Riess et al. 2004, 2007; Barbary et al. 2012a)

[L] SN is classified as Type Ia from light curve (Riess et al. 2004, 2007; Barbary et al. 2012a)

[h] SN light curve passes Union2.1 cuts (Suzuki et al. 2012)

[x] SN has SALT2 X1 uncertainty less than 1.0 (Suzuki et al. 2012)

[c] SN has SALT2 color uncertainty less than 0.1 (Suzuki et al. 2012)

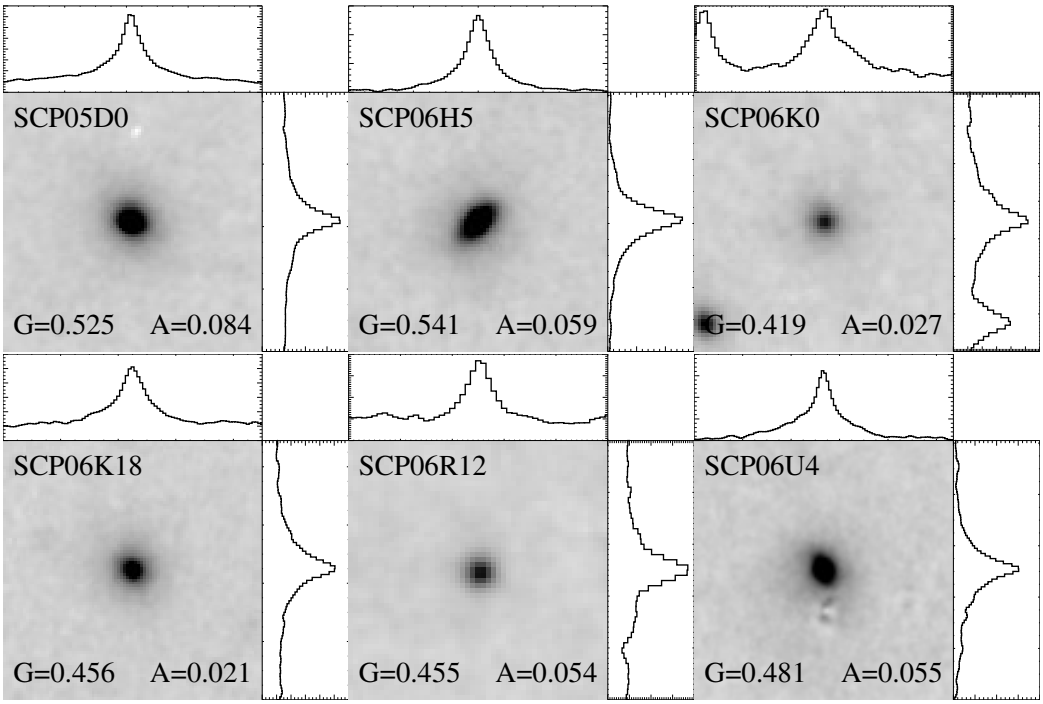

Figure 6.1. Interloper- and SN-subtracted z_{850} cutouts of SCP cluster early-type SN hosts. X- and Y-profiles are shown as histograms to the top and right of each image. The Gini coefficient, shown in the lower left corner of each image, is related to the sharpness of the X- and Y- peaks, with sharper peaks producing larger Gini coefficients, and hence implying more consistency with early-type galaxies. The asymmetry index, shown in the bottom right corner of each image, is related to the mirror symmetry of each profile. The more symmetric the profiles, the lower the asymmetry and the more consistency with early-type classification. Note that the cutouts are from the specifications of the GALAPAGOS algorithm, and have been stretched into a square shape; i.e. for display purposes only, the pixels in this series of figures are generally not square.

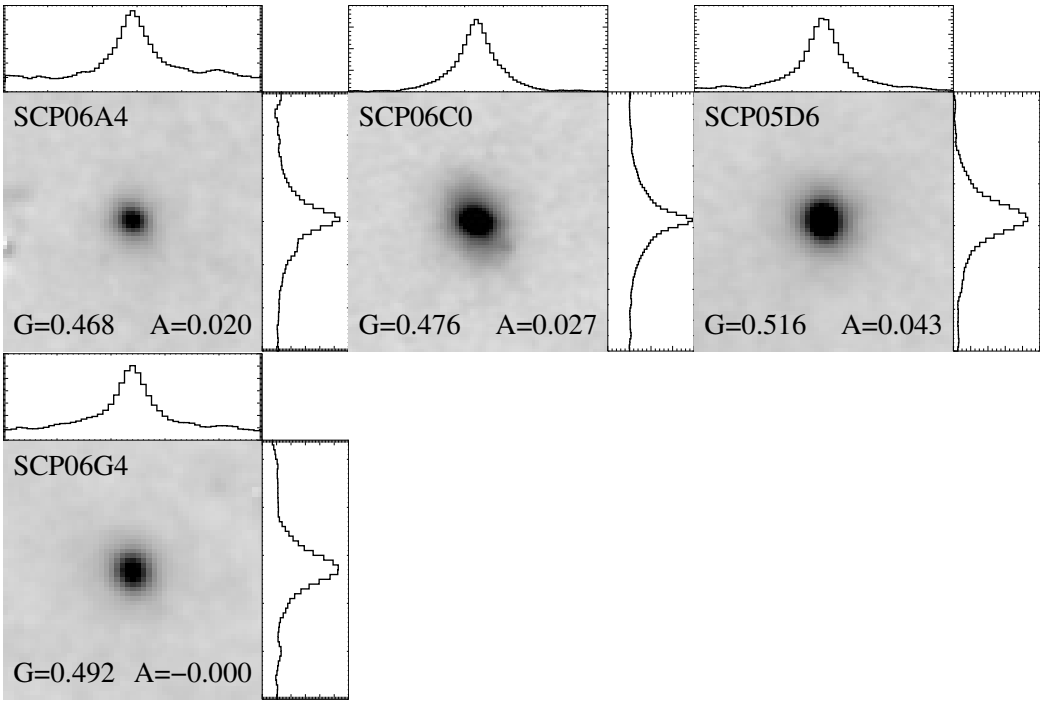

Figure 6.2. SCP field early-type hosts. Image cutouts, profiles, and text are the same as Figure 6.1.

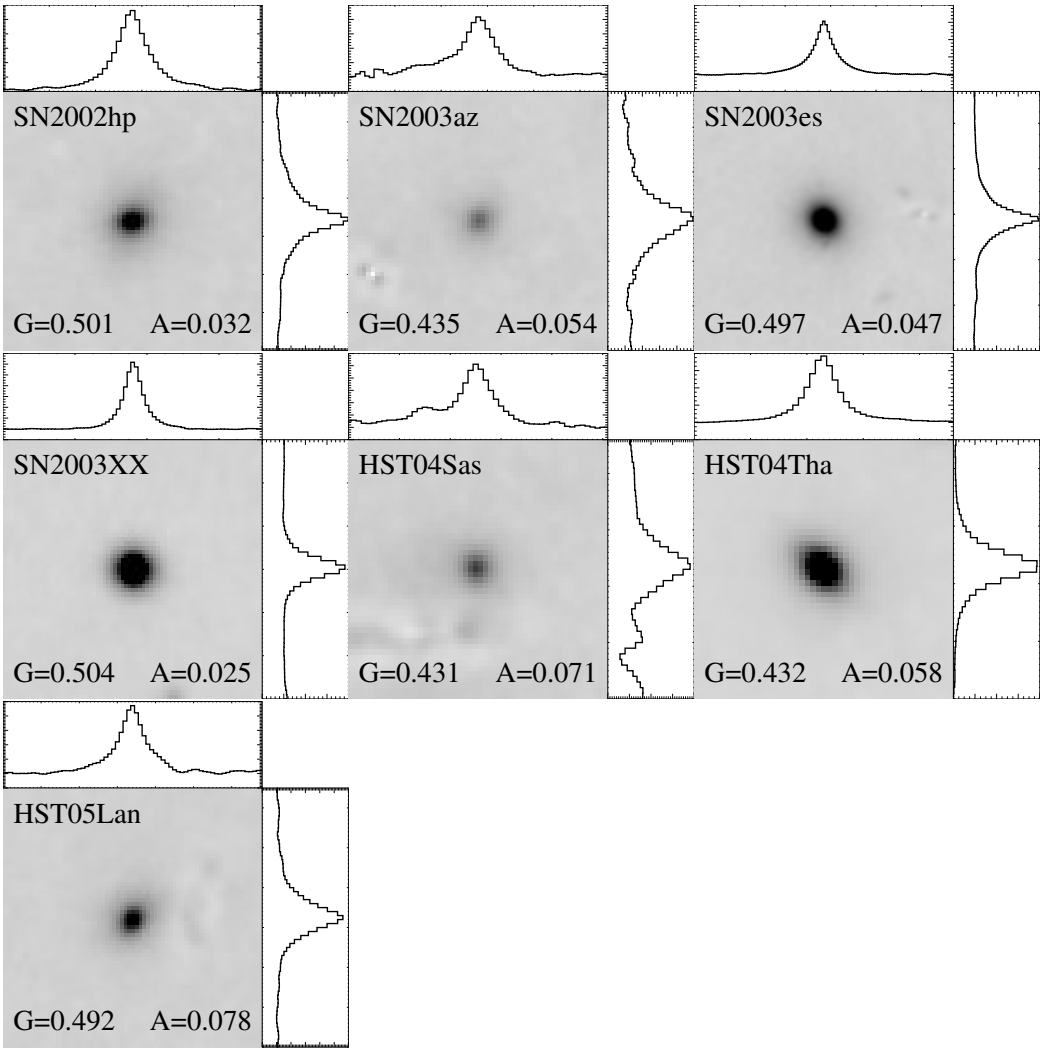

Figure 6.3. GOODS field early-type hosts. Image cutouts, profiles, and text are the same as Figure 6.1.

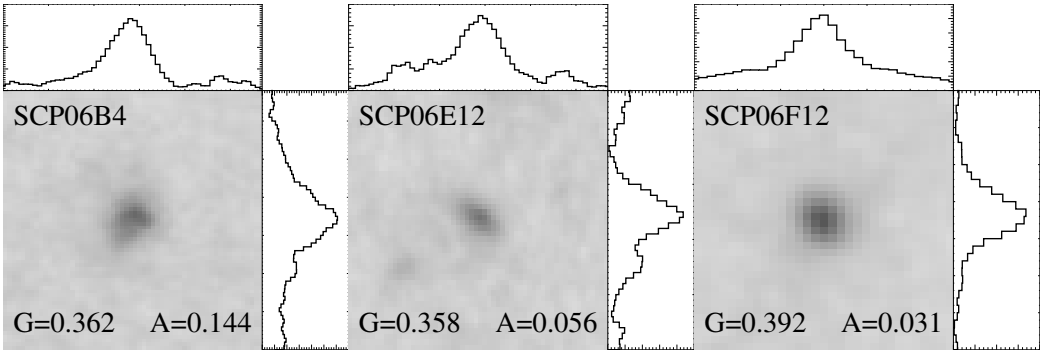

Figure 6.4. SCP cluster late-type hosts. Image cutouts, profiles, and text are the same as Figure 6.1.

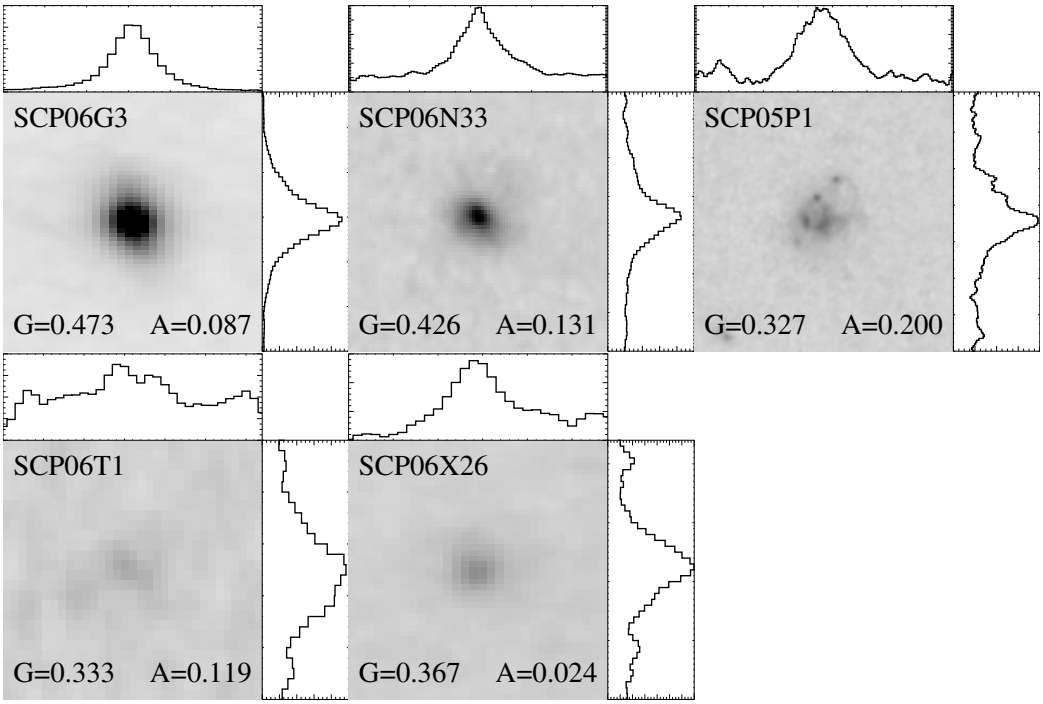

Figure 6.5. SCP field late-type hosts. Image cutouts, profiles, and text are the same as Figure 6.1. Note that the cutout for the host of SN SCP06G3 is considerably distorted. This galaxy is likely an edge-on disk galaxy.

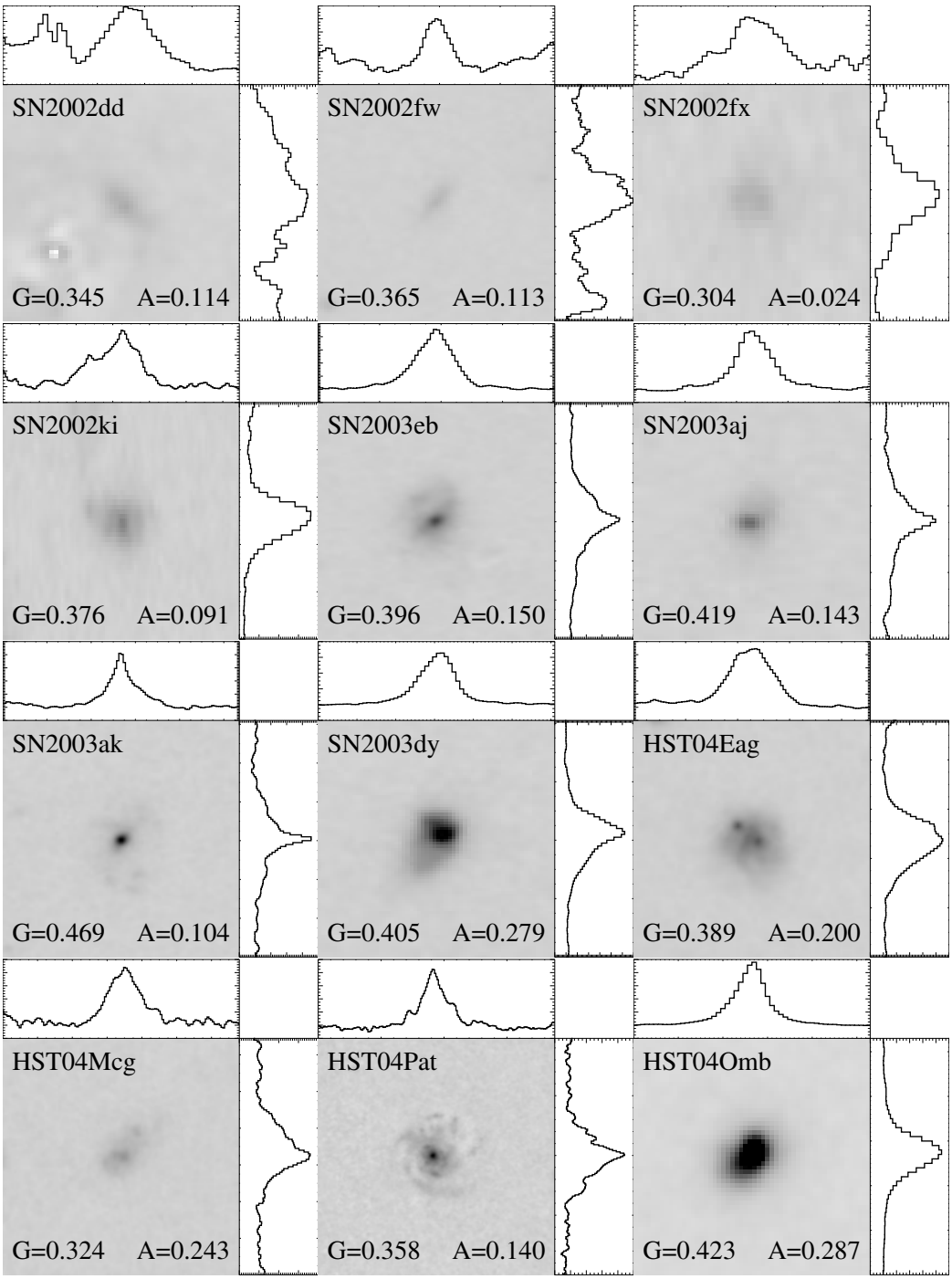

Figure 6.6. GOODS field late-type hosts. Image cutouts, profiles, and text are the same as Figure 6.1.

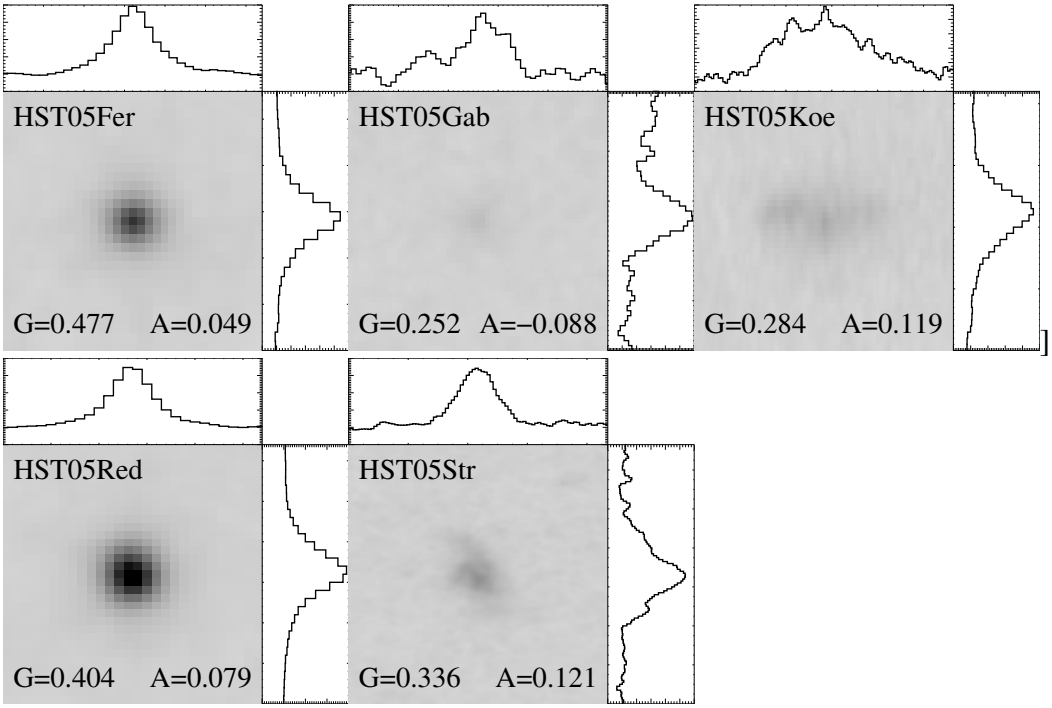

Figure 6.6. GOODS field late-type hosts (continued).

CHAPTER 7

SN Typing by Host Galaxy

The classification of the supernovae discovered in the *HST* Cluster SN Survey uses several approaches simultaneously (see Barbary et al. (2012a) for a discussion of the photometric and light curve constraints). Here we discuss the typing constraints that come from just the host galaxy information. These constraints are already quite strong.

As described in §3.1, classifying a SN as Type Ia when hosted by an early-type galaxy is a robust alternative to spectroscopic typing. However, it is natural to wonder if misclassification of the host galaxy and subsequently the SN is more frequent at high redshift, where morphological classification is more difficult and star formation more prevalent. To investigate this potential shortcoming, we estimate the *a priori* relative rates of detecting SNe Ia and SNe CC in the host galaxies from the *HST* Cluster SN Survey which are classified as early-type in Chapter 6 (we also include the host of SN SCP06E12 for analysis in this chapter, as it is plausibly early-type, although we leave it as unclassified in Chapter 6).

A rough estimate of the *intrinsic* rate of SNe Ia in an individual galaxy can be made using the popular A+B SN Ia rate parameterization in which the rate is the sum of a term proportional to the ongoing star-formation rate and a term proportional to the stellar mass:

$$R_{SN_{Ia}} = AM + B\dot{M} \tag{7.1}$$

Several choices of A and B are available in the literature. We choose the values derived from photometric estimates of SN host masses and star formation rates in the SNLS: $A = 5.3 \times 10^{-14}\mathrm{yr}^{-1}{\mathrm{M}_{\odot}}^{-1}$, $B = 3.9 \times 10^{-4}{\mathrm{M}_{\odot}}^{-1}$ (Sullivan et al. 2006). The values for A and B depend on which initial mass function (IMF) is assumed. The values above are derived assuming a Kroupa (2001) IMF, which is very similar to the Chabrier IMF with which the BC03 SSPs we have been using are generated.

The cosmic SN CC rate has been shown to be proportional to the cosmic star formation rate. By dividing the cosmic SN CC rate found in Bazin et al. (2009) at $z = 0.3$ ($R_{SN_{CC}} = 1.63 \times 10^{-4}(h_{70}^{-1}\mathrm{Mpc})^{-3}$) by the cosmic star formation rate at $z = 0.3$ found in Hopkins & Beacom (2006) of $0.03 M_{\odot}\mathrm{yr}^{-1}\mathrm{Mpc}^{-3}$ (and converting from the modified Salpeter IMF used there to a Kroupa IMF) we can obtain a similar formula for SNe CC:

$$R_{SN_{CC}} = C\dot{M} \tag{7.2}$$

with $C = 6.52 \times 10^{-3} \mathrm{M}_{\odot}{}^{-1}$.

To estimate the star formation rate in these galaxies we rely on the the spectroscopic [O II] luminosity. As mentioned earlier, while [O II] may indicate star formation, it may also indicate LINER activity in an otherwise passive galaxy. The [O II]-inferred star formation rate should thus be viewed as an upper limit to the true star formation rate, which may be much less or even zero. We investigate the [O II]-inferred star formation rate parameterization of Kennicutt (1998) scaled to a Kroupa IMF:

$$\mathrm{SFR}_{[\mathrm{O\ II}]}(M_{\odot}\mathrm{yr}^{-1}) = 2.65 \times 10^{-41} L_{[\mathrm{O\ II}]}(\mathrm{erg\ s}^{-1}) \tag{7.3}$$

The [O II]-inferred star formation rate is sensitive to galactic metallicity and dust. These are in turn correlated with the galaxy's stellar mass. Gilbank et al. (2010) have investigated the correlation of the nominal [O II]-inferred star formation rate with other more robust star formation rate indicators in different mass bins and derived an empirical correction as a function of galaxy stellar mass that accounts for trends in galaxy metallicity and dust:

$$\mathrm{SFR}_{\mathrm{corr}} = \frac{\mathrm{SFR}_{\mathrm{nom}}}{a \tanh[(x-b)/c] + d} \tag{7.4}$$

where $\mathrm{SFR}_{\mathrm{corr}}$ is the corrected star formation rate, $\mathrm{SFR}_{\mathrm{nom}}$ is the nominal star formation rate from Equation 7.3, $x = \log(M_*/M_{\odot})$, $a = -1.424$, $b = 9.827$, $c = 0.572$, and $d = 1.700$. Since the cluster early-type SN hosts are quite massive, this correction is significant. We carry out our analysis both with and without this mass correction.

No [O II] is detected in the spectroscopy of many of the host galaxies in the *HST* Cluster SN Survey. Rather than infer that the star formation is simply zero for these galaxies, we use Bayes' theorem to derive the probability distribution of the true [O II] luminosity given the observed value, taking into account the observational uncertainties, and enforcing a prior that the [O II] luminosity must be positive (i.e. we perform a likelihood analysis). The median star formation rates (both nominal and mass-corrected) from the posterior distributions are reported in Table 7.1.

To estimate the host galaxy stellar mass, we fit BC03 SSP templates as in Equation 5.1 to the observed i_{775} and z_{850} magnitudes, assuming $z_{\mathrm{form}} = 3.0$. The best fitting value of M_{gal} is then the *initial* stellar mass of the template, but the *current* stellar mass, factoring in the rapid deaths of massive stars, is also supplied by BC03. With only two photometric bands available, we only attempt this mass measurement for galaxies which are classified as early-types in Chapter 6. The more complicated SEDs of late-type galaxies will generally require information from more photometric bands and a more sophisticated approach to mass measurements. The statistical uncertainty of this mass measurement is limited by the uncertainty in our photometric measurements, both in z_{850} magnitude and in $i_{775} - z_{850}$ color. To this uncertainty, we also add a systematic uncertainty (in quadrature) to capture our ignorance of the precise star-formation histories and metallicities of these galaxies. By fitting BC03 composite stellar spectra of a variety of exponential and delayed exponential

star-formation histories and various metallicities to the i_{775} and z_{850} photometry, we estimate that this systematic uncertainty in mass is around 25% or 0.1 dex. The host galaxy masses are reported in Table 7.1.

With the masses and star formation rates derived above, we apply Equations 7.1 and 7.2 to estimate the *intrinsic* rates of SNe Ia and SNe CC in each host galaxy. One interesting consequence of Equation 7.1 is that the expected increase in the SN Ia rate due to recent star-formation (the B component) is only $\sim$ 1% - 5% for all of our early-type hosts except that of SN SCP06U4 for which the increase is $\sim$ 30%. The true enhancement may, in fact, be smaller if the observed [O II] luminosity contains LINER emission. This implies that our early-type hosted SNe Ia probably have old progenitors and hence are not associated with dust from recent star formation.

The intrinsic rates are a start, however, since we know *a priori* that the particular galaxies we are analyzing each hosted a *detectable* SN, it is more informative to estimate the *apparent* SN rates. For example, the apparent rate of a SN of type X given its intrinsic rate can be written:

$$R_{SN_X}^{\rm apparent} = R_{SN_X}^{\rm intrinsic} f_{SN_X}^{\rm detectable} \tag{7.5}$$

where $f_{SN_X}^{\rm detectable}$ is the fraction of detectable SNe of type X for a particular galaxy. The z_{850} detection threshold for a point source in a single epoch of the *HST* Cluster SN Survey is about 25.3 (Barbary et al. 2012a). However, since the SNe in question have passed quality cuts requiring detection in multiple epochs and multiple bands we adopt an effective z_{850} detection threshold for SN peak brightness of ~ 24.7. For each host galaxy, we estimate the fraction of SNe Ia and SNe CC with peak z_{850} magnitude brighter than this detection threshold using the rest frame *R*-band luminosity functions derived from the Lick Observatory Supernova Search (LOSS) Li et al. (2011). Using the maximum light spectral templates of Hsiao et al. (2007) for normal SNe Ia and Nugent et al. (2002) for SN1991bg-like and SN1991T-like SNe Ia, SNe Ibc, SNe II-N, SNe II-P, and SNe II-L we *K*-correct our z_{850} detection threshold to the rest frame *R*-band for each SN subtype. We estimate the fractions of detectable SNe Ia and SNe CC as the fractions of LOSS SNe Ia and SNe CC that exceed these *K*-corrected thresholds:

$$f_{SN_X}^{\rm detectable} = N_{SN_X}^{>}/N_{SN_X} \tag{7.6}$$

where $N_{SN_X}^{>}$ and N_{SN_X} are the number of SNe of type X brighter than their respective R-band threshold and the total number of SNe of type X, respectively. We find that even at $z = 0.9$, none of the 25 SNe Ibc and only four (three SNe II-N and one SN II-L) out of 80 SNe II from LOSS would have been detected in our survey. On the other hand, our survey would have discovered 55 out of 74 LOSS SNe Ia, or 53 out of 59 if sub-luminous SN1991bg-like and SN2002cx-like SNe Ia are excluded. We again employ Bayes' theorem to derive the probability distribution of the expected value of $N_{SN_X}^{>}$ (and hence the probability distribution of $f_{SN_X}^{\rm detectable}$) assuming the observed number is Poisson distributed and a positive flat prior.

With probability distribution functions for the masses (assumed to be log-normally distributed), [O II] luminosities, and detectable fractions of SNe Ia and SNe CC for each galaxy, we can use a Monte Carlo simulation to sample from these distributions and derive a probability distribution function of the apparent rates of SNe Ia and SNe CC. Given the apparent rates, the probability that a SN is a SN CC is:

$$P(CC) = \frac{R_{SN_{CC}}^{\text{apparent}}}{R_{SN_{CC}}^{\text{apparent}} + R_{SN_{Ia}}^{\text{apparent}}} \tag{7.7}$$

The results of this analysis are shown in Table 7.1. Even under the assumption that [O II] traces star formation and not LINER activity, five of eleven SNe have $P(CC) \leq 0.02$, and four others have $P(CC) \leq 0.15$. One of the two remaining SNe, SN SCP06U4, is a spectroscopically confirmed Type Ia. The final remaining SN, SN SCP06E12, was already considered uncertain due to its lack of spectroscopic redshift, though its light curve is consistent with a Type Ia at the redshift of the cluster in the same field of view. In fact, for almost all of the early-type hosted SCP SNe, the already strong type constraints derived here from just the host galaxy information can be supplemented with additional constraints by considering the full SN light curve shapes, colors and magnitudes. Ten out of the eleven early-type hosted SCP SNe analyzed in this chapter have evidence independent of their hosts or spectra indicating that they are SNe Ia (for details, see paper II of this series: Barbary et al. 2012a). (These SNe are indicated with a "L" in the Notes column of Table 7.1). The one remaining SN, SN SCP06K18, does not have sufficient early time coverage to constrain its type through its light curve. However, as indicated in Table 7.1, its massive early-type host and lack of [O II] emission strongly suggest it is a Type Ia.

Table 7.1. A Priori Rate Estimates for Early-type SCP SN Host Galaxies

Name	log(Mass)	median SFR $M_\odot yr^{-1}$	median $R^a_{SN_{CC}}$ $10^{-3}yr^{-1}$		median $R^a_{SN_{Ia}}$ $10^{-3}yr^{-1}$		$P(CC)$	Notes
Nominal Star Formation Rates								
SN SCP05D0	10.9	0.53	0.13	(3.43)	2.73	(3.95)	0.04	s,L
SN SCP05D6	11.4	2.56	0.23	(16.44)	7.82	(14.71)	0.03	L
SN SCP06A4	10.7	0.29	0.04	(1.85)	1.58	(2.53)	0.02	L
SN SCP06C0	11.2	2.20	0.42	(14.18)	6.60	(9.85)	0.06	L
SN SCP06E12[b]	9.9	0.50	0.11	(3.19)	0.42	(0.63)	0.21	L
SN SCP06G4	11.2	0.12	<0.01	(0.75)	4.66	(9.02)	<0.01	s,L
SN SCP06H5	11.6	0.32	0.04	(2.06)	12.11	(20.77)	<0.01	L
SN SCP06K0	11.4	0.32	0.02	(2.09)	4.84	(14.08)	<0.01	L
SN SCP06K18	11.8	0.17	0.01	(1.08)	11.00	(32.12)	<0.01	
SN SCP06R12	10.4	0.02	<0.01	(0.12)	0.78	(1.33)	<0.01	L
SN SCP06U4	11.1	7.45	1.90	(47.95)	6.82	(10.22)	0.22	s,L
Mass-Corrected Star Formation Rates								
SN SCP05D0	10.9	1.93	0.47	(12.44)	3.11	(4.51)	0.13	s,L
SN SCP05D6	11.4	9.26	0.84	(59.57)	9.20	(17.35)	0.08	L
SN SCP06A4	10.7	1.04	0.13	(6.70)	1.79	(2.87)	0.06	L
SN SCP06C0	11.2	7.99	1.51	(51.37)	8.13	(12.13)	0.15	L
SN SCP06E12[b]	9.9	1.80	0.41	(11.55)	0.77	(1.18)	0.35	L
SN SCP06G4	11.2	0.42	0.03	(2.71)	4.78	(9.27)	<0.01	s,L
SN SCP06H5	11.6	1.16	0.15	(7.46)	12.42	(21.32)	0.01	L
SN SCP06K0	11.4	1.18	0.09	(7.57)	5.09	(14.86)	0.02	L
SN SCP06K18	11.8	0.61	0.05	(3.92)	11.14	(32.58)	<0.01	
SN SCP06R12	10.4	0.07	<0.01	(0.44)	0.81	(1.38)	0.01	L
SN SCP06U4	11.1	27.01	6.87	(173.73)	11.94	(17.90)	0.36	s,L

[a] Rates in parentheses are *intrinsic* quantities. Rates not in parentheses are *apparent* and factor in SN detectability.

[b] Redshift undetermined; assumed to be a cluster member at $z = 1.026$. This galaxy is left unclassified in §6.2.

[s] Spectroscopically confirmed SN Ia.

[L] Light curve shape, color and magnitude consistent with Type Ia (Barbary et al. 2012a).

CHAPTER 8

Early-type Host Dust Constraints

In this chapter we use measurements of the red sequence scatter to place constraints on the scatter of reddening affecting these galaxies. Under the assumption that at least some red-sequence galaxies have very low dust content, this scatter constraint also sets an absolute scale for dust.

8.1 Red-sequence scatter

Color-magnitude diagrams of each of our clusters are presented in Figure 8.1. For most clusters, the red sequence is clearly visible as an overdensity of morphologically early-type galaxies with $i_{775} - z_{850} \approx 1$. For 23 of the 25 clusters, the marginal likelihood distributions for the cluster CMR intrinsic scatters show clear maxima between 0.0 and 0.1 magnitudes. The intrinsic scatter marginal likelihood distributions for clusters ISCS J1434.7+3519 and ISCS J1433.8+3325 are essentially flat from 0.0 up to 0.3 magnitudes (the largest scatter for which we sampled the posterior likelihood) because the clusters contain too few red early-type galaxies to constrain the fit. Using the CMR fits as a baseline with which to combine clusters, we find that the intrinsic scatter of the stacked "color-magnitude" diagram is 0.046 mag (Figure 8.2). Turning to individual clusters, we find that the best-fit intrinsic scatters of three clusters are consistent with zero. The best-fit intrinsic scatters of the remaining clusters range from 0.023 mag to 0.087 mag (see Table 5.1 for the best-fit values and uncertainties of each cluster's intrinsic scatter).

To compare these observer-frame CMR scatter measurements to published scatter measurements at other redshifts, we first convert to the rest-frame $\sigma(U-V)_{z=0}$ scatter. Using BC03 SSPs, we construct a library of mock galaxy spectra with a variety of formation redshifts, exponentially declining star-formation timescales, and metallicities. For each cluster redshift, we determine the relation between observer-frame $i_{775} - z_{850}$ color and rest-frame $U-V$ color through synthetic photometry of these library spectra. The slope of this relation evaluated at the observed CMR color ranges from ~ 1.9 to ~ 3.2 depending on the redshift; this is the desired multiplicative conversion factor from $\sigma(i_{775} - z_{850})$ to $\sigma(U-V)_{z=0}$. Our rest-frame $\sigma(U-V)_{z=0}$ estimates lie in the range $\sim 0.02 - 0.19$ mag

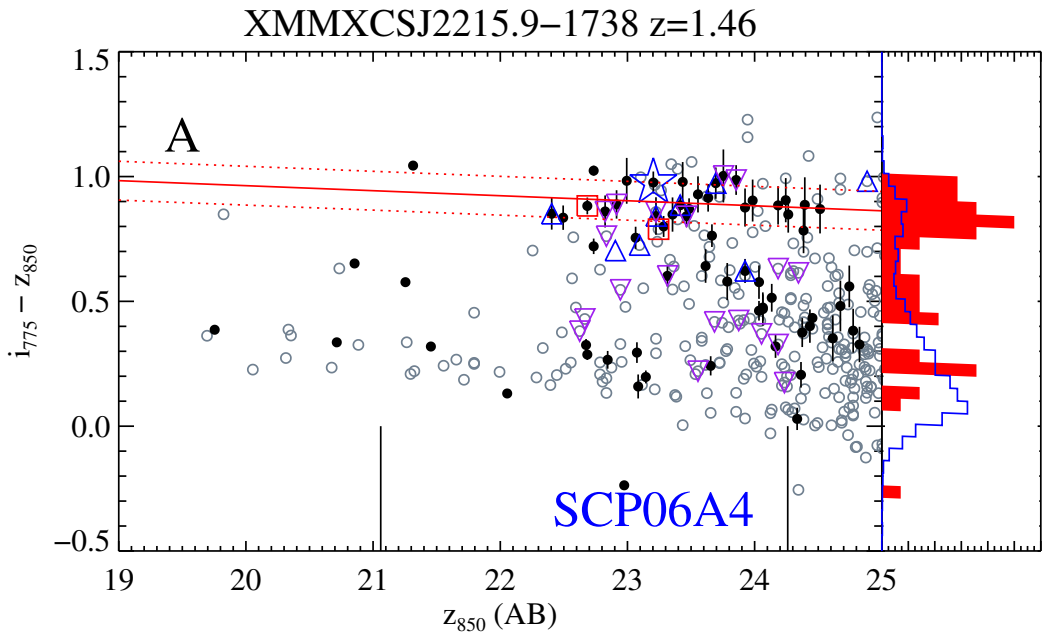

Figure 8.1. Cluster color-magnitude diagrams. Small circles indicate galaxies located within $0.65\mathrm{Mpc}$ of the cluster center. Dark solid circles pass our broader quantitative morphology cuts, light open circles do not. The slightly larger squares and triangles indicate galaxies spectroscopically confirmed to be cluster members, including those that lie outside of the $0.65\mathrm{Mpc}$ aperture. Red squares indicate spectroscopically confirmed members lacking significant [O II] emission ($EW > -5\AA$.) Blue upward pointing triangles indicate spectroscopically confirmed members with significant [O II] emission. Purple downward pointing triangles indicate spectroscopically confirmed members found in the literature but with unpublished [O II] EWs. Stars indicate SN hosts. Blue stars are foreground SN hosts, gold stars are cluster members SN hosts, and red stars are background SN hosts. The solid red line is the best-fit linear color-magnitude relation, and the dashed lines indicate the measured scatter (including contributions from both measurement uncertainties and the intrinsic scatter). The red histogram indicates CMR residuals of cluster galaxies passing our broader morphology cuts falling in the magnitude range $M^* - 2.2 < z_{850} < M^* + 1.0$, which is indicated by the long tick marks on the x-axis. The blue histogram is the solid-angle-scaled analog for the GOODS control fields.

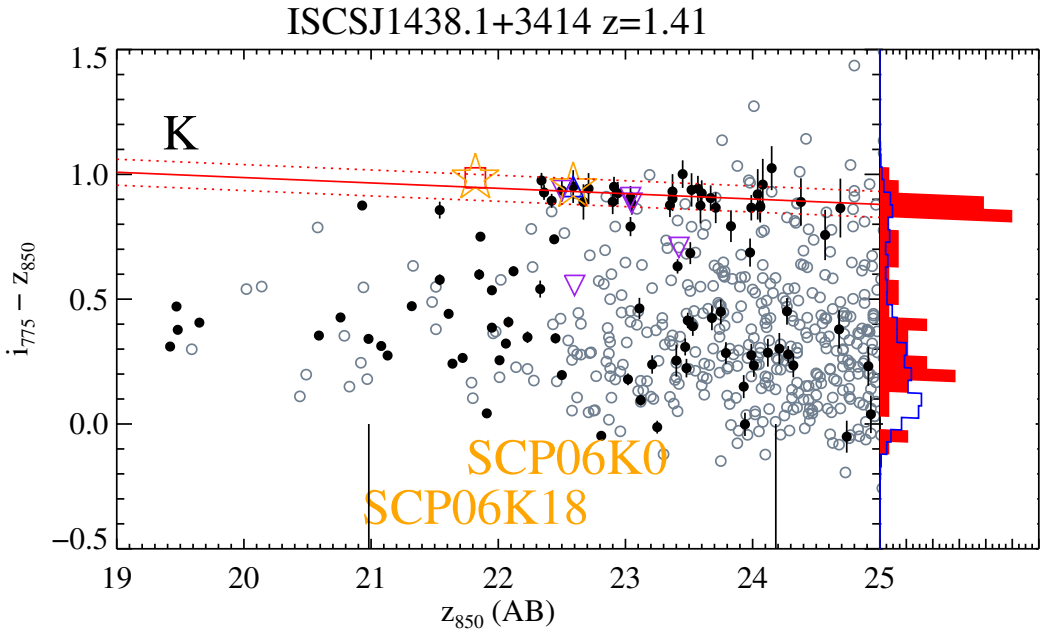

Figure 8.1. Color magnitude diagrams (continued)

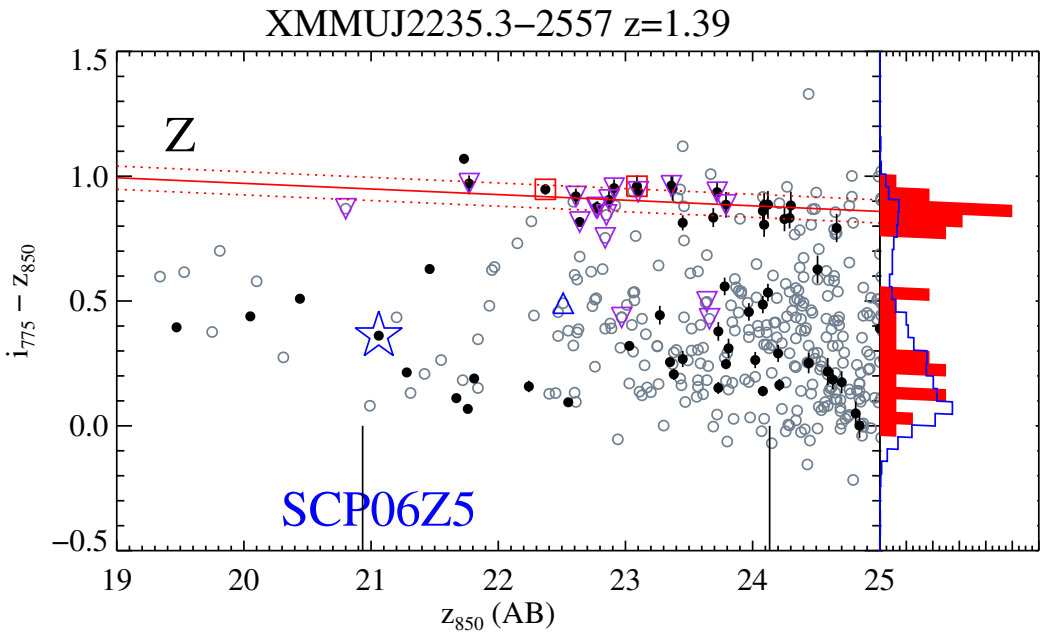

Figure 8.1. Color magnitude diagrams (continued)

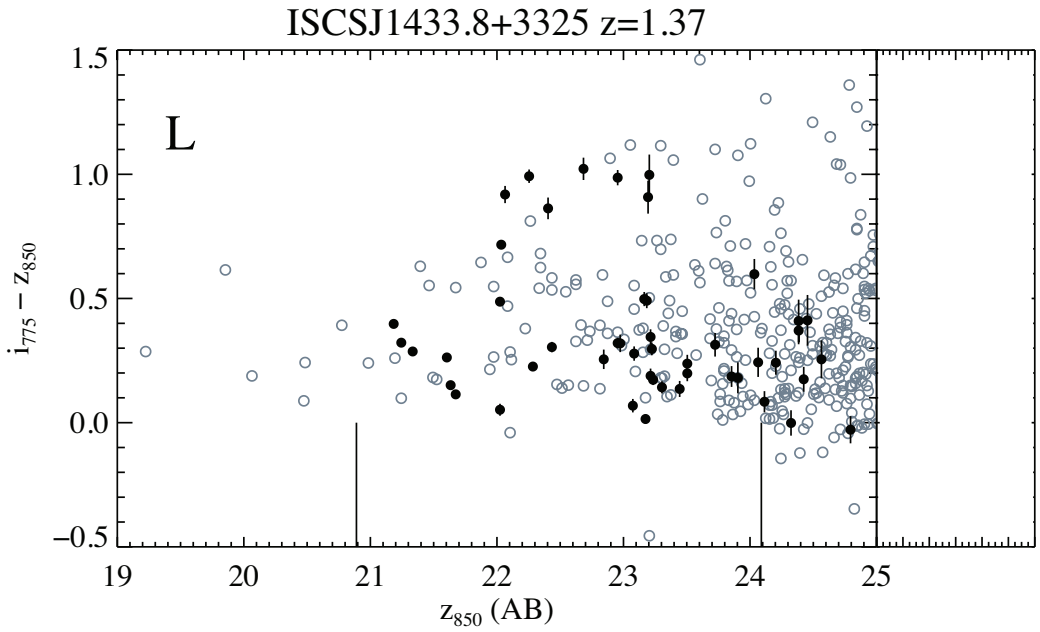

Figure 8.1. Color magnitude diagrams (continued)

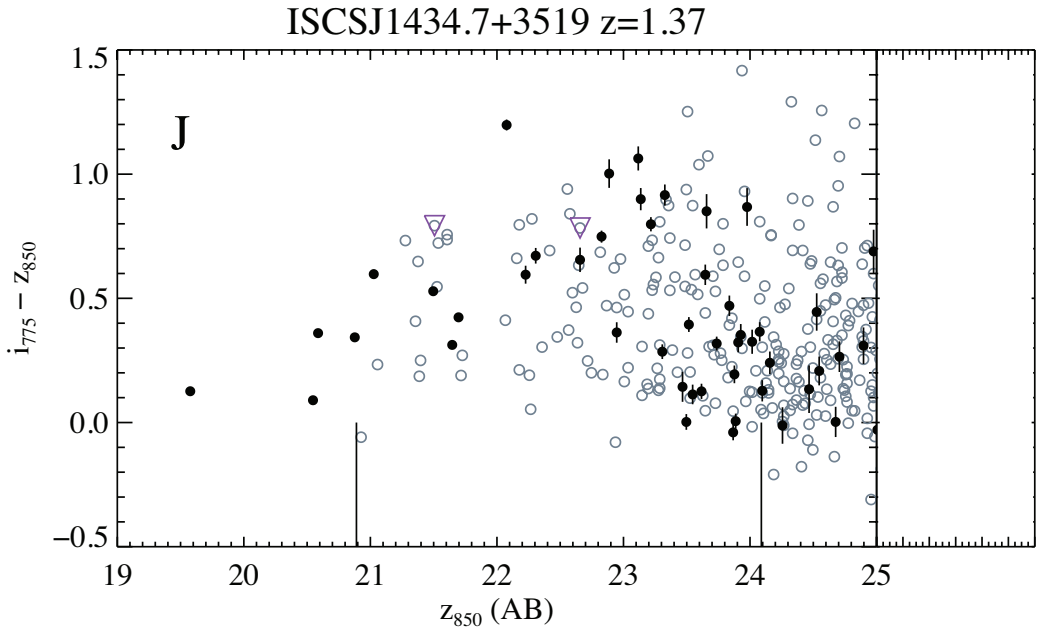

Figure 8.1. Color magnitude diagrams (continued)

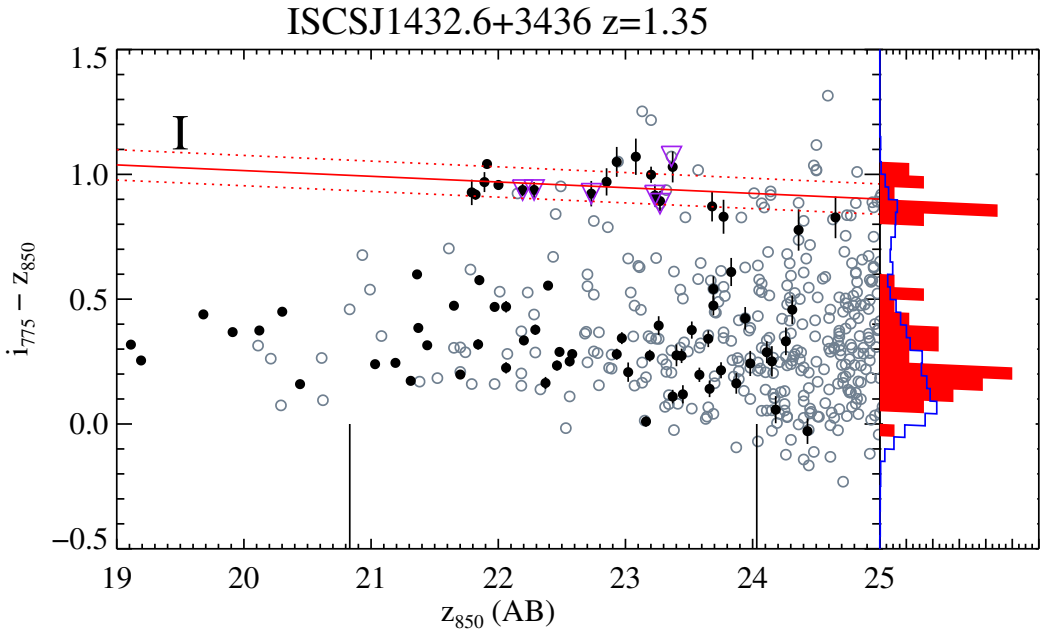

Figure 8.1. Color magnitude diagrams (continued)

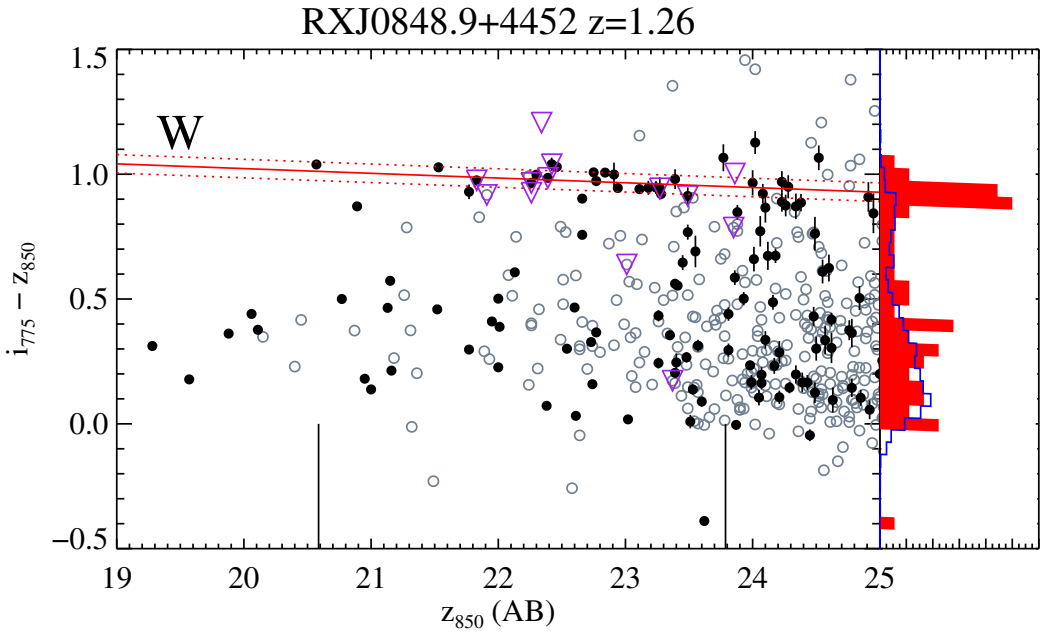

Figure 8.1. Color magnitude diagrams (continued)

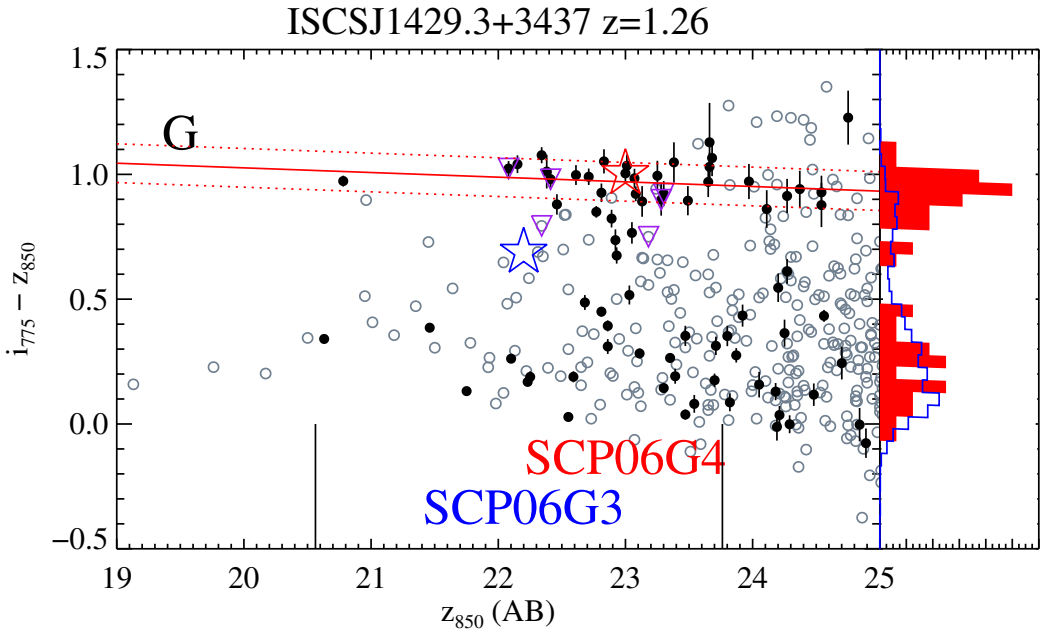

Figure 8.1. Color magnitude diagrams (continued)

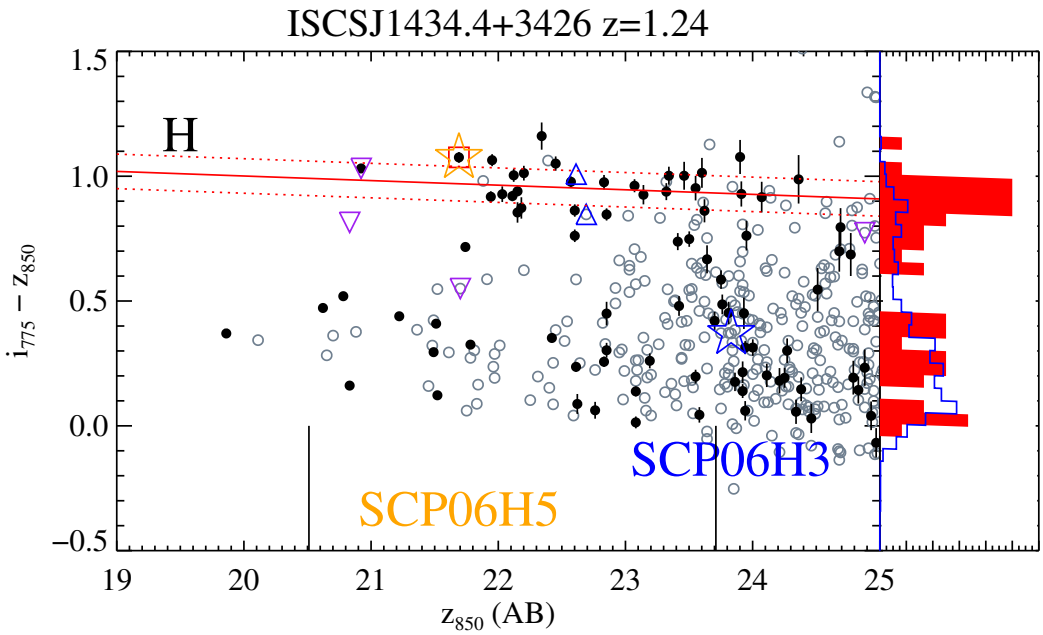

Figure 8.1. Color magnitude diagrams (continued)

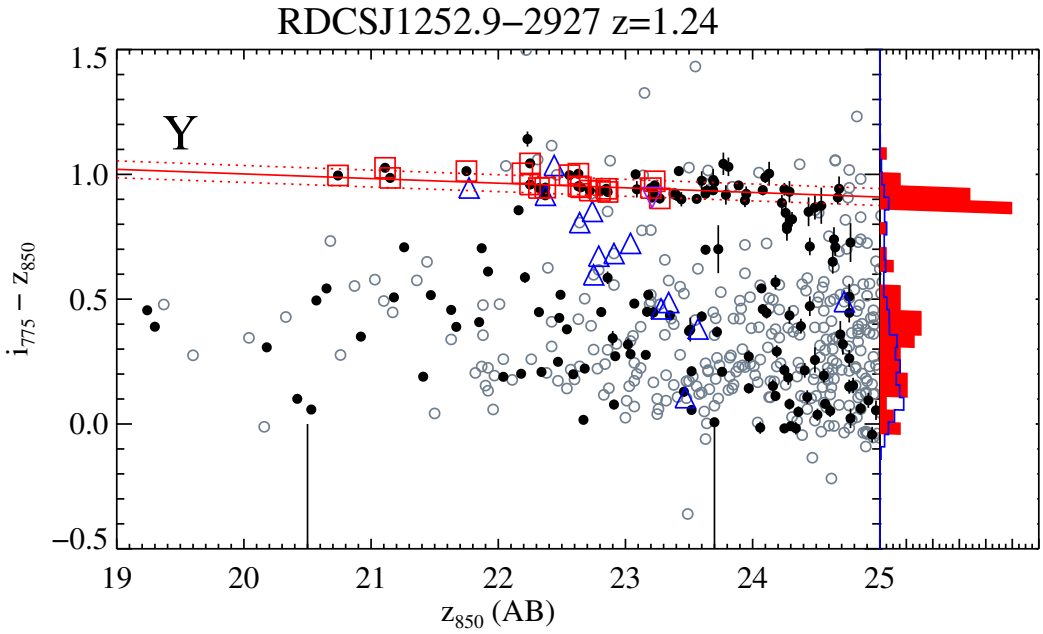

Figure 8.1. Color magnitude diagrams (continued)

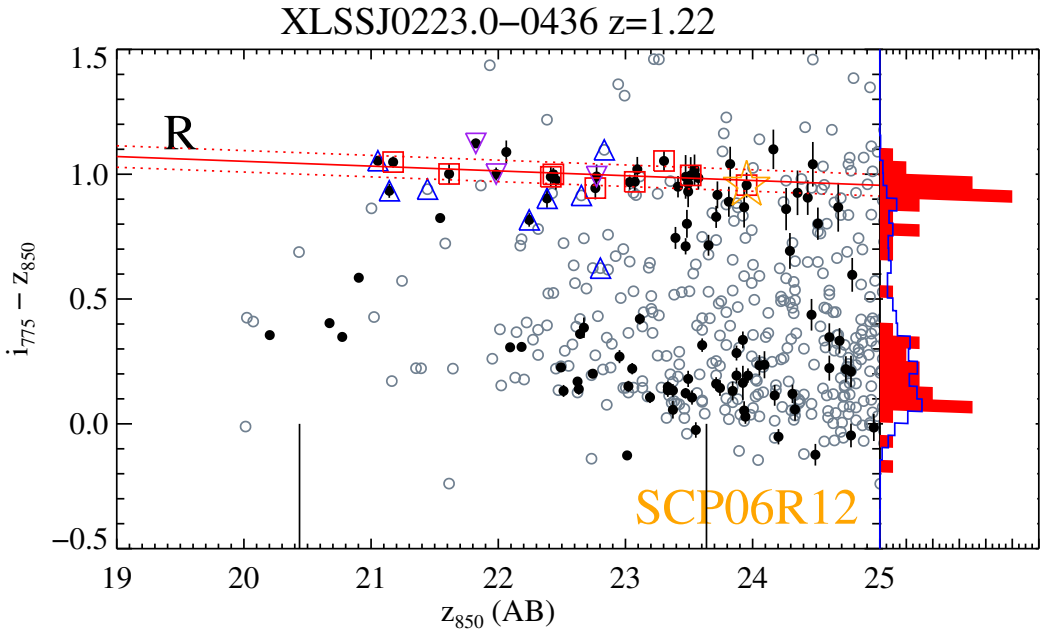

Figure 8.1. Color magnitude diagrams (continued)

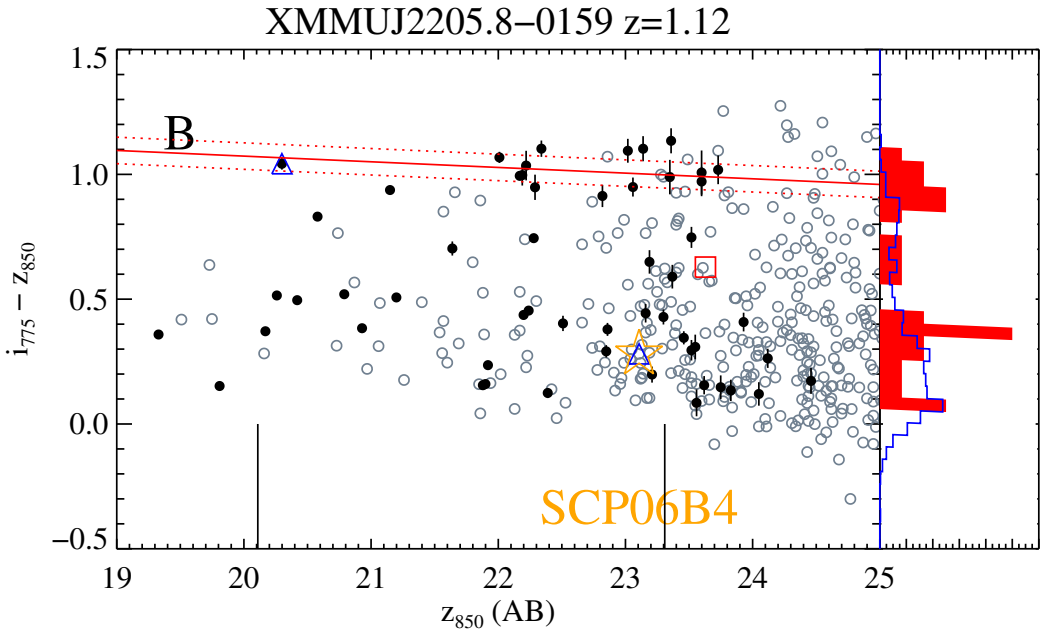

Figure 8.1. Color magnitude diagrams (continued)

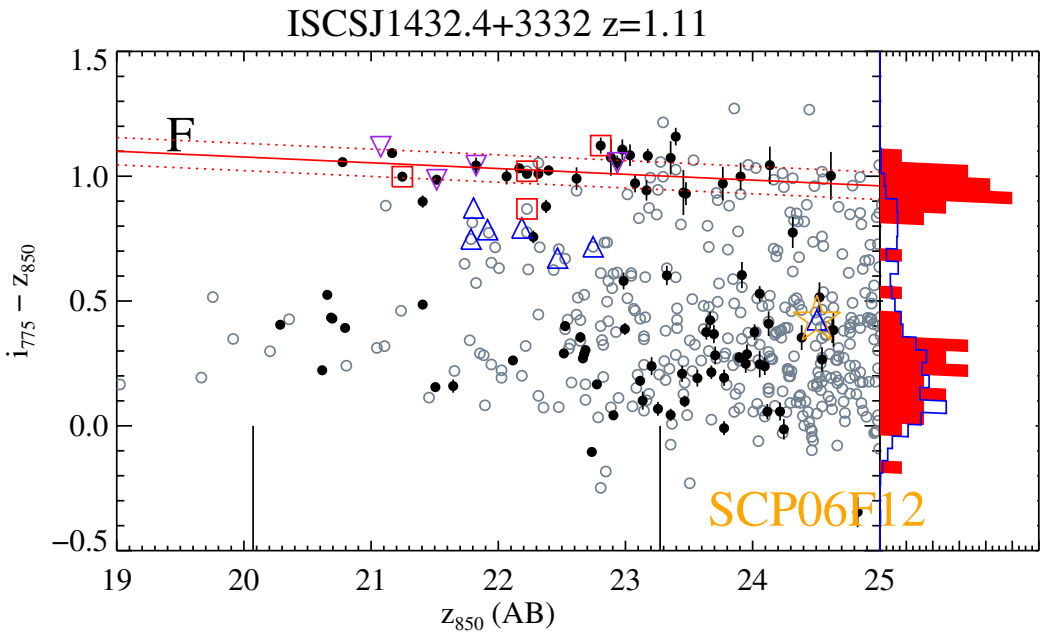

Figure 8.1. Color magnitude diagrams (continued)

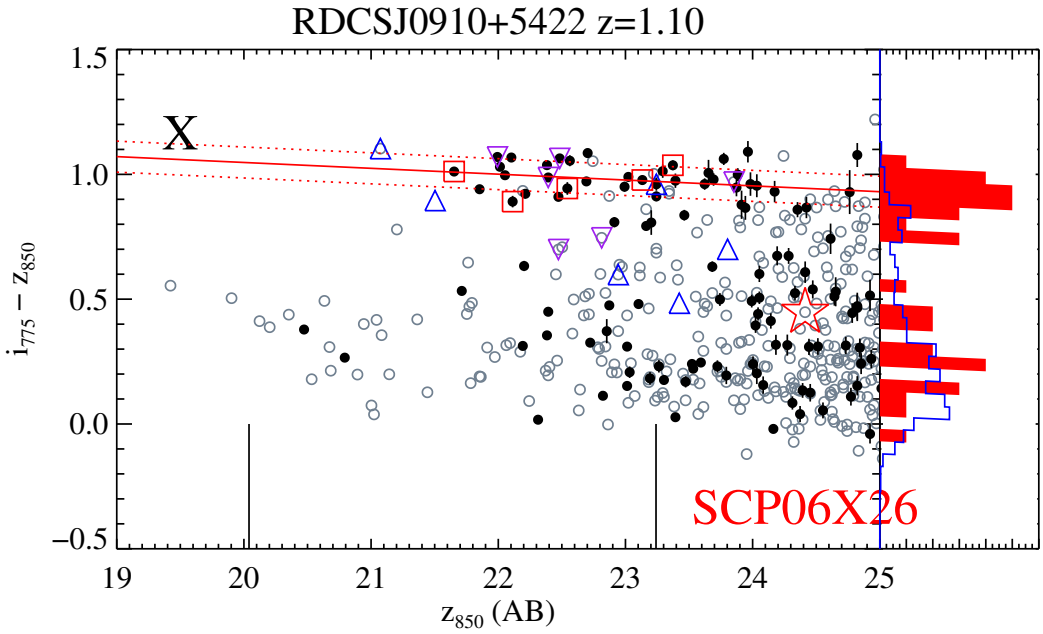

Figure 8.1. Color magnitude diagrams (continued)

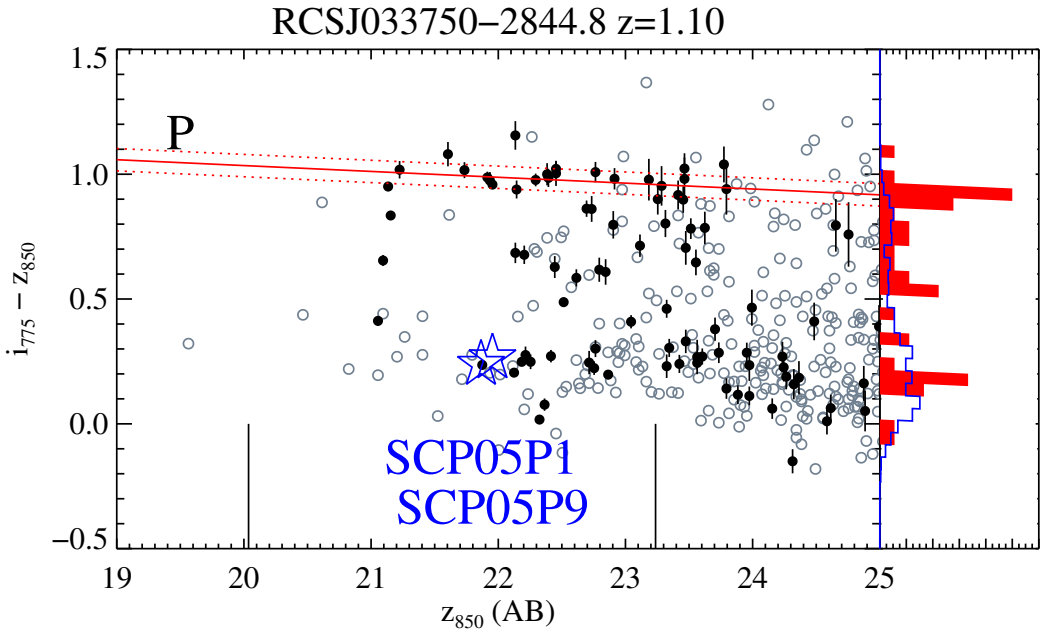

Figure 8.1. Color magnitude diagrams (continued)

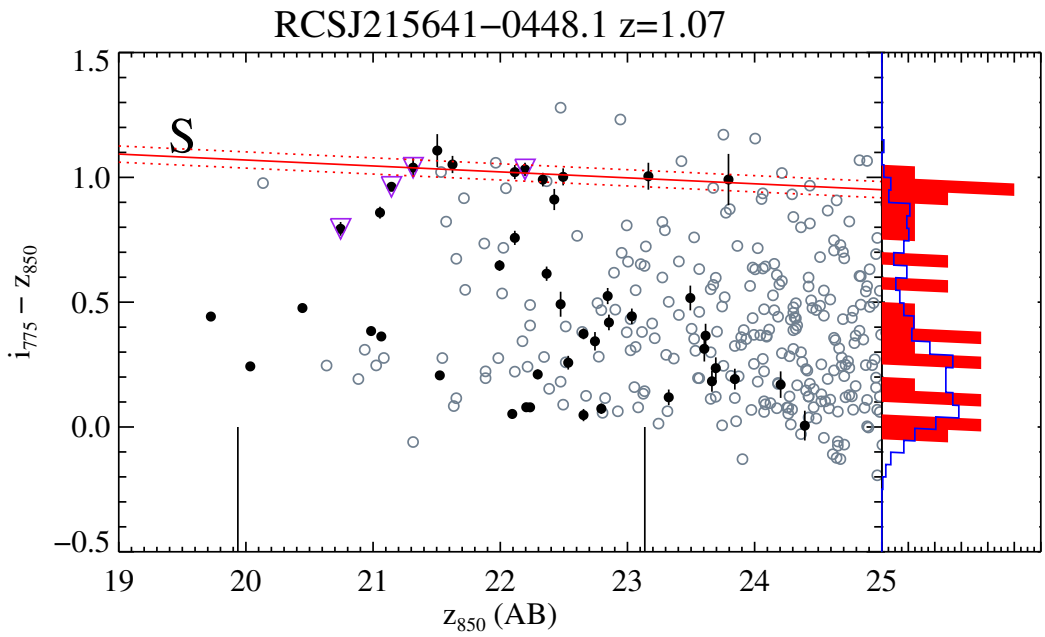

Figure 8.1. Color magnitude diagrams (continued)

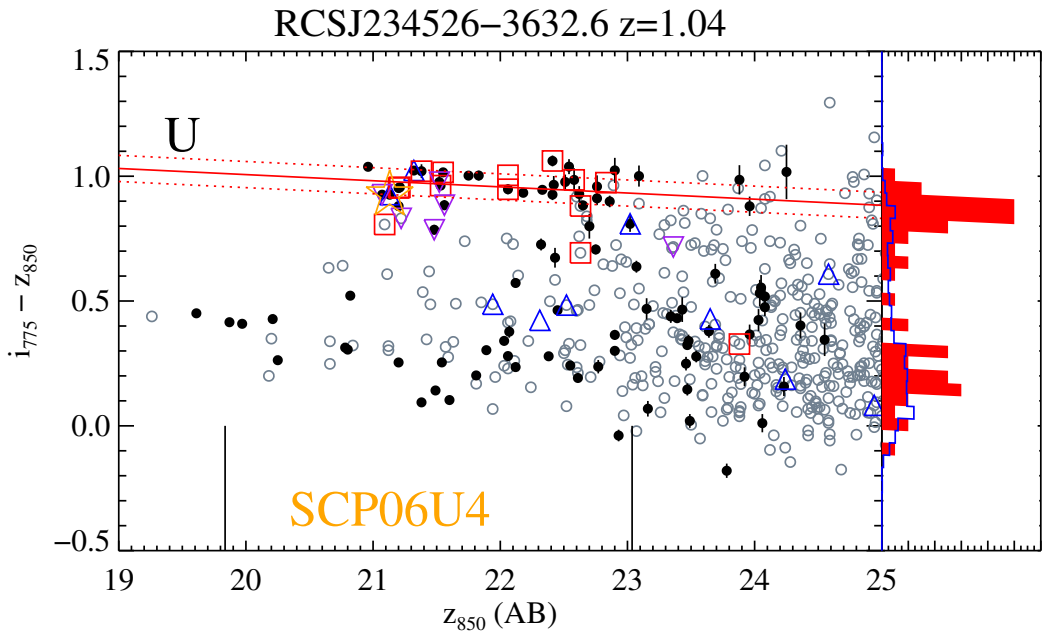

Figure 8.1. Color magnitude diagrams (continued)

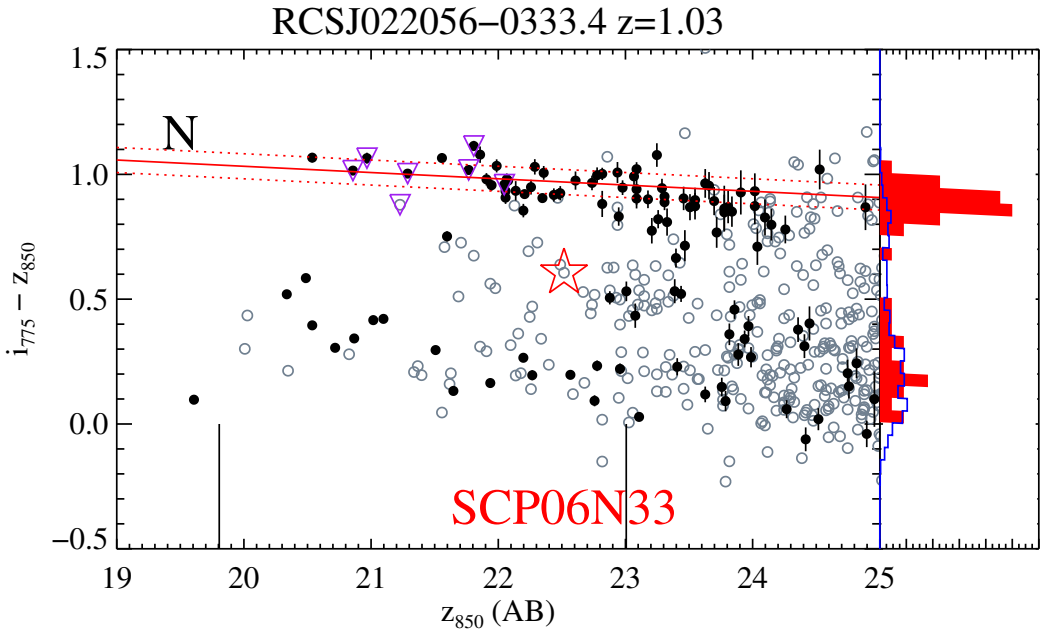

Figure 8.1. Color magnitude diagrams (continued)

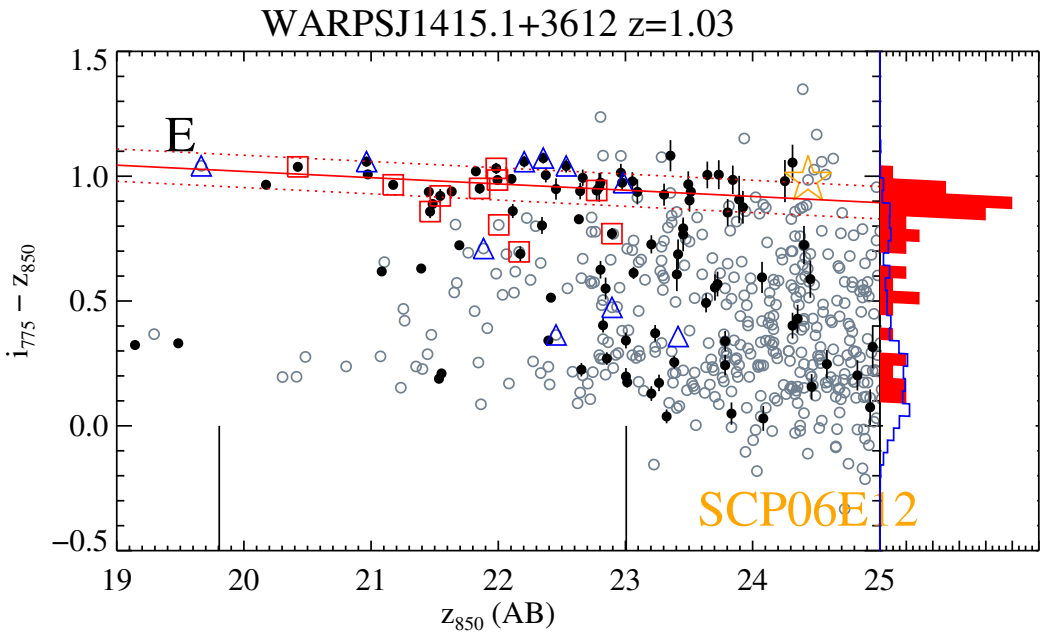

Figure 8.1. Color magnitude diagrams (continued)

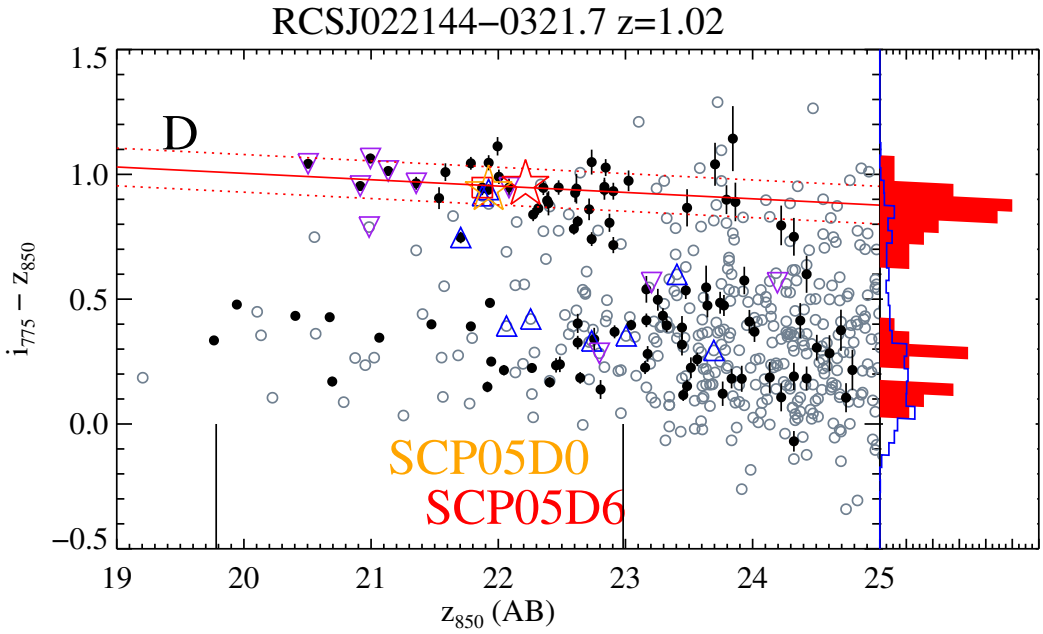

Figure 8.1. Color magnitude diagrams (continued)

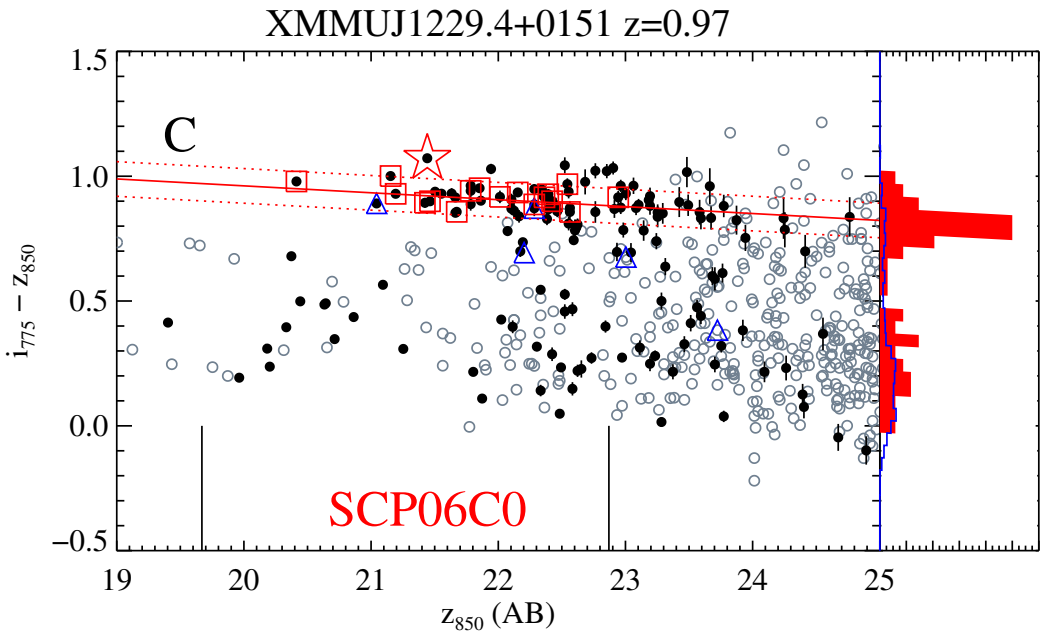

Figure 8.1. Color magnitude diagrams (continued)

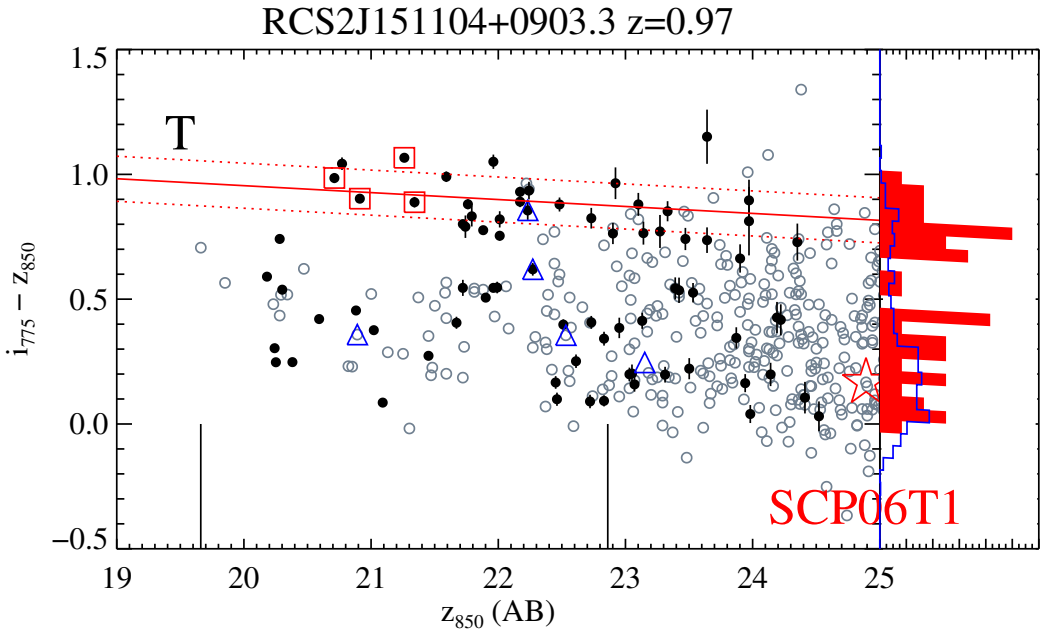

Figure 8.1. Color magnitude diagrams (continued)

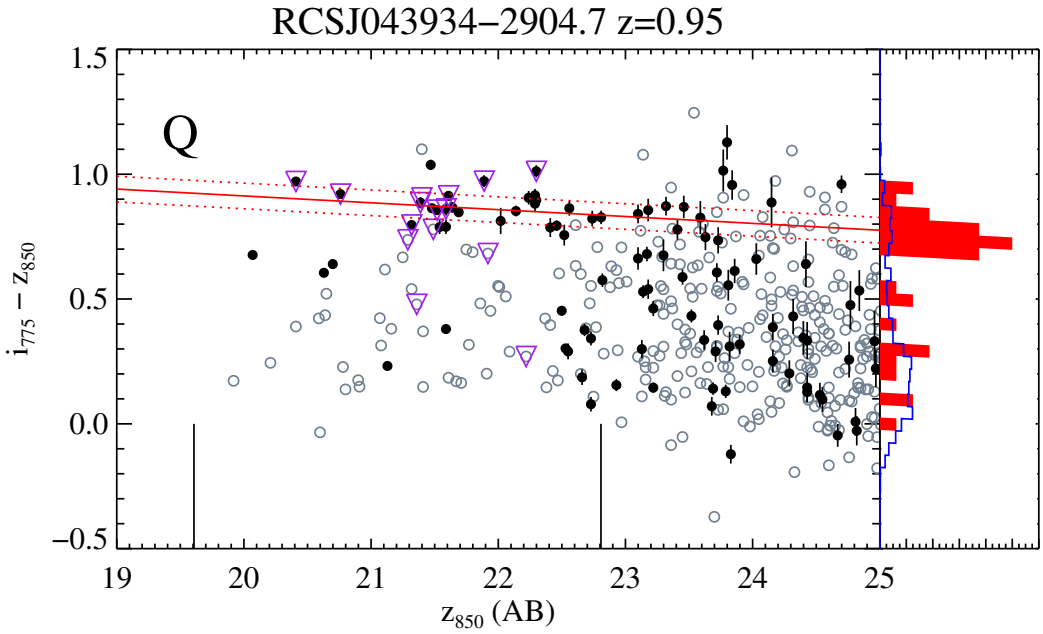

Figure 8.1. Color magnitude diagrams (continued)

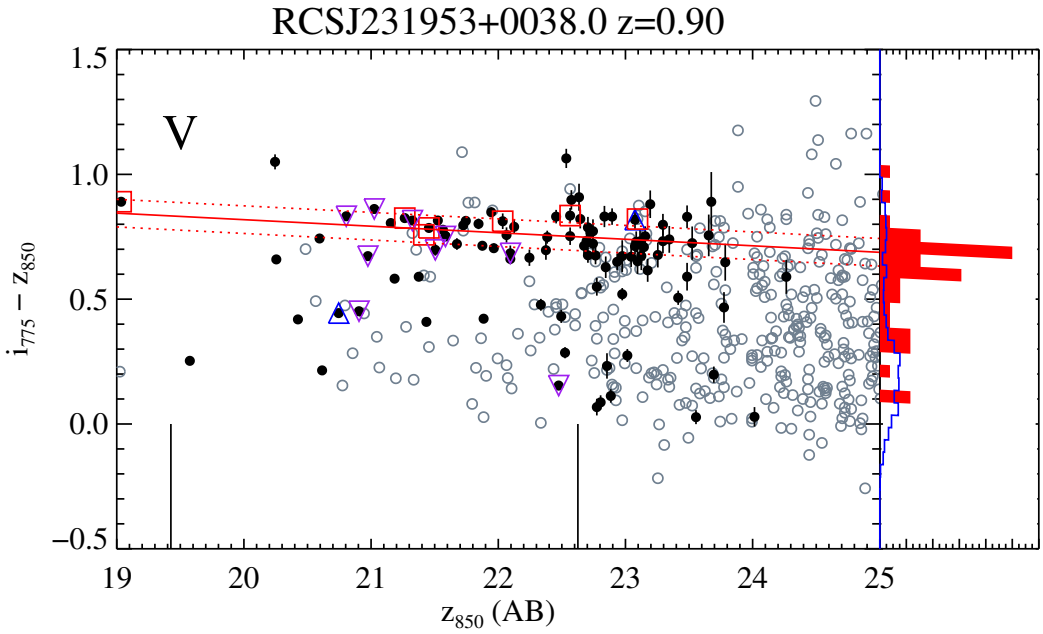

Figure 8.1. Color magnitude diagrams (continued)

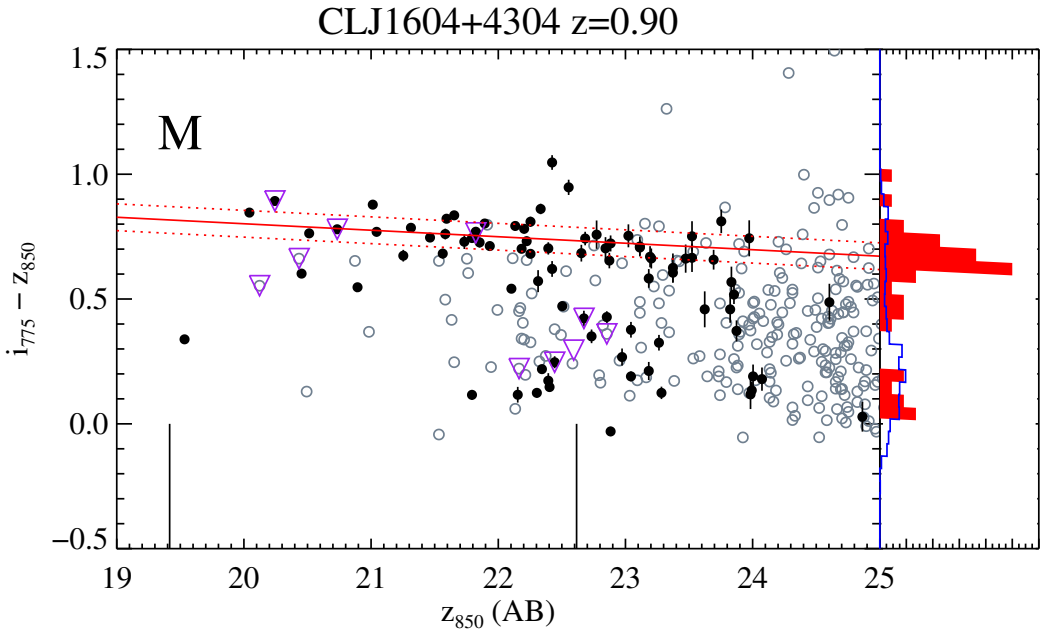

Figure 8.1. Color magnitude diagrams (continued)

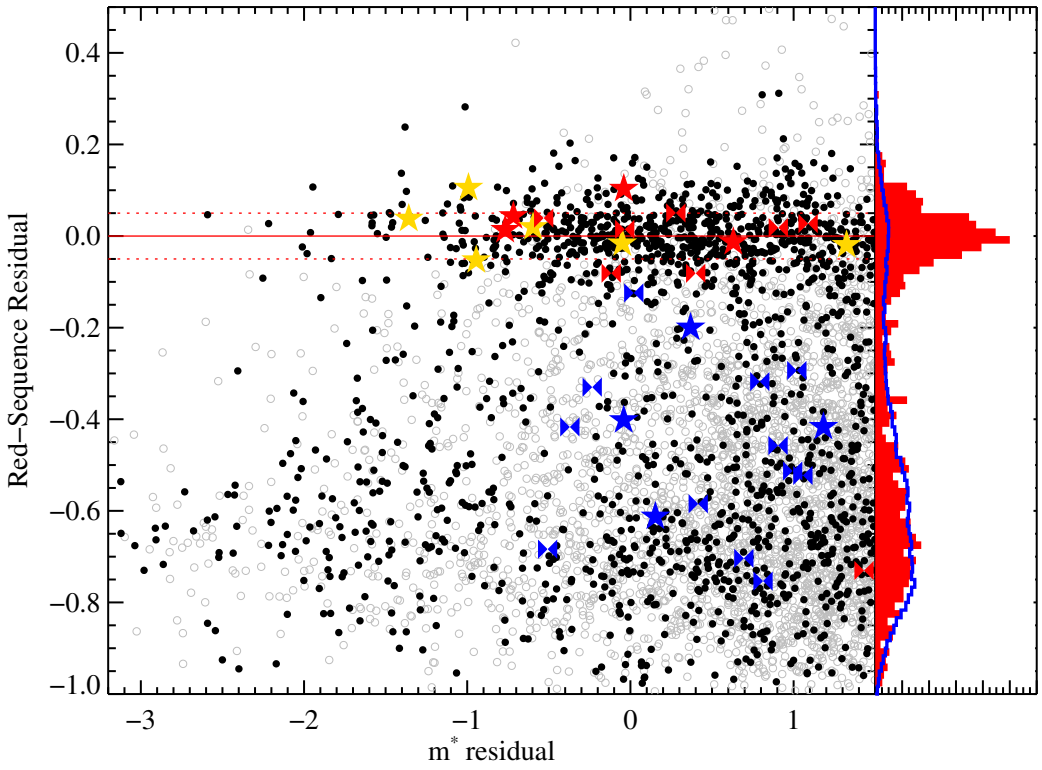

Figure 8.2. Stacked "Color-Magnitude" Diagram. The x-axis is galaxy $z_{850} - m^*$ (where the characteristic magnitude, m^*, is modeled to passively evolve with redshift as described in the text) while the y-axis is galaxy color-magnitude relation residual: $(i_{775} - z_{850}) - \mathrm{CMR}$. Open grey circles indicate galaxies which do not pass our broader morphological cuts; solid black circles do. The solid red line indicates zero CMR residual. The dashed red lines indicate the 1σ intrinsic scatter of the stacked red sequence CMR. The red histogram on the right is the projection of CMR residuals for the stacked cluster galaxies. The blue histogram is the projection of CMR residuals for the GOODS control fields. The $z > 0.9$ SN Ia hosts brighter than $m^* + 1.5$ are overplotted as stars (HST Cluster SN Survey) or bowties (GOODS field SN surveys). Red (gold) stars and bowties indicate field (cluster) SN Ia hosts that meet our morphological and spectroscopic early-type criteria as described in Chapter 6. Blue stars and bowties indicate field or cluster SN Ia hosts that do not meet these criteria. Both the cluster and field early-type SN Ia hosts are consistent with the red sequence and may have similar properties such as low dust content and old stellar populations.

with a typical value of ~ 0.10 mag and are listed in Table 5.1. This range and typical value are consistent with the compilation of rest-frame cluster scatters presented in Jaffé et al. (2011), which span the redshift range $0.0 < z < 1.46$. In the rest of this section we use the properties of cluster red sequences to constrain the amounts of dust present in cluster galaxies.

A precision upper limit on dust along the line of sight to each SN Ia seen in the early-type hosts analyzed here is not possible with this particular data set (this rest-frame color, in particular, is not as sensitive to dust as a broader color baseline would be); nonetheless, it is useful to outline a rough analysis to see that dust limits on these $z > 1$ cluster-hosted SNe are consistent with the low dust values expected for red and dead hosts as outlined in §3.2.

We can estimate such limits using the expectation that dust will both redden the intercept of the CMR and broaden the scatter of CMR residuals. While it is conceivable that one could construct dust distributions such that blue star-forming galaxies are reddened to *precisely* fall on the CMR (and subsequently decrease the CMR scatter), we take this to be an unlikely scenario requiring fine tuning. In fact, since the effects of dust and age show different redshift evolution (see Figure 8.3), the amount of dust required in such a scenario would need to be fine-tuned to the specific cluster redshift. Furthermore, the typical timescale for dust destruction, $\sim 10^7 - 10^8$ yr (Jones et al. 1996; Temi et al. 2007; Clemens et al. 2010), is significantly shorter than the typical ages of even the youngest $z \sim 1.2$ red-sequence ellipticals ($\sim 10^9$ yr)(Rettura et al. 2010), so we do not expect a difference in dust between blue and red extremes of the red sequence to play a role in the CMR residual scatter. Finally, a dust distribution in which each galaxy is reddened the same amount is a similarly unlikely fine-tuning scenario, and is inconsistent with findings in nearby ellipticals, in which infrared-inferred dust masses vary by several orders of magnitude (Tran et al. 2001; Temi et al. 2004, 2007).

8.2 Dust scatter

We begin by considering the dust constraints obtainable from the CMR scatter and then return below to the constraints from the CMR intercept. Although both age and metallicity affect the unextinguished colors of galaxies, following the literature (Bower et al. 1992; van Dokkum et al. 1998; Blakeslee et al. 2003a; Mei et al. 2009; Jaffé et al. 2011), we assume that age is the dominant variable affecting the unextinguished CMR residual scatter (and that metallicity is primarily responsible for the CMR slope). We therefore assume a constant metallicity model in which differences in age and differences in dust reddening create the observed CMR scatter.

As mentioned above, the observer-frame CMR scatter $\sigma(i_{775} - z_{850})$ attributable to differences in galaxy ages evolves with redshift (Figure 8.3) due to the shifting overlap of filters with spectral features. In particular, above $z \sim 1.2$, the i_{775} and z_{850} filters no longer bracket the redshifted age-sensitive 4000Å Balmer break and the predicted scatter

for a given age distribution consequently sharply decreases. On the other hand, because the Cardelli et al. (1989) reddening law is smooth over the relevant wavelengths, the scatter attributable to a given distribution of dust is nearly constant with redshift. This complementary behavior permits us to simultaneously fit both the average cluster star-formation history and average cluster dust distribution using the scatter – redshift data gathered in §5.3.

We investigate the age-scatter model first described by van Dokkum et al. (1998) in which early-type galaxies are formed in delta function starbursts at times uniformly distributed in the interval $(t(z_0), t_z - t_{\rm delay})$. Here $t(z_0)$ indicates the epoch when cluster galaxies first form at redshift z_0, t_z indicates the epoch at which the cluster is observed, and $t_{\rm delay}$ corrects for *progenitor bias* (van Dokkum & Franx 2001) by allowing time for galaxies which recently ceased star formation to become red and evolve morphologically so that they will be identified as red-sequence early-types. At any redshift, the scatter due to age variation can be computed from a population of synthetic BC03 galaxies generated with ages drawn from the distribution defined by z_0 and $t_{\rm delay}$. The amplitude of the effects of age variation may in general depend on the assumed metallicity. To test this dependency, we have carried out the present analysis for both $Z = 0.02$ and $Z = 0.05$, which are appropriate for the masses of early-type galaxies studied here (Trager et al. 2000a). The final results are essentially the same with either choice of metallicity. To additionally account for the effects of dust, we use the parameter $\sigma(E(B-V)_{z=0})$, the rest-frame scatter of $B-V$ reddening. This is related to $\sigma(E(i_{775} - z_{850}))$ by a redshift dependent multiplier, which we compute through synthetic photometry of typical early-type galaxy SEDs with and without dust, similar to the analysis above in which we compare our scatter measurements to the literature. The measured cluster scatters are fit with three parameters – z_0, $t_{\rm delay}$, and $\sigma(E(B-V)_{z=0})$ – using a Markov Chain Monte Carlo. We find that the value of z_0 has little effect on the model likelihood within the range $4.0 < z_0 < 10.0$. The most likely value for $t_{\rm delay}$ is 2.0 Gyr, which corresponds nicely to youngest spectroscopically measured red-sequence galaxy age in cluster RDCS J1252-2927 of 1.9 ± 0.5 Gyr (Rettura et al. 2010). The maximum likelihood value for $\sigma(E(B-V)_{z=0})$ is 0.031 mag, with 68% and 95% upper limits of 0.035 mag and 0.042 mag, respectively.

If clusters with higher intrinsic CMR residual scatter at a given redshift in fact contain dustier galaxies (such as ISCS J1434.4+3426 which hosts SN SCP06H5), then their CMR intercepts should also be redder. We have further investigated this possibility by searching for a correlation between $\Delta\sigma(i_{775} - z_{850})$ and Δb_{22} using pairs of clusters with $|\Delta z| < 0.02$. We find that the pair members with higher scatter are as likely to have bluer intercepts as redder intercepts. Thus the difference between the measured intrinsic scatter and the age-attributed intrinsic scatter should be interpreted only as an upper limit to the dust content of a cluster, and not as a dust detection.

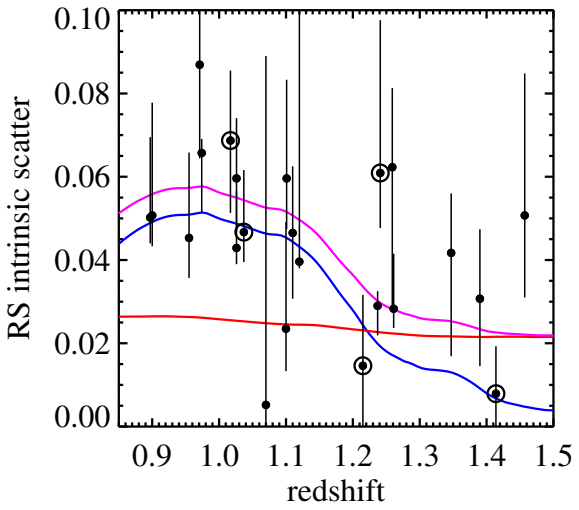

Figure 8.3. Measured early-type red-sequence scatter and fit assuming that CMR scatter is produced by scatter in galaxy ages and dust. The data points and error bars are our measurements and confidence intervals for the 23 clusters with scatter constraints. The blue line indicates the scatter attributable to age differences in our model, the red line indicates the scatter attributable to dust, and the magenta line indicates the combined scatter that is fit to the data. Clusters which hosted SNe Ia in early-type galaxies are circled. The steep evolution of the age-related scatter at $z \sim 1.15$ is due to the shifting of the 4000Å Balmer break through the z_{850} filter. The SEDs of passive galaxies of different ages have smaller $i_{775} - z_{850}$ color differences above this redshift because the filters no longer bracket the break. In contrast, the smooth dust extinction law produces scatter roughly independent of redshift.

8.3 Absolute scale for dust

So far we have estimated approximately how much CMR residual *scatter* is attributable to dust. However, for SN measurements we are principally interested in the corresponding amount of *reddening* or *extinction*. To convert from residual scatter to reddening, we consider a toy model for dust. In a mid-infrared study of the cluster RXJ1716.4+6708, Koyama et al. (2008) found that only $\sim 10\%$ of red cluster galaxies showed emission at 15μm from dust (compared to $\sim 50\%$ of blue cluster galaxies). As discussed in §3.2, studies of nearby early-type galaxies also suggest that at least some have very small levels of extinction. We therefore assume that most cluster early-type galaxies are unaffected by dust and that the distribution of dust in the remaining galaxies follows a half-Gaussian (we have also considered exponential, tophat and Dirac delta function distributions for the remaining galaxies; the differences are small). This highly simplified model captures the main features we wish to study here: a fraction of dusty galaxies (and hence a remaining fraction of nearly dust-free galaxies) and a characteristic scale for the amount of dust. The full probability distribution function for our toy dust model is:

$$f(X; f_d, \mu_d) = (1 - f_d)\,\delta(X) + f_d \frac{2\Theta(X)}{\pi\mu_d} \exp\left(\frac{-X^2}{\pi\mu_d^2}\right) \tag{8.1}$$

where the parameters f_d and μ_d specify the fraction of dusty galaxies and the mean dust content of the subset of dusty galaxies, respectively; $\delta(\cdot)$ is the Dirac delta function, which represents the dust-free galaxies (this term ensures that the integral over the full distribution is one), $\Theta(\cdot)$ is the Heaviside step function, and $X = E(B-V)_{z=0}$ quantifies the rest-frame

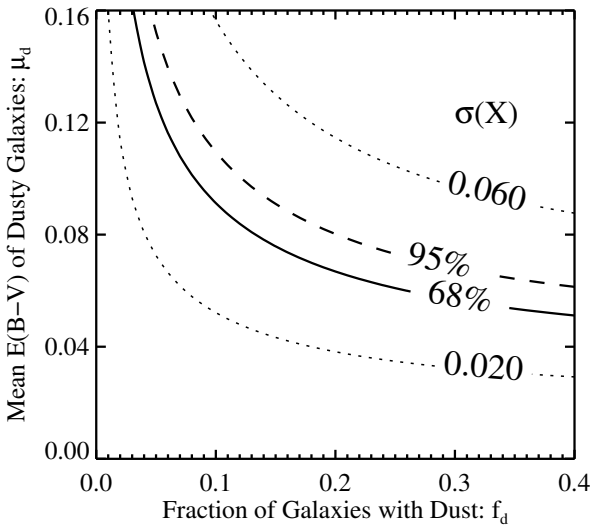

Figure 8.4. Contours of constant CMR residual scatter attributable to dust, $\sigma(X)$, in our toy model, in magnitudes. The model parameters f_d and μ_d specify the fraction of dusty galaxies and the mean dust extinction of the subset of dusty galaxies, respectively. The solid and dashed contours indicate the 1σ and 2σ upper limits on $\sigma(X)$ respectively. The μ_d – f_d parameter space above these curves are excluded at the indicated level, implying that either the amount of dust in an individual cluster member is low (μ_d is small), or that the probability that an individual cluster member is dusty is small (f_d is small).

galaxy reddening due to dust.

The scatter of our toy model can be calculated analytically as $\sigma(X) = \mu_d\sqrt{(\frac{\pi}{2} - f_d)f_d}$ (Figure 8.4). Thus, for $\sigma(X) = 0.035$ (the 68% upper limit) we obtain constraints of $f_d \lesssim 15\%$ if μ_d is large (> 0.08) or $\mu_d \lesssim 0.06$ if f_d is large (> 0.3). The implication for SNe hosted by red-sequence galaxies is that either the probability of being affected by dust at all is small or alternatively that the amount of dust affecting the SN is small. Turning our attention to individual SN host clusters, we see that the scatters of clusters RCS J234526-3632.6 (hosts SN SCP06U4), XLSS J0223.0-0436 (hosts SN SCP06R12), and ISCS J1438.1+3414 (hosts SCP06K0 and SCP06K18) at redshifts 1.037, 1.215, and 1.414 respectively, are below or just above the age-related scatter curve in Figure 8.3. Cluster RCS J022144-0321.7 (host of SCP06D0) at redshift 1.017 has more scatter than the three other clusters within $|\Delta z < 0.02|$, but has the bluest intercept. Similarly, cluster ISCS J1434.4+3426 (host of SCP06H5) at redshift 1.241 has large intrinsic scatter but no more red an intercept than cluster RDCS J1252.9-2927 at redshift 1.237, which has only half as much scatter.

The dust constraints derived to this point apply to cluster early-type galaxies. However, Figure 8.2 demonstrates that the field early-type SN hosts have similar red-sequence residuals as cluster early-type SN hosts. The weighted mean residual of cluster early-type SN hosts is 0.03 ± 0.03 whereas the weighted mean residual of field early-type SN hosts is -0.01 ± 0.02. Thus, the field early-types are actually slightly bluer than cluster early-types and unlikely to have significant reddening.

8.4 MIPS constraints on emission from dust

In addition to absorbing and scattering the optical light from galaxies (and SNe Ia), dust also emits thermal radiation in the near infrared. Six of the clusters in the *HST* Cluster SN Survey (ISCS J1432.4+3332, ISCS J1429.3+3437, ISCS J1434.4+3426, ISCS J1432.7+3519, ISCS J1438.1+3414 and ISCS J1433.8+3325) were also imaged using the 24μm band of the Multiband Imaging Photometer for Spitzer (MIPS) aboard the *Spitzer Space Telescope* (Houck et al. 2005). Here we investigate whether the low dust population of galaxies investigated above also show low MIPS fluxes.

One complication to the comparison of ACS images to MIPS images is the large difference in the size of the PSF of each instrument. The ACS PSF has FWHM $\sim 0.1''$, but the MIPS PSF has FWHM $\sim 5.5''$, potentially leading to source confusion in the comparison. To mitigate this effect, we categorize galaxies into three groups depending on both their own ACS-inferred dust properties and also the ACS-inferred dust properties of neighboring galaxies.

The first group we consider consists of galaxies for which we have no expectation of being low in dust content: galaxies more than 2σ away from the red sequence or that fail our broader morphology cuts. The fraction of objects in this group detected at $>5\sigma$ in 24 μm is $\sim$35%, though many are substantially brighter than this. The second group we consider consists of galaxies which we expect to be free of dust (color within 2σ of the red sequence and passes our early-type morphology cuts), but has a dusty neighbor within a radius equal to the FWHM of the MIPS PSF. Only $\sim$ 20% of these galaxies are detected at 5σ. The final group consists of galaxies we infer to be low-dust in the ACS images, and are also isolated by at least $5.5''$ from any potential contaminating dusty galaxies. This group has just one galaxy out of 36 brighter than the 5σ detection limit (2.8%), and that one galaxy is only just detected at 5.25σ. We interpret this as further evidence that our color and morphology cuts are successfully identifying low dust content galaxies, including SN hosts.

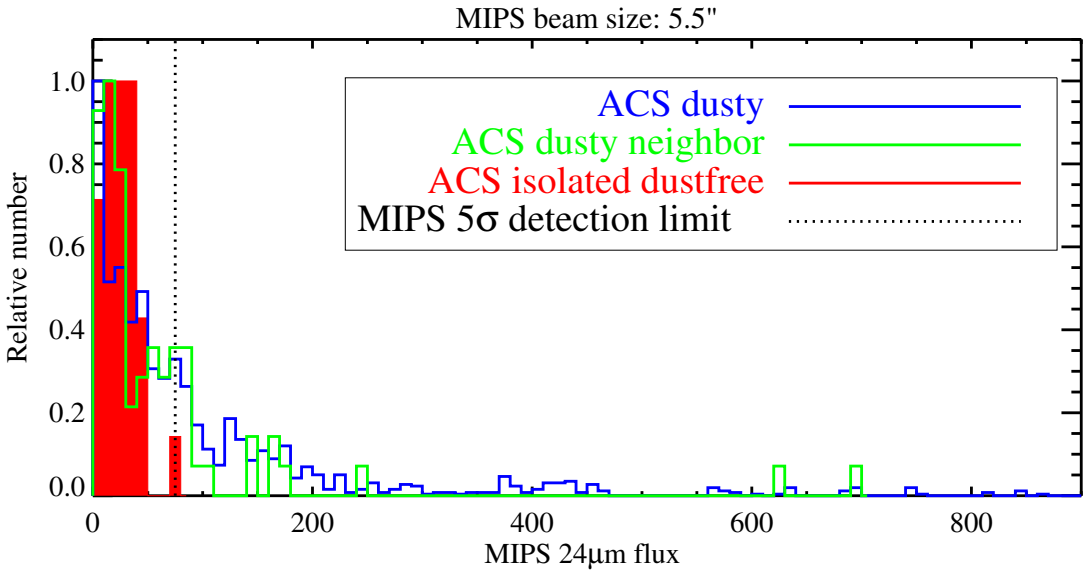

Figure 8.5. The distribution of flux at 24μm derived from MIPS observations, separated by the optical classification of the dust properties of galaxies and their neighbors. The blue histogram shows the 24μm flux distribution of morphologically late type galaxies or galaxies that are off of the red sequence, i.e. galaxies which are expected to be "dusty". The green histogram shows the distribution for red sequence member galaxies with early-type morphologies (i.e. "dust-free" galaxies), but that have dusty neighbors within the MIPS beam of $5.5''$. The red histogram shows the distribution for "dust-free" galaxies with no dusty neighbors within the MIPS beam radius. The black vertical dotted line indicates the MIPS 5σ detection limit. Note that all but one isolated "dust-free" galaxy is below this limit, and most are also below the 3σ detection limit.

CHAPTER 9

SN Ia Correlations with Host Galaxies

In this chapter we look at correlations between the properties of SN Ia light curves and the properties of SN Ia host galaxies at high redshift.

9.1 Stretch and color

One easily observed distance independent property of SNe Ia is the rate at which their light curves rise and fall. This property has been parameterized several ways in the literature: as the stretch, s, which linearly stretches the time axis of a template light curve to match the observed (rest-frame) light curve (Perlmutter et al. 1997), $\Delta m_{15}(B)$, which is the decline in B-band magnitudes from peak to 15 rest-frame days later (Phillips 1993), or x_1, which is roughly the coefficient of the first component in a principle component analysis of SN Ia spectral time series (Guy et al. 2007). The light curve shape has been shown to correlate with SN Ia host type at lower redshifts with the light curves of SNe Ia hosted by early-type galaxies rising and falling more quickly than the light curves of SNe Ia hosted by late-type galaxies (i.e. early-type galaxies host SNe Ia with smaller stretch) (Hamuy et al. 1996; Gallagher et al. 2005; Sullivan et al. 2006). Here we compare SN stretch as a function of host type for our $z > 0.9$ SN Ia dataset.

In Suzuki et al. (2012) we use SALT2 to fit light curves of $z > 0.9$ SNe Ia from the *HST* Cluster SN Survey and the GOODS SN Surveys in the ACS i_{775}, z_{850} filters and also the F110W and F160W filters of NICMOS. To convert the SALT2 light curve shape parameter x_1 to stretch, we use the cubic relation from Guy et al. (2007). The distributions of stretch (and x_1) for SN Ia subsets split by host type are shown in Figure 9.1. To prevent poorly measured SNe Ia from influencing our results, we have only included SNe Ia with x_1 uncertainty less than 1.0, which is roughly the size of the histogram bins. The SNe Ia whose hosts we classify as passively evolving early-type galaxies show smaller stretch than the SNe Ia whose hosts we classify as late-type galaxies, consistent with lower redshift results. A Kolmogorov-Smirnov (K-S) test reveals that the probability that the stretch values from the two host subsets are drawn from the same distribution is < 0.01.

We have also compared the light curve shape distributions of these $z > 0.9$ SNe Ia to

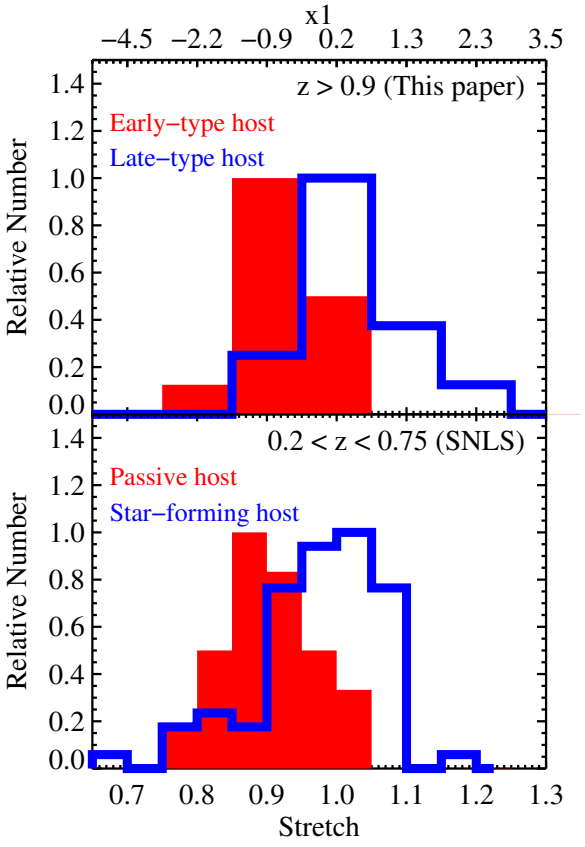

Figure 9.1. Distribution of SN light curve shape parameters stretch (bottom axis) and x_1 (top axis). The x_1 axis labels are computed using the cubic polynomial conversion from stretch given in Guy et al. (2007). Both axes apply to both panels. **Top:** Light curve shape distribution for the HST-observed $z > 0.9$ SNe Ia discussed in the current paper. The red (blue) histogram corresponds to SNe Ia with hosts classified as early (late) type. **Bottom:** Light curve shape distribution for SNe drawn from the first year of SNLS as given in Sullivan et al. (2006). The red (blue) histogram corresponds to SNe Ia with hosts classified as passively-evolving (star-forming).

that of the first year of SNLS SNe Ia at $0.2 \lesssim z \lesssim 0.8$ presented in Sullivan et al. (2006, Figure 9.1). We assume that the individual values of stretch in the histogram plotted there are uniformly distributed within their bins. We find that the K-S probability that the s values of the early-type hosted SNe Ia analyzed here and the s values of the passively hosted first year SNLS SNe Ia are drawn from the same distribution is quite high at 0.91. The K-S probability comparing the s distribution in $z > 0.9$ late-type galaxies to that from the star-forming galaxies of first year SNLS SNe is also suggestive of similar distributions at 0.63. Finding similar demographics across such a wide redshift baseline instills confidence that SNe Ia are truly standardizable candles over this range.

Likewise, we can compare the distribution of the color parameter in both host subsets. In Figure 9.2 we compare the distribution of color for SN subsets of different host types. The K-S test reveals that the probability that the c values from the two host subsets are drawn from the same distribution is 0.75, also consistent with findings at lower redshift (Lampeitl et al. 2010). One possible explanation for this result is that the dominant source of color for these SNe Ia is intrinsic or circumstellar and that host galaxy extinction plays a smaller role.

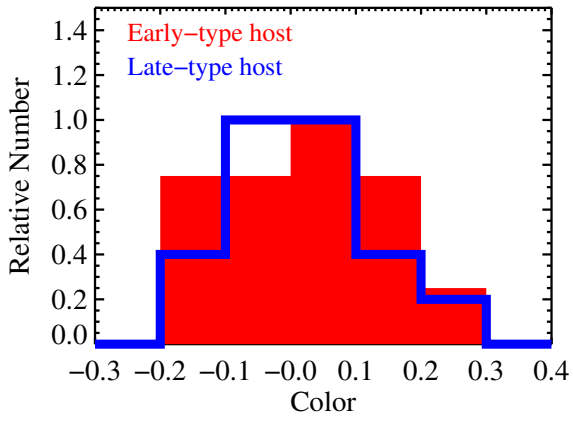

Figure 9.2. Distribution of $z > 0.9$ SN Ia color for SNe with hosts classified as either early-type (red) or late-type (blue).

9.2 SN Ia Hubble residual vs. host mass

Recent analyses of SN Ia hosts have indicated that after corrections for stretch and color have been applied, SNe Ia are brighter in galaxies with more stellar mass (Kelly et al. 2010; Sullivan et al. 2010; Lampeitl et al. 2010). Kelly et al. have parameterized this effect both as a step function at $\log \frac{M}{M_\odot} = 10.8$ and as a linear function. In §3.1 we argued that the relatively simple SEDs of early-type galaxies (as opposed to the generally more complicated SEDs of late-type galaxies) allow us to measure stellar masses of early-type hosts using just the i_{775} and z_{850} photometry collected here. Thirteen of our $z > 0.9$ SNe have both host mass measurements and Hubble residuals (uncorrected for host mass) from Suzuki et al. (2012). To extend this sample, we have also used the masses of $z > 0.9$ GOODS SN hosts from Thomson & Chary (2011), which are derived from SED fits to ACS optical, IRAC near infrared and MIPS 24 μm photometry. The Hubble residuals for these SNe are also available from Suzuki et al. (2012), increasing the sample from 13 to 23. Five galaxies with mass estimates are in common between the Thomson & Chary (2011) dataset and the early-type hosts analyzed here. For four of these galaxies, the difference in mass is less than 1σ, and it is less than 2σ for the fifth. In Figure 9.3, we plot Hubble residuals against host stellar masses, using our own mass estimates for the galaxies with two mass estimates. A suggestion of the trend of negative residuals for higher mass hosts is apparent. A linear fit to these data results in a slope measurement of -0.098 ± 0.085 mag dex^{-1}, (i.e. a 1.1σ detection significance). The next generation of SN Ia studies (such as the SNe Ia discovered and followed with Wide Field Camera 3 as part of the *HST* Multi-Cycle Treasury Programs) may have sufficiently better data to confirm this trend at high redshift.

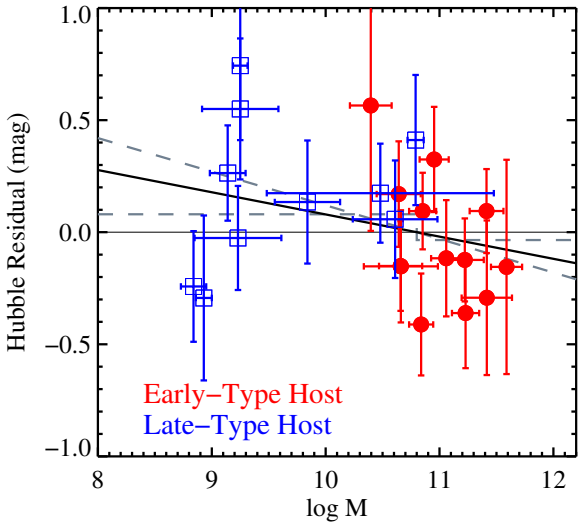

Figure 9.3. Hubble residual as a function of host galaxy stellar mass. Open blue squares are late-type galaxies with masses from Thomson & Chary (2011). Filled red circles are early-type galaxies with masses derived from SED fits to i_{775} and z_{850} as described in Chapter 9. The solid line is the best-fit linear relationship with slope -0.098 ± 0.085 mag dex^{-1}. The dashed line and step function are the relations plotted in Kelly et al. (2010) when using the SALT2 light curve fitter.

CHAPTER 10

Discussion

In this analysis, we have studied the relation between SNe Ia and their host galaxies at high redshift ($z > 0.9$). In total, we study 16 SNe Ia (seven in clusters, eight in the field, and one with uncertain cluster membership) from the ACS cluster fields and 24 SNe Ia from the GOODS fields (Dawson et al. 2009; Gilliland et al. 1999; Blakeslee et al. 2003b; Riess et al. 2004, 2007). Using color-magnitude diagrams constructed from i_{775} and z_{850} photometry and measurements of quantitative morphology, we have developed a technique to segregate high-redshift, early-type galaxies from high-redshift, late-type galaxies in these fields. Additional measurements of the [O II] emission line strength in the spectra of SN host galaxies were used to estimate galaxy star formation rates and the rate of core collapse SNe. This classification scheme was applied to the hosts of the 40 SNe, first in conjunction with the [O II] emission line strengths to determine the likelihood of early-type hosted SNe being Type Ia, then to identify trends in the supernova properties with host galaxy type. Of the SNe Ia studied here, 17 have host galaxies classified as early-type, 22 have host galaxies classified as late-type, and one galaxy has a host which we have left unclassified.

From our analysis of these data, our principle results are:

(i) SN Classification A review of the literature (Hakobyan et al. 2008) shows that the confidence level is quite high for the classification of a SN Ia based on the identification of its host galaxy as early-type. We here confirm, on the basis of host morphology and spectroscopic limits on star formation, that SNe hosted by early-type galaxies in our current sample are likely Type Ia. Using the A+B SN Ia rate parameterization from Sullivan et al. (2006) (Eqn. 7.1), and by deriving a similar formula for SNe CC (Eqn. 7.2), we estimate the intrinsic rate of SNe Ia and SNe CC in individual early-type galaxies. By multiplying the intrinsic rates by the detectable fractions (derived from the detection threshold of the survey and the luminosity functions of different types of SNe) we calculate the rate of *detectable* SNe Ia and SNe CC for each early-type SN host. For most of the early-type hosted SNe in our survey, the probability of misclassification is very small, even if relying on only the host galaxy information. The three examples where the purely host galaxy classification is weakest ($P(Ia) \lesssim 90\%$) can be traced back to observations of [O II] emission. If some or all of early-type galaxy [O II] emission is due to LINER activity instead of star formation,

then these misclassification probabilities may be significantly overestimated. Fortunately, in this particular case two of these three SNe have been spectroscopically confirmed as a Type Ia. Of course, our combined classification for cosmological analysis includes the full light curve data and thus the classifications become much stronger (Barbary et al. 2012a; Suzuki et al. 2012). In the *HST* Cluster SN Survey, ten $z > 0.9$ SNe in all can be typed by their early-type hosts, six more than a comparable blank field search would have found since this many were found in the clusters themselves.

(ii) Contamination from Dust The narrow color scatter about cluster red sequences directly constrains the amount of dust extinction affecting SNe in red-sequence hosts. We measure a typical intrinsic scatter in the observed $i_{775} - z_{850}$ color of morphologically selected early-type galaxies of ~ 0.045 magnitudes. While other authors have modeled this scatter as a distribution of galaxy ages (e.g. Jaffé et al. 2011), we have investigated extinction due to dust as an additional parameter. By simultaneously fitting the average cluster galaxy formation history and dust content, we conclude that the rest-frame $B - V$ scatter of red sequence residuals attributable to dust is likely $\lesssim 0.04$ magnitudes. By modeling this distribution as the sum of a dust-free galaxy population (with fraction $1 - f_d$) and a dusty galaxy population (with fraction f_d and mean rest-frame $E(B - V)$ reddening μ_d), we show that either the probability that any particular red-sequence member is reddened by dust is small ($f_d \lesssim 15\%$) or alternatively that the amount of reddening is small ($\mu_d \lesssim 0.06$). These limits are comparable to early-type galaxy reddening limits set at low redshift obtained by exploiting the correlation of the Mg_2 absorption line and intrinsic $B - V$ colors of early-type galaxies (Ferguson 1993; Schlegel et al. 1998). We also find that the clusters with higher scatter have the same CMR intercepts as clusters with low scatter, contrary to expectation if dust were the primary factor in producing the color scatter.

(iii) SN Light Curve Properties The light curves of $z > 0.9$ SNe Ia rise and fade more quickly (have smaller stretch) in early-type hosts than in late-type hosts. The distribution of SN colors is similar in both host subsets, suggesting that SN Ia color is largely intrinsic or due to circumstellar dust and not dominated by host galaxy extinction. These trends are well known at lower redshifts (Hamuy et al. 1996; Gallagher et al. 2005; Sullivan et al. 2006; Lampeitl et al. 2010), but have not been demonstrated before at $z > 0.9$.

(iv) Galaxy Mass and Hubble Residuals We have obtained mass estimates of the early-type classified SN host subset by fitting passively-evolving SEDs to their i_{775} and z_{850} photometry. Together with infrared-derived mass estimates of a subset of the late-type classified SN hosts from Thomson & Chary (2011), we have found a suggestion of a correlation between SN Ia host mass and stretch-and-color-corrected Hubble residual (1.1σ). This effect has been seen with more significance in three datasets at lower redshifts (Kelly et al. 2010; Sullivan et al. 2010; Lampeitl et al. 2010) and may be related to the metallicity or age of SN progenitors or to extinction by dust, all of which correlate with galaxy mass.

While the present analysis focuses on the astrophysical properties of SNe Ia and their host galaxies, the results clearly have implications for the cosmological interpretation of SN observations. The evolution of host demographics with survey strategy or with redshift

can lead to biases in cosmological parameter fits if not accounted for. In particular, many low redshift surveys explicitly target massive galaxies to improve their discovery rates. The cluster galaxies targeted by the *HST* Cluster SN Survey are also more massive on average than those in an untargeted survey and may produce SNe Ia which lead to biases in cosmological interpretation. A detailed analysis of the cosmological impact of host dependent properties is discussed in Suzuki et al. (2012). In that work, we present several other trends in SN Ia parameters as a function of host type, including the values of color-magnitude relation coefficient $\beta = \Delta M_B/\Delta c$ in star-forming galaxies and in passive galaxies, and the residual scatter about the Hubble diagram for SNe Ia hosted by star-forming galaxies and by early-type galaxies. These studies are compared to similar studies at lower redshift (Sullivan et al. 2003; Jha et al. 2007; Sullivan et al. 2010; Lampeitl et al. 2010).

The ability to identify early-type galaxies, and their overdensity in clusters, provides many advantages in SN cosmology studies at $z > 0.9$. SNe hosted by early-type galaxies are essentially all Type Ia, reducing the need for potentially expensive confirmation spectroscopy that must be obtained during the narrow time window that the SN is active. Cluster early-type galaxies are minimally contaminated with dust (either less than 15% are dusty or the reddening is less than 0.06 mag), and can be directly checked for dust via the cluster red-sequence scatter. The cluster galaxies provide additional potential SN Ia progenitors and hence yield a higher rate of SNe Ia than a comparable blank field search, especially of early-type hosted SNe Ia. Finally, the relatively simple SEDs expected for early-type galaxies permit SN host mass measurements with fewer photometric bands than for late-type hosts. Targeting clusters is therefore not only the most efficient method to discover and type SNe Ia at $z > 0.9$, but is likely the most efficient way to collect the host galaxy information necessary for the next generation of $z > 0.9$ SN Ia studies.

Part II

Ages and Abundances of Passive Progenitor Populations

CHAPTER 11

Introduction

Type Ia supernovae (SNe Ia) have proven themselves useful cosmological distance indicators both by virtue of their extreme brightness, which allows them to be observed from $z \sim 0$ up to $z \gtrsim 1.7$ (Rubin et al. 2012), and because their absolute peak magnitudes are readily inferred from the shapes and colors of their light curves. Specifically, SNe Ia with light curves that rise and fall more slowly are intrinsically more luminous (the broader–brighter relation; Phillips 1993), as are SNe Ia with bluer colors near the time of maximum light (the bluer–brighter relation; Tripp 1998). Using the light curve fitter SALT2.2 (Guy et al. 2007) to measure the light curve shape parameter x_1, the SN peak color excess $c = (B - V) - \langle B - V \rangle$, and the apparent B-band peak magnitude m_B, the SN-inferred distance modulus can then be written:

$$\mu_{\rm SN} = m_B - M_B - \alpha x_1 + \beta c \tag{11.1}$$

where α, β, and M_B are SN calibration parameters determined simultaneously with cosmological parameters. The 1σ scatter of $\mu_{\rm SN}$ about the best fit cosmological distance modulus model μ_z (i.e. the scatter of SN Hubble residuals) is about 15%, considerably smaller than the $\sim 50\%$ scatter of uncorrected SN Ia absolute peak magnitudes (Suzuki et al. 2012).

Recently, several analyses of large compilations of SNe Ia in various redshift intervals have shown that additional empirical calibrations of $\mu_{\rm SN}$ exist, in particular, SNe Ia hosted by passively evolving or massive galaxies appear slightly brighter after the application of standard light curve shape and color corrections than SNe Ia hosted by star-forming or less massive galaxies (the bigger–brighter relation; Kelly et al. 2010; Sullivan et al. 2010; Lampeitl et al. 2010). Using all three empirical relations, Suzuki et al. (2012) derived cosmological constraints from a compilation of 580 SNe Ia. When combined with measurements of the Cosmic Microwave Background radiation (Komatsu et al. 2011), and Baryon Acoustic Oscillations (Percival et al. 2010), these SNe Ia constrain the time-independent dark energy equation of state to $w = -1.013^{+0.068}_{-0.073}$, though parameters characterizing time-varying dark energy are still relatively unconstrained. The myriad SN Ia measurements of imminent and planned SN Ia surveys (e.g. The Dark Energy Survey[4] or the Large Synoptic Survey

[3]This part is meant to stand alone, and some material from Chapter 1 may be repeated here.

Telescope (LSST Science Collaboration 2009)) will increase the number of available well measured SN light curves by orders of magnitude and push SN Ia dark energy statistical uncertainties far below their current values. To also keep systematic uncertainties small, a detailed understanding of the physics of SN Ia brightness variations, empirical brightness calibrations and the possible evolution of these calibrations and evolution of SN Ia demographics will be required. One particularly vexing question is: what is the origin of the bigger – brighter relation? Likely candidates include progenitor age and metallicity, as these are known to be correlated with the stellar mass and specific star-formation rates of galaxies. The most probable candidates, progenitor age and metallicity, both evolve over the redshift interval probed by SNe Ia, but in distinct ways producing distinct potential biases in the cosmological interpretation of SNe Ia. An accurate correction thus depends on an accurate identification of the underlying physics.

Current theoretical understanding proposes that SNe Ia arise when the degenerate cores of white dwarfs with masses near the Chandrasekhar limit ignite, burning their C/O cores into iron-peak and intermediate mass elements. The radioactive decay of $^{56}\mathrm{Ni}$ produced during the explosion powers their optical light curves near peak brightness, thus SN Ia peak magnitudes are directly tied to the quantity of $^{56}\mathrm{Ni}$ produced. Theorists have long predicted that differences in the ages or compositions of the progenitor white dwarfs may influence SN Ia explosion products and subsequently affect light curve properties (Höflich et al. 1998; Umeda et al. 1999; Timmes et al. 2003; Kasen et al. 2009).

Indeed, several correlations between SN Ia brightness and their progenitor environments have been observed. The clearest is that SNe Ia with slower decline rates (and hence brighter peak magnitudes) are associated with younger stellar populations (Hamuy et al. 1996; Gallagher et al. 2005), a trend even apparent at $z \sim 1$ (Meyers et al. 2012, also see Part I of this thesis). This, together with the fact that galaxies with young stellar populations also produce many times more SNe Ia per unit stellar mass than galaxies with older stars (Mannucci et al. 2005; Sullivan et al. 2006), implies that progenitor age is a key variable affecting SN Ia diversity, although progenitor metallicity may also play a role as the ages and metallicities of stellar populations are frequently correlated and difficult to decouple.

Several photometric studies have investigated progenitor population age constraints in detail: In a study of nearby SNe Ia, Neill et al. (2009) showed tentative evidence that the light curve shape and color corrected peak magnitudes of SNe Ia in a subsample hosted by galaxies with low extinction are correlated with host age in the sense that older progenitors produce brighter SNe Ia. However, using the SNLS sample, Howell et al. (2009) were unable to find any correlation between corrected brightnesses and host properties. More recently, Gupta et al. (2011) analyzed the SNe Ia from the SDSS-II sample, finding a correlation between Hubble residual and host age. As mentioned above, however, all of these photometric results are somewhat hampered by the well-known age–metallicity degeneracy, where differences in age affect galaxy colors similarly to differences in metallicity.

Other host studies have focused on making detailed metallicity measurements. Gal-

[4] www.darkenergysurvey.org

lagher et al. (2005) measured emission line ratios to derive gas-phase metallicities of a sample of low redshift SN Ia host galaxies. Their results indicate that metallicity does not strongly affect the uncorrected peak brightnesses of SNe Ia. However, they did find a tenuous correlation indicating that higher metallicity galaxies host brighter SNe Ia after correcting for light curve shape and color. Sullivan et al. (2010) used the mass–metallicity relation derived from SDSS spectra (Tremonti et al. 2004) together with its measured redshift evolution (Lamareille et al. 2009) to convert their photometric host mass estimates into metallicity estimates, and showed that the inferred progenitor metallicity variations are consistent with the SN Ia bigger–brighter relation. Finally, D'Andrea et al. (2011) show that emission-line-ratio-derived gas-phase metallicities of the SDSS-II SN sample are correlated with SN Ia Hubble residuals in the sense that higher metallicity hosts produce brighter corrected SNe Ia.

While emission line metallicity studies do not suffer from the age-metallicity degeneracy, neither do they probe any possible influence of progenitor age. In contrast, absorption line spectroscopic studies, while requiring substantially larger signal-to-noise ratio spectra and restricted to passively evolving stellar populations, can probe age, metallicity, and even the abundances of some individual elements. Furthermore, these studies probe the compositions of stellar atmospheres directly, including SN progenitors, as opposed to the composition of galaxies' interstellar gas. Gallagher et al. (2008, hereafter G08) conducted the first landmark study of SN Ia host absorption lines, presenting evidence that SNe Ia hosted by higher metallicity galaxies produce brighter corrected SN Ia magnitudes. The signal-to-noise ratio of their spectra (~ 10 per resolution element), however, was not sufficient to completely decouple the age and metallicity of their sample galaxies. Neither did they attempt any analysis of individual element abundances.

Here we present a spectroscopic survey of 40 passive SN Ia hosts at the high signal-to-noise ratio of ~ 100 Å^{-1}, sufficient to cleanly separate age and metallicity constraints. We also present, for the first time, constraints on the abundances of individual elements of SN Ia host galaxies. In Chapter 12 we discuss the SN surveys that were used to source passively evolving host galaxies and how the host galaxies were selected from each survey. In Chapter 13 we describe our spectroscopic observations and reductions, and discuss how we obtained stellar population parameters from these spectra. In Chapter 14 we compare the light curve properties of SNe Ia to the spectroscopically derived properties of their hosts. Finally, in Chapter 15 we discuss implications of these SN – host correlations for cosmological measurements and present our conclusions.

CHAPTER 12

Supernova Selection and Photometry

The ages and compositions of galaxies are encoded in the variations of the strengths of absorption lines present in the integrated spectra of the stellar atmospheres of their constituent stars. Because these variations can be subtle, on the order of tenths of Ångströms in equivalent width, and because individual absorption lines are often sensitive to more than one underlying age or composition parameter, high signal-to-noise ratio spectroscopy is required to make detailed inferences of stellar properties from absorption line diagnostics. Furthermore, emission lines commonly present in galaxy spectra from non-stellar sources can fill in diagnostic lines, complicating their interpretation. Hence, absorption line studies are most easily accomplished using a sample of emission-line-free galaxies.

The signal-to-noise requirements and the strong preference for galaxies with only weak emission lines dictated the selection of SN host targets for this study. Even with 10-m class telescopes, observations of $z \sim 0.2$ galaxies required over an hour of integration to reach our target signal-to-noise ratio. To this end, we selected SNe Ia from three nearby sources: the SN sample targeted for follow-up by the *Swift* satellite (Gehrels et al. 2004), the Nearby SuperNova Factory (SNfactory) (Aldering et al. 2002), and the Sloan Digital Sky Survey II (SDSS-II) SN Survey (Frieman et al. 2008). Below we briefly describe these surveys and the selection criteria we used for each to identify galaxies likely to have only weak-emission lines.

The lowest redshift host galaxies in our sample come from SNe Ia observed by the ultraviolet and optical telescope (UVOT; Roming et al. 2005) on board the *Swift* satellite. Since 2005, this telescope has been used to follow ~ 175 very nearby ($z \lesssim 0.02$) SNe discovered from multiple ground based searches. Observations typically include exposures in two ultraviolet filters as well as u-, b-, and v-band optical filters (although the UVOT u-band is a few hundred Å bluer than the Bessell (1990) u-band filter). *Swift*-observed SNe Ia with early-type hosts (either E or S0 in NED[5]), which typically show weak or no emission lines, were selected as candidates for the spectroscopic observations presented here. We obtained SN photometry from Brown et al. (2013), who employed the updated UVOT zeropoints from Breeveld et al. (2011). Light curve fits were obtained from SALT2.2, following the procedures detailed in Rubin et al. (2013, hereafter Union3). The standard Union3 cuts ex-

clude any observer-frame u-band (or bluer) photometry, so only b- and v-band photometry were used to constrain the light curve parameters of *Swift* SNe. The availability of only one photometric color, combined with the relatively uncertain calibration of *Swift*, prevented us from obtaining reliable Hubble residual measurements for these SNe, many of which are at such low redshift that peculiar velocity uncertainties dominate μ_z. Measurements of x_1 are less sensitive to zeropoint uncertainties and independent of μ_z, however, permitting their use in the following analysis.

At slightly higher redshift, the SNfactory has discovered over 1000 SNe of all types with $z < 0.1$ by surveying roughly 25,000 deg^2 of sky. From these discoveries, ≈ 185 SNe Ia most promising for use as cosmological distance indicators were selected for follow up with the SuperNova Integral Field Spectrograph (SNIFS), which is continuously mounted on the University of Hawaii 2.2-m telescope on Mauna Kea. SNIFS is a fully integrated instrument optimized for automated observation of point sources on a structured background over the full optical window at moderate spectral resolution. With this instrument, complete spectrophotometric time series of SNe were obtained covering a wavelength range of 3200-9700Å and having a typical cadence of 3-4 days. A brief discussion of the spectrographic pipeline is presented in Aldering et al. (2006), and updated in Buton et al. (2012). For the purpose of light curve fitting, photometry of SNfactory SNe was synthesized from the spectrophotometric time series of each SN using tophat filters at approximately the central wavelengths of the B-, V-, and R-bands. The flux calibration of SNIFS is excellent, leading to SN Ia Hubble residual scatters $\sigma \sim 0.13$ (Bailey et al. 2009) and flux density uncertainties in standard star spectra of $\lesssim 2\%$ (Buton et al. 2012). For the spectroscopic observations presented here, we selected hosts with large bulge-to-disc ratios, as galaxy bulges usually consist of passively evolving stellar populations with low emission line contamination.

The highest redshift SNe we probed were drawn from the SDSS-II SN Survey, which used the dedicated 2.5-m SDSS telescope at the Apache Point Observatory to search for SNe in the redshift range $0.1 < z < 0.35$ in two narrow strips with a combined area of ≈ 300 deg^2. Observations included exposures in u-, g-, r-, i-, and z-band filters, though we only use g-, r-, and i- for our light curve fits. We took advantage of the deep multicolor photometry from SDSS to select host galaxies on the red sequence, which are typically composed of passively evolving stellar populations, for the spectroscopic observations presented here.

Photometry of the first year of SDSS SN observations have been published in Holtzman et al. (2008). These SNe are part of the Union2 analysis (Amanullah et al. 2010) and have now been updated for the Union3 analysis. Photometry of SDSS SNe discovered in the second and third years of the survey, however, have not yet been published. To analyze the seven SNe with unpublished photometry whose hosts form part of our sample, we rely on the light curve fits and Hubble residuals published by Gupta et al. (2011). Gupta et al. use

[5]The NASA/IPAC Extragalactic Database (NED) is operated by the Jet Propulsion Laboratory, California Institute of Technology, under contract with the National Aeronautics and Space Administration.

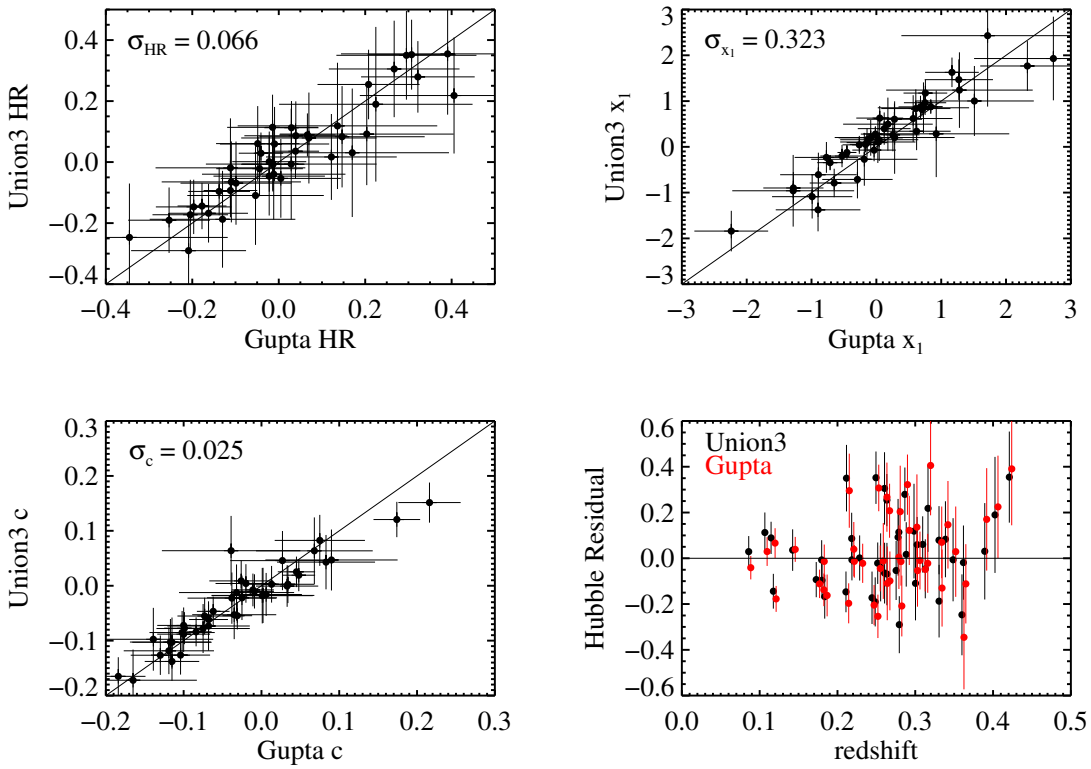

Figure 12.1. Comparison of Union3 light curve fits to the light curve fits in Gupta et al. (2011). Top left: Hubble residual comparison, the scatter is 0.070 mag. Top right: The SALT2.2 x_1 parameter, the scatter is 0.305. Bottom left: The SALT2.2 color parameter; the scatter is 0.027 mag. Bottom right: Hubble diagram comparison with Union3 values in black and Gupta et al. (2011) values in red.

the same light curve fitter (SALT2.2) as in Union3, but apply different quality control cuts and a different technique for measuring the correction coefficients α and β. Using the 49 SNe Ia from the first year of the SDSS-II SN Survey in common between the Gupta analysis and Union3, we are able to test what the effects of the different procedures are. Figure 12.1 shows the differences in x_1, c, and Hubble residual for the two techniques. While some scatter in the parameters describing each SN light curve is present, it is generally much smaller than the typical associated uncertainties.

Table 12.1. Host Spectroscopy Details

SN Name	Host Name	$z_{\rm helio}$	Date observed	Instrument	Setup(s)
Swift-observed SNe and Hosts					
PTF10fps	NGC 5177	0.0216	2011-05-09	OSIRIS	R1000B
SN2007cv	IC 2597	0.0098	2010-02-20	LRIS	B560/R7500
SN2007on	NGC 1404	0.0063	2011-08-29	LRIS	B560/R7500
SN2008Q	NGC 0524	0.0080	2009-09-24	LRIS	B560/R7500
SN2008hs	NGC 0910	0.0173	2009-09-24	LRIS	B560/R7500
SN2008hv	NGC 2765	0.0125	2010-02-20	LRIS	B560/R7500
SN2009cz	NGC 2789	0.0210	2010-02-20	LRIS	B560/R7500
SN2009gf	NGC 5525	0.0184	2010-02-20	LRIS	B560/R7500
SN2011ay	NGC 2315	0.0205	2011-05-09	OSIRIS	R1000B
SNfactory-observed SNe and Hosts					
PTF09dnp	2MASX J15192538+49	0.0373	2011-05-09	OSIRIS	R1000B
SN2007fr	UGC 11780	0.0507	2009-09-24	LRIS	B460/R5000,B560/R7500
SN2007nq	UGC 00595	0.0451	2009-09-24	LRIS	B460/R5000,B560/R7500
SN2009hi	NGC 7647	0.0411	2009-09-24	LRIS	B460/R5000,B560/R7500
SN2009hs	NGC 6521	0.0275	2009-09-25	LRIS	B560/R7500
SNF20060521-008	2MASX J12440303-05	0.0551	2009-05-02	LRIS	B560/R7500
SNF20070417-002	2MASX J13205225+21	0.0891	2009-05-02	LRIS	B560/R7500
SNF20070727-016	2MASX J16143012+56	0.0666	2009-04-02	LRIS	B560/R7500
SNF20080512-010	UGC 10261	0.0633	2010-02-20	LRIS	B460/R5000
SNF20080514-002	NGC 5162	0.0219	2010-02-20	LRIS	B560/R7500
SNF20080614-010	2MASXi J1426530+23	0.0746	2009-04-02	LRIS	B560/R7500
SNF20080720-001	2MASX J01052718+37	0.0210	2009-09-25	LRIS	B560/R7500
SNF20080731-000	2MASS J17440332+33	0.0760	2009-05-02	LRIS	B560/R7500
SNF20080815-017	2MASX J22301679+24	0.0648	2009-09-24	LRIS	B460/R5000
SNF20080825-010	IC 0144	0.0406	2009-09-24	LRIS	B460/R5000,B560/R7500
SNF20080913-031	2MASX J02113233+23	0.0551	2009-09-24	LRIS	B460/R5000,B560/R7500
SNF20080919-000	2MFGC 00051	0.0601	2009-09-25	LRIS	B460/R5000
SDSS SNe and Hosts					
SN2005ex	2MASX J01415126-00	0.0934	2011-08-30	LRIS	B460/R5000
SN2005ez	SDSS J030711.02+01	0.1297	2011-08-30	LRIS	B460/R5000
SN2005ff	SDSS J223041.15-00	0.0898	2011-10-20	OSIRIS	R2000B,R2500R
SN2005fh	2MASX J23172973+00	0.1189	2011-08-29	LRIS	B460/R5000
SN2005je	2MASX J02352657+01	0.0939	2009-09-25	LRIS	B460/R5000
SN2005kn	SDSS J211531.80-00	0.1974	2011-08-29	LRIS	B460/R5000
SN2005kt	2MASX J01105805+00	0.0654	2009-09-25	LRIS	B460/R5000
SN2006er	2MASX J00213789-01	0.0843	2011-08-30	LRIS	B460/R5000
SN2006fa	SDSS J213530.84-00	0.1670	2011-08-29	LRIS	B460/R5000
SN2006jp	SDSS J205656.18-00	0.1610	2011-08-30	LRIS	B460/R5000
SN2006ni	SDSS J205452.51-00	0.1751	2011-08-29	LRIS	B460/R5000
SN2007la	2MASX J22295461+01	0.1309	2011-08-29	LRIS	B460/R5000
SN2007or	SDSS J014238.34+01	0.1662	2011-08-30	LRIS	B460/R5000
SN2007ph	2MASX J20511361-00	0.1294	2011-08-30	LRIS	B460/R5000

R1000B, R2000B, and R2500R label grisms on OSIRIS. The B460/R5000 setup indicates the 600ℓ/4000Å grism, d4600Å dichroic and 600ℓ/5000Å grating on LRIS. The B560/R7500 setup indicates the 600ℓ/4000Å grism, d5600Å dichroic and 600ℓ/7500Å grating on LRIS.

CHAPTER 13

Host Measurements

13.1 Observations and reductions

Host galaxy spectra were obtained using the 10-m Keck I telescope and the 10.4-m Gran Telescopio Canarias (GTC). On both telescopes, we made observations using a $1\farcs0$ longslit placed along the major-axis of the target galaxy. Although progenitor population measurements of SNe with very short delay times (for instance, core-collapse SNe) may benefit from choosing a position angle which places the slit directly over the location of the SN, the expected delay times for the SNe probed here ($\gtrsim$ 1 Gyr) are expected to be significantly longer than the rotational period of the host galaxies ~ 0.1 Gyr. Therefore, the SN progenitor could have been born at almost any position angle within the galaxy, which makes a targeted position angle less meaningful. Below we present the observational details used for each telescope.

We observed 36 SN Ia host galaxies with the Low Resolution Imaging Spectrometer (LRIS Oke et al. 1995; Rockosi et al. 2010) optical spectrograph mounted on the 10-m Keck-I telescope at the summit of Mauna Kea. A selectable dichroic is used to split light into a red path and a blue path, each of which lead to a number of selectable dispersing elements providing flexibility in resolution and wavelength coverage. For our pilot program during two nights in the spring of 2009, we used the d5600Å dichroic, the 600ℓ/4000Å grism on the blue side, and 600ℓ/7500Å grating on the red side to obtain continuous coverage from rest frame 3000Å to 8000Å at a resolution of $\lambda/\Delta\lambda \sim 2500$. This resolution is equivalent to a rest-frame velocity dispersion of ~ 120 km/s, which is fine enough to measure the velocity dispersions of early-type galaxies. On subsequent LRIS observing nights, we used one of two different setups (and occasionally both) depending on the redshift of the target galaxy. This was to ensure that absorption lines of interest always occurred at wavelengths far away from the transition wavelength of the dichroic where flux calibration can be less certain. For $z < 0.04$, the absorption lines of interest all lie well to the blue of the dichroic cutoff for the configuration listed above using the d5600Å dichroic. For galaxies with $z > 0.06$, we instead used the d4600Å dichroic, the same 600ℓ/4000Å grism on the blue side, but the bluer-blazed 600ℓ/5000Å grating on the red side. This setup has

nearly identical resolution and wavelength coverage as the first setup, but places the lines of interest all well to the red of the dichroic transition wavelength. We observed five galaxies with $0.04 < z < 0.06$ in both setups.

Our five LRIS observing runs contain data from three different red side CCD mosaics, as the red detector was upgraded twice during the course of this study. The intermediate red side CCD (in use during September 2009 and February 2010) suffered from several defects which locally altered its quantum efficiency, including some defects that cannot be completely removed by flat-fielding[6]. Fortunately, for most affected spectra, the reddest Lick index of interest (Fe5270) fell on the blue CCD and was not lost. In the six cases where this index and also Fe5335 were compromised, we use an alternative $[\mathrm{Fe/H}]$sensitive index Fe4383, which falls on the blue CCD in each case. We did use affected red-side spectra to carefully measure the [O III]λ[5007] and $\mathrm{H}\alpha$ emission lines in order to correct for the infill of the $\mathrm{H}\gamma$ and $\mathrm{H}\delta$ absorption lines. However, due to the Balmer decrement, the necessary accuracy for these measurements is 3-6 times less than that required for the Fe-indices.

We observed four additional targets during two runs with the Optical System for Imaging and low Resolution Integrated Spectroscopy (OSIRIS) (Cepa et al. 2000, 2003) mounted on the 10.4-m GranTeCan (GTC) telescope located at the Roque de los Muchachos Observatory on the island of La Palma in the Canary Islands. On the night of the first run, we observed three SN Ia host galaxies with the R1000B grism, which covers the wavelength range 3700Å to 7000Å at resolution $\lambda/\Delta\lambda \sim 1000$, equivalent to velocity dispersion of ~ 300 km/s. On the night of the second run, weather limited our observations to one target galaxy, which we observed with both the R2000B and R2500R grisms to increase the resolution to ~ 2000 (~ 150 km/s velocity dispersion equivalent) but maintain wavelength coverage from 4000Å to 7540Å.

All of the LRIS and OSIRIS data were reduced using the package LOWREDUX[7]. This IDL pipeline performs standard spectroscopy reduction steps (bias subtraction, flat-fielding, wavelength calibration, 2D sky subtraction, 1D extraction, and coaddition of spectra from separate exposures) in an automated way. We observed CALSPEC[8] flux standard stars each night which we then used to flux calibrate our spectra. The unextinguished spectra of the standards we chose are smooth at the wavelengths of telluric absorption, which we exploited to make a telluric correction for each exposures 1D extraction. This was done by assuming that the extinct flux F_λ is related to the unextinct flux F^0_λ by:

$$\log(F_\lambda) = \log(\mathrm{F}^0_\lambda) + \log(\mathrm{A}_\lambda) \times X^\rho \tag{13.1}$$

where A_λ is the strength of the telluric absorption at wavelength λ, X is the average airmass of the exposure and ρ is measured to be ~ 0.6 (Buton et al. 2012). By fitting a spline to the observed standard star spectrum while masking out telluric wavelengths, we estimate A_λ for each night. We then apply Equation 13.1 to each host spectrum to produce telluric-corrected spectra.

[6] www2.keck.hawaii.edu/inst/lris/lris-red-upgrade-notes.html#dewar2

[7] www.ucolick.org/~xavier/LowRedux/

[8] www.stsci.edu/hst/observatory/cdbs/calspec.html

We noticed during the reductions that a few spectra on the red-side of LRIS were grossly miscalibrated in wavelength (by $\sim 10 - 100$Å, probably due to problems we observed during the night with the grating tilt mechanism of LRIS. We recalibrated the wavelength solutions of these observations by fitting a linear function to the measured centers of 45 sky lines between 5578Å and 7872Å in the observed spectra to the centers of the same 45 sky lines in the published sky spectrum of Hanuschik (2003) convolved to the same resolution as the LRIS spectra. For consistency, we implemented the same recalibration on all LRIS red-side spectra, though the difference for most spectra was insignificant when measuring the strengths of absorption indices.

13.2 Progenitor population measurements

Stellar population synthesis aims to model galaxy spectra as the sum of contributions from individual stars of various masses, ages, and compositions. Although early-type galaxies are composed of stars of many ages, the simplest approach to modeling these galaxies considers collections of stars of a single age. From these single stellar populations (SSPs), we can make comparisons of model spectra to observed spectra, or comparisons of derived properties such as the strength of particular absorption lines. This latter approach has the advantage that it is relatively insensitive to potential systematic SED uncertainties that change slowly with wavelength, such as flux-calibration or dust extinction.

13.2.1 Velocity dispersion

To make a fair assessment of the absorption line strengths in our observed spectra, we must first measure the smearing of spectral features caused by both the finite line-spread function of the spectrographs used and by the internal velocity dispersions of each target galaxy's stars. To measure each instrumental setup's wavelength-dependent resolution, we fit a fourth order polynomial to the full-width half maxima of arc lines as a function of wavelength in calibration spectra. We then use the program PPXF (Cappellari & Emsellem 2004) to measure the additional smearing attributable to each target galaxy's velocity dispersion. This program models each observed spectrum as a positive definite combination of library stellar spectra (we use the MILES spectral library (Sánchez-Blázquez et al. 2006; Cenarro et al. 2007)) convolved with the instrumental resolution measured above and a candidate velocity dispersion and offset (i.e. redshift refinement). To account for potential flux-calibration errors and other errors that evolve slowly with wavelength, the model also contains low-order additive and multiplicative polynomials. We mask out wavelengths corresponding to emission lines and telluric absorption during the fit. PPXF then minimizes a χ^2 statistic constructed from the residuals of the observed spectrum from the model spectrum and the estimated error spectrum. A sample comparison of data to the best fit PPXF model is show in Figure 13.2. The redshift and velocity dispersion results from PPXF are shown in Figure 13.3, which also compare our results to published results from SDSS

where available. The scatter of both our redshift and velocity dispersion measurements is ~ 20 km/s. We have confirmed that this level of uncertainty has a negligible effect on our absorption line measurements.

13.2.2 Equivalent widths

The equivalent widths in the EZ_AGES model spectra are measured at the resolution of the original Lick/IDS system, about $8.5 - 11$ Å FWHM. To facilitate comparison, we must therefore first match the resolution of galaxy spectra to the Lick/IDS system for every spectrum and index of interest. In the case of a galaxy index with combined spectrograph and velocity dispersion resolution less than the Lick/IDS resolution, we simply convolve the spectrum with the necessary Gaussian kernel to make the resulting resolution match the Lick/IDS resolution. In the case of a galaxy index in which the observed resolution already exceeds that specified by the Lick/IDS system, we use an empirical formula, similar to that employed by Trager et al. (1998), to estimate a correction to the equivalent width. The IDL routine LICK_EW, distributed with EZ_AGES, applies both of these corrections automatically, and also estimates uncertainties in the equivalent widths from the 1d error-spectra following the formalism of Cardiel et al. (1998). In cases where more than one spectrum covers the wavelength range of a particular Lick index of interest, we use the measurement from the spectrum with higher signal-to-noise ratio.

In a number of cases we are able to test the accuracy of equivalent width error estimates by comparing independently obtained overlapping spectra of a single galaxy. For instance, five host galaxies were observed using both the B4600 and B5600 blue-side setups on LRIS. For each of these galaxies, indices with observed-frame wavelengths bluer than about 5000Å are present at reasonable signal-to-noise ratio in reduced spectra taken with both setups. Unfortunately, the defects in the intermediate red-side CCD prevented us from making similar comparisons of the R5000 and R7500 setups for these galaxies. However, we can make some limited comparisons of the B4600 setup to the R5000 setup and the B5600 setup to the R7500 setup by comparing indices near the transition wavelengths of the dichroics used. For example, indices with observed-frame wavelengths near 4600Å are visible in both the B4600 and R5000 spectra.

To test the error estimates, we investigate the distribution of the pull statistic defined as:

$$p = \frac{W_A - W_B}{\sqrt{\sigma(W_A)^2 + \sigma(W_B)^2}} \tag{13.2}$$

where W_A and W_B are the equivalent widths of a particular Lick index of a particular galaxy from independent spectra A and B, and $\sigma(W_A)$ and $\sigma(W_B)$ are their respective uncertainties. The distribution of p should be approximately Gaussian with zero mean and unit standard deviation if the uncertainties are properly estimated. Figure 13.4 shows the dependence of p on wavelength and on the weaker signal-to-noise ratio of spectrum A and B near the wavelength of the index being measured. The distribution of p is approximately

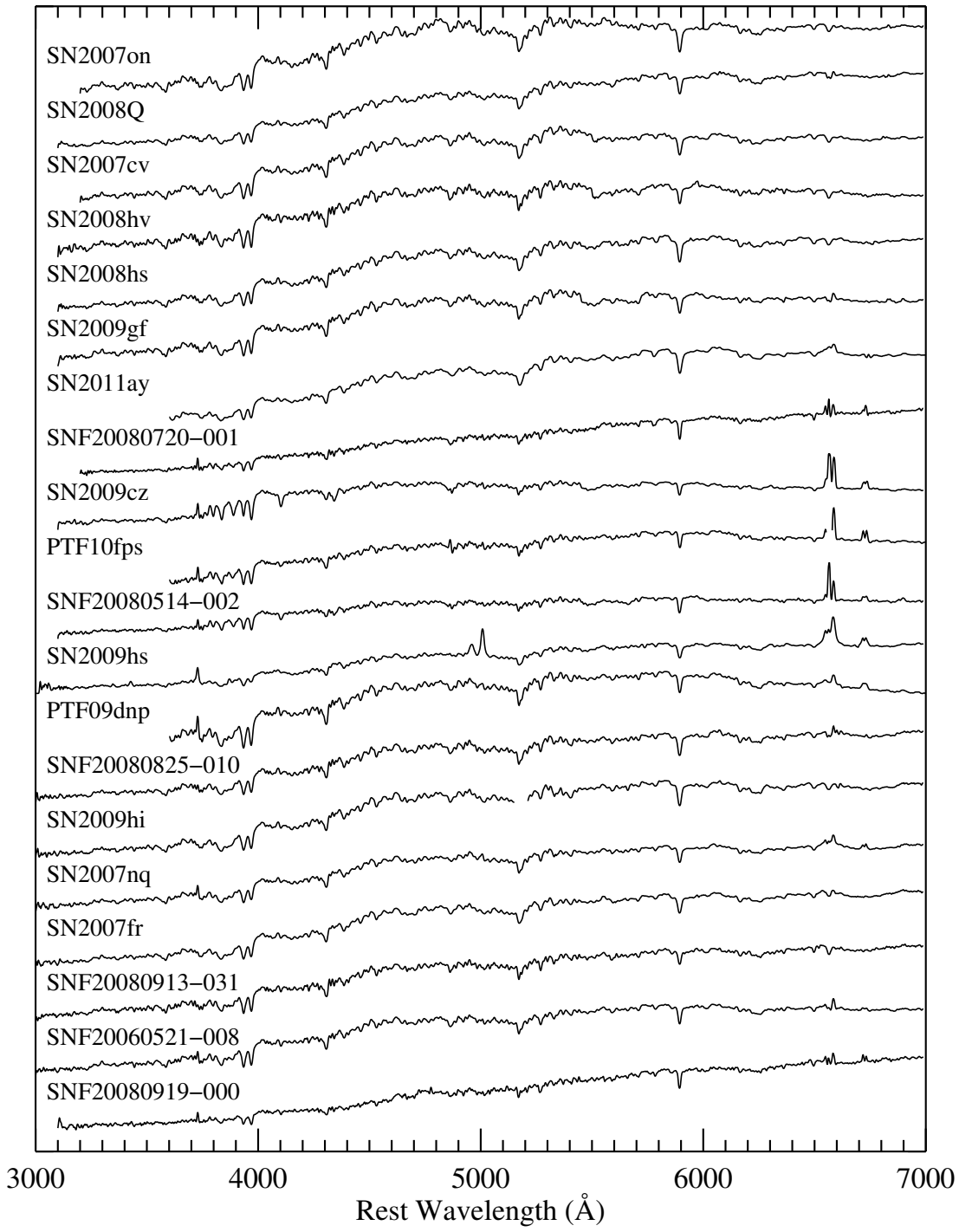

Figure 13.1. All 40 host galaxy spectra targeted by this program, in ascending redshift order. Spectra have been smoothed with a $5\mathring{A}$ wide Gaussian kernel. All features visible at this resolution are real, i.e. not noise.

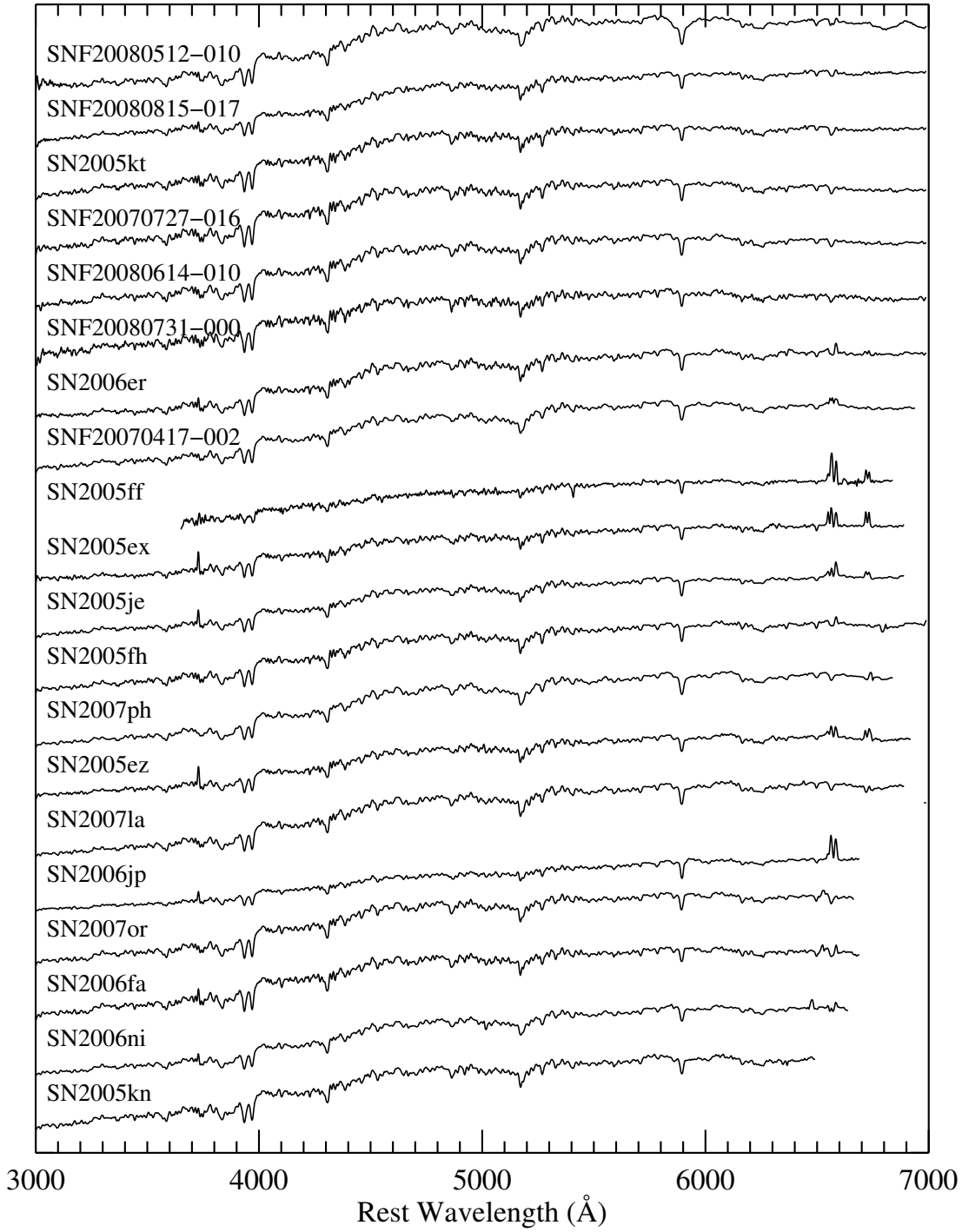

Figure 13.1. Host spectra (continued)

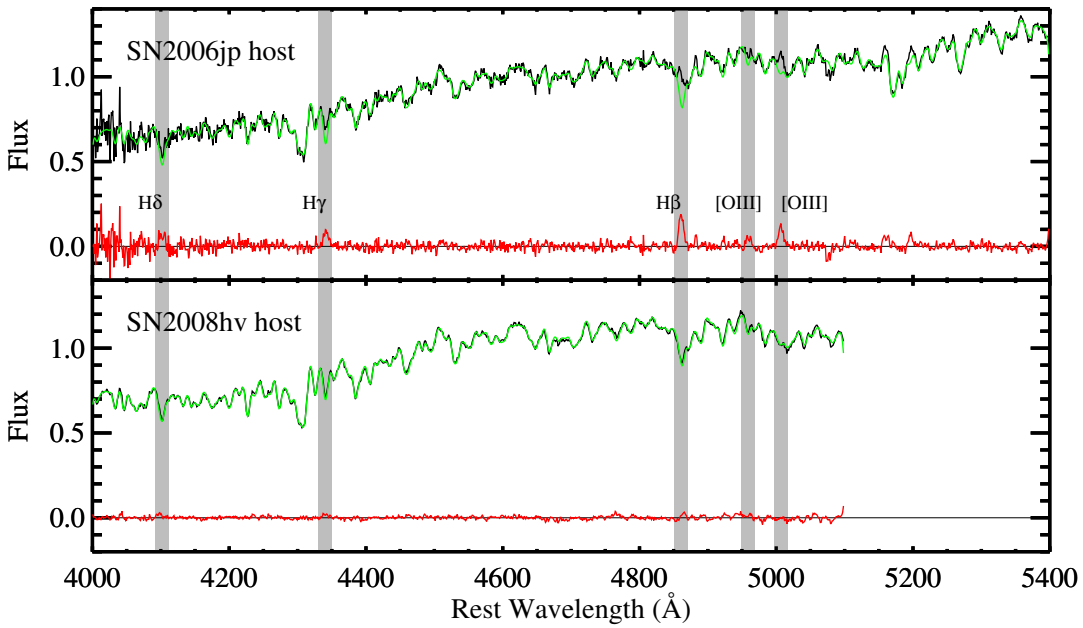

Figure 13.2. Sample spectra of SN host galaxies. **Top:** Spectrum of the host of SN2006jp taken with the B560 setup of LRIS. Data is plotted in black, and the best fit PPXF spectrum is overplotted in green. Emission line regions, indicated in light grey, are masked during the PPXF fit. The residual, shown in red, indicates the presence of weak emission lines which must be accounted for before the absorption line diagnostics can be used to measure the age and abundances of this galaxy. **Bottom:** Spectrum of the host of SN2008hv taken with the R5000 setup of LRIS. Colors are the same as above. This spectrum shows no hints of emission in its residual.

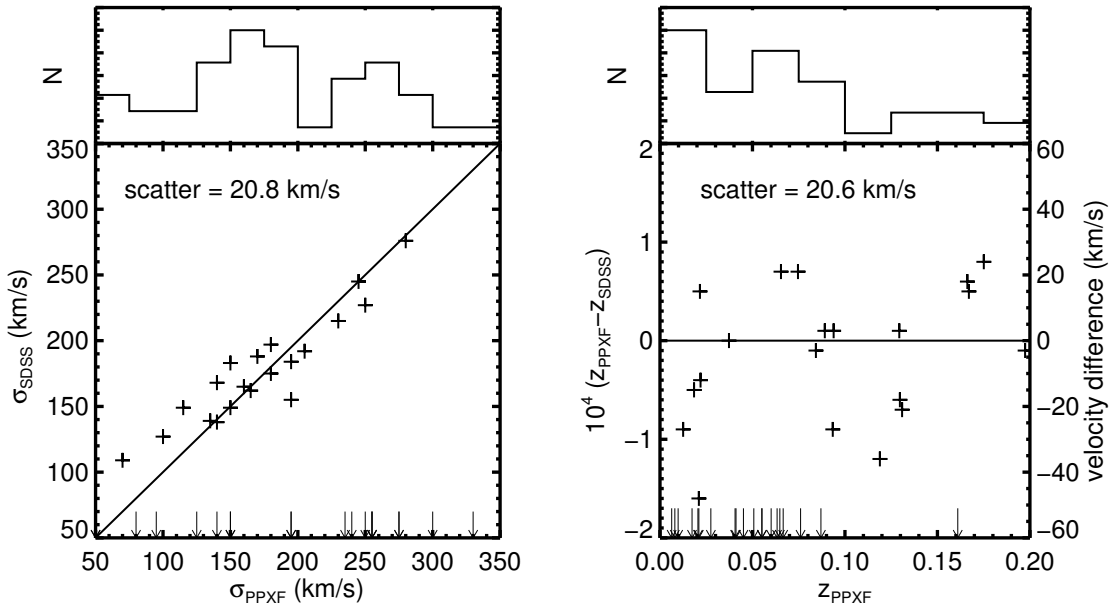

Figure 13.3. Left: Velocity dispersion measurements obtained by using PPXF on our host spectra (x-axis). For comparison, the published SDSS velocity dispersions, where available, are plotted on the y-axis. Arrows indicate measurements for which no SDSS comparison exists. The histogram on top shows the velocity dispersion distribution of our sample. **Right:** Redshift measurements obtained by using PPXF on our host spectra (x-axis). For comparison, the residuals to published SDSS redshifts, where available, are plotted on the y-axis. Arrows indicate measurements for which no SDSS comparison exists. The histogram on top shows the redshift distribution of our sample.

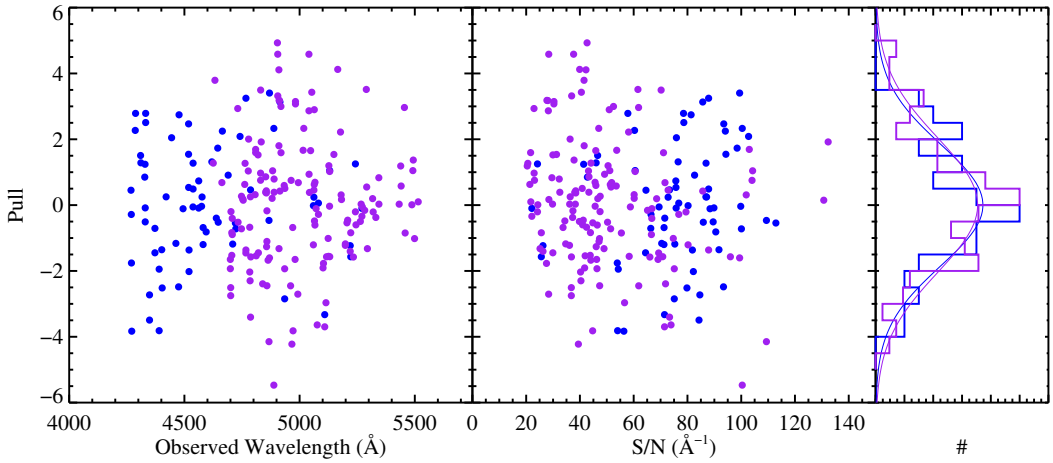

Figure 13.4. The equivalent width pull statistic as a function of the observed wavelength (left panel) or the smaller of the two signal-to-noise ratios of the compared spectra (middle panel). Blue points compare independently obtained spectra from the B460 and B560 setups on LRIS. Purple points compare either B460 spectra to R5000 spectra, or B560 spectra to R7500 spectra. The histogram in the right panel collapses the data along the wavelength or signal-to-noise ratio axes and also shows the best Gaussian fits. The standard deviations of the Gaussians are 1.8 (2.1) for the blue (purple) points, indicating that the equivalent width uncertainties are underestimated by about a factor of 2. There are no obvious trends in the underestimation of errors with either wavelength or signal-to-noise ratio.

Gaussian with zero mean, but has a standard of deviation of ~ 2.0. Since the distribution of p shows no dependence on the signal-to-noise ratios or on the wavelengths of the indices being measured, we simply correct the uncertainties derived from photon statistics by multiplying them by a factor of 2.0. These larger uncertainties turn out to still be smaller than the typical intrinsic dispersions of the correlations we investigate in the next chapter, and hence the significances of our results are not greatly affected by this adjustment.

13.2.3 Emission correction

The spectra of the stellar atmospheres of the SN progenitor environments we wish to probe are dominated by absorption lines set against thermal continua. However, galaxies commonly present emission line components in their spectra as well from non-stellar sources such as HII regions ionized by the UV flux of young stars or active galactic nuclei. Weak emission lines can fill in and bias the diagnostic absorption lines we wish to study, especially the Balmer lines which we are using to probe stellar ages. Strong emission can obliterate any possibility of accurately recovering the underlying absorption features of interest.

To mitigate the effect of emission lines filling in absorption lines, we have attempted to select SN host galaxies that are largely free of emission. The primary selection crite-

ria: early-type morphologies, red colors, or large bulges, are all properties which correlate strongly with galaxies having smaller amounts of interstellar gas and older stellar populations less likely to ionize this gas and produce emission lines. Small amounts of ongoing star-formation can still be observed, however, as can emission with nuclear origins. In an analysis of ~ 55000 red galaxies from SDSS, Yan et al. (2006) found that nearly half show some amount of emission. In the majority of these cases, the emission was characteristic of a Low Ionization Nuclear Emission Region (LINER), although a small number showed signs of star formation. As illustrated in the PPXF residual spectrum of the host of SN2006jp (Figure 13.2), some of our spectra contain emission features as well ranging from subtle (equivalent widths of a few tenths of Å) to obvious (equivalent widths of ~ 10Å). To accurately derive ages and metallicities from these spectra, a correction must be applied for this emission infill.

Fortunately, the strengths of galactic emission lines are usually quite correlated, and follow only a few patterns. By identifying the particular pattern of emission in each host galaxy, and measuring the strength of a line with a well-constrained underlying continuum, we can infer the appropriate corrections to contaminated absorption features.

The most common tool for classifying the type of emission present in a spectrum is the BPT diagram (Baldwin et al. 1981), which separates emission types based on the flux ratios of the closely separated emission pairs Hα/[N II]λ6583 and Hβ/[O III]λ5007. Galaxies with emission due to star-formation occupy a different locus on the BPT diagram than galaxies with emission due to AGNi or LINERs. However, the emission lines in our sample are frequently very weak or consistent with zero, which introduces large uncertainties in the computation of flux ratios.

An alternate approach applicable to red galaxies (such as our hosts) is suggested by Yan et al. (2006), in which the equivalent widths of [O II] and $\mathrm{H}\alpha$ are used to separate LINERs from other types of AGN and star-forming galaxies. For this diagnostic, we measure the equivalent widths of [O II] and $\mathrm{H}\alpha$ assuming the underlying continua are well-approximated by the PPXF residual spectra. Figure 13.5 shows that a) most of our spectra have at most very modest emission, and b) where it is present, most of the emission can be classified as LINER-like.

For the galaxies with LINER-like emission, we implement the correction described in the appendix of Graves & Faber (2010). Briefly, trial values of age and $[\mathrm{Fe/H}]$ are first computed using EZ_AGES. The nearest spectrum in age and $[\mathrm{Fe/H}]$ from the SSP library of Bruzual & Charlot (2003, hereafter BC03) is then scaled to the spectrum in question in the region of the [O III]λ5007 emission line, which has a relatively predictable underlying continuum. The equivalent width of this line is then measured. The BC03 templates are finely sampled in age, but only sparsely sampled in $[\mathrm{Fe/H}]$, so an empirical correction is applied to this measurement based on the difference between the EZ_AGES $[\mathrm{Fe/H}]$ and the $[\mathrm{Fe/H}]$ of the nearest BC03 template. The correction to $\mathrm{H}\beta$ is then derived from $\mathrm{EW(H}\beta) = 0.7\mathrm{EW([O\ III]}\lambda 5007)$, as suggested by Trager et al. (2000b); Graves & Faber (2010). Corrections for $\mathrm{H}\gamma$ and $\mathrm{H}\delta$ are then derived assuming a case B Balmer decrement (Osterbrock & Ferland 2006).

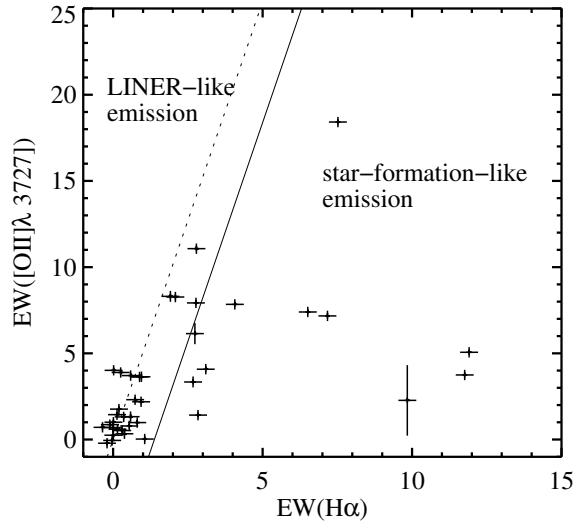

Figure 13.5. Equivalent width of the [O II] emission line versus the equivalent width of the $\mathrm{H}\alpha$ emission line for the SN host galaxies in our sample. The dotted line shows the locus of galaxies with LINER type emission identified by (Graves et al. 2007). The solid line indicates our demarcation for classifying emission as LINER-like. Galaxies to the right of this line show emission characteristic of star-formation or Seyfert AGN. Note that many of our hosts have very little emission in either line.

For galaxies with emission line ratios more characteristic of star-formation than of LINER activity, we follow Gallagher et al. (2008) and use the strength of the $\mathrm{H}\alpha$ emission line together with the Balmer decrement to estimate the infill of higher order Balmer lines. In order to measure the excess of $\mathrm{H}\alpha$ due to star-formation, we must first estimate what the depth of the underlying absorption spectrum is. Uncertainty in the underlying absorption directly translates to uncertainty in the applied emission corrections. From analysis of the BC03 SSPs, we find that the equivalent width of $\mathrm{H}\alpha$ in stellar populations with ages older than 1 Gyr and $[\mathrm{Fe/H}]$ greater -1 (consistent with our sample) spans a range of about 2Å. The absorption strength is highly correlated with the Rose (1984) index $\mathrm{H8/Fe}\lambda 3859$, however, which is relatively unaffected by star-formation related emission by virtue of being a significantly higher order Balmer transition than $\mathrm{H}\alpha$. We therefore estimate the underlying spectrum for each of our galaxies as the BC03 spectrum closest in $\mathrm{H8/Fe}\lambda 3859$. The range of $\mathrm{H}\alpha$ absorption at fixed $\mathrm{H8/Fe}\lambda 3859$ is only $\sim 0.1 - 0.25$ Å in the BC03 templates, which, after the application of the Balmer decrement, translates to a negligible uncertainty in $\Delta\mathrm{EW}(\mathrm{H}\gamma_\mathrm{F})$ or $\Delta\mathrm{EW}(\mathrm{H}\delta_\mathrm{F})$.

13.2.4 Ages and abundances

Here, we use the stellar population synthesis code EZ_AGES (Graves & Schiavon 2008), which uses the models of Schiavon (2007) to constrain not only age and $[\mathrm{Fe/H}]$, but also the abundances of several additional elements: $[\mathrm{Mg/Fe}]$, $[\mathrm{C/Fe}]$, $[\mathrm{N/Fe}]$, and $[\mathrm{Ca/Fe}]$. The code uses the well known Lick absorption indices (Worthey et al. 1994; Worthey & Ottaviani 1997) as the basis for model – data comparison. Particular indices are sensitive in different degrees to age, $[\mathrm{Fe/H}]$, or other abundances. As some of indices are dependent on more than one model parameter, EZ_AGES fits model parameters hierarchically. Age and

$[\mathrm{Fe/H}]$ are determined first, as they can be determined relatively independently of other abundances by using a Balmer index and an iron index. Our fiducial choice for a Balmer index is $\mathrm{H}\gamma_{\mathrm{F}}$ both because it is well measured for almost all of our host galaxies and because it is less susceptible to emission infill correction uncertainties than $\mathrm{H}\beta$ due to the Balmer decrement ($\mathrm{H}\delta_{\mathrm{F}}$ would also be a good choice). Our fiducial choice for an iron index is Fe_{5270} due to its relative insensitivity to other model parameters. The next indices to be considered are $\mathrm{Mg_b}$ and G4300, which are sensitive to $[\mathrm{Mg/Fe}]$ and $[\mathrm{C/Fe}]$ respectively, but also depend on the fitted value of $[\mathrm{Fe/H}]$. The CN_1 index, which is sensitive to $[\mathrm{N/Fe}]$, $[\mathrm{C/Fe}]$, and $[\mathrm{Fe/H}]$, is then fit, followed by Ca_{4227}, which is sensitive to $[\mathrm{Ca/Fe}]$, $[\mathrm{C/Fe}]$, $[\mathrm{N/Fe}]$, and $[\mathrm{Fe/H}]$. EZ_AGES propagates uncertainties in equivalent width measurements through the fitting hierarchy to estimate an uncertainty for each of the model parameters. The code also iterates its fitting up to four times to ensure that changes in parameters estimated at the bottom of the hierarchy do not affect parameters estimated at the top of the hierarchy. In a few cases, our fiducial choice of Balmer and iron indices ($\mathrm{H}\gamma_{\mathrm{F}}$ and Fe_{5270}) could not be used due to reduction artifacts or contamination from bright sky line residuals. In these cases, we substituted $\mathrm{H}\delta_{\mathrm{F}}$ for the Balmer index, or Fe_{5335} for the iron index as noted in Table 13.2.

Table 13.1. Host Ages and $[\mathrm{Fe/H}]$

SN Name	Balmer Index	Fe Index	Age(Gyr)	[Fe/H]
Hosts of Swift-observed SNe				
PTF10fps	$\mathrm{H}\gamma_\mathrm{F}$	Fe_{5270}	...	...
SN2007cv	$\mathrm{H}\gamma_\mathrm{F}$	Fe_{5270}	...	...
SN2007on	$\mathrm{H}\gamma_\mathrm{F}$	Fe_{4383}	$17.70^{+2.85}_{-2.46}$	$-0.009^{+0.129}_{-0.129}$
SN2008Q	$\mathrm{H}\delta_\mathrm{F}$	Fe_{5270}	$14.95^{+1.90}_{-1.68}$	$-0.225^{+0.079}_{-0.079}$
SN2008hs	$\mathrm{H}\gamma_\mathrm{F}$	Fe_{5270}	$17.70^{+2.85}_{-2.46}$	$-0.114^{+0.129}_{-0.129}$
SN2008hv	$\mathrm{H}\gamma_\mathrm{F}$	Fe_{5270}	$7.28^{+1.02}_{-0.89}$	$-0.062^{+0.095}_{-0.095}$
SN2009cz	$\mathrm{H}\gamma_\mathrm{F}$	Fe_{5270}	...	...
SN2009gf	$\mathrm{H}\gamma_\mathrm{F}$	Fe_{5270}	$17.70^{+2.85}_{-2.46}$	$-0.235^{+0.129}_{-0.129}$
SN2011ay	$\mathrm{H}\gamma_\mathrm{F}$	Fe_{5270}	$4.70^{+1.41}_{-1.09}$	$0.132^{+0.055}_{-0.055}$
Hosts of SNfactory SNe				
PTF09dnp	$\mathrm{H}\gamma_\mathrm{F}$	Fe_{5270}	$10.53^{+1.35}_{-1.19}$	$-0.133^{+0.082}_{-0.082}$
SN2007fr	$\mathrm{H}\gamma_\mathrm{F}$	Fe_{5270}	$14.95^{+2.41}_{-2.08}$	$-0.027^{+0.150}_{-0.150}$
SN2007nq	$\mathrm{H}\gamma_\mathrm{F}$	Fe_{5270}	$9.38^{+1.19}_{-1.06}$	$-0.137^{+0.161}_{-0.161}$
SN2009hi	$\mathrm{H}\gamma_\mathrm{F}$	Fe_{5270}	$13.57^{+1.85}_{-1.63}$	$0.037^{+0.129}_{-0.129}$
SN2009hs	$\mathrm{H}\gamma_\mathrm{F}$	Fe_{5270}	...	...
SNF20060521-008	$\mathrm{H}\gamma_\mathrm{F}$	Fe_{4383}	$6.65^{+1.07}_{-0.92}$	$0.200^{+0.129}_{-0.129}$
SNF20070417-002	$\mathrm{H}\gamma_\mathrm{F}$	Fe_{5270}	$8.33^{+1.10}_{-0.97}$	$-0.125^{+0.114}_{-0.114}$
SNF20070727-016	$\mathrm{H}\gamma_\mathrm{F}$	Fe_{5270}	$5.32^{+0.67}_{-0.60}$	$0.076^{+0.129}_{-0.129}$
SNF20080512-010	$\mathrm{H}\gamma_\mathrm{F}$	Fe_{4383}	$15.06^{+2.43}_{-2.09}$	$-0.287^{+0.191}_{-0.191}$
SNF20080514-002	$\mathrm{H}\gamma_\mathrm{F}$	Fe_{4383}	...	...
SNF20080614-010	$\mathrm{H}\gamma_\mathrm{F}$	Fe_{5270}	$5.81^{+1.57}_{-1.24}$	$0.169^{+0.129}_{-0.129}$
SNF20080720-001	$\mathrm{H}\gamma_\mathrm{F}$	Fe_{4383}	$2.24^{+0.36}_{-0.31}$	$0.200^{+0.129}_{-0.129}$
SNF20080731-000	$\mathrm{H}\gamma_\mathrm{F}$	Fe_{5270}	$13.51^{+2.18}_{-1.88}$	$-0.631^{+0.403}_{-0.403}$
SNF20080815-017	$\mathrm{H}\gamma_\mathrm{F}$	Fe_{4383}	$10.51^{+2.66}_{-2.12}$	$-0.430^{+0.209}_{-0.209}$
SNF20080825-010	$\mathrm{H}\gamma_\mathrm{F}$	Fe_{5270}	$8.40^{+1.13}_{-1.00}$	$0.090^{+0.106}_{-0.106}$
SNF20080913-031	$\mathrm{H}\gamma_\mathrm{F}$	Fe_{4383}	$5.50^{+0.89}_{-0.76}$	$0.013^{+0.141}_{-0.141}$
SNF20080919-000	$\mathrm{H}\gamma_\mathrm{F}$	Fe_{4383}	$2.57^{+0.41}_{-0.36}$	$0.200^{+0.129}_{-0.129}$
Hosts of SDSS SNe				
SN2005ex	$\mathrm{H}\gamma_\mathrm{F}$	Fe_{5270}	$1.20^{+0.19}_{-0.17}$	$0.126^{+0.129}_{-0.129}$
SN2005ez	$\mathrm{H}\gamma_\mathrm{F}$	Fe_{5270}	$4.59^{+2.54}_{-1.63}$	$0.021^{+0.153}_{-0.153}$
SN2005ff	$\mathrm{H}\gamma_\mathrm{F}$	Fe_{5270}	$1.91^{+1.37}_{-0.80}$	$0.033^{+0.129}_{-0.129}$
SN2005fh	$\mathrm{H}\gamma_\mathrm{F}$	Fe_{5270}	$14.46^{+2.33}_{-2.01}$	$-0.025^{+0.118}_{-0.118}$
SN2005je	$\mathrm{H}\gamma_\mathrm{F}$	Fe_{4383}	$5.30^{+0.72}_{-0.64}$	$-0.212^{+0.230}_{-0.230}$
SN2005kn	$\mathrm{H}\gamma_\mathrm{F}$	Fe_{5270}	$17.22^{+2.78}_{-2.39}$	$-0.382^{+0.150}_{-0.150}$
SN2005kt	$\mathrm{H}\gamma_\mathrm{F}$	Fe_{4383}	$2.27^{+0.00}_{-0.00}$	$0.163^{+0.129}_{-0.129}$
SN2006er	$\mathrm{H}\gamma_\mathrm{F}$	Fe_{5270}	$8.37^{+2.32}_{-1.82}$	$0.103^{+0.122}_{-0.122}$
SN2006fa	$\mathrm{H}\gamma_\mathrm{F}$	Fe_{5270}	$3.00^{+0.41}_{-0.36}$	$0.049^{+0.129}_{-0.129}$
SN2006jp	$\mathrm{H}\gamma_\mathrm{F}$	Fe_{5270}	$1.20^{+0.19}_{-0.17}$	$-0.001^{+0.129}_{-0.129}$
SN2006ni	$\mathrm{H}\gamma_\mathrm{F}$	Fe_{5270}	$9.70^{+2.89}_{-2.23}$	$0.026^{+0.142}_{-0.142}$
SN2007la	$\mathrm{H}\gamma_\mathrm{F}$	Fe_{5270}	$9.24^{+3.22}_{-2.39}$	$-0.065^{+0.126}_{-0.126}$
SN2007or	$\mathrm{H}\gamma_\mathrm{F}$	Fe_{5270}	$3.69^{+1.06}_{-0.82}$	$0.102^{+0.129}_{-0.129}$
SN2007ph	$\mathrm{H}\delta_\mathrm{F}$	Fe_{5270}	$11.72^{+3.20}_{-2.52}$	$-0.098^{+0.112}_{-0.112}$

The Balmer Index and Fe Index columns indicate which indices were used by EZ_AGES to determine the age and $[\mathrm{Fe/H}]$ of each galaxy.

Table 13.2. Host Metal Abundances

SN Name	Balmer Index	Fe Index	[Mg/Fe]	[C/Fe]	[N/Fe]	[Ca/Fe]
Hosts of Swift-observed SNe						
PTF10fps	$H\gamma_F$	Fe_{5270}	···	···	···	···
SN2007cv	$H\gamma_F$	Fe_{5270}	···	···	···	···
SN2007on	$H\gamma_F$	Fe_{4383}	$0.200^{+0.200}_{-0.200}$	$-0.183^{+0.007}_{-0.007}$	···	$0.000^{+0.113}_{-0.113}$
SN2008Q	$H\delta_F$	Fe_{5270}	$0.400^{+0.046}_{-0.046}$	$-0.060^{+0.028}_{-0.028}$	$0.755^{+0.755}_{-0.755}$	$0.027^{+0.178}_{-0.178}$
SN2008hs	$H\gamma_F$	Fe_{5270}	$0.322^{+0.322}_{-0.322}$	$-0.222^{+0.020}_{-0.020}$	···	$0.000^{+0.113}_{-0.113}$
SN2008hv	$H\gamma_F$	Fe_{5270}	$0.160^{+0.066}_{-0.066}$	$-0.160^{+0.057}_{-0.057}$	$0.395^{+0.059}_{-0.059}$	$-0.080^{+0.061}_{-0.061}$
SN2009cz	$H\gamma_F$	Fe_{5270}	···	···	···	···
SN2009gf	$H\gamma_F$	Fe_{5270}	$0.225^{+0.225}_{-0.225}$	$-0.183^{+0.017}_{-0.017}$	$0.690^{+0.690}_{-0.690}$	$-0.065^{+0.092}_{-0.092}$
SN2011ay	$H\gamma_F$	Fe_{5270}	$0.410^{+0.045}_{-0.045}$	$0.047^{+0.063}_{-0.063}$	$0.950^{+0.115}_{-0.115}$	$0.228^{+0.069}_{-0.069}$
Hosts of SNfactory-observed SNe						
PTF09dnp	$H\gamma_F$	Fe_{5270}	$0.267^{+0.073}_{-0.073}$	$-0.010^{+0.057}_{-0.057}$	$0.475^{+0.064}_{-0.064}$	$0.002^{+0.072}_{-0.072}$
SN2007fr	$H\gamma_F$	Fe_{5270}	$0.260^{+0.052}_{-0.052}$	$-0.085^{+0.045}_{-0.045}$	$0.705^{+0.705}_{-0.705}$	$-0.090^{+0.106}_{-0.106}$
SN2007nq	$H\gamma_F$	Fe_{5270}	$0.457^{+0.093}_{-0.093}$	$0.040^{+0.072}_{-0.072}$	$0.865^{+0.071}_{-0.071}$	$0.075^{+0.117}_{-0.117}$
SN2009hi	$H\gamma_F$	Fe_{5270}	$0.233^{+0.089}_{-0.089}$	$-0.280^{+0.032}_{-0.032}$	···	$0.000^{+0.113}_{-0.113}$
SN2009hs	$H\gamma_F$	Fe_{5270}	···	···	···	···
SNF20060521-008	$H\gamma_F$	Fe_{4383}	$0.070^{+0.033}_{-0.033}$	$-0.180^{+0.040}_{-0.040}$	$0.355^{+0.047}_{-0.047}$	$-0.055^{+0.055}_{-0.055}$
SNF20070417-002	$H\gamma_F$	Fe_{5270}	$0.483^{+0.089}_{-0.089}$	$-0.260^{+0.089}_{-0.089}$	$0.805^{+0.087}_{-0.087}$	$-0.015^{+0.104}_{-0.104}$
SNF20070727-016	$H\gamma_F$	Fe_{5270}	$0.087^{+0.058}_{-0.058}$	$-0.060^{+0.072}_{-0.072}$	$0.425^{+0.104}_{-0.104}$	$-0.090^{+0.057}_{-0.057}$
SNF20080512-010	$H\gamma_F$	Fe_{4383}	$0.000^{+0.073}_{-0.073}$	$-0.180^{+0.069}_{-0.069}$	$0.885^{+0.119}_{-0.119}$	$0.070^{+0.113}_{-0.113}$
SNF20080514-002	$H\gamma_F$	Fe_{4383}	···	···	···	···
SNF20080614-010	$H\gamma_F$	Fe_{5270}	$0.120^{+0.068}_{-0.068}$	$-0.040^{+0.072}_{-0.072}$	$0.480^{+0.064}_{-0.064}$	$-0.080^{+0.065}_{-0.065}$
SNF20080720-001	$H\gamma_F$	Fe_{4383}	$0.097^{+0.040}_{-0.040}$	$0.000^{+0.120}_{-0.120}$	$-0.075^{+0.063}_{-0.063}$	$-0.080^{+0.078}_{-0.078}$
SNF20080731-000	$H\gamma_F$	Fe_{5270}	$0.195^{+0.290}_{-0.290}$	$0.020^{+0.246}_{-0.246}$	$0.160^{+0.282}_{-0.282}$	$0.272^{+0.316}_{-0.316}$
SNF20080815-017	$H\gamma_F$	Fe_{4383}	···	$-0.010^{+0.129}_{-0.129}$	$0.485^{+0.186}_{-0.186}$	$0.165^{+0.181}_{-0.181}$
SNF20080825-010	$H\gamma_F$	Fe_{5270}	$0.180^{+0.064}_{-0.064}$	$-0.060^{+0.036}_{-0.036}$	···	$0.000^{+0.113}_{-0.113}$
SNF20080913-031	$H\gamma_F$	Fe_{4383}	$0.130^{+0.074}_{-0.074}$	$0.120^{+0.058}_{-0.058}$	$0.170^{+0.095}_{-0.095}$	$-0.040^{+0.086}_{-0.086}$
SNF20080919-000	$H\gamma_F$	Fe_{4383}	···	$-0.105^{+0.280}_{-0.280}$	$0.120^{+0.214}_{-0.214}$	$-0.045^{+0.262}_{-0.262}$
Hosts of SDSS SNe						
SN2005ex	$H\gamma_F$	Fe_{5270}	$0.298^{+0.047}_{-0.047}$	$0.120^{+0.080}_{-0.080}$	$0.075^{+0.092}_{-0.092}$	$0.040^{+0.099}_{-0.099}$
SN2005ez	$H\gamma_F$	Fe_{5270}	$0.260^{+0.086}_{-0.086}$	$0.100^{+0.144}_{-0.144}$	$0.280^{+0.131}_{-0.131}$	$0.020^{+0.127}_{-0.127}$
SN2005ff	$H\gamma_F$	Fe_{5270}	$0.053^{+0.181}_{-0.181}$	$0.080^{+0.322}_{-0.322}$	$-0.485^{+0.535}_{-0.535}$	$-0.788^{+1.107}_{-1.107}$
SN2005fh	$H\gamma_F$	Fe_{5270}	$0.030^{+0.060}_{-0.060}$	$-0.290^{+0.027}_{-0.027}$	$0.445^{+0.446}_{-0.446}$	$-0.230^{+0.326}_{-0.326}$
SN2005je	$H\gamma_F$	Fe_{4383}	···	$0.080^{+0.072}_{-0.072}$	$0.275^{+0.070}_{-0.070}$	$0.115^{+0.133}_{-0.133}$
SN2005kn	$H\gamma_F$	Fe_{5270}	$0.360^{+0.046}_{-0.046}$	$-0.107^{+0.080}_{-0.080}$	$0.435^{+0.439}_{-0.439}$	$0.010^{+0.196}_{-0.196}$
SN2005kt	$H\gamma_F$	Fe_{4383}	···	$0.235^{+0.080}_{-0.080}$	$0.130^{+0.063}_{-0.063}$	$0.063^{+0.067}_{-0.067}$
SN2006er	$H\gamma_F$	Fe_{5270}	$0.095^{+0.062}_{-0.062}$	$-0.160^{+0.057}_{-0.057}$	$0.405^{+0.085}_{-0.085}$	$-0.145^{+0.063}_{-0.063}$
SN2006fa	$H\gamma_F$	Fe_{5270}	$0.182^{+0.081}_{-0.081}$	$0.120^{+0.089}_{-0.089}$	$-0.170^{+0.134}_{-0.134}$	$-0.107^{+0.155}_{-0.155}$
SN2006jp	$H\gamma_F$	Fe_{5270}	$0.500^{+0.090}_{-0.090}$	$0.560^{+0.160}_{-0.160}$	$0.145^{+0.193}_{-0.193}$	$0.355^{+0.235}_{-0.235}$
SN2006ni	$H\gamma_F$	Fe_{5270}	$0.180^{+0.089}_{-0.089}$	$-0.060^{+0.068}_{-0.068}$	$0.440^{+0.445}_{-0.445}$	$-0.080^{+0.114}_{-0.114}$
SN2007la	$H\gamma_F$	Fe_{5270}	$0.300^{+0.090}_{-0.090}$	$-0.230^{+0.089}_{-0.089}$	$0.845^{+0.092}_{-0.092}$	$-0.020^{+0.113}_{-0.113}$
SN2007or	$H\gamma_F$	Fe_{5270}	$0.200^{+0.055}_{-0.055}$	$0.080^{+0.072}_{-0.072}$	$0.145^{+0.095}_{-0.095}$	$-0.057^{+0.114}_{-0.114}$
SN2007ph	$H\delta_F$	Fe_{5270}	$0.340^{+0.072}_{-0.072}$	$-0.180^{+0.074}_{-0.074}$	$0.655^{+0.657}_{-0.657}$	$-0.008^{+0.077}_{-0.077}$

The Balmer Index and Fe Index columns indicate which indices were used by EZ_AGES to determine the age and $[Fe/H]$ of each galaxy.

CHAPTER 14

SN – Host Correlations

While light curve shape and color (and host mass) effectively control for much of the variation observed in SN Ia peak brightnesses, a $\sim 15\%$ scatter in SN Ia Hubble residuals still remains after these corrections are applied. In this chapter we investigate what host measurements of progenitor population age, metallicity, and particular element abundances reveal about the nature of the empirical corrections applied to SNe Ia and the remaining scatter about the Hubble diagram.

Correlations between SN properties and host properties have generally been characterized in the literature by fitting straight lines to scatter plots. We follow this precedent here, though note that care must be taken to properly handle observational uncertainties. For instance, the uncertainties in the Hubble residuals studied here do not directly include the $\sim 15\%$ intrinsic scatter required to make their reduced χ^2 equal to one. Instead, we characterize the strengths of the correlations (including those with x_1 and c in addition to Hubble residuals) using a model that incorporates intrinsic scatter as one of its terms. Adding the scatter before fitting inhibits the abscissa from explaining as much scatter in the ordinate as might otherwise be possible. On the other hand, failure to include such a term will in general bias the resulting intercept and slope inferences and distort their confidence regions. Following Kelly et al. (2010) and D'Andrea et al. (2011) we use the Bayesian inference tool LINMIX (Kelly 2007), and report the significance of correlations both by the number of standard deviations by which the median fit slope differs from zero and by the posterior probability that the slope has the sign opposite from the that of the median.

14.1 Age and $[\mathrm{Fe/H}]$

Most of the variation in the stellar component of early-type galaxies can be attributed to the age and metallicity of the underlying stellar populations. Indeed, existing studies of correlations between SN Ia properties and early-type progenitor parameters are limited to these two properties. Hence, we start our analysis by looking at SN Ia properties as functions of their hosts' $[\mathrm{Fe/H}]$ and the log of their ages.

The strongest correlation between any SN Ia property and host galaxy property in our

sample is that of the SALT2.2 SN light curve shape parameter x_1 with the log of the host galaxy age; older hosts produce more rapid SNe Ia (Figure 14.1, upper left). The significance of this trend is 3.5σ using all available data. One SN, SN2005fh, appears to be an outlier on this plot and also an outlier on the plot of x_1 vs $[\mathrm{C/Fe}]$ discussed below. We re-examined the host spectrum and photometry of this object but were unable to find anything to suggest a failure of either the host parameter estimation or the light curve parameter estimation. The occurrence of an outlier in this study is not particularly alarming, however, since we are attempting to infer the properties of one star, the SN progenitor, from the integrated light of many stars within the spectroscopic aperture. If we remove SN2005fh from the log age – x_1 fit, the significance improves dramatically to 4.7σ. Because the difference when ignoring SN2005fh is so large, we will exclude it from further analysis except when specifically noted, though we present results both including and excluding this SN in Tables 14.1 and 14.2. Since x_1 is a proxy for SN peak brightness, the correlation we observe between host galaxy age and x_1 essentially reproduces the strong trend discovered by G08 between host age and SN Ia peak M_V. We also see a tantalizing trend between x_1 and $[\mathrm{Fe/H}]$ (Figure 14.1, upper right), with a significance of 1.8σ, analogous to the trend reported in G08 between total host metallicity $[\mathrm{M/H}]$ and M_V.

The early-type hosts targeted by this study should, to first order, contain at most small amounts of dust making measurements of SN color potentially interesting as they likely reflect intrinsic or possibly circumstellar effects. The fact that the SNe hosted by galaxies with traces of star-formation have no discernible difference in their colors compared to SNe hosted by galaxies with no emission or LINER-like emission supports this view. We find a 1.7σ correlation between the host galaxy $[\mathrm{Fe/H}]$ and SN color, but no correlation with host age. The change in color with metallicity may be related to the relative importance of iron absorption lines in the B and V parts of the SN spectrum at maximum light (Domínguez et al. 2001).

Host parameters affecting x_1 and color are important for understanding the underlying physics of SNe Ia, but host parameters affecting Hubble residuals are more likely to impact cosmological measurements. The apparent trend between Hubble residuals and the mass or specific star-formation rates of their host galaxies was part of the motivation for the present study. Two of the most probable candidates for the source of this bigger–brighter relation are progenitor age and $[\mathrm{Fe/H}]$, as these both correlate with galaxy mass and specific star-formation rates. However, we find no significant evidence in our sample that either host variable affects SN Hubble residuals (Figure 14.1 bottom). In fact, there is weak evidence (1.1σ), that older progenitor environments produce *fainter* SNe Ia; opposite what might be inferred from host mass. These results stand in stark contrast to those obtained by G08, who report a 98% probability that SN Ia Hubble residuals are larger for SNe hosted by higher metallicity hosts (i.e. in the opposite direction from what would be required to explain the bigger-brighter relation). Part of this discrepancy is due to their use of a correlation statistic that does not incorporate the intrinsic dispersion into the fit model. Reanalyzing the G08 data with LINMIX, for example, we find that their reported probability should only be 82%. One possible explanation for not discovering a correlation with Hubble residuals is that by

selecting early-type hosts, we are only selecting massive and low specific star-formation rate galaxies, and hence are suffering from a loss of dynamic range in the pertinent abscissae. We note, however, that the x_1 trend with age is strongly detected above, suggesting that our dynamic range in age is in fact sufficient for discoveries. Our range in $[\mathrm{Fe/H}]$ is somewhat smaller, though still sufficient to hint at trends with x_1 and SN color.

14.2 Individual element abundances

Although age and metallicity explain most of the variation in early-type galaxy spectra, variations in the abundances of other metals, such as Mg, C, N, and Ca, have also been observed in high signal-to-noise ratio spectroscopy. It is natural to ask then, what correlations might exist between SNe Ia and these other galaxy parameters. Figures 14.2, 14.3, and 14.4 explore trends in the enhancement of these metals with x_1, color and Hubble residuals. The slopes and significances of correlations are reported in Table 14.2. We find that x_1 is correlated with $[\mathrm{N/Fe}]$ (at 2.7σ) and $[\mathrm{C/Fe}]$ (at 2.5σ), though the latter correlation is weakened considerably if SN2005fh is included. SN color also correlates with host $[\mathrm{N/Fe}]$ at 2.4σ. Finally, SN Hubble residuals are correlated with host $[\mathrm{C/Fe}]$, but this appears to be due to a single data point which is an extremum in both the distributions of Hubble residuals and host $[\mathrm{C/Fe}]$.

We note that since we had no previous expectations for trends between SN properties and particular metal abundances of SN hosts from published studies, the strengths of these correlations must be de-weighted due to the "look elsewhere" effect. For example, the probability of observing an event which has a single trial probability of 0.34% (e.g. the probability that the correlation between x_1 and $[\mathrm{C/Fe}]$ is a false positive) at least once in 12 trials (the size of our "fishing expedition") is $100\% - (100\% - 0.34\%)^{12} = 4.00\%$, or about 1.7σ. Similarly, the significances for the trends of x_1 vs $[\mathrm{N/Fe}]$, color vs $[\mathrm{N/Fe}]$, and Hubble residual vs. $[\mathrm{C/Fe}]$ are diluted to 1.4σ, 1.1σ, and 0.0σ, respectively.

It is interesting to ask if the individual metal enhancement correlations we have found are independent of the stronger correlations with age or $[\mathrm{Fe/H}]$, or if they contain only redundant information. To test this, we have fit the residuals from the strongest observed correlation, that of x_1 vs age, against the remaining host parameters: $[\mathrm{Fe/H}]$, $[\mathrm{C/Fe}]$, and $[\mathrm{N/Fe}]$. In each case, the correlation disappears, confirming that the host metal abundances contain no additional information not present in the host age. Similarly, SN color residuals from the color – $[\mathrm{Fe/H}]$ relation do not correlate with $[\mathrm{N/Fe}]$.

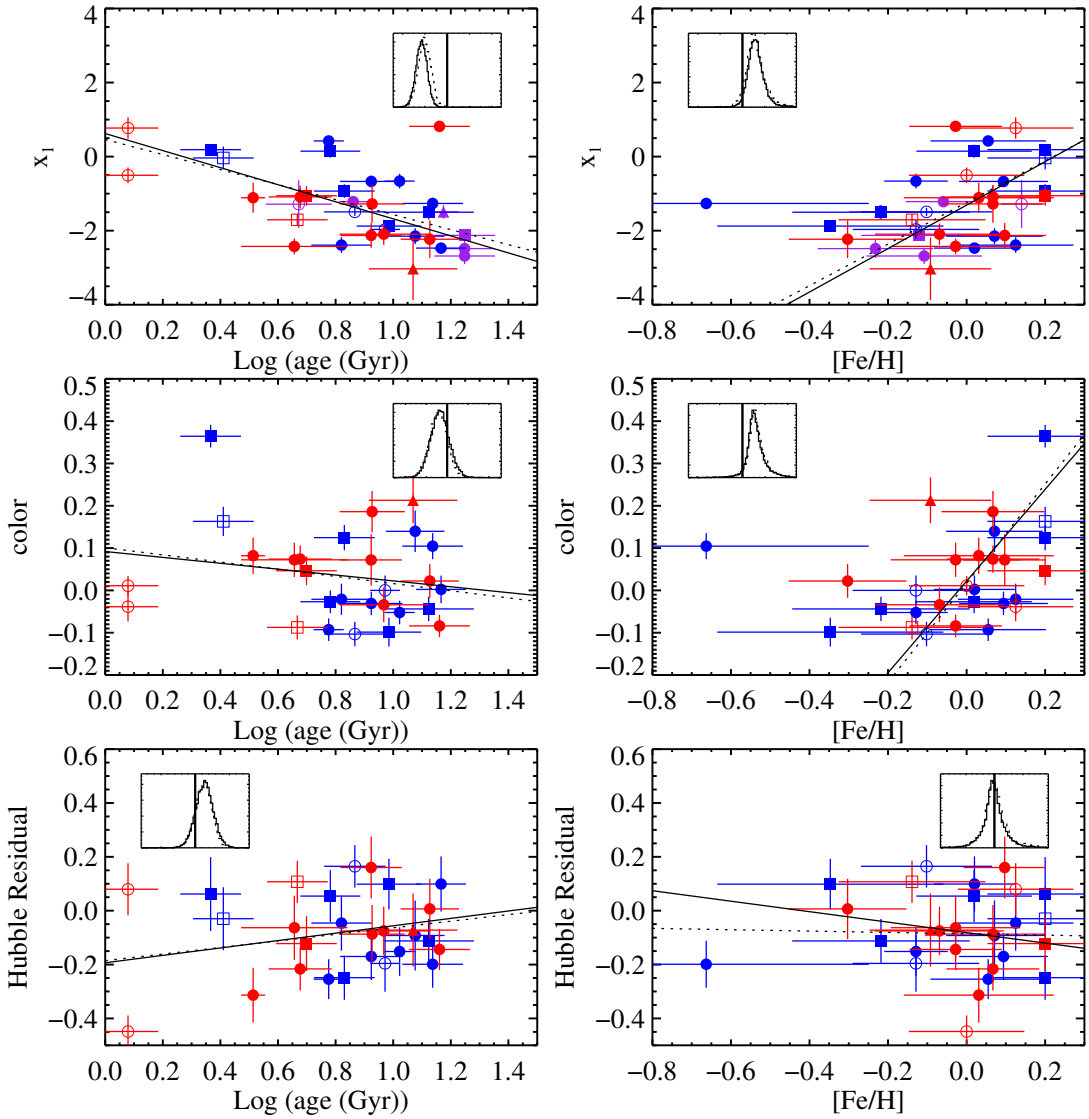

Figure 14.1.
Host galaxy logarithmic age (left column) and [Fe/H] (right column) plotted against the SALT2.2 SN light curve shape parameter x_1 (top row), light curve color parameter (middle row), and Hubble residual (bottom row). All panels share the following characteristics: Colors indicate the source of the SN photometry with purple indicating *Swift*, blue indicating SNfactory, and red indicating SDSS-II. Symbols indicate the choice of Lick indices used to fit the host age and [Fe/H]: circles indicate $H\gamma_F$ and Fe_{5270}, squares indicate $H\gamma_F$ and Fe_{4383}, and triangles indicate $H\delta_F$ and Fe_{5270}. Filled symbols indicate hosts with no emission or LINER-like emission, while open symbols indicate hosts with star-formation-like emission. The solid (dashed) line indicates the best fit linear regression excluding (including) the outlier SN2005fh. The inset solid (dashed) histogram shows the posterior probability distribution for the slope of the linear regression excluding (including) the outlier SN2005fh. In the inset, a vertical line is shown at zero slope.

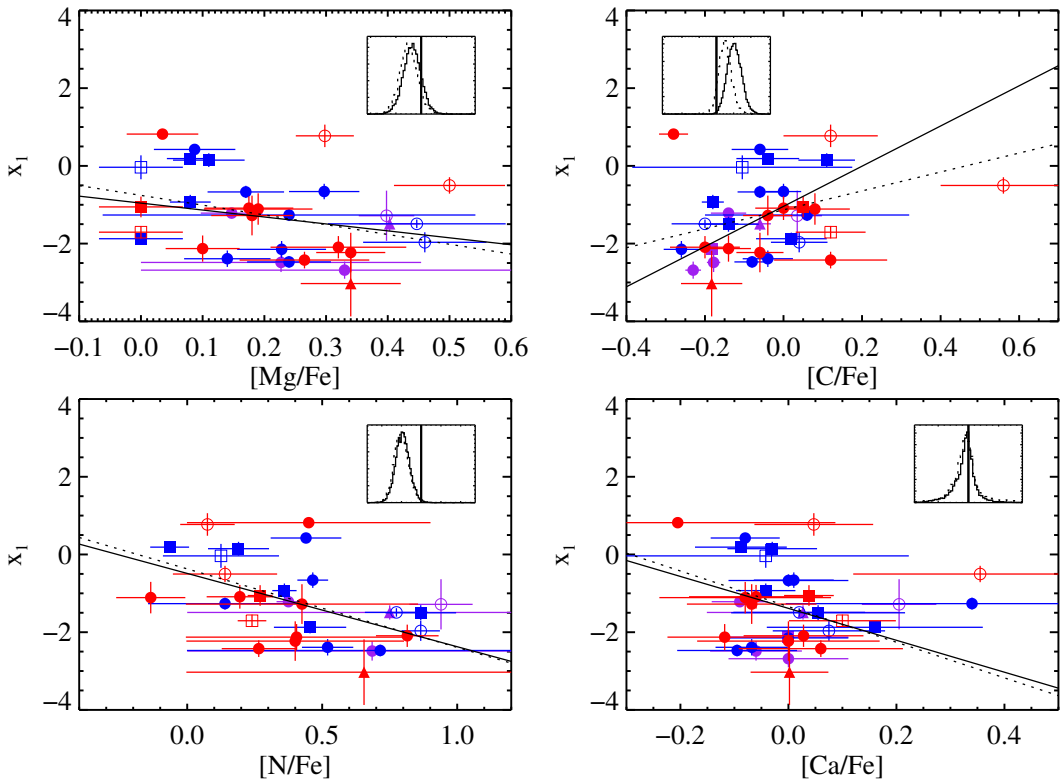

Figure 14.2. SALT2.2 x_1 parameter plotted against host galaxy metal abundances: $[\mathrm{Mg/Fe}]$, $[\mathrm{C/Fe}]$, $[\mathrm{N/Fe}]$, and $[\mathrm{Ca/Fe}]$. The symbols and the inset carry the same meaning as in Figure 14.1.

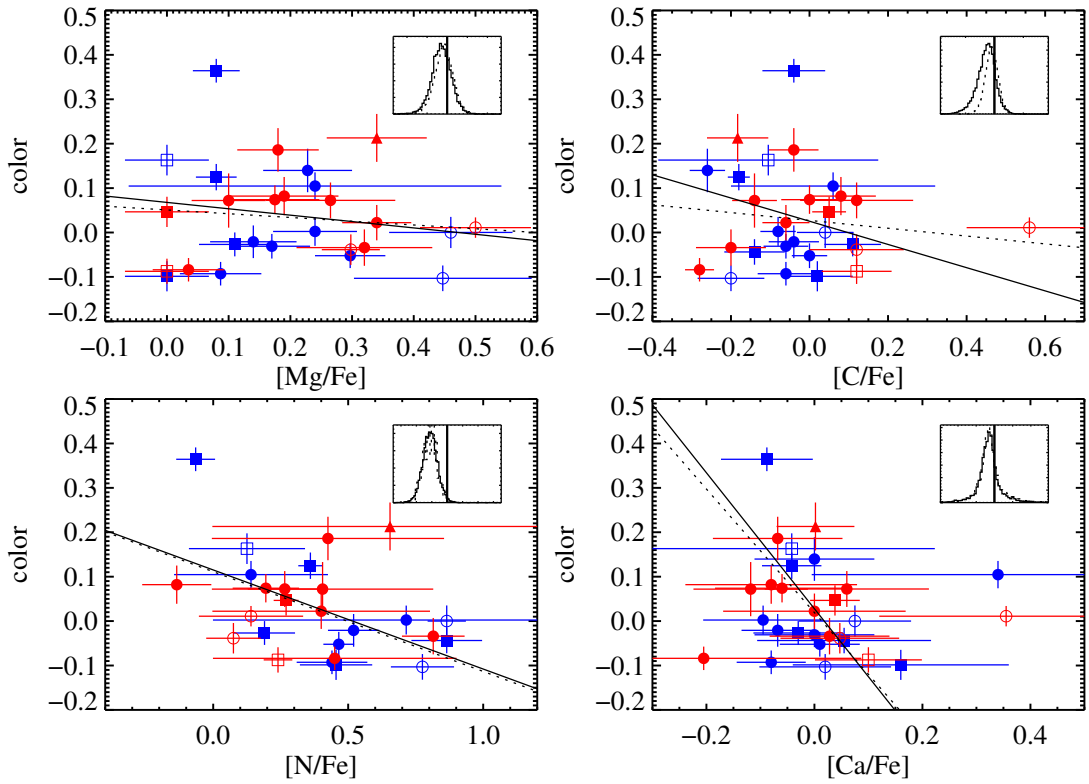

Figure 14.3. The SALT2.2 color parameter plotted against host galaxy metal abundances: [Mg/Fe], [C/Fe], [N/Fe], and [Ca/Fe]. The symbols and the inset carry the same meaning as in Figure 14.1.

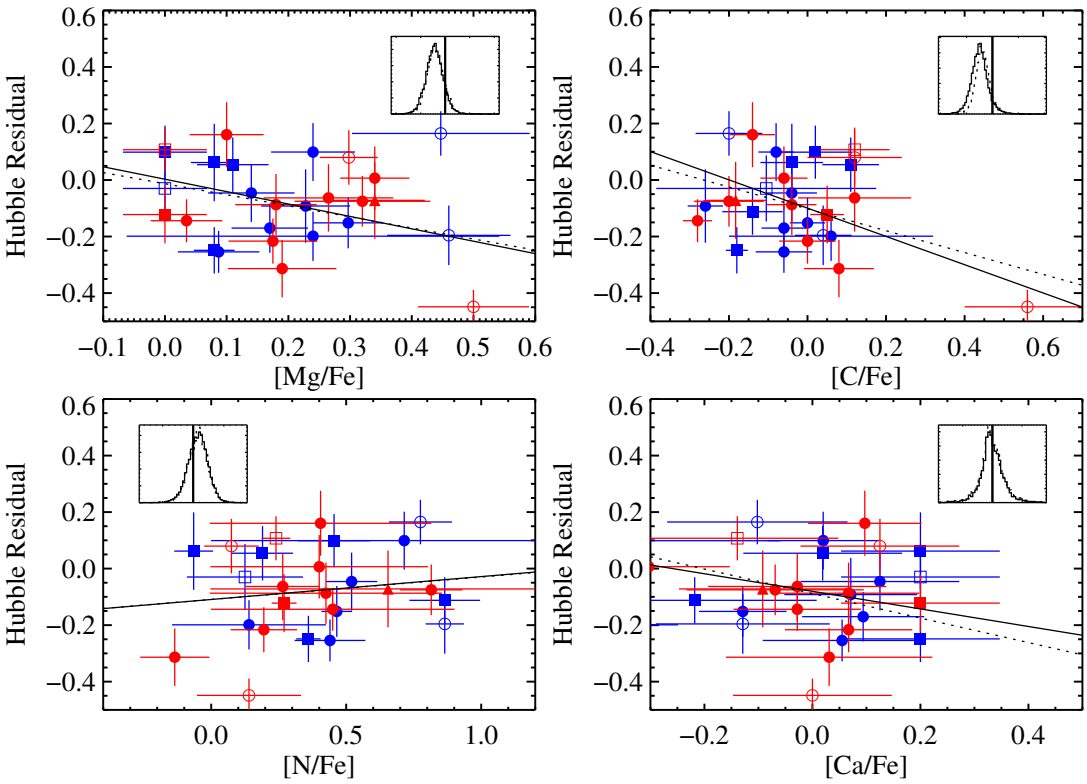

Figure 14.4. SN Hubble residuals plotted against host galaxy metal abundances: [Mg/Fe], [C/Fe], [N/Fe], and [Ca/Fe]. The symbols and the inset carry the same meaning as in Figure 14.1.

Table 14.1. Fits to Age and $[\mathrm{Fe/H}]$

Ordinate	Abscissa	slope	P(sign flip)
Fits including SN2005fh			
x_1	log(age)	-2.028 (3.5σ)	0.00125
x_1	$[\mathrm{Fe/H}]$	5.618 (1.5σ)	0.06380
color	log(age)	-0.085 (1.0σ)	0.15355
color	$[\mathrm{Fe/H}]$	1.171 (1.8σ)	0.03723
HR	log(age)	0.122 (1.0σ)	0.15677
HR	$[\mathrm{Fe/H}]$	-0.025 (0.0σ)	0.49335
Fits excluding SN2005fh			
x_1	log(age)	-2.302 (4.7σ)	0.00000
x_1	$[\mathrm{Fe/H}]$	5.868 (1.8σ)	0.03228
color	log(age)	-0.069 (0.8σ)	0.21407
color	$[\mathrm{Fe/H}]$	1.083 (1.7σ)	0.04610
HR	log(age)	0.137 (1.1σ)	0.14702
HR	$[\mathrm{Fe/H}]$	-0.194 (0.1σ)	0.44590

The slope column indicates both the median slope of the posterior distribution returned by LINFIT and, in parentheses, the significance computed as the median slope divided by half the range of the smallest interval containing 68% of the posterior probability.

Table 14.2. Fits to Metal Enhancements

Ordinate	Abscissa	slope	P(sign flip)
Fits including SN2005fh			
x_1	[Mg/Fe]	-2.514 (1.4σ)	0.07740
x_1	[C/Fe]	2.437 (1.3σ)	0.08672
x_1	[N/Fe]	-2.020 (2.8σ)	0.00955
x_1	[Ca/Fe]	-4.582 (0.3σ)	0.36757
color	[Mg/Fe]	-0.084 (0.4σ)	0.34767
color	[C/Fe]	-0.088 (0.4σ)	0.34385
color	[N/Fe]	-0.225 (2.5σ)	0.01300
color	[Ca/Fe]	-1.391 (0.6σ)	0.26830
HR	[Mg/Fe]	-0.391 (1.2σ)	0.13000
HR	[C/Fe]	-0.386 (1.5σ)	0.09185
HR	[N/Fe]	0.080 (0.5σ)	0.30905
HR	[Ca/Fe]	-0.434 (0.1σ)	0.44750
Fits excluding SN2005fh			
x_1	[Mg/Fe]	-1.786 (1.0σ)	0.15163
x_1	[C/Fe]	5.173 (2.5σ)	0.00340
x_1	[N/Fe]	-1.885 (2.7σ)	0.00708
x_1	[Ca/Fe]	-4.104 (0.3σ)	0.34910
color	[Mg/Fe]	-0.144 (0.6σ)	0.27138
color	[C/Fe]	-0.261 (0.9σ)	0.16387
color	[N/Fe]	-0.223 (2.4σ)	0.01155
color	[Ca/Fe]	-1.531 (0.7σ)	0.23022
HR	[Mg/Fe]	-0.439 (1.3σ)	0.10430
HR	[C/Fe]	-0.500 (1.7σ)	0.06768
HR	[N/Fe]	0.081 (0.5σ)	0.30867
HR	[Ca/Fe]	-0.311 (0.1σ)	0.46288

The slope column indicates both the median slope of the posterior distribution returned by LINFIT and, in parentheses, the significance computed as the median slope divided by half the range of the smallest interval containing 68% of the posterior probability.

CHAPTER 15

Discussion

In this analysis we have investigated correlations between SN Ia light curve properties and spectroscopically derived properties of early-type host galaxies. We confirm the results of earlier studies that show that the age of the host galaxy is strongly correlated with the decline rate of the SN, characterized here by the SALT2.2 variable x_1. Additionally, we show that $[\mathrm{Fe/H}]$, $[\mathrm{C/Fe}]$, and $[\mathrm{N/Fe}]$ are also correlated with x_1 to varying degrees, but none in a way that is independent of the stronger age correlation. In contrast to studies of mixed-host-type samples of SNe Ia, we do not find any correlation of host properties with SN Hubble residuals.

15.1 x_1 correlations

Several theoretical attempts to explain the diversity of SN Ia light curve rise and fall times (i.e. x_1) and absolute magnitudes are potentially relevant to our findings. First, Umeda et al. (1999) have computed that the carbon mass fraction $X(C)$ is smaller in C/O white dwarfs that form in lower metallicity or older environments. They further show that smaller $X(C)$ progenitors lead to less luminous SNe Ia. Since x_1 is a good proxy for peak luminosity, our results support both implied trends: x_1 appears to decrease with increased age and with decreased $[\mathrm{Fe/H}]$ metallicity.

In contrast, other authors have predicted that lower metallicity progenitors should lead to the production of more light-curve-powering $^{56}\mathrm{Ni}$, and hence brighter SNe Ia (Höflich et al. 1998; Timmes et al. 2003). The most abundant metals in the atmosphere of a SN Ia progenitor during its main sequence evolutionary phase are CNO and Fe. By the end of the helium-burning phase, the CNO are transformed into the neutron-enhanced species $^{22}\mathrm{Ne}$. This, together with the neutron-enriched $^{56}\mathrm{Fe}$ present since the progenitor's formation, set the neutronization of the white dwarf, and ultimately, set the neutronization of the SN Ia explosion products (weak interactions are slower than the time scale to disrupt the white dwarf (Brachwitz et al. 2000)). Since $^{56}\mathrm{Ni}$ is neutron-deficient compared to other iron-peak explosion products, less of it is produced by the explosion of a neutron-enhanced white dwarf progenitor.

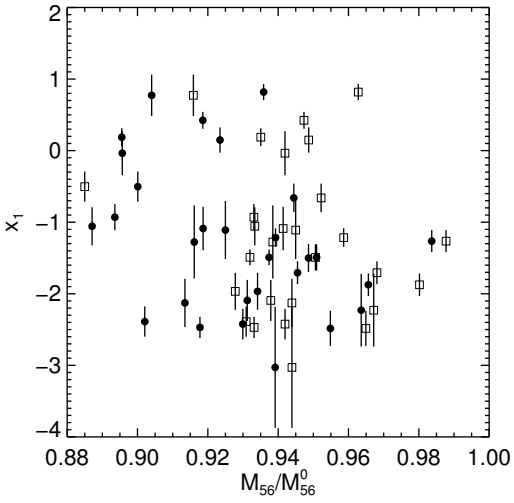

Figure 15.1. The SALT2.2 variable x_1 vs. the expected mass of ^{56}Ni assuming the neutronization effect of CNO and Fe detailed in Timmes et al. (2003) and Howell et al. (2009). Oxygen abundances required for the ^{56}Ni estimate are not directly measured, but are derived from the $[\mathrm{O/Fe}]$ – $[\mathrm{Fe/H}]$ relation for halo stars published by Ramírez et al. (2007) (filled circles) or by setting $[\mathrm{O/Fe}]$=$[\mathrm{Mg/Fe}]$(open squares).

We have direct measurements of three (C, N, and Fe) of the four elements responsible for the predicted neutronization of the progenitor white dwarf. Unfortunately, the most abundant of the four elements, oxygen, is notoriously difficult to measure in stellar atmospheres due to a lack of uncontaminated absorption lines. We investigate two indirect approaches to estimating the abundance of oxygen. The first is to assume that oxygen, as an α element, tracks the enhancement of the measurable α element Mg (i.e. $[\mathrm{Mg/Fe}]$=$[\mathrm{O/Fe}]$). The second, following Howell et al. (2009), is to use a relation between $[\mathrm{O/Fe}]$ and $[\mathrm{Fe/H}]$, such as that for halo stars presented by Ramírez et al. (2007). Figure 15.1 shows the resulting scatter plots of x_1 against the predicted mass of ^{56}Ni synthesized by the explosion under both oxygen estimation approaches. There is no obvious trend in either case, implying that the progenitor metallicity–neutronization effect as predicted by Höflich et al. (1998); Timmes et al. (2003) is not the dominant source of x_1 diversity, at least for passively hosted SNe Ia. A similar result was reached by Howell et al. (2009) who studied SNLS hosts using photometrically derived $[\mathrm{Fe/H}]$ and various scaling relations for CNO abundances.

15.2 Hubble residual correlations

In contrast to multiple mixed host type SN Ia correlation studies (Kelly et al. 2010; Lampeitl et al. 2010; Sullivan et al. 2010; D'Andrea et al. 2011; Gupta et al. 2011), we see no significant relations between galaxy variables and the Hubble residuals of the SNe Ia they host. It is natural to ask if our measurements are sensitive enough to have seen a correlation assuming one exists. If we split the range of log age that our sample probes approximately in half at $\log(\mathrm{age(Gyr)}) = 0.7$, we create two bins, one of 9 young hosts and another of 19 old hosts. The weighted mean Hubble residuals are -0.11 ± 0.03 for the SNe with young hosts and -0.07 ± 0.02 for the SNe with old hosts. As the size of the

Hubble residual step when analyzed against host mass or specific star formation rate (~ 0.1 mag) is 3-5 times larger than our binned Hubble residual uncertainties, it is doubtful that we have missed a correlation large enough to explain the bigger–brighter relation.

Trends with metallicity are more difficult to measure in our data set, as most hosts occupy a small region only about 0.3 dex wide, and are only separated from each other by a few σ. In contrast, the mixed-host gas-phase metallicities probed by D'Andrea et al. (2011) span almost 1.0 dex. Extending the metallicity range covered below our lowest metallicity (~ -0.2) would be helpful but is a nontrivial task. Early-type galaxies with smaller metallicities certainly exist, (dwarf ellipticals and dwarf spheroidals in the local group and Virgo clusters span a range of -2.0 to -0.5 in $[\mathrm{Fe/H}]$(Da Costa, G. S. et al. 1998; Jerjen et al. 2004)), but their orders of magnitude smaller masses compared to the galaxies probed here imply orders of magnitude smaller rates of SNe Ia and also a greatly restricted volume in which suitable spectroscopy can be obtained. If we are fortunate enough to discover a SN Ia in a small elliptical galaxy, spectroscopy of its host should be a top priority.

Our expectation that the same underlying mechanism responsible for the bigger–brighter relation observed in mixed host samples should also apply to early-type galaxies is complicated by the fact that early-type galaxies mostly occupy only the most massive end of the galaxy mass function and also only span a limited range in specific star formation rates. The mixed-host samples probed by Sullivan et al. (2010) and Lampeitl et al. (2010), for example, span ~ 2 dex in stellar mass, and the sample probed by Kelly et al. (2010) spans ~ 2 dex, where our early-type hosts only probe the top ~ 1 dex of stellar mass. Nevertheless, the range of stellar mass probed should be secondary to the range of host parameters probed. It would be unsatisfactory, for example, to invoke progenitor age or metallicity to explain differences in the Hubble residuals of SNe Ia hosted by galaxies with different masses, but for the same variable to not have an effect at fixed host mass.

The ability to reveal the underlying physics of the bigger–brighter relation may depend on the nature of the effect. For instance, the effect may be due to the addition of a second class of SN Ia associated with high mass or low specific star-formation rate galaxies. If this second class of SN Ia has a different average absolute peak magnitude, then its presence in high host mass galaxies would shift the SN Ia peak absolute magnitude when averaged over all SNe Ia in these galaxies, producing an effect similar to what has been observed. Such a two-class scenario for SNe Ia has, in fact, already been proposed to explain the apparent bimodality of SN Ia rates (Mannucci et al. 2005; Scannapieco & Bildsten 2005), and could also be related to the two proposed classes of SN Ia progenitor systems (single degenerate and double degenerate). Under this scenario, differences in host ages or metallicity at fixed host mass could show up as discernible differences in the Hubble residuals. The fact that we do not see any trends with Hubble residuals could be viewed as evidence against the existence of an additional class of SN Ia at high host mass.

CHAPTER 16

Epilogue

This thesis has described several ways in which photometric, morphological and spectroscopic observations of SN Ia host galaxies may be used to improve cosmological measurements using Type Ia SNe. It is shown that such observations can help classify SNe as Type Ia, guard against the deleterious effects of dust, identify particularly well characterized host environments, and clarify the relationships between SN Ia diversity and progenitor diversity.

The deep host images to be generated by imminent and future massive SN surveys such as the Dark Energy Survey, Hyper-Suprime Cam, and the Large Synoptic Survey Telescope, will be well suited to take advantage of the photometric studies investigated here. For example, these surveys will discover many times more SNe than can be classified spectroscopically, so typing by host (Chapter 7) will become increasingly important. Dust-free SNe (Chapter 8) spanning the redshift interval from zero to above one should become common. The large redshift intervals spanned by these surveys will also lead to increased tests for the evolution of SN demographics (Chapter 9).

Spectroscopic studies will similarly benefit from future large aperture telescopes such as the Thirty Meter Telescope, the European Extremely Large Telescope, and the Giant Magellan Telescope. These facilities will extend high signal-to-noise ratio spectroscopy of SN hosts (Part II) to higher redshifts and fainter hosts, the latter of which may be particularly important to unraveling the physics underlying the bigger-brighter relation (Chapter 14).

These advances and those of other cosmological probes will continue to shed light on the nature of dark energy. With orders of magnitude more data, some existing questions may be answered, but what is almost certain is that new questions will arise. After all, dark energy itself was a question more or less unanticipated at the time the initial distant SN Ia measurements were being made $\sim 15-20$ years ago. In this short time, our understanding of the Universe has increased dramatically, as it had done before since the time of Shapley and Curtis, and had done numerous times before that. It is intriguing to ponder what we will think of the 2012 model of the Universe $\sim 15-20$ or a hundred years from now.

Bibliography

Abraham, R. G., et al. 2007, ApJ, 669, 184

Abraham, R. G., et al. 1996, ApJS, 107, 1

Abraham, R. G., van den Bergh, S., & Nair, P. 2003, ApJ, 588, 218

Agol, E., et al. 2011, submitted

Aldering, G., et al. 2002, in Presented at the Society of Photo-Optical Instrumentation Engineers (SPIE) Conference, Vol. 4836, Survey and Other Telescope Technologies and Discoveries. Edited by Tyson, J. Anthony; Wolff, Sidney. Proceedings of the SPIE, Volume 4836, pp. 61-72 (2002)., ed. J. A. Tyson & S. Wolff, 61–72

Aldering, G., et al. 2006, ApJ, 650, 510

Amanullah, R., et al. 2010, ApJ, 716, 712

Andreon, S., et al. 2008, MNRAS, 385, 979

Andreon, S., Punzi, G., & Grado, A. 2005, MNRAS, 360, 727

Appenzeller, I., et al. 1998, The Messenger, 94, 1

Astier, P., et al. 2006, A&A, 447, 31

Athey, A., et al. 2002, ApJ, 571, 272

Baade, W. 1938, ApJ, 88, 285

Bailey, S., et al. 2009, A&A, 500, L17

Baldwin, J. A., Phillips, M. M., & Terlevich, R. 1981, PASP, 93, 5

Barbary, K., et al. 2012a, ApJ, 745, 32

—. 2012b, ApJ, 745, 31

Barbary, K., et al. 2009, ApJ, 690, 1358

Bazin, G., et al. 2009, A&A, 499, 653

Bertin, E. & Arnouts, S. 1996, A&AS, 117, 393

Bessell, M. S. 1990, PASP, 102, 1181

Blakeslee, J. P., et al. 2003a, ApJ, 596, L143

Blakeslee, J. P., et al. 2003b, ApJ, 589, 693

Bower, R. G., Lucey, J. R., & Ellis, R. S. 1992, MNRAS, 254, 601

Brachwitz, F., et al. 2000, ApJ, 536, 934

Breeveld, A. A., et al. 2011, in American Institute of Physics Conference Series, Vol. 1358, American Institute of Physics Conference Series, ed. J. E. McEnery, J. L. Racusin, & N. Gehrels, 373–376

Bremer, M. N., et al. 2006, MNRAS, 371, 1427

Brodwin, M., et al. 2006, ApJ, 651, 791

Brodwin, M., et al. 2011, ApJ, 732, 33

Brown, P. J. et al. 2013, in prep

Bruzual, G. & Charlot, S. 2003, MNRAS, 344, 1000

Buton, C., et al. 2012, ArXiv e-prints

Caon, N., Macchetto, D., & Pastoriza, M. 2000, ApJS, 127, 39

Cappellari, M. & Emsellem, E. 2004, PASP, 116, 138

Cardelli, J. A., Clayton, G. C., & Mathis, J. S. 1989, ApJ, 345, 245

Cardiel, N., et al. 1998, A&AS, 127, 597

Cenarro, A. J., et al. 2007, MNRAS, 374, 664

Cepa, J., et al. 2000, in Society of Photo-Optical Instrumentation Engineers (SPIE) Conference Series, Vol. 4008, Society of Photo-Optical Instrumentation Engineers (SPIE) Conference Series, ed. M. Iye & A. F. Moorwood, 623–631

Cepa, J., et al. 2003, in Society of Photo-Optical Instrumentation Engineers (SPIE) Conference Series, Vol. 4841, Society of Photo-Optical Instrumentation Engineers (SPIE) Conference Series, ed. M. Iye & A. F. M. Moorwood, 1739–1749

Chabrier, G. 2003, PASP, 115, 763

Chotard, N., et al. 2011, A&A, 529, L4

Clemens, M. S., et al. 2010, A&A, 518, L50+

Conley, A., et al. 2007, ApJ, 664, L13

Conley, A., et al. 2008, ApJ, 681, 482

Da Costa, G. S. et al. 1998, in VIII Canary Islands Winter School of Astrophysics, ed. A. Aparicia, A. Herrerro, & F. Sanchez, Canary Islands Winter School of Astrophysics, 351

D'Andrea, C. B., et al. 2011, ApJ, 743, 172

Davies, J. I., et al. 2011, ArXiv e-prints

Dawson, K. S., et al. 2009, AJ, 138, 1271

Demarco, R., et al. 2007, ApJ, 663, 164

Domínguez, I., Höflich, P., & Straniero, O. 2001, ApJ, 557, 279

Donas, J., et al. 2007, ApJS, 173, 597

Dressler, A. & Gunn, J. E. 1983, ApJ, 270, 7

—. 1992, ApJS, 78, 1

Dunkley, J., et al. 2005, MNRAS, 356, 925

Dunkley, J., et al. 2009, ApJS, 180, 306

Eisenhardt, P. R. M., et al. 2008, ApJ, 684, 905

Eisenstein, D. J., et al. 2005, ApJ, 633, 560

Ellis, R. S., et al. 1997, ApJ, 483, 582

Faber, S. M., et al. 2003, in Society of Photo-Optical Instrumentation Engineers (SPIE) Conference Series, Vol. 4841, Society of Photo-Optical Instrumentation Engineers (SPIE) Conference Series, ed. M. Iye & A. F. M. Moorwood, 1657–1669

Faber, S. M., et al. 1989, ApJS, 69, 763

Ferguson, H. C. 1993, MNRAS, 263, 343

Ferrarese, L., et al. 2006, ApJS, 164, 334

Fioc, M. & Rocca-Volmerange, B. 1997, A&A, 326, 950

—. 1999, ArXiv Astrophysics e-prints

Frieman, J. A., et al. 2008, AJ, 135, 338

Fruchter, A. S. & Hook, R. N. 2002, PASP, 114, 144

Förster, F. & Schawinski, K. 2008, MNRAS, 388, L74

Gallagher, J. S., et al. 2005, ApJ, 634, 210

Gallagher, J. S., et al. 2008, ApJ, 685, 752

Gallazzi, A., et al. 2006, MNRAS, 370, 1106

Gehrels, N., et al. 2004, ApJ, 611, 1005

Giavalisco, M., et al. 2004, ApJ, 600, L93

Gilbank, D. G., et al. 2010, MNRAS, 405, 2594

Gilliland, R. L., Nugent, P. E., & Phillips, M. M. 1999, ApJ, 521, 30

Gladders, M. D., et al. 1998, ApJ, 501, 571

Gladders, M. D. & Yee, H. K. C. 2000, AJ, 120, 2148

Goudfrooij, P. & de Jong, T. 1995, A&A, 298, 784

Goudfrooij, P., et al. 1994, A&AS, 105, 341

Graves, G. J. & Faber, S. M. 2010, ApJ, 717, 803

Graves, G. J., et al. 2007, ApJ, 671, 243

Graves, G. J. & Schiavon, R. P. 2008, ApJS, 177, 446

Gupta, R. R., et al. 2011, ApJ, 740, 92

Guy, J., et al. 2007, A&A, 466, 11

Hakobyan, A. A., et al. 2008, A&A, 488, 523

Hamuy, M., et al. 1996, AJ, 112, 2391

Hanuschik, R. W. 2003, A&A, 407, 1157

Häussler, B., et al. 2007, ApJS, 172, 615

Hicken, M., et al. 2009, ApJ, 700, 1097

Hilton, M., et al. 2007, ApJ, 670, 1000

Hilton, M., et al. 2009, ApJ, 697, 436

Holtzman, J. A., et al. 2008, AJ, 136, 2306

Hopkins, A. M. & Beacom, J. F. 2006, ApJ, 651, 142

Houck, J. R., et al. 2005, ApJ, 622, L105

Howell, D. A., et al. 2009, ApJ, 691, 661

Hsiao, E. Y., et al. 2007, ApJ, 663, 1187

Hsiao, E. Y., et al. 2011, in The 2010 HST Calibration Workshop, ed. S. Deustua, C. Oliveira

Huang, X., et al. 2009, ApJ, 707, L12

Höflich, P., Wheeler, J. C., & Thielemann, F. K. 1998, ApJ, 495, 617

Jaffé, Y. L., et al. 2011, MNRAS, 410, 280

Jee, M. J., et al. 2011, arXiv:1105.3186

Jee, M. J., et al. 2009, ApJ, 704, 672

Jerjen, H., Binggeli, B., & Barazza, F. D. 2004, AJ, 127, 771

Jha, S., Riess, A. G., & Kirshner, R. P. 2007, ApJ, 659, 122

Jones, A. P., Tielens, A. G. G. M., & Hollenbach, D. J. 1996, ApJ, 469, 740

Kaneda, H., et al. 2007, PASJ, 59, 107

Kasen, D., Röpke, F. K., & Woosley, S. E. 2009, Nature, 460, 869

Kashikawa, N., et al. 2002, PASJ, 54, 819

Kauffmann, G. & Charlot, S. 1998, MNRAS, 294, 705

Kaviraj, S., et al. 2008, MNRAS, 388, 67

Kaviraj, S., et al. 2007, ApJS, 173, 619

Kaviraj, S., et al. 2011, ArXiv e-prints

Kawabata, K. S., et al. 2010, Nature, 465, 326

Kelly, B. C. 2007, ApJ, 665, 1489

Kelly, P. L., et al. 2010, ApJ, 715, 743

Kennicutt, Jr., R. C. 1998, ARA&A, 36, 189

Knapp, G. R., et al. 1989, ApJS, 70, 329

Kodama, T. 1997, PhD thesis, PhD thesis, Institute of Astronomy, Univ. Tokyo , (1997)

Kodama, T. & Arimoto, N. 1997, A&A, 320, 41

Koekemoer, A. M., et al. 2002, in The 2002 HST Calibration Workshop : Hubble after the Installation of the ACS and the NICMOS Cooling System, ed. S. Arribas, A. Koekemoer, & B. Whitmore, 337

Komatsu, E., et al. 2011, ApJS, 192, 18

Kowal, C. T. 1968, AJ, 73, 1021

Kowalski, M., et al. 2008, ApJ, 686, 749

Koyama, Y., et al. 2008, MNRAS, 391, 1758

Kroupa, P. 2001, MNRAS, 322, 231

Kuntschner, H., et al. 2006, MNRAS, 369, 497

Lamareille, F., et al. 2009, A&A, 495, 53

Lampeitl, H., et al. 2010, ApJ, 722, 566

Lauer, T. R., et al. 2005, AJ, 129, 2138

Lemaux, B. C., et al. 2010, ApJ, 716, 970

Leonard, D. C. 2010, The Astronomer's Telegram, 2750, 1

Li, W., et al. 2011, MNRAS, 412, 1441

Lidman, C., et al. 2008, A&A, 489, 981

Lotz, J. M., Primack, J., & Madau, P. 2004, AJ, 128, 163

LSST Science Collaboration. 2009, ArXiv e-prints

Mannucci, F., et al. 2005, A&A, 433, 807

Mathews, W. G. & Brighenti, F. 2003, ApJ, 599, 992

Mei, S., et al. 2006a, ApJ, 639, 81

Mei, S., et al. 2009, ApJ, 690, 42

Mei, S., et al. 2006b, ApJ, 644, 759

Melbourne, J., et al. 2007, AJ, 133, 2709

Meyers, J., et al. 2012, ApJ, 750, 1

Minkowski, R. 1941, PASP, 53, 224

Morokuma, T., et al. 2010, PASJ, 62, 19

Neill, J. D., et al. 2009, ApJ, 707, 1449

Nobili, S. & Goobar, A. 2008, A&A, 487, 19

Nugent, P., Kim, A., & Perlmutter, S. 2002, PASP, 114, 803

Oke, J. B., et al. 1995, PASP, 107, 375

Osterbrock, D. E. & Ferland, G. J. 2006, Astrophysics of gaseous nebulae and active galactic nuclei

Peng, C. Y., et al. 2010, AJ, 139, 2097

Percival, W. J., et al. 2010, MNRAS, 401, 2148

Perets, H. B., et al. 2010, Nature, 465, 322

Perlmutter, S., et al. 1999, ApJ, 517, 565

Perlmutter, S., et al. 1997, ApJ, 483, 565

Phillips, M. M. 1993, ApJ, 413, L105

Postman, M., et al. 2005, ApJ, 623, 721

Postman, M., Lubin, L. M., & Oke, J. B. 1998, AJ, 116, 560

—. 2001, AJ, 122, 1125

Ramírez, I., Allende Prieto, C., & Lambert, D. L. 2007, A&A, 465, 271

Rest, A., et al. 2001, AJ, 121, 2431

Rettura, A., et al. 2010, ApJ, 709, 512

Riess, A. G., et al. 1998, AJ, 116, 1009

Riess, A. G., et al. 2001, ApJ, 560, 49

Riess, A. G., et al. 2007, ApJ, 659, 98

Riess, A. G., et al. 2004, ApJ, 607, 665

Ripoche, P. et al. 2011, in prep

Rix, H.-W., et al. 2004, ApJS, 152, 163

Rockosi, C., et al. 2010, in Society of Photo-Optical Instrumentation Engineers (SPIE) Conference Series, Vol. 7735, Society of Photo-Optical Instrumentation Engineers (SPIE) Conference Series

Rodney, S. A., et al. 2012, ApJ, 746, 5

Roming, P. W. A., et al. 2005, Space Sci. Rev., 120, 95

Rosati, P., et al. 1999, AJ, 118, 76

Rosati, P., et al. 2009, A&A, 508, 583

Rose, J. A. 1984, AJ, 89, 1238

Rubin, D., et al. 2012, ArXiv e-prints

Rubin, D. et al. 2013, in prep

Sandage, A. & Tammann, G. A. 1993, ApJ, 415, 1

Santos, J. S., et al. 2009, A&A, 501, 49

Sarzi, M., et al. 2006, MNRAS, 366, 1151

Scannapieco, E. & Bildsten, L. 2005, ApJ, 629, L85

Schawinski, K., et al. 2007, ApJS, 173, 512

Schechter, P. 1976, ApJ, 203, 297

Schiavon, R. P. 2007, ApJS, 171, 146

Schlegel, D. J., Finkbeiner, D. P., & Davis, M. 1998, ApJ, 500, 525

Sirianni, M., et al. 2005, PASP, 117, 1049

Stanford, S. A., et al. 2005, ApJ, 634, L129

Stanford, S. A., Eisenhardt, P. R., & Dickinson, M. 1998, ApJ, 492, 461

Stanford, S. A., et al. 2002, AJ, 123, 619

Strazzullo, V., et al. 2010, A&A, 524, A17+

Suh, H., et al. 2011, ApJ, 730, 110

Sullivan, M., et al. 2010, MNRAS, 406, 782

Sullivan, M., et al. 2003, MNRAS, 340, 1057

Sullivan, M., et al. 2006, ApJ, 648, 868

Suzuki, N., et al. 2012, ApJ, 746, 85

Sánchez-Blázquez, P., et al. 2006, MNRAS, 371, 703

Sérsic, J. L. 1968, Atlas de galaxias australes, ed. Sérsic, J. L.

Temi, P., Brighenti, F., & Mathews, W. G. 2007, ApJ, 660, 1215

—. 2009a, ApJ, 695, 1

—. 2009b, ApJ, 707, 890

Temi, P., et al. 2004, ApJS, 151, 237

Thomson, M. G. & Chary, R. R. 2011, ApJ, 731, 72

Timmes, F. X., Brown, E. F., & Truran, J. W. 2003, ApJ, 590, L83

Tomita, A., et al. 2000, AJ, 120, 123

Trager, S. C., et al. 2000a, AJ, 120, 165

Trager, S. C., et al. 2000b, AJ, 119, 1645

Trager, S. C., et al. 1998, ApJS, 116, 1

Tran, H. D., et al. 2001, AJ, 121, 2928

Tremonti, C. A., et al. 2004, ApJ, 613, 898

Tripp, R. 1998, A&A, 331, 815

Umeda, H., et al. 1999, ApJ, 522, L43

van Dokkum, P. G. & Franx, M. 1995, AJ, 110, 2027

—. 2001, ApJ, 553, 90

van Dokkum, P. G., et al. 1998, ApJ, 500, 714

Wood-Vasey, W. M., et al. 2007, ApJ, 666, 694

Worthey, G., et al. 1994, ApJS, 94, 687

Worthey, G. & Ottaviani, D. L. 1997, ApJS, 111, 377

Yan, R., et al. 2006, ApJ, 648, 281

Yi, S. K., et al. 2005, ApJ, 619, L111

APPENDIX A

Low Redshift High Signal-to-noise Ratio Host Spectroscopy

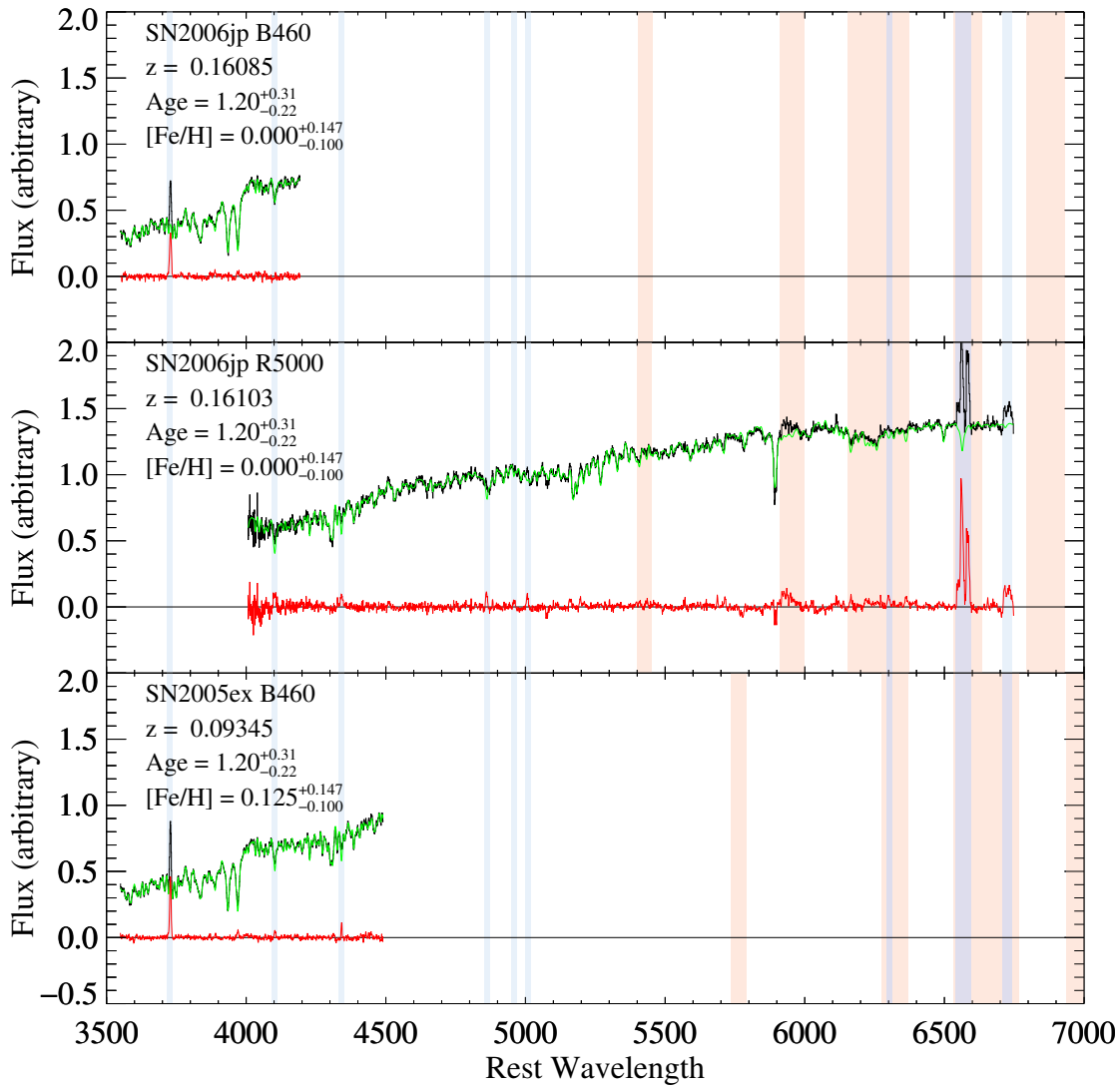

Figure A.1.
High signal-to-noise ratio spectra of SN Ia host galaxies analyzed in Part II. Data are in black, green shows the best fit PPXF model, and the residual from this model is shown in red. The emission lines [O II]λ3727, Hδ, Hγ, [O III]λ4959, [O III]λ5007, [O I]λ6300, [N II]λ6548, Hα, [N II]λ6584, [S II]λ6717 and [S II]λ6731, which are indicated in light blue, are masked during the fit, as are telluric regions, indicated in light red. The associated SN name, observing setup, and redshift are indicated for each spectrum. The indicated EZ_AGES age and [Fe/H] are derived using all of the spectra of a given galaxy. Spectra are ordered by their inferred ages.

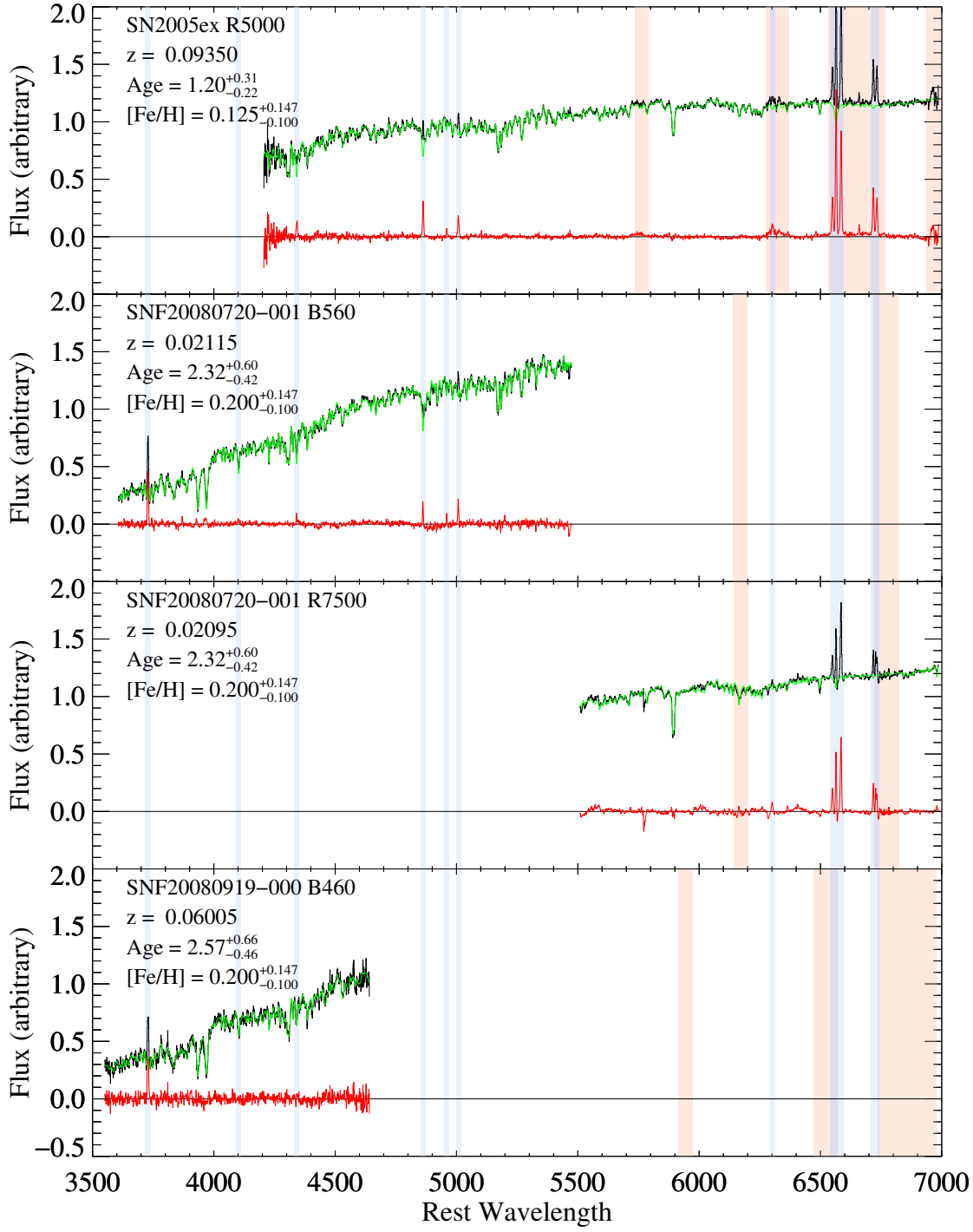

Figure A.1. High signal-to-noise ratio spectra (continued).

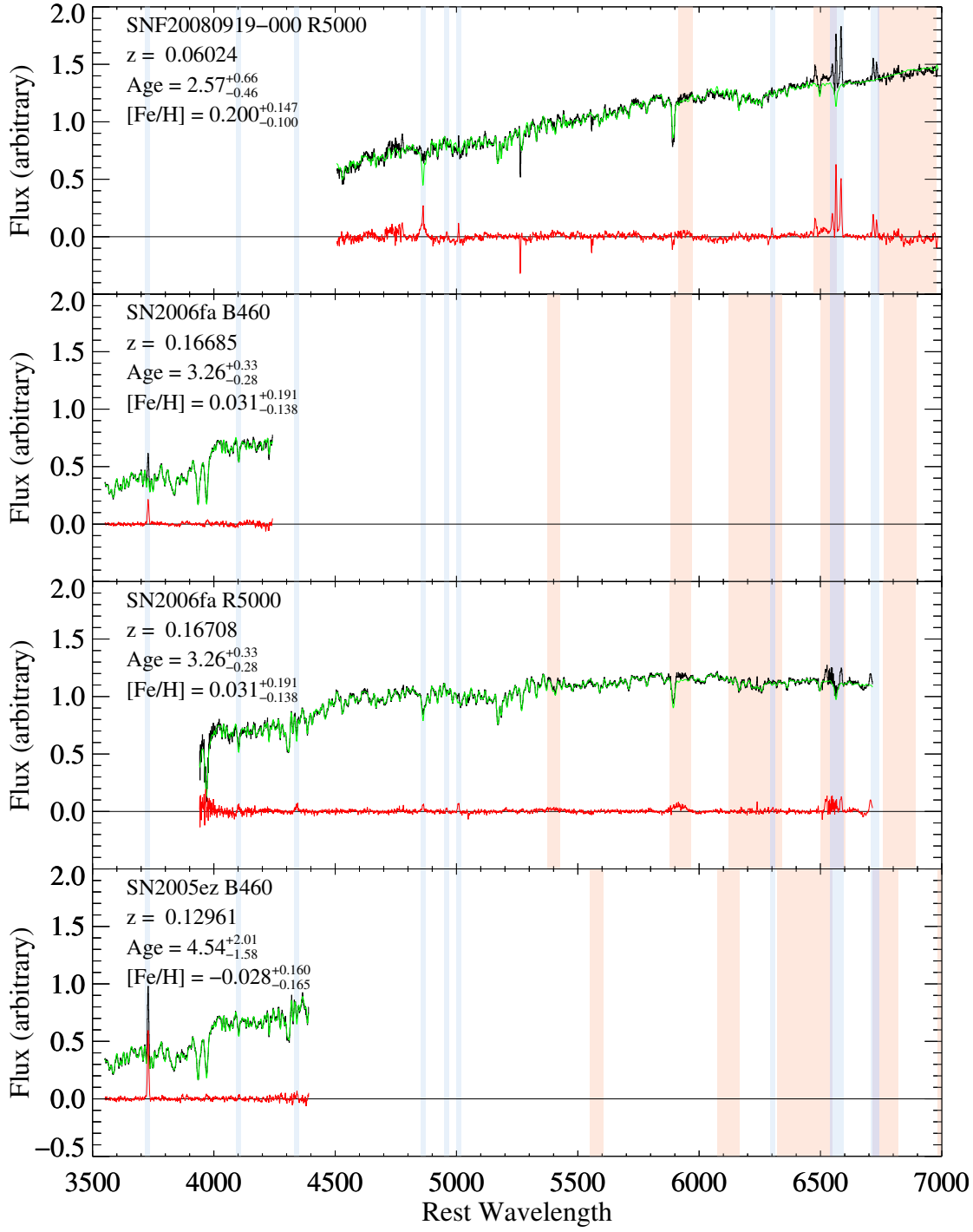

Figure A.1. High signal-to-noise ratio spectra (continued).

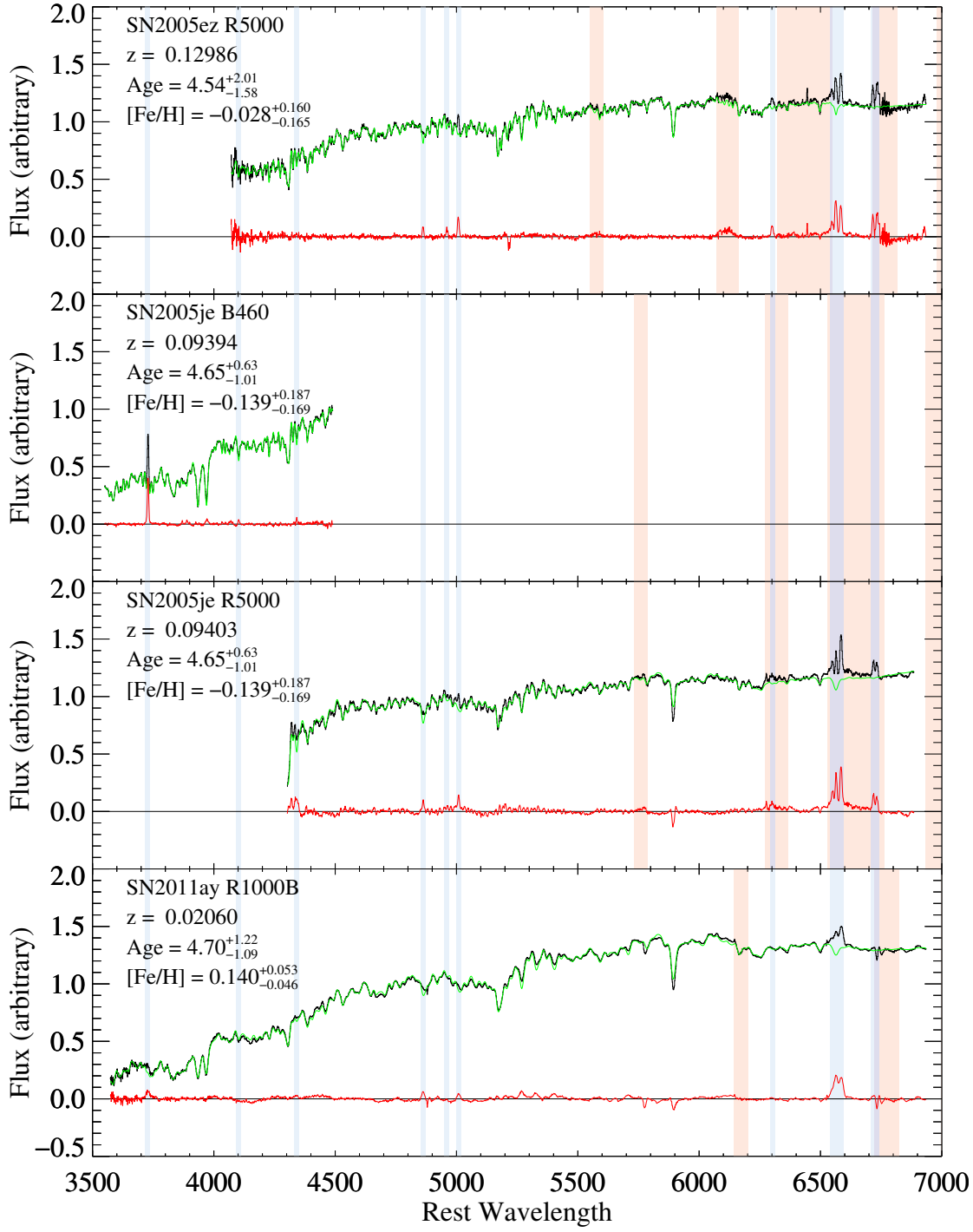

Figure A.1. High signal-to-noise ratio spectra (continued).

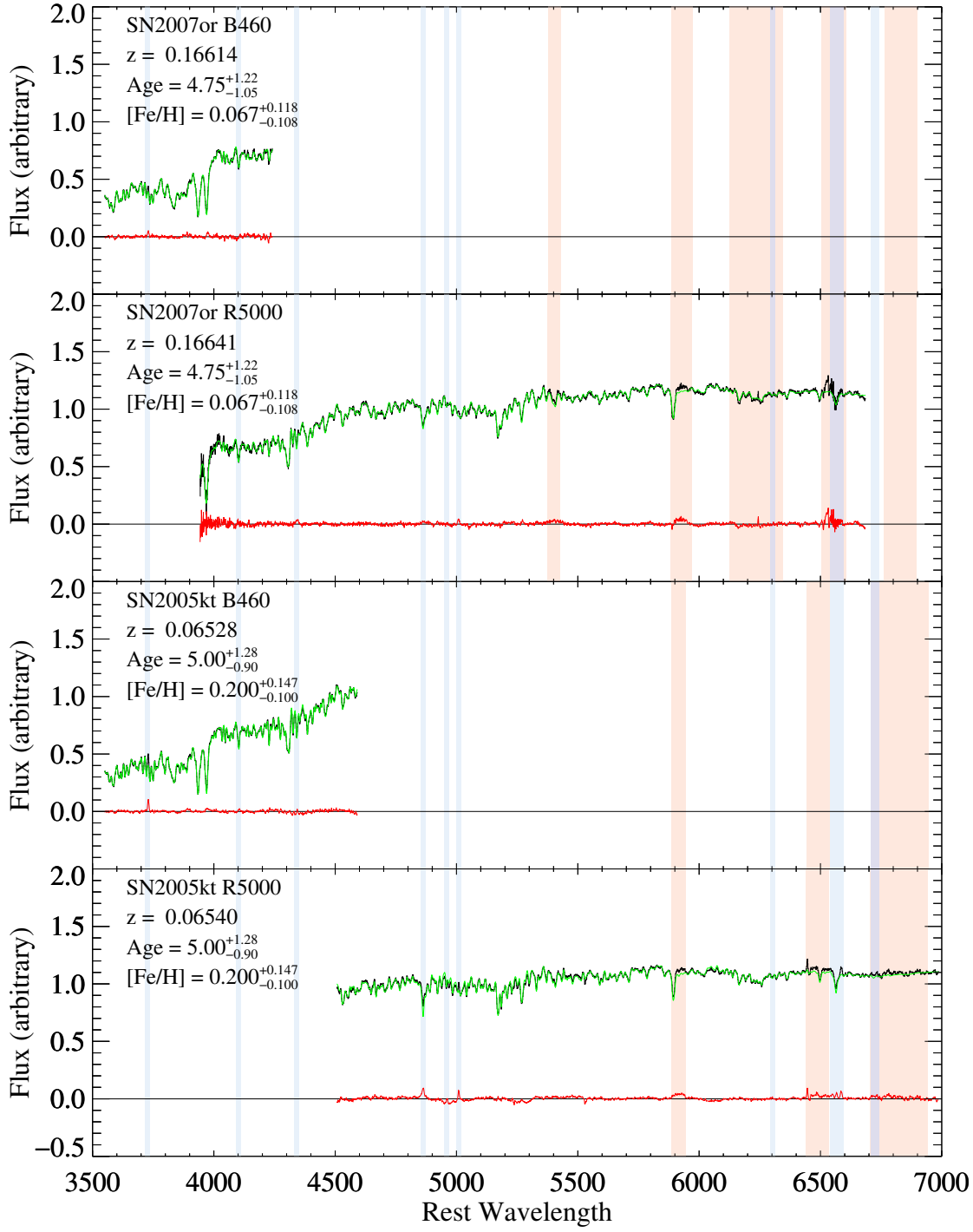

Figure A.1. High signal-to-noise ratio spectra (continued).

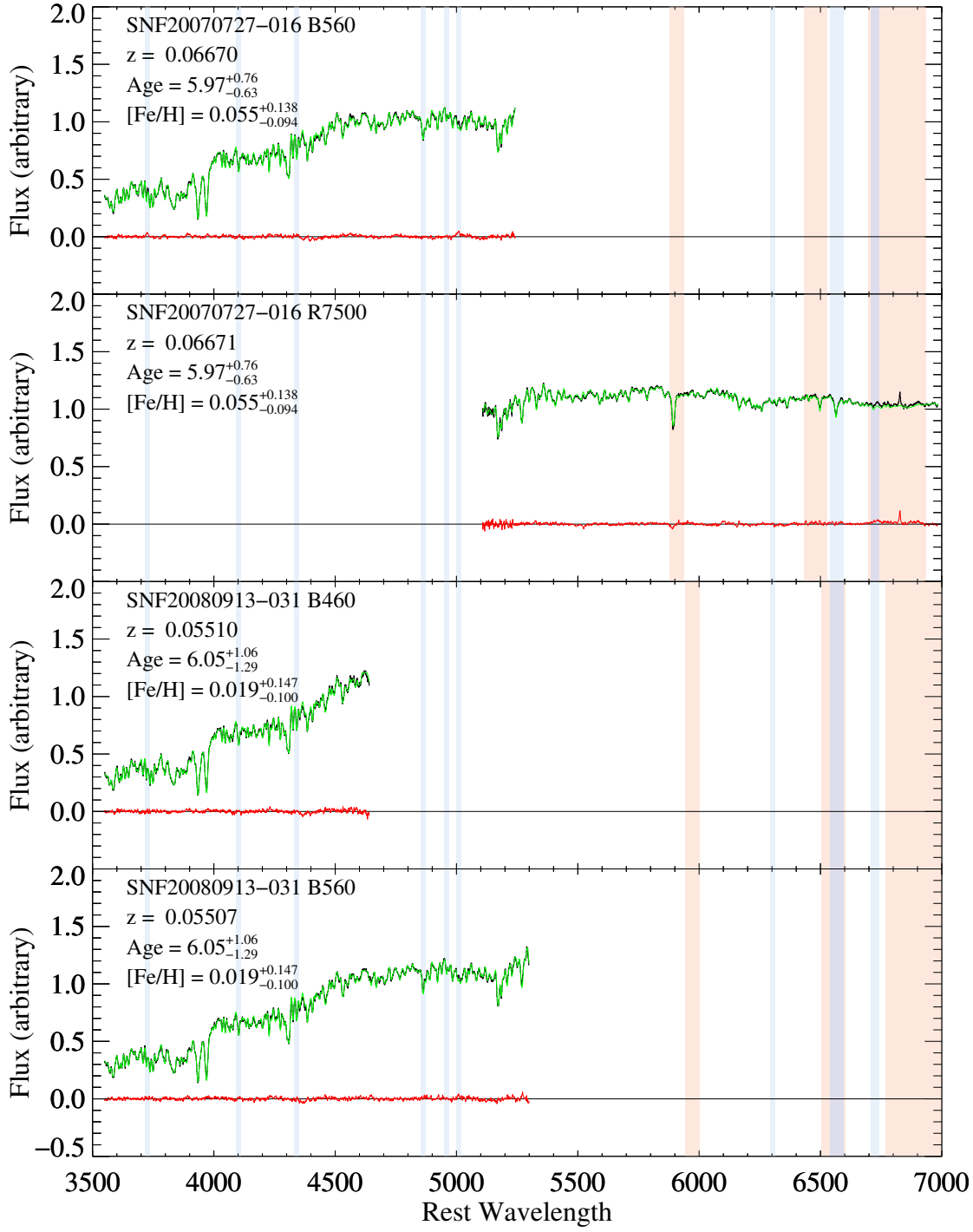

Figure A.1. High signal-to-noise ratio spectra (continued).

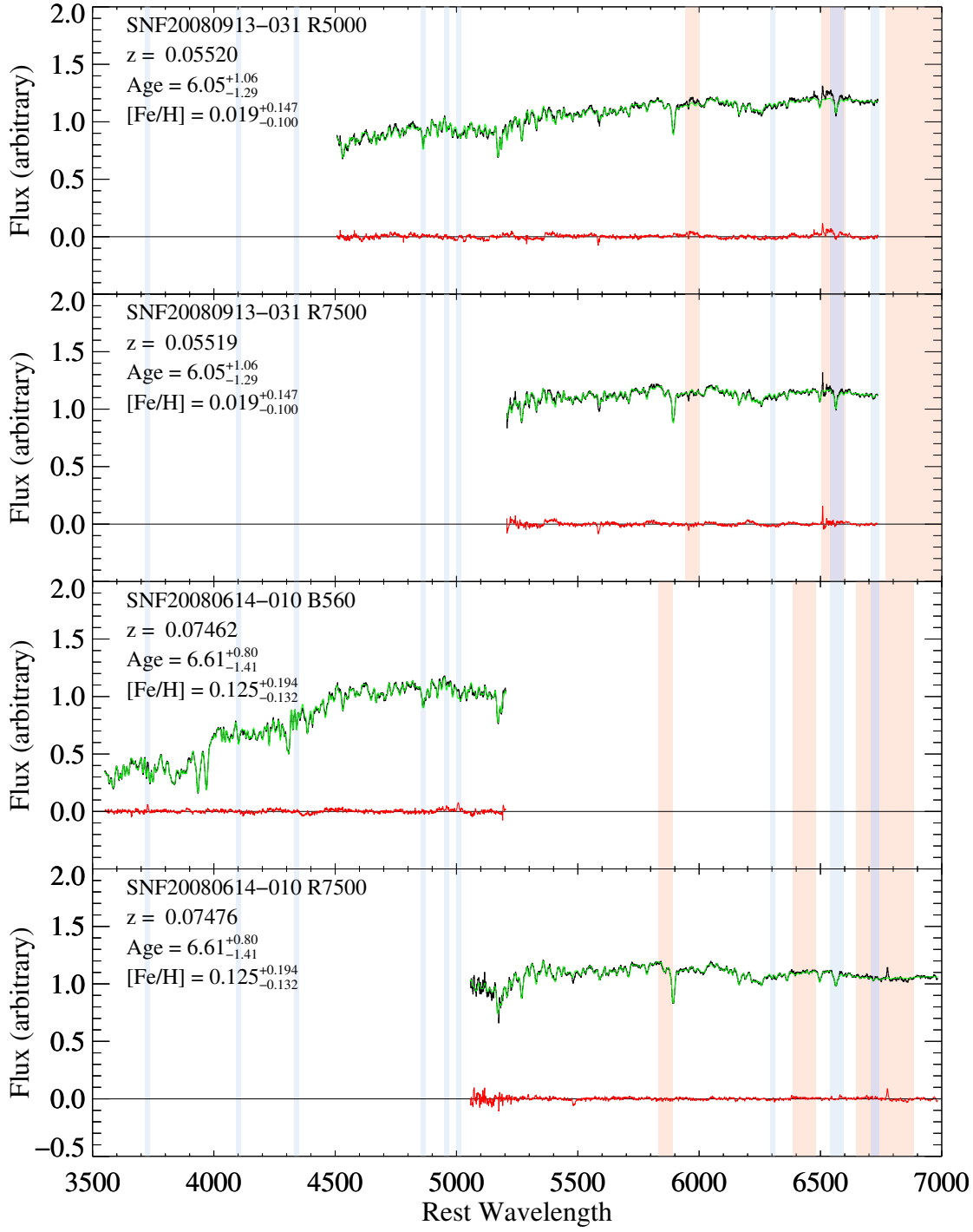

Figure A.1. High signal-to-noise ratio spectra (continued).

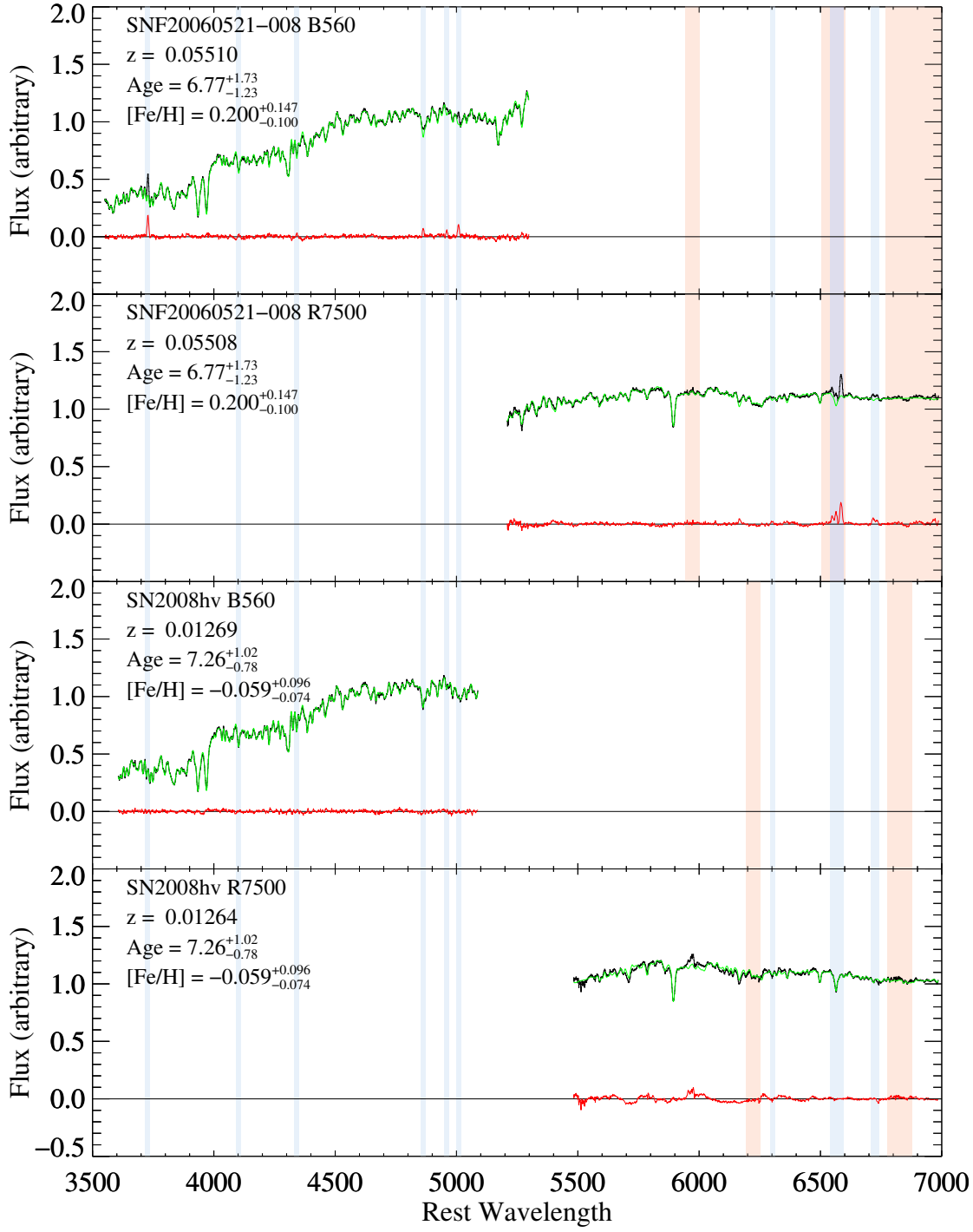

Figure A.1. High signal-to-noise ratio spectra (continued).

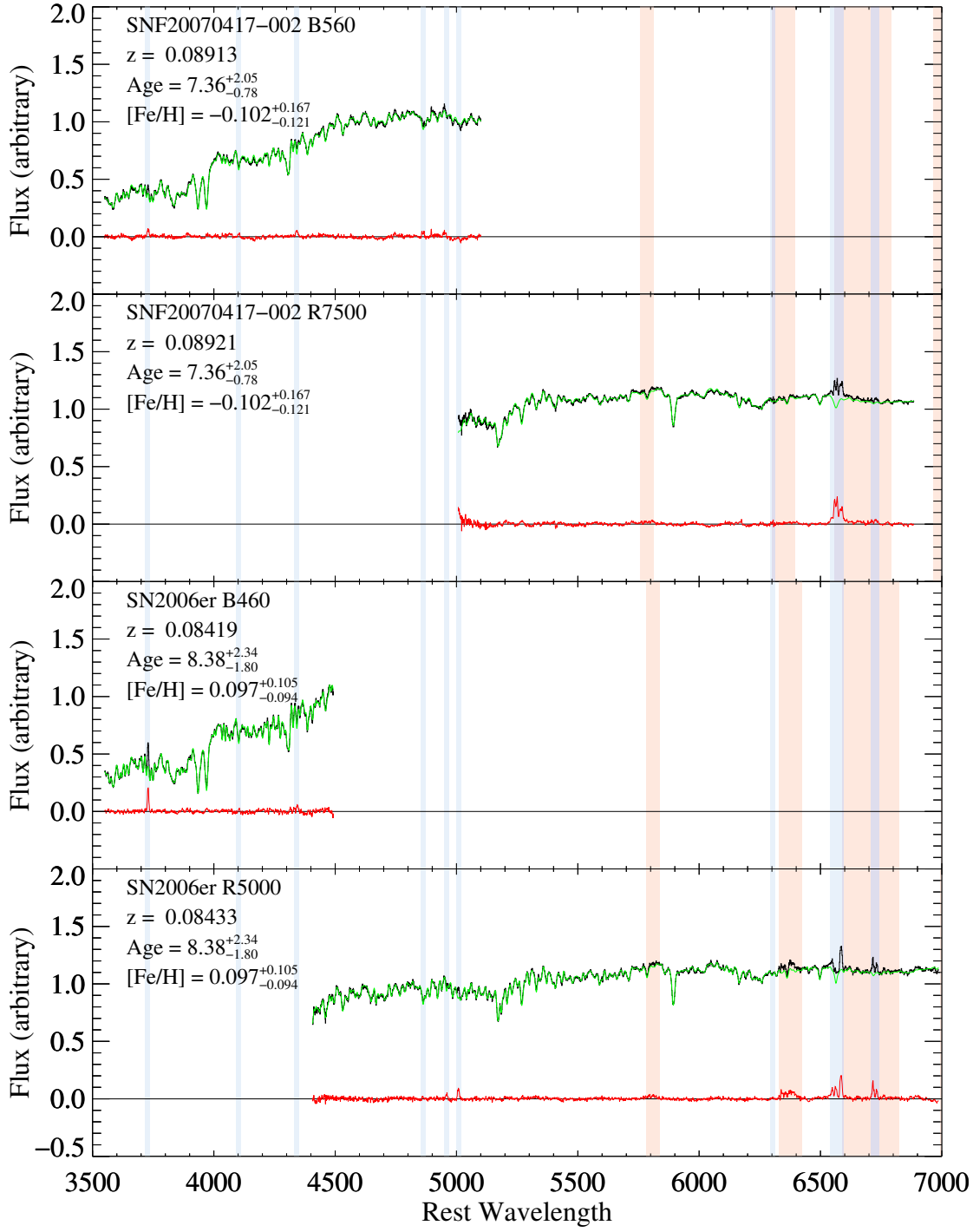

Figure A.1. High signal-to-noise ratio spectra (continued).

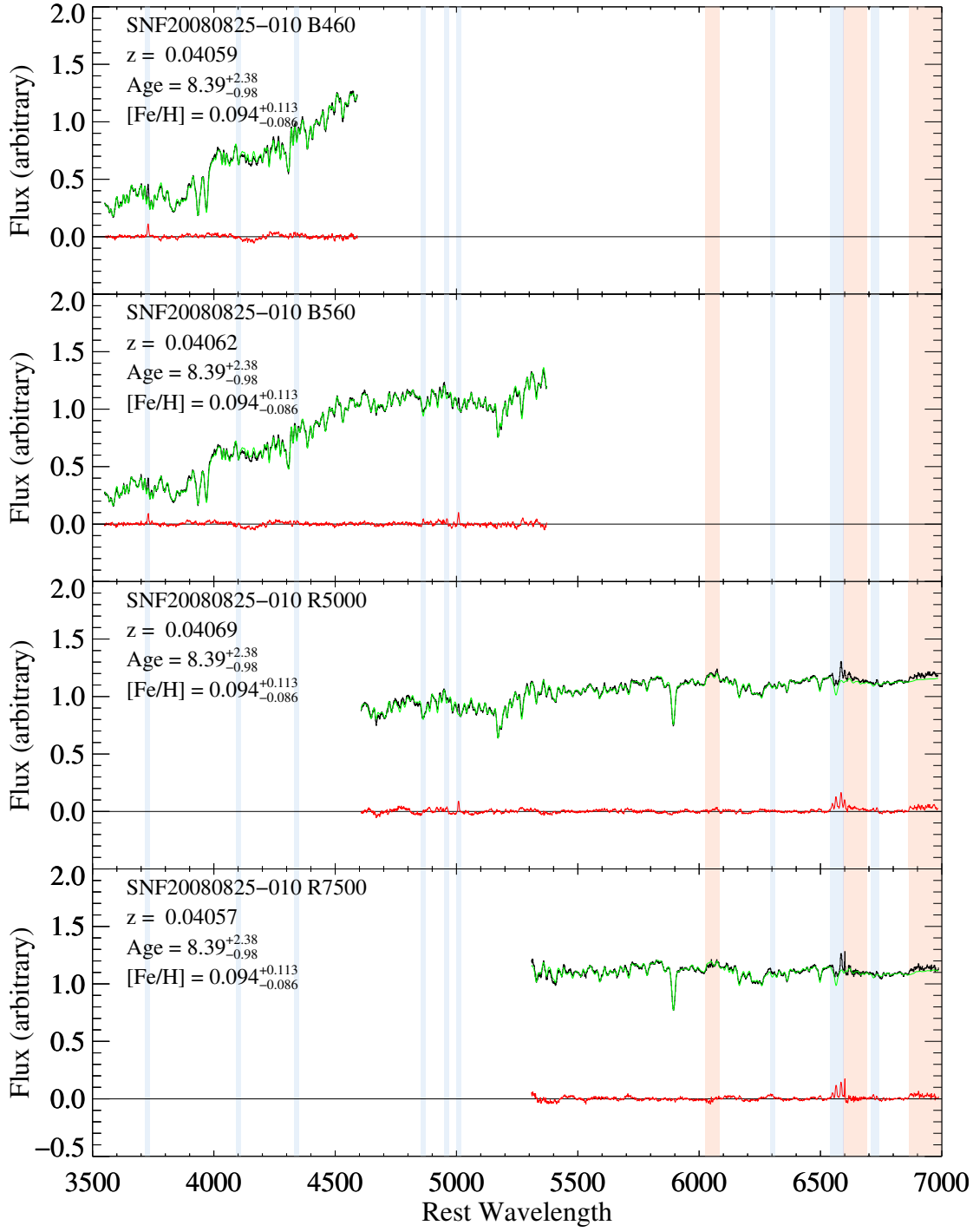

Figure A.1. High signal-to-noise ratio spectra (continued).

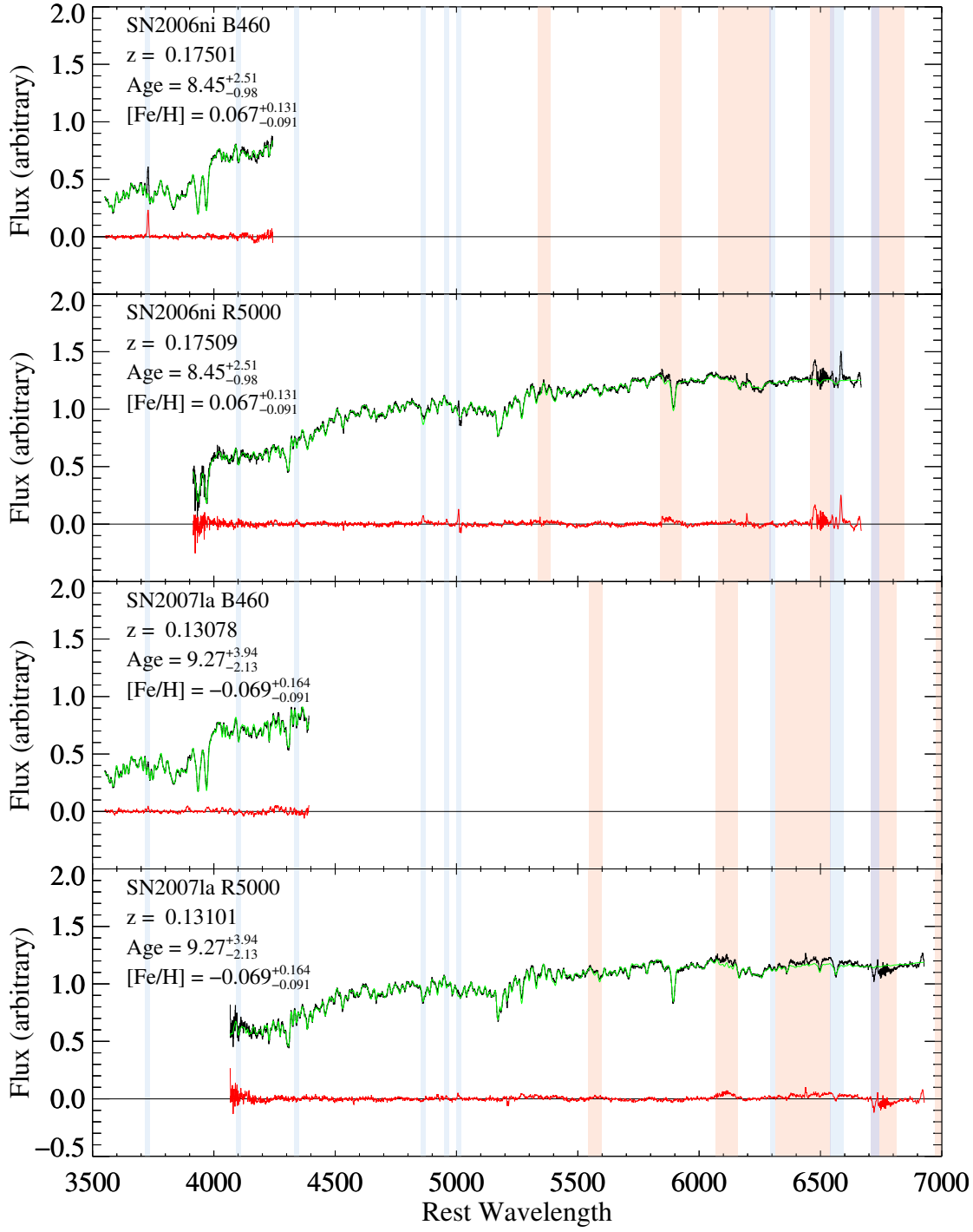

Figure A.1. High signal-to-noise ratio spectra (continued).

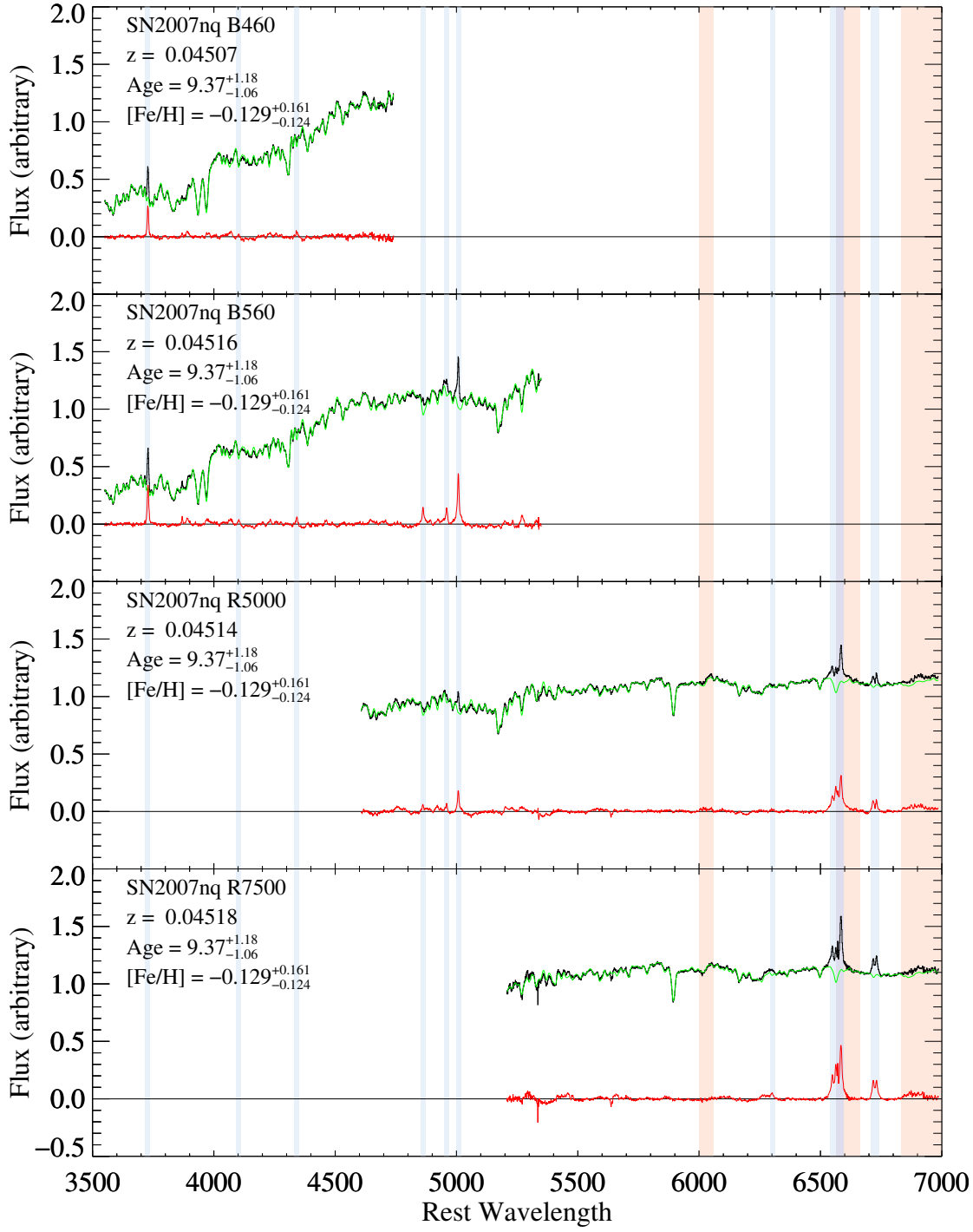

Figure A.1. High signal-to-noise ratio spectra (continued).

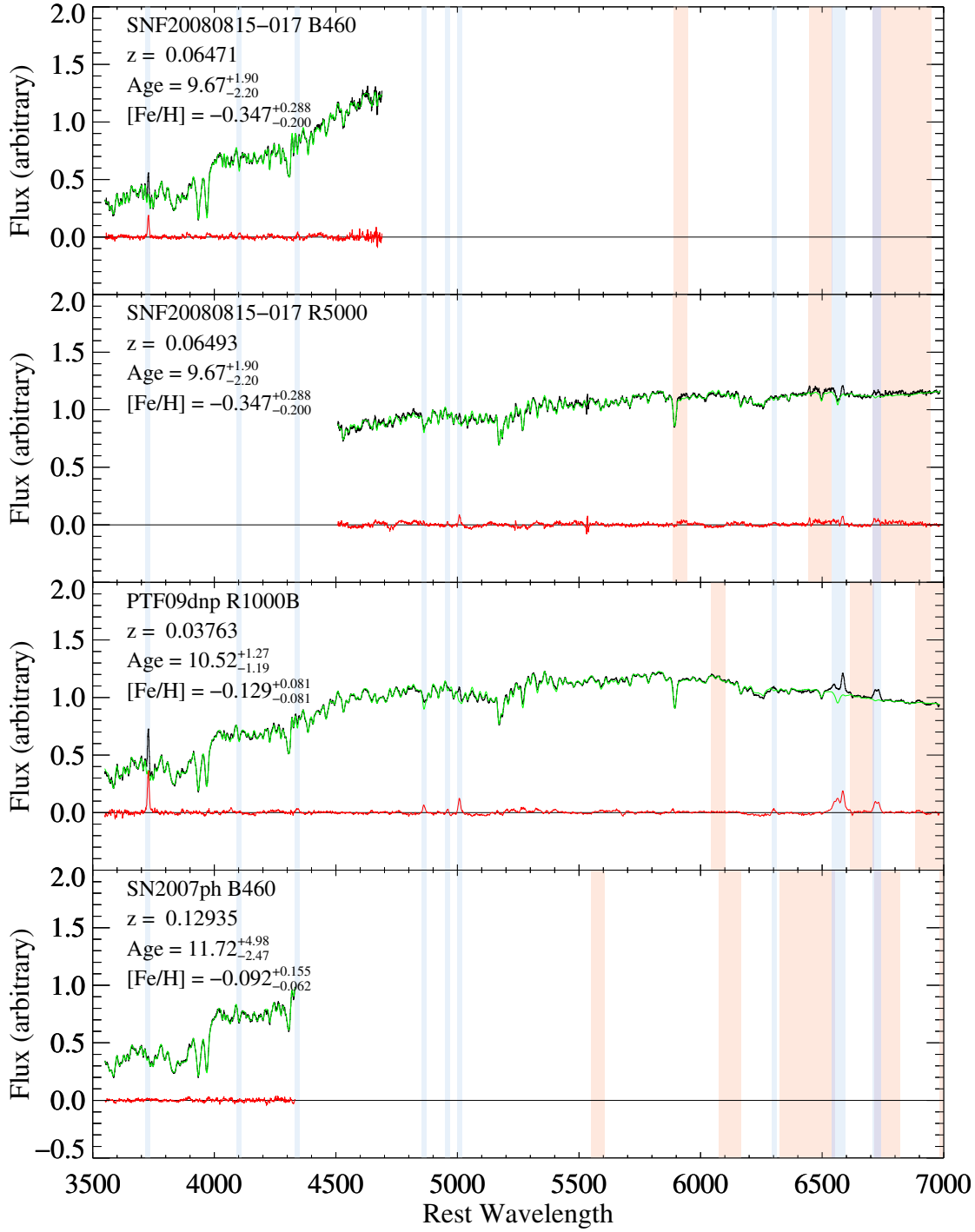

Figure A.1. High signal-to-noise ratio spectra (continued).

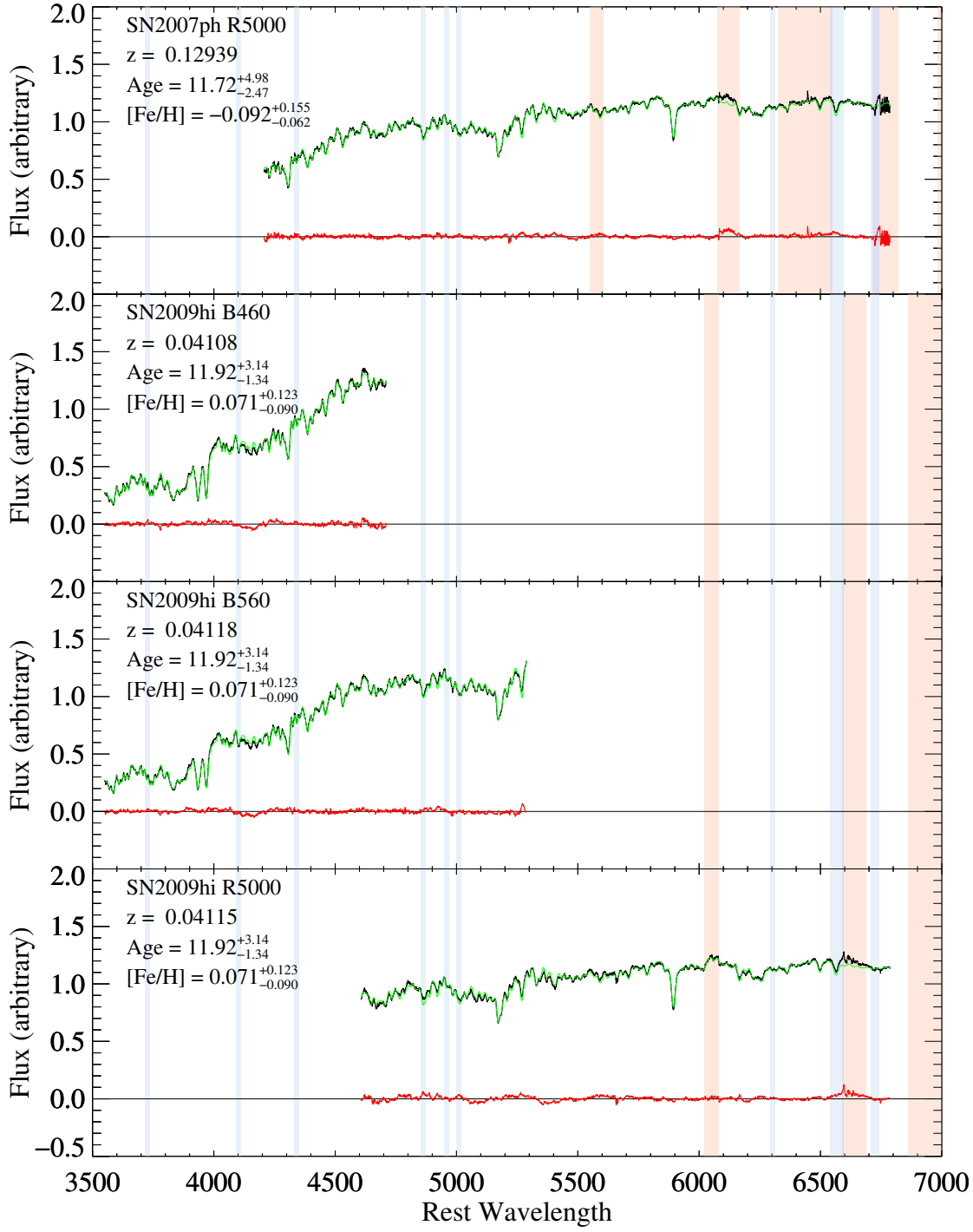

Figure A.1. High signal-to-noise ratio spectra (continued).

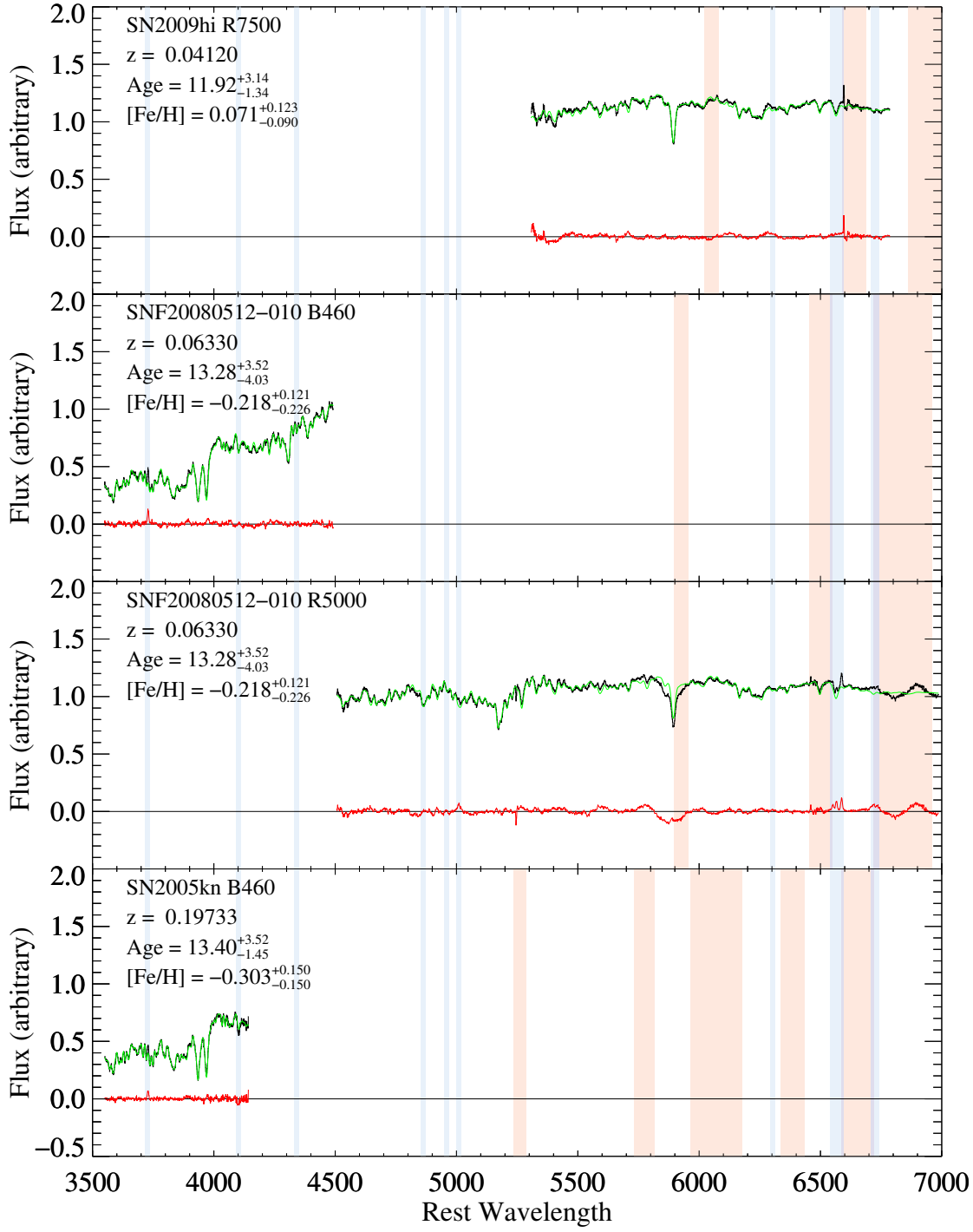

Figure A.1. High signal-to-noise ratio spectra (continued).

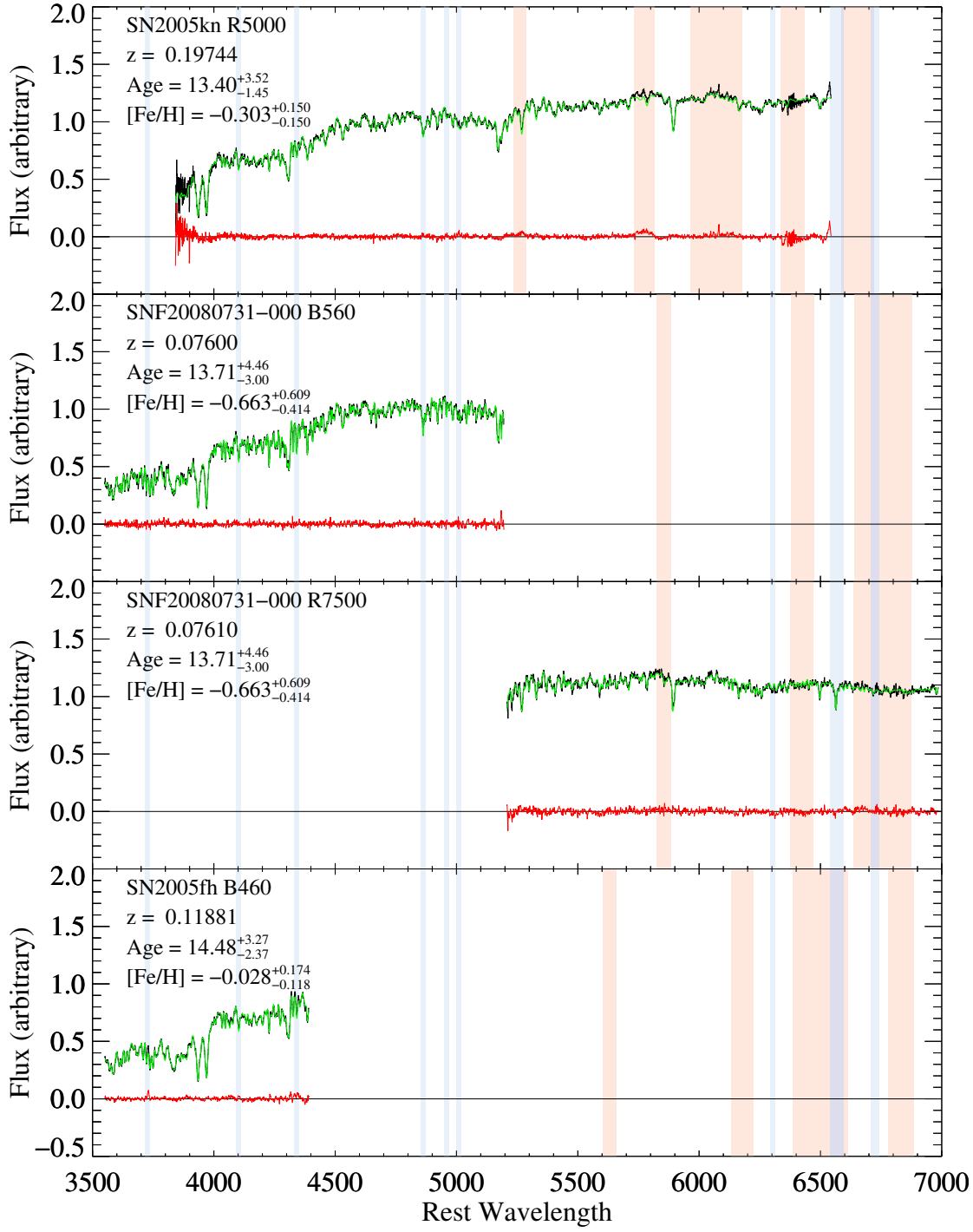

Figure A.1. High signal-to-noise ratio spectra (continued).

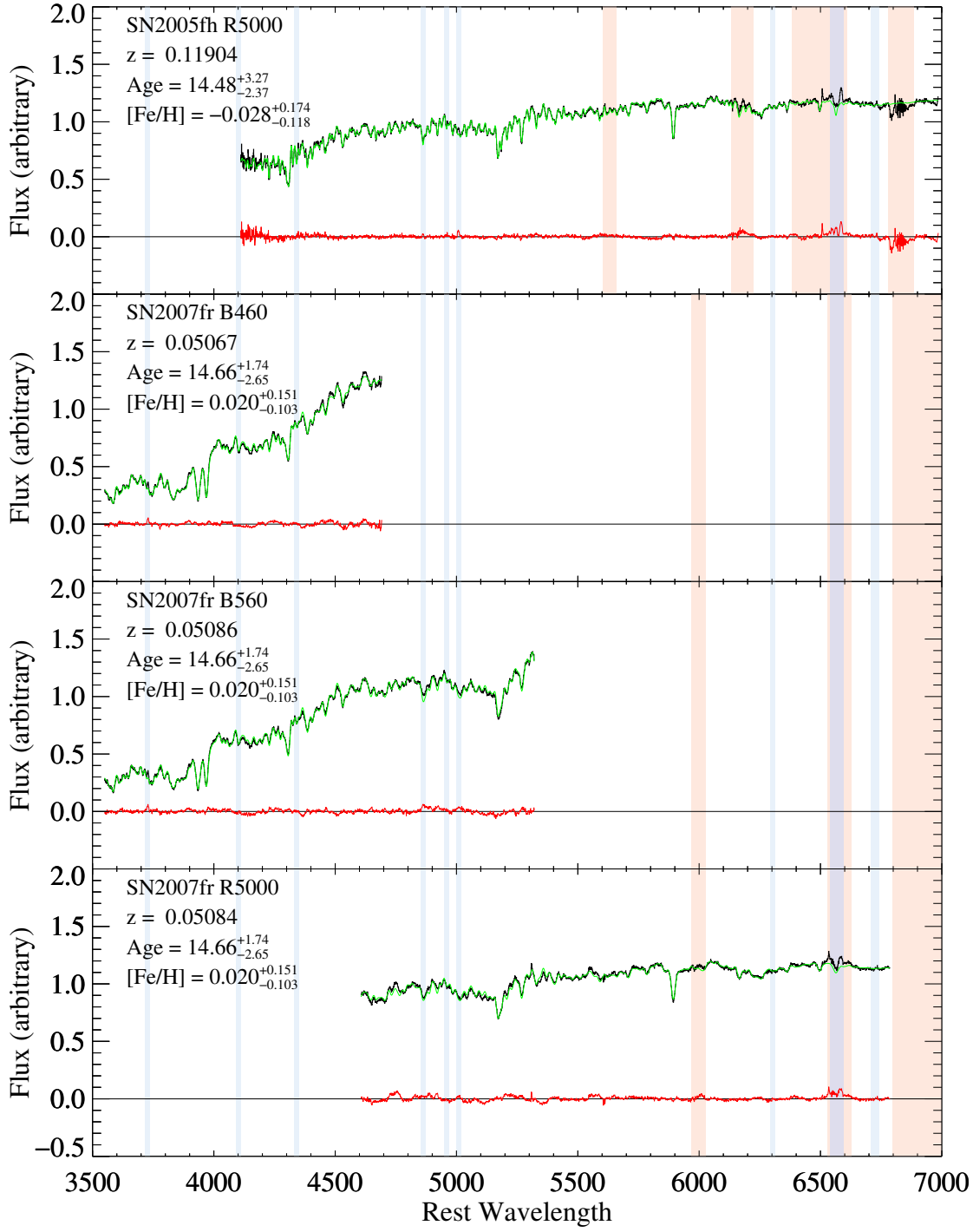

Figure A.1. High signal-to-noise ratio spectra (continued).

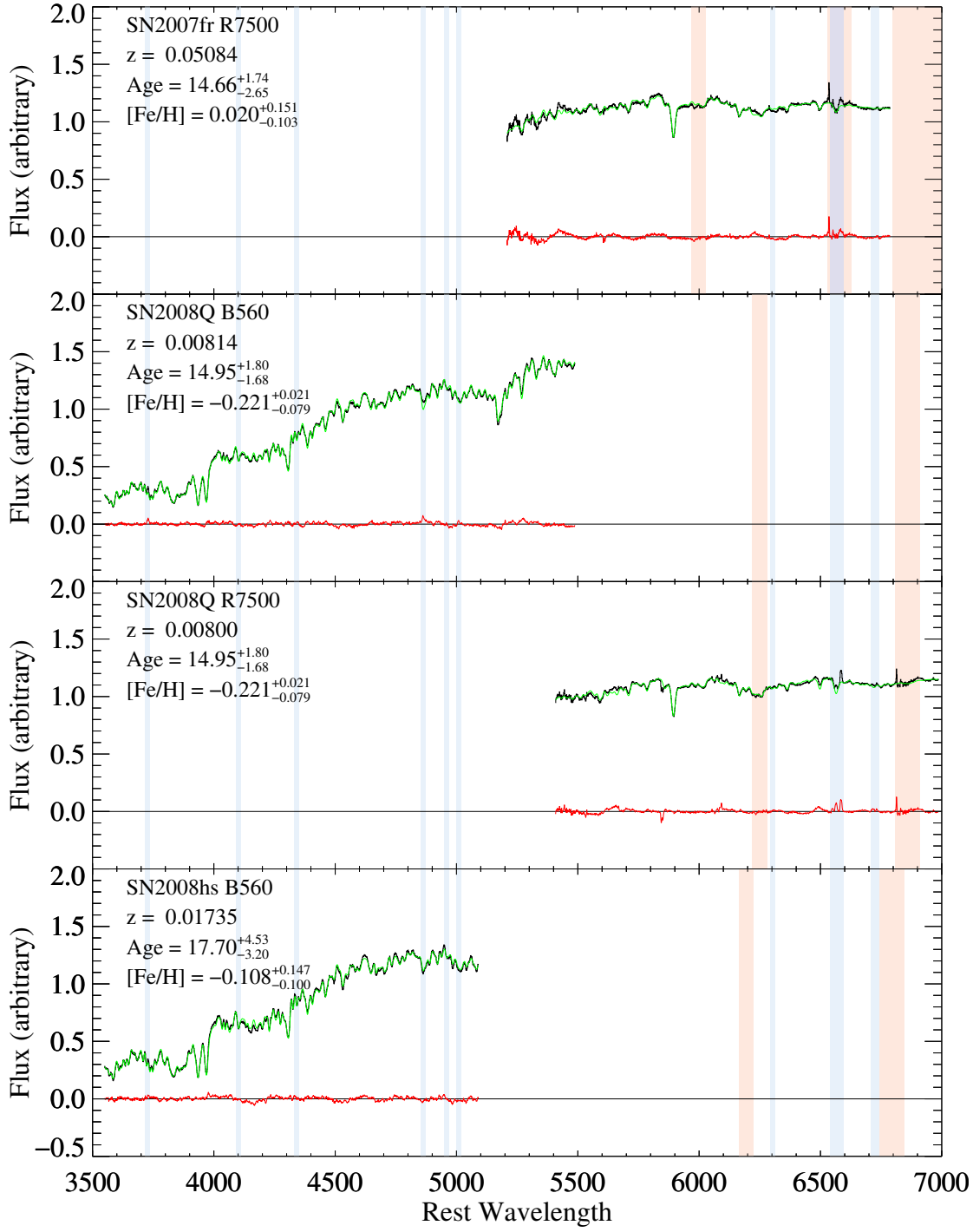

Figure A.1. High signal-to-noise ratio spectra (continued).

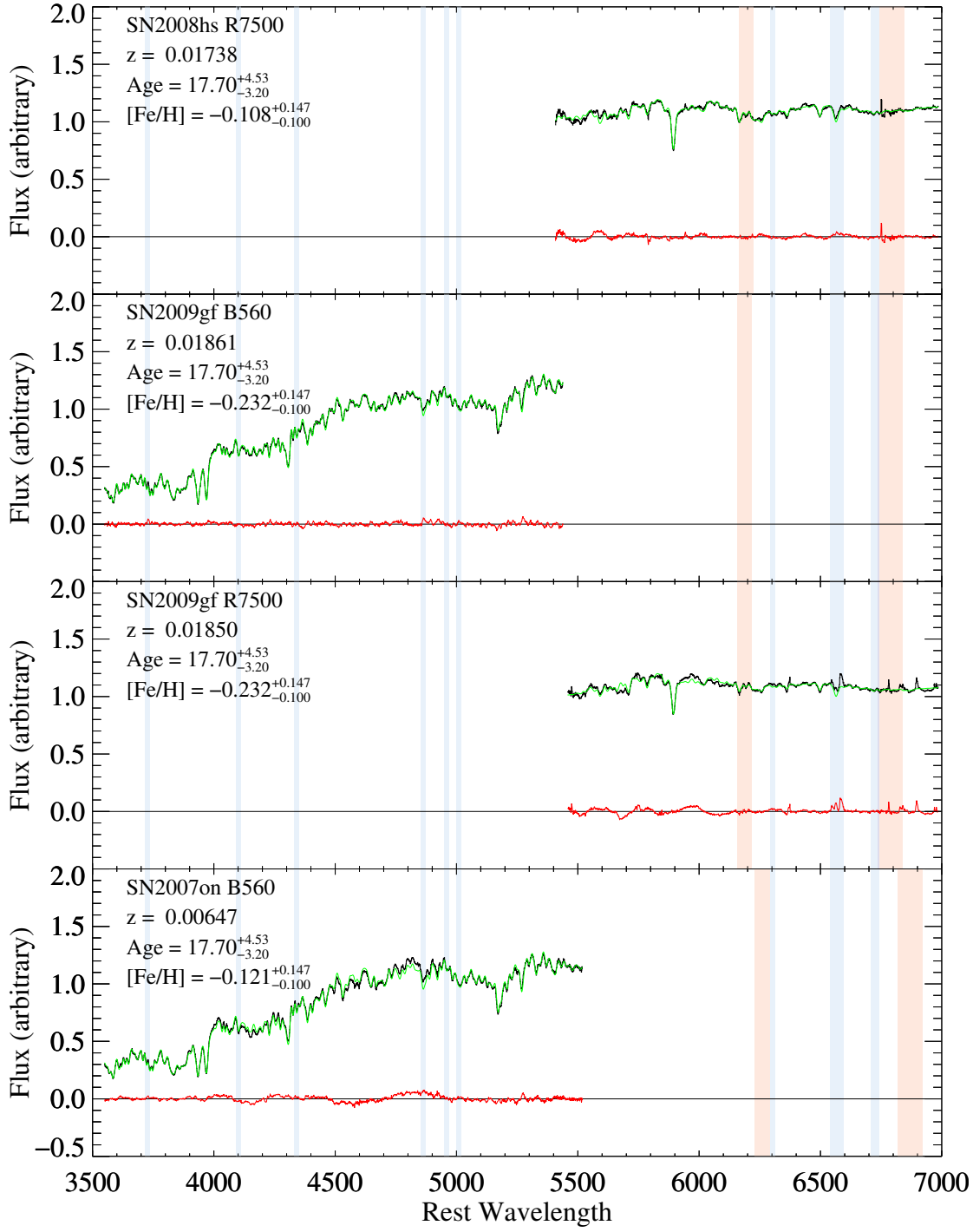

Figure A.1. High signal-to-noise ratio spectra (continued).

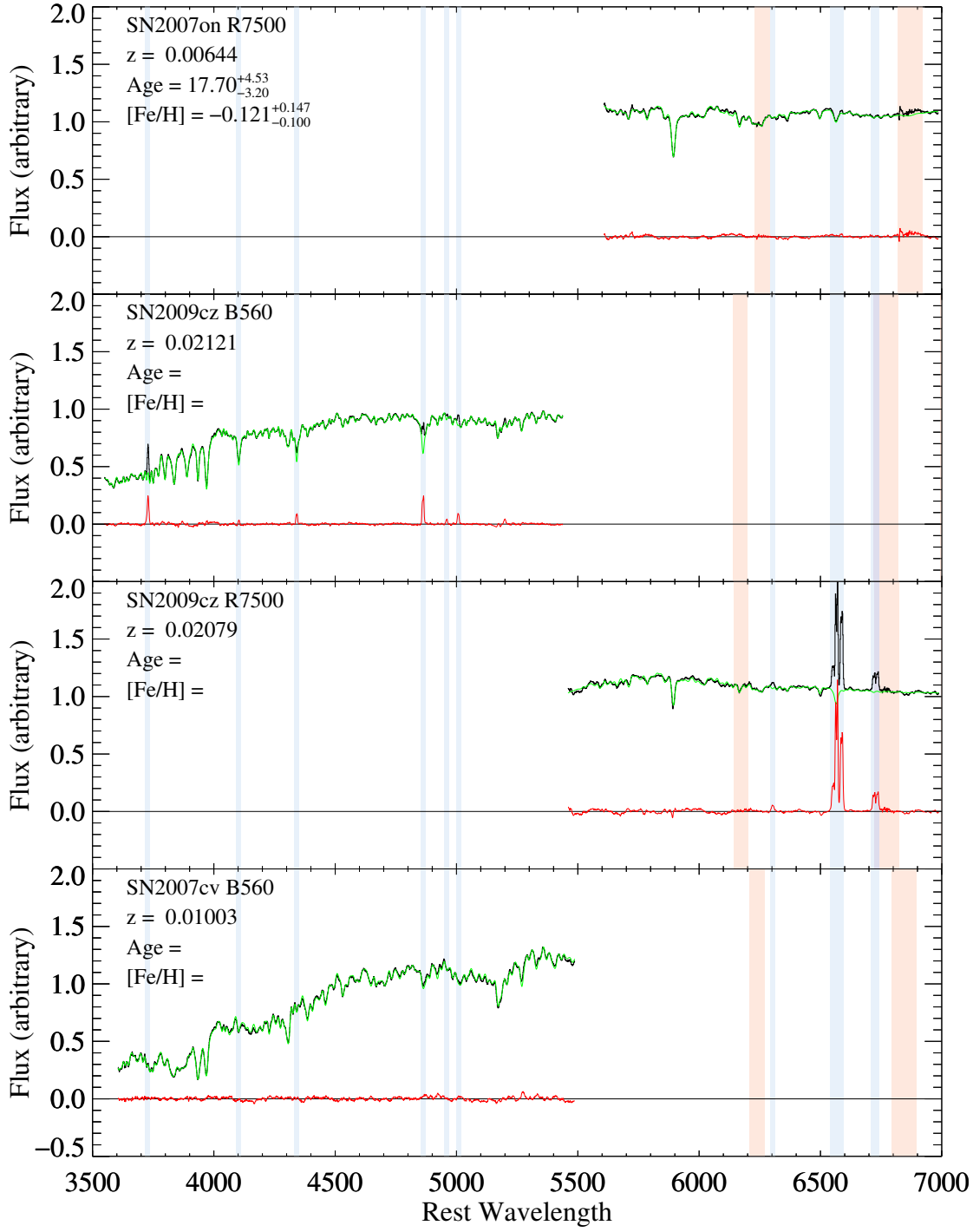

Figure A.1. High signal-to-noise ratio spectra (continued).

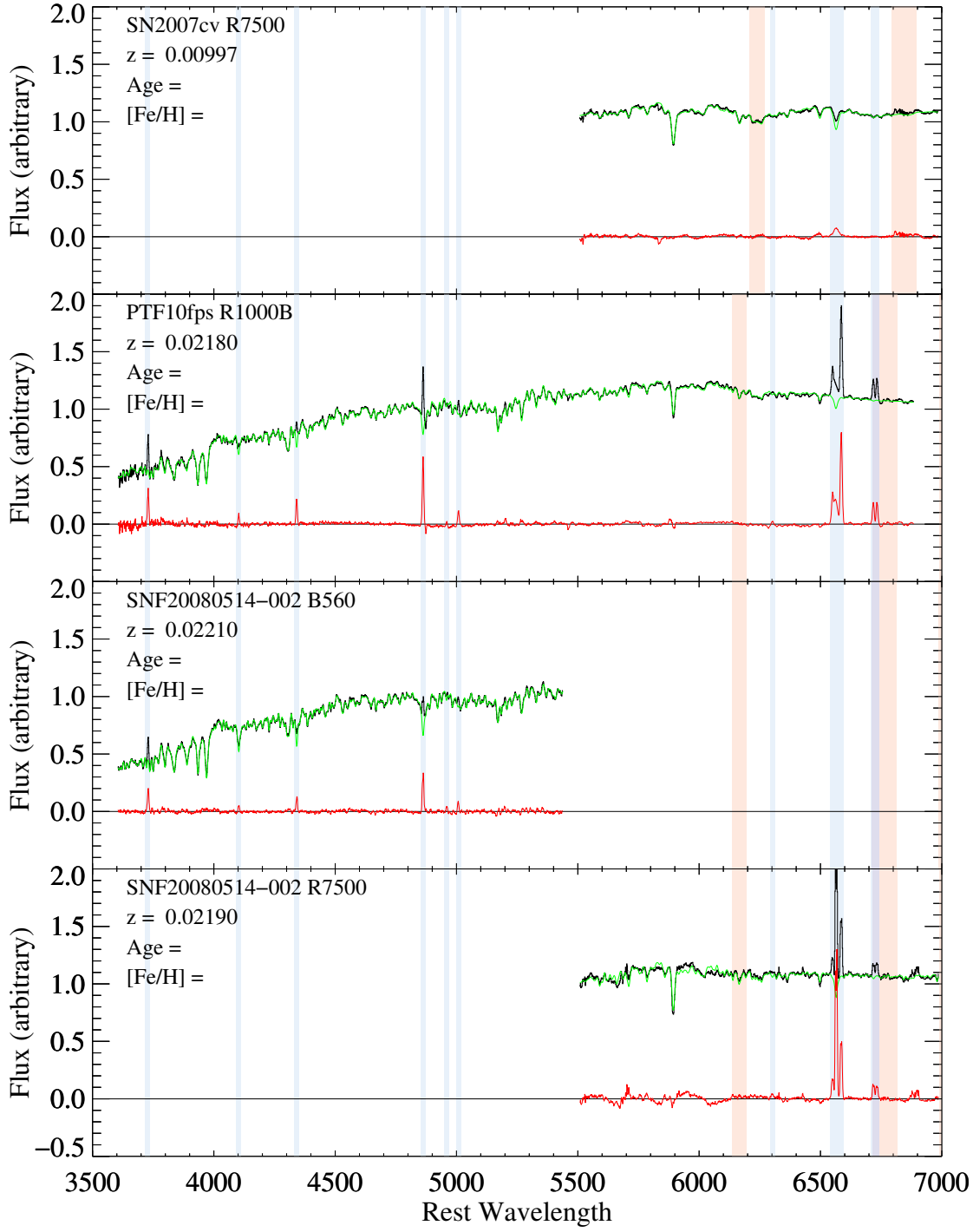

Figure A.1. High signal-to-noise ratio spectra (continued).

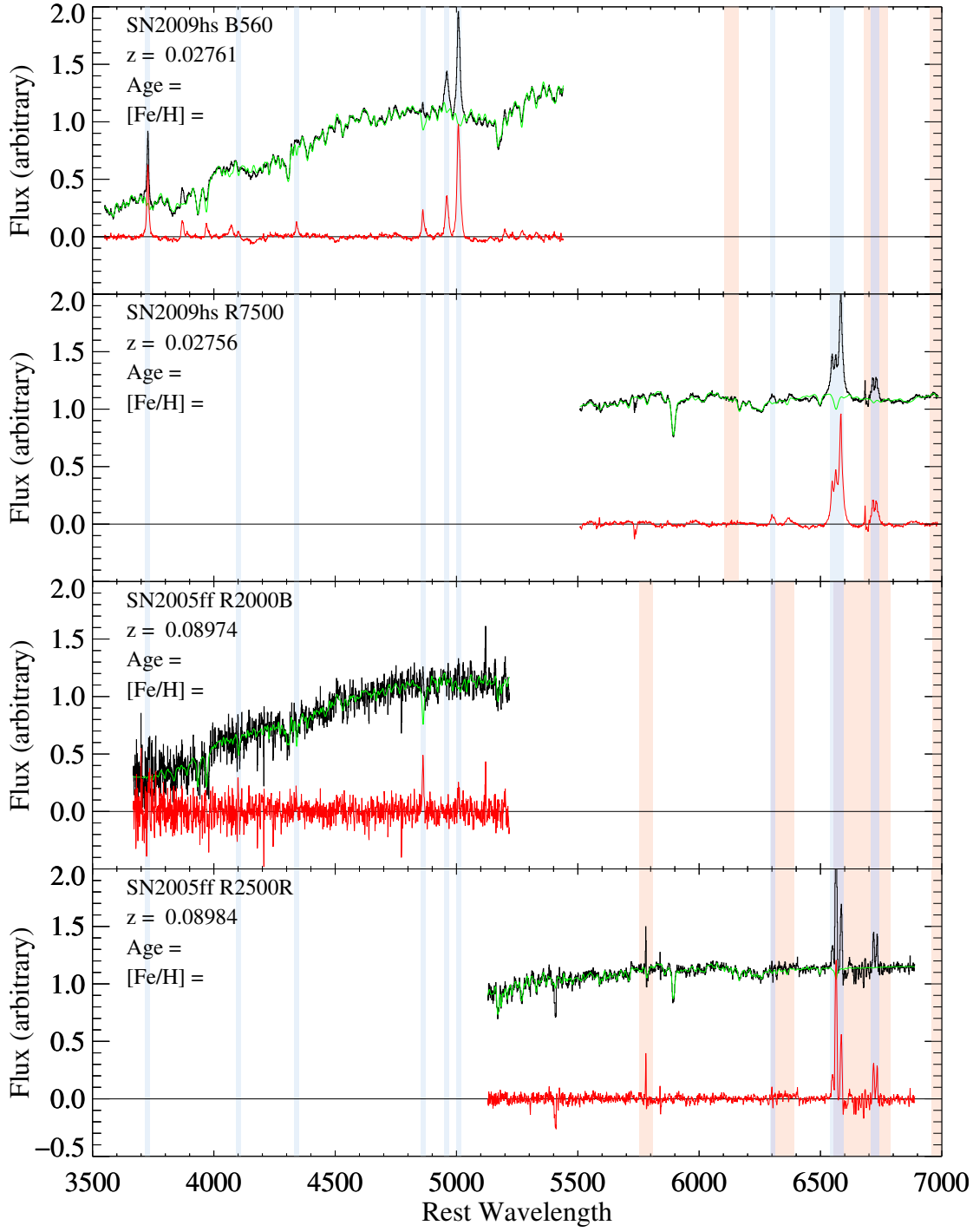

Figure A.1. High signal-to-noise ratio spectra (continued).